Università degli Studi di Parma

Dottorato di ricerca in Scienza e Tecnologia
dei Materiali Innovativi

Ciclo XXVIII (2013-2015)

Intermolecular and Intramolecular
Charge Transfer
in Functional Molecular Materials

Coordinatore:
Prof. Enrico Dalcanale

Tutors:
Prof. Anna Painelli
Prof. Francesca Terenziani

Dottorando:
Francesca Delchiaro

2016

Costei chiama inimica; e incontro a questa
congiunta esser pensando,
siccome vero, ed ordinata in pria
l'umana compagnia,
tutti fra se confederati estima
gli uomini, e tutti abbraccia
con vero amor, porgendo
valida e pronta ed aspettando aita
negli alterni perigli e nelle angosce
della guerra comune.

Giacomo Leopardi, La ginestra

Contents

List of Abbreviations

CT	charge transfer
D/A	electron donor/acceptor
NLO	nonlinear optics
PES	potential energy surface
OPA	one-photon absorption
TPA	two-photon absorption
ESA	excited-state absorption
SE	stimulated emission
PB	photobleaching
HRS	Hyper-Rayleigh Scattering
CV	Crystal Violet
BG	Brilliant Green
a. u.	arbitrary units
N/I	neutral/ionic
NIT	neutral to ionic phase transition
IR	infrared
1D/3D	one/three dimensional
$e - ph$	electron-phonon (coupling)
$e - mv$	electron-molecular vibration (coupling)
mf	mean field

(DM)TTF-CA	(4,4'-dimethyl-)tetrathiafulvalene-chloranil
TTF-2,5Cl$_2$BQ	TTF-2,5-dichloro-p-benzoquinone
TTF-BA	TTF-bromanil
TMB-TCNQ	3,3',5,5'-tetramethylbenzidine -7,7',8,8'-tetracyanoquinodimethane
BT-TCNQ	2,7-didecyl[1]benzothieno-[3,2-b][1] benzothiophene-TCNQ
DBTTF-TCNQ	Dibenzotetrathiafulvalene-TCNQ
TMPD-TCNQ	tetramethyl-p-phenylenediamine-TCNQ
TMB-CA	3,3',5,5'-tetramethyl-benzidine-TCNQ
ClMePD-	2-chloro-5-methyl$p$-phenylenediamine-
DMeDCNQI	2,5-dimethyldicyanoquinonediimine
MO	molecular orbital
PCM	Polarizable Continuum Model
(TD)DFT	(Time Dependent) Density Functional Theory
ZINDO	intermediate neglect of differential overlap with spectrosocpic parametrization
(U)/RHF	(un)/restricted Hartree Fock
TTF-PTM	TTF-perchlorotriphenylmethyl
MPTTF-PTM	N'-Vinylenephenyl-2-(1,3-dithiol-2-ylidene) -(1,3)-dithiolo[4,5-c]pyrrole-2,3,5,6-PTM
Fc-PTM	ferrocene-perchlorotriphenylmethyl

Introduction

Molecular multifunctional materials are currently investigated for advanced applications in electronics and photonics. Smart molecular materials for organic electronics are in demand for the development of plastic light-emitting diodes (OLEDs) [1], innovative photovoltaic and solar cells [2]. Photonic materials may find novel applications in microfabrication [3], drug delivery [4], in vivo optical microscopy [5, 6], photodynamic therapy [7, 8]. In a different context, plants use solar antennae, an intriguing example of multifunctional molecular materials, to capture incident photons and efficiently transmit the excitation energy to reaction centres, where photosynthesis is initiated [9].

Molecular multifunctional materials offer a wide spectrum of interesting features. They are low-weight materials and can be easily and conveniently processed at low temperatures on flexible substrates with large area-coverage. They do not contain rare elements and are most often bio-compatible and easy to degrade. The powerful tools of molecular and supramolecular synthesis offer unlimited possibilities to build structures with different properties and complexity with no counterpart in traditional hard materials for electronics. To fulfil the promise of molecular materials for advanced applications and to fully exploit the enormous potential of synthetic chemistry in the field, it is fundamental to be able to guide the design of new materials and in this respect it is important to understand the physics that governs their complex behaviour.

Delocalized electrons either within each single molecule or among different molecules are a key towards smart behaviour and, charge transfer (CT) degrees of freedom represent a strategy towards intra or intermolecular delocalization as well as add the interest features of the tunability of CT energies, a strong coupling to internal or external electric fields etc. In this Thesis we undertook a study, mainly from a theoretical perspective, of intra and intermolecular CT in molecular materials of interest for advanced applications.

The first Chapter is devoted to intramolecular CT, as observed in CT dyes, a large and interesting family of π-conjugated molecules decorated with electron donor (D) and acceptor (A) groups in different geometries, ranging from simple dipolar D-π-A dyes, to quadrupolar D-π-A-π-D or A-π-D-π-A, to octupolar DA_3 or AD$_3$ structures. The

spectral properties of these dyes can be tuned affecting the electron-donating/accepting character of D/A groups and by modifying the bridge length and structure, making them an interesting and variegated family of compounds with applications in OLED, solar cells, nonlinear optics, bioimaging etc [10, 11]. The low-energy photophysics of CT dyes is governed by charge resonance between D and A groups and can be effectively described by a family of parametric Hamiltonian, developed and extensively applied in the host laboratory, known as essential-state models [12–16]. Here we develop and validate a new essential state model for Brilliant Green, a commercial dye, whose extensive linear and nonlinear spectroscopic investigation is done in collaboration with the group of Prof. W. Wenseleers (Antwerp University) [17]. Moreover, we attack the problem of coherent oscillations observed in pump-probe measurements for CT dyes in solution upon impulsive excitation [18]. Quite interestingly, the non-adiabatic approach adopted in essential-state models, allows us to quantitatively address the dynamics of systems undergoing symmetry breaking in the excited state, following the dynamical Jahn-Teller motion in real time.

Chapter II is devoted to intermolecular CT in mixed-stack CT (MS-CT) crystals. These are an interesting class of multifunctional molecular materials, where electron donor (D) and acceptor (A) molecules arrange themselves to form stacks, leading to delocalized electrons in one dimension. The interplay between intermolecular CT, electrostatic interactions, lattice phonons and molecular vibrations leads to intriguing physical properties that include (photoinduced) phase transitions [19], multistability [20], antiferromagnetism [21], ferroelectricity [22] and potential multiferroicity [23]. The standard microscopic model to describe this family of materials is the Modified Hubbard model accounting for electron-phonon coupling (Peierls coupling), electron-molecular vibrations coupling (Holstein coupling) and electrostatic interactions. We adopt and validate a method, based on DFT calculations on dimeric DA structures, to extract relevant model parameters [24]. Calculations were done, in collaboration with Dr. G. D'Avino (Mons University) and Prof. S. Pati (Bangalore, JNCASR), on a wide family of MS-CT salts. The approach offers a powerful tool to shed light on the complex physics of MS-CT salts.

A fairly intense research effort is currently done in the host laboratory on materials where intra and intermolecular CT play a role at the same time. The work, started with the aim to understand spectral properties of self-forming aggregates of TTF-PTM molecules [25, 26], recently led the researchers in the host laboratory to the suggestion of a new family of molecular materials with room-temperature ferromagnetic properties and prospective multiferroicity [23]. The main building blocks of these materials belong to the family of dipolar D-π-A dyes, but with the A-group represented by a stable

radical species: D-π-R$^{\cdot}$. Chapter III, in collaboration with Prof. J. Veciana (ICMAB-Barcellona) for the experimental part, is devoted to set up essential-state models for this interesting and complex family of dyes that associate the electronic and optical properties of CT dyes with magnetic properties from the unpaired electron. The experimental validation of essential-state models is hindered in these dyes by the very weak and broad CT absorption bands observed as a result of the weak conjugation between the D and R$^{\cdot}$ groups. Therefore we undertook an extensive effort to parametrize the model from quantum-chemical calculations. Two strategies were adopted, one based on the calculation of the low-energy spectral properties, the other based on the variation of ground state properties with an applied static electric field. Our results were fairly disappointing, demonstrating that, quite irrespective of the adopted functional, DFT is not able to properly describe the ground state behaviour of these dyes, and that TD-DFT is similarly inadequate. Apparently semiempirical methods (ZINDO) are somewhat more reliable, even if further studies are needed to validate these results.

The first three Chapters, attacking intra and intermolecular CT represent the main core of this Thesis. The last Chapter summarizes a theoretical analysis to support recent experimental results on spectral properties of organic nanoparticles based on radical species, obtained in collaboration with Dr. Imma Ratera (ICMAB-Barcellona). Organic nanoparticles based on radical dyes show an anomalous dependence of the emission intensity and frequency with the concentration of the radical themselves, suggesting the presence of excimer states. Unfortunately the size of the molecules is too large to allow for extensive calculations, and the preliminary results obtained in this work do not support excimer states.

Chapter 1

Spectral properties of organic dyes

"There is no science without fancy nor art without facts"

-Vladimir Nabokov

1.1 Introduction

In this Chapter we focus attention on spectral properties of charge-transfer (CT) chromophores. CT dyes are an interesting class of π-conjugated molecules composed by electron donor and acceptor moieties linked togheter by a conjugated bridge to form molecules with different symmetry and dimensionality, as sketched in Figure 1.1.
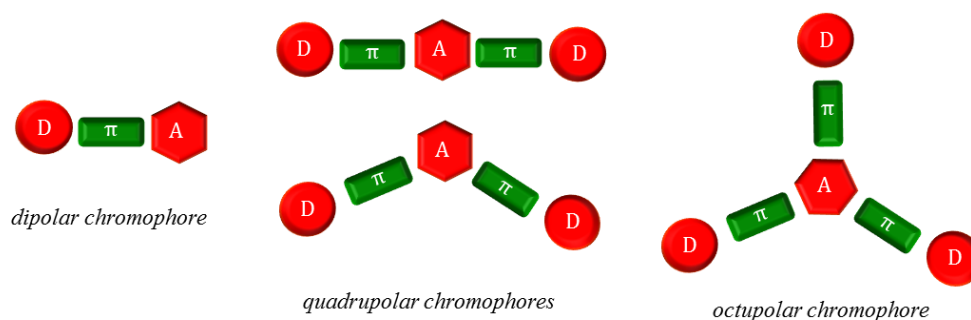

dipolar chromophore

quadrupolar chromophores

octupolar chromophore

FIGURE 1.1: *A schematic representation of CT dyes with different symmetry and dimensionality.*

In the simplest structure a D moiety is linked to an A group to give a *dipolar* or *push-pull chromophore*. In *quadrupolar dyes*, two D (A) are linked to an A (D) group in a linear molecule or bent structure. *Octupolar dyes* are characterized by a planar geometry with three D (A) groups linked to a central A (D) one. CT chromophores find interesting applications in the field of nonlinear optics and molecular electronics, since they combine delocalized electrons, a powerful source of nonlinearity, with low cost and low weight.

The low-energy photophysics of CT dyes is governed by the charge resonance between D and A and is efficiently and accurately described by *essential-state models*. Instead of attempting a detailed first-principle description of the system, essential-state models rely on chemical intuition and select for each dye a minimal set of electronic basis states. These states, corresponding to the main resonating structures, account for charge delocalization through CT. Different essential-state models have been developed for the description of spectroscopic properties of dipolar, quadrupolar and octupolar dyes [12–16].

In the 50's Mulliken proposed a two-state model to describe the optical spectra of charge-transfer complexes in solution [27]. The same model is at the heart of the Marcus-Hush theory of electron transfer [28]. Oudar and Chemla in the 70's applied the same model to investigate nonlinear optical properties for π-conjugated D-A molecules [29]. Starting from these pioneering works, essential-state models have been extended to account for electron-phonon coupling [30] and environment effects, such as polar solvation and interchromophoric interactions [31–33].

The charge resonance implies a rearrangement of the electronic distribution in the molecule, with important consequences on the molecular geometry: vibrational and electronic degrees of freedom are stronlgly coupled. The coupling between electrons and molecular vibrations is important in several respects: it contributes in non-trivial ways to nonlinear optical properties of molecular materials [30] and a recent paper demonstrates the coupling between electrons and vibrations in the bridge of a donor-bridge-acceptor structure enhances the electron-transfer rates, suggesting a vibrational control of electron-transfer [34]. In the framework of essential-state models, molecular vibrations are described in terms of effective vibrational modes that linearly modulate the energy of the relevant states [30]. Typically, one vibrational coordinate is introduced for each CT degree of freedom, as to account for the variation of the molecular geometry due to the different electronic charge distribution. The small dimensions of the electronic and vibrational basis make the physics of the system fairly transparent and help to grasp the common physics underlying the behavior of different families of compounds. Moreover, the *coupled electron-vibration problem* is easily amenable to an exact and fully *non-adiabatic* solution [35], opening the way to an accurate treatment

of delicate issues, including optical spectra of systems undergoing symmetry breaking in either the ground or excited state [36].

The band-shape and the energy of the CT transitions of some dyes depend on the solvent: medium effects have been successfully included in essential-state models [12, 13, 36, 37]. In particular, polar solvation enters the model as an effective overdamped coordinate, responsible for inhomogeneous broadening effects in steady-state optical spectra, while its (Smoluchowsky) dynamics, describes solvent relaxation in time-resolved spectra [38, 39].

Electrostatic interchromophore interactions are also modeled in the essential-state picture, leading to fairly interesting results [40, 41] including multiexciton generation in aggregates of polar dyes [32, 33], biexciton stabilization in aggregates of quadrupolar dyes [42], bistability in molecular crystals [43], efficient energy transfer to dark states [37, 44] and modulation of nonlinear optical properties in multichromophoric assemblies [45, 46] .

As with all semiempirical approaches, essential-state models must be parameterized against experimental data. Typically, absorption and fluorescence spectra in different solvents offer enough information for a reliable parameterization but, depending on the molecular complexity, additional information may be needed about the location of dark states, as it can be inferred from nonlinear spectroscopy. However, when molecular parameters are fixed from a minimal set of spectroscopic data, essential-state models can reliably predict other spectral properties of the same molecule in different environments. Accurate results have been obtained for several dyes on two-photon absorption spectra [31, 36, 47], Hyper-Rayleigh Scattering (HRS) [46], excited state absorption (ESA) [14, 15], resonant and non-resonant Raman [48], fluorescence anisotropy [49] and two-dimensional electronic-vibrational (2D-EV) spectra [39].

This chapter is organized as follows: the next Section shortly summarizes essential-state models for polar, quadrupolar and octupolar dyes. Then, in Section 1.3, the robustness of the modeling strategy is demonstrated by the razionalization of spectroscopic properties of Brilliant Green. In the Section 1.4, we investigate the early-stage dynamics of coherent states in polar and quadrupolar dyes, generated upon ultrafast excitation, that allows for the direct observation of vibrational coherences. This represents a first step of a more ambitious project aimed to investigate the dynamics of excited states.

1.2   Essential-state models for polar, quadrupolar and octupolar dyes

This Section is dedicated to an overview of the work about the two-, three- and four-state model for dipolar, quadrupolar and octupolar chromophores, respectively, developed in the host laboratory.

1.2.1   Two-state model for dipolar dyes

Push-pull chromophores are a class of asymmetric molecules with the general structure D-A. The intrinsic structure of push-pull dyes allows the displacement of electrons upon excitation from the donor to the acceptor or vice-versa (CT transition). The presence of a low-lying transition makes these molecules highly polarizable, and therefore interesting for nonlinear optical (NLO) applications.

The essential-state model for dipolar dyes relies on the definition of two orthogonal basis states: a neutral ($|N\rangle = |DA\rangle$) and a zwitterionic structure ($|Z\rangle = |D^+A^-\rangle$). The two basis states are separated by an energy gap $2z$ and mixed by the mixing element $-\tau$. The electronic Hamiltonian reads:

$$H_{el} = 2z\hat{\rho} - \tau\hat{\sigma} = \begin{pmatrix} 0 & -\tau \\ -\tau & 2z \end{pmatrix} \tag{1.1}$$

where $\hat{\rho}$ and $\hat{\sigma}$ are the operators defined as:

$$\hat{\rho} = \begin{pmatrix} 0 & 0 \\ 0 & 1 \end{pmatrix} \tag{1.2}$$

$$\hat{\sigma} = \begin{pmatrix} 0 & 1 \\ 1 & 0 \end{pmatrix} \tag{1.3}$$

The eigenstates of the electronic Hamiltonian are:

$$|g\rangle = \sqrt{1-\rho}|DA\rangle + \sqrt{\rho}|D^+A^-\rangle \tag{1.4}$$

$$|e\rangle = \sqrt{\rho}|DA\rangle - \sqrt{1-\rho}|D^+A^-\rangle \tag{1.5}$$

where ρ is the expectation value of the operator $\hat{\rho}$ in the ground state and corresponds to the degree of charge transferred from D to A (the so-called *ionicity*); ρ only depends of the z/τ ratio:

$$\rho = \frac{1}{2}\left(1 - \frac{\frac{z}{\tau}}{\sqrt{(\frac{z}{\tau})^2 + 1}}\right) \tag{1.6}$$

Depending on the value of the ionicity of the ground state, polar dyes can be classified as neutral if $\rho < 0.5$ or zwitterionic if $\rho > 0.5$. The $\rho = 0.5$ case describes systems characterized by the degeneracy of the two electronic basis states and is called *cyanine-limit*.

Being interested in optical spectra, the dipole moment operator must be defined. As originally suggested by Mulliken, the contribution to the dipole moment of the $|D^+A^-\rangle$ state is largely dominant with respect to all other terms [27]. In this assumption, the dipole moment operator is:

$$\hat{\mu} = \mu_0 \hat{\rho} \tag{1.7}$$

where μ_0 is the dipole moment of the $|D^+A^-\rangle$ state. All spectroscopically relevant quantities can be expressed in function of ρ:

$$\mu_{ge} = \mu_0 \sqrt{\rho(1-\rho)} \tag{1.8}$$

$$\hbar\omega_{CT} = \frac{\tau}{\sqrt{\rho(1-\rho)}} \tag{1.9}$$

where μ_{ge} is the transition dipole moment and $\hbar\omega_{CT}$ is the transition energy. The permanent ground and excited state dipole moments read:

$$\mu_g = \mu_0\rho \tag{1.10}$$

$$\mu_e = \mu_0(1-\rho) \tag{1.11}$$

In order to reproduce spectral bandshapes, the electronic problem must be extended to account for the coupling between electronic and vibrational degrees of freedom. The potential energy surfaces relevant to the two basis states have different equilibrium geometry and the displacement of the two molecules is related to the *electron-phonon coupling*. We therefore introduce an effective vibrational coordinate, q. The vibrational Hamiltonian reads:

$$H_{vib} = -\sqrt{2\omega}\,g\hat{q}\hat{\rho} + \frac{1}{2}(\omega^2\hat{q}^2 + \hat{p}^2) \tag{1.12}$$

where $g = \sqrt{\omega\varepsilon_{sp}}$ is the electron-phonon coupling constant and ω is the vibrational frequency. The strength of the coupling is measured by ε_{sp}, the vibrational relaxation energy, that corresponds to the small polaron binding energy of the Holstein model; $\hat{q}$ and $\hat{p}$ are the position and momentum operator of the harmonic oscillator ($\hbar = 1$):

$$\hat{q} = (a^\dagger + a)\sqrt{\frac{1}{2\omega}} \tag{1.13}$$

$$\hat{p} = -i(a^\dagger - a)\sqrt{\frac{2}{\omega}} \tag{1.14}$$

where a and $a^\dagger$ are the phonon annihilation and creation operators, respectively.

Different strategies can be adopted to solve the coupled electronic and vibrational problem. The *adiabatic approximation* is often employed, taking advantage of the different timescales of nuclear and electronic motions. In this approximation, the vibrational momentum $\hat{p}$ is neglected, and $\hat{q}$ becomes a classical variable. The eigenvalues of the electronic problem, calculated as a function of q, are the adiabatic PESs, representing the potential energy for the vibrational motions, as shown in Figure 1.2.
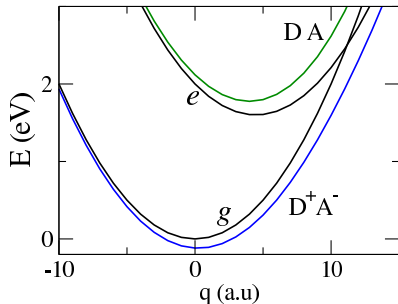

FIGURE 1.2: *The q-dependent energies of the two electronic basis states (black lines) and the adiabatic eigenstate PESs (coloured lines) obtained from the diagonalization of the total Hamiltonian resulting from eq. 1.1 plus 1.12. The figure is obtained for z = 1 eV, τ = 0.5 eV, ω = 0.2 eV and ε_{sp} = 0.4 eV.*

In addition, Figure 1.2 points out that, while the vibrational coordinate enters the Hamiltonian as strictly harmonic (see eq. 1.12), the interaction with the delocalized electrons leads to anharmonic PES.

Essential-state models are simple enough to allow for the non-adiabatic solutions of the total Hamiltonian ($H = H_{el} + H_{vib}$). In the *non-adiabatic approach*, the basis states of the coupled problem are defined as the direct product of the electronic basis states times the eigenstates of the harmonic oscillator. Of course, the infinite eigenstate basis is truncated to the first M states, with M large enough as to reach convergence of relevant quantities (typically M amounts to $\sim$ 10). The diagonalization of the Hamiltonian matrix written on the non-adiabatic basis leads to the (numerically exact) vibronic eigenstates and to relevant transition energies.

To complete the picture, the solvent and its interaction with the CT dye have to be introduced. To account for solvation effects, the reaction-field approach was followed. Shortly, a polar solute molecule polarizes the surrounding medium and therefore feels a *reaction electric field*, F, proportional to the dipole moment of the solute. The reaction field has two contributions characterized by distinctively different dynamics [50, 51]. The *electronic contribution* to F (F_{el}) is due to the deformation of the electronic clouds of the solvent molecules close to a polar solute. The relevant dynamics is very fast (corresponding frequencies in the UV region), much faster than CT degrees of freedom

of the solvent. The electronic contribution to F is therefore treated in the antiadiabatic approximation simply leading to the renormalization of electronic parameters (τ and z), that, therefore, acquire a dependence on the refractive index of the solvent [12]. This dependence can be safely disregarded in most cases in view of the marginal variation of the refractive index in common organic solvents. The *orientational contribution* (F_{or}) to the reaction field is due to the re-orientation of polar solvent molecules around the solute. The relevant dynamics is very slow compared to both electronic and vibrational degrees of freedom. Due to its intrinsically over-damped nature, F_{or} can be treated as a classical variable: basically, in this picture, it acts as an additional Holstein vibration that can be described in the adiabatic approximation. The orientational component of the reaction field is proportional to the solute dipole moment via a proportionality factor, r_{or}:

$$F_{or} = r_{or}\langle\mu\rangle \tag{1.15}$$

where r_{or} depends on both the solvent refractive index and the static dielectric constant, vanishing for nonpolar solvents. Assuming that the solvent behaves as an elastic medium, the Hamiltonian relevant to polar solvation reads [12]:

$$H_{or} = -F_{or}\hat{\mu} + \frac{F_{or}^2}{2r_{or}} = -F_{or}\mu_0\hat{\rho} + \frac{F_{or}^2}{2r_{or}} = -Q\hat{\rho} + \frac{Q^2}{4\varepsilon_{or}} \tag{1.16}$$

where we introduced an effective solvation coordinate $Q = F_{or}\mu_0$ whose coupling to the electronic degrees of freedom is $\varepsilon_{or} = r_{or}\mu_0^2/2$, with the same meaning as ε_{sp} for vibrations. The parameter ε_{or} is directly related to the solvent polarity: non-polar solvents have $\varepsilon_{or}=0$, and ε_{or} increases with solvent polarity.

A *positive solvatochromism*, defined as a red-shift of both absorption and fluorescence bands for increasing solvent polarity, is observed for neutral molecules ($z > 0$, $\rho < 0.5$). By variance, *negative solvatochromism* characterizes zwitterionic molecules ($z < 0$ and $\rho > 0.5$): increasing the polarity of the solvent the bands in absorption and in fluorescence shift to the blue because the energy gap between the states $|DA\rangle$ and $|D^+A^-\rangle$ increases with the solvent polarity. Polar solvation is also responsible for inhomogeneous broadening in optical spectra of DA chromophores: from experimental data, it is evident that the vibronic structure is resolved only in non polar or weakly polar solvent. The origin of this behavior is related to the presence of disorder in the system, caused by a thermal fluctuation of the orientational component of the reaction field around its equilibrium value.

To account for thermal disorder, the total Hamiltonian ($H_{tot} = H_{el} + H_{vib} + H_{or}$) is diagonalized for fixed values of the reaction field, and each configuration is weighted for the Boltzmann probability. A narrow Boltzmann distribution is expected for weakly polar

solvents in agreement with the resolved vibronic structure observed in apolar solvents; by contrast, a large Boltzmann distribution is expected for polar solvent (large ε_{or}), as confirmed by optical data. Of course the distribution is different for absorption and fluorescence: the ground state Boltzmann distribution applies to absorption spectra (both for linear and nonlinear processes); for fluorescence, the solvent relaxes after excitation, and the distribution has to be calculated based on the relaxed excited state energy.

We underline that in the calculation of optical spectra, a Gaussian line is assigned to each vibronic band, for each F_{or}, with a fixed width at half maximum Γ, independent on the solvent polarity. Γ can be estimated by spectra in apolar solvents, when inhomogeneous broadening is minimized.

1.2.2 Three-state model for quadrupolar dyes

Quadrupolar dyes can have a linear or a bent geometry, as drawn in Panel (a) of Figure 1.3.
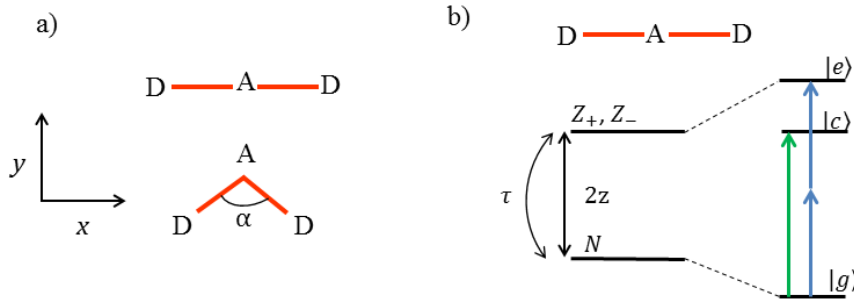
FIGURE 1.3: *Panel a: schematic representation of quadrupolar dyes and their orientation in the (x,y) plane. Panel b: sketch of the OPA and TPA transitions in a linear quadrupolar dye.*

In both cases, a three-state description is adopted with three orthogonal basis states, corresponding to the resonance structures of quadrupolar molecules, $|DAD\rangle$, $|D^+A^-D\rangle$, $|DA^-D^+\rangle$. The two zwitterionic states are degenerate and are separated from the neutral state by an energy gap $2z$ and are mixed to it by $-\tau$. The integral hopping between the two zwitterionic states is set to zero. By exploiting symmetry, the zwitterionic states are combined in a symmetric and an antisymmetric wavefunction; the symmetrized basis set reads:

$$|N\rangle = |DAD\rangle \tag{1.17}$$

$$|Z_+\rangle = \frac{1}{\sqrt{2}}(|D^+A^-D\rangle + |DA^-D^+\rangle) \tag{1.18}$$

$$|Z_-\rangle = \frac{1}{\sqrt{2}}(|D^+A^-D\rangle - |DA^-D^+\rangle) \tag{1.19}$$

On the symmetrized basis, the following operators are defined:

$$\hat{\rho} = \begin{pmatrix} 0 & 0 & 0 \\ 0 & 1 & 0 \\ 0 & 0 & 1 \end{pmatrix} \tag{1.20}$$

$$\hat{\delta} = \begin{pmatrix} 0 & 0 & 0 \\ 0 & 0 & 1 \\ 0 & 1 & 0 \end{pmatrix} \tag{1.21}$$

$$\hat{\sigma} = \begin{pmatrix} 0 & 1 & 0 \\ 1 & 0 & 0 \\ 0 & 0 & 0 \end{pmatrix} \tag{1.22}$$

where $\hat{\rho}$ and $\hat{\sigma}$ define the charge distribution of the molecule: $\hat{\rho} = \hat{\rho}_1 + \hat{\rho}_2$ measures the average charge on the acceptor site; $\hat{\delta} = \hat{\rho}_1 - \hat{\rho}_2$ instead measures the unbalance of the charge on the two external sites; as for dipolar dyes, $\hat{\sigma}$ is the mixing operator between the two gerade states.

In terms of these operators, the electronic Hamiltonian reads:

$$H_{el} = 2z\hat{\rho} - \tau\hat{\sigma} = \tag{1.23}$$

The diagonalization of the Hamiltonian leads to the ground state $|g\rangle$ and two excited states $|c\rangle$ and $|e\rangle$:

$$\begin{aligned} |g\rangle &= \sqrt{1-\rho}|N\rangle + \sqrt{\rho}|Z_+\rangle \\ |c\rangle &= |Z_-\rangle \\ |e\rangle &= \sqrt{\rho}|N\rangle - \sqrt{1-\rho}|Z_+\rangle \end{aligned} \tag{1.24}$$

$|Z_-\rangle$ does not mix with the other basis states because of its different parity.

In the same approximation adopted for dipolar dyes, we assume that just $|D^+A^-D\rangle$ and $|DA^-D^+\rangle$ states have a large permanent dipole of magnitude μ_0. The x and y components of the dipole operator (see Figure 1.3 for the reference system and for α angle) are:

$$\begin{aligned} \hat{\mu}_x &= \mu_0 \sin\left(\frac{\alpha}{2}\right)\hat{\delta} \\ \hat{\mu}_y &= \mu_0 \cos\left(\frac{\alpha}{2}\right)\hat{\rho} \end{aligned} \tag{1.25}$$

For a linear quadrupolar dye, $\alpha = 180°$, $\mu_y = 0$ and $\mu_x = \mu_0\hat{\delta}$.

The expectation value of $\hat{\rho}$ in the ground state defines the amount of charge separation in the ground state, and therefore the quadrupolar moment of the molecule. As for dipolar dyes, ρ is a function of the z/τ ratio:

$$\rho = \frac{1}{2}\left(1 - \frac{\frac{z}{\tau}}{\sqrt{(\frac{z}{\tau})^2 + 2}}\right) \tag{1.26}$$

In a *linear* centrosymmetric molecule, the odd state ($|c\rangle$) is one-photon (OP) allowed, while the even $|e\rangle$ state is two-photon (TP) allowed. This simple scheme must be slightly modified in bent molecules where the reduced symmetry makes the two transitions allowed both in linear absorption (OPA) and two-photon absorption (TPA) [37].

In quadrupolar dyes, the charge rearrangement from $|DAD\rangle$ to $|D^+A^-D\rangle$ or to $|DA^-D^+\rangle$ states occurs along the two molecular arms of the dye: two mutually independent effective coordinates (q_1 and q_2), describing the nuclear motion along each arm, are introduced to describe *electron-phonon coupling*. The two coordinates have the same frequency ω and the same relaxation energy ε_{sp}. The vibrational Hamiltonian reads:

$$H_{vib} = -\sqrt{2\varepsilon_{sp}}\omega\hat{q}_1\hat{\rho}_1 - \sqrt{2\varepsilon_{sp}}\omega\hat{q}_2\hat{\rho}_2 + \frac{1}{2}(\omega^2\hat{q}_1^2 + \hat{p}_1^2) + \frac{1}{2}(\omega^2\hat{q}_2^2 + \hat{p}_2^2) \tag{1.27}$$

The operators $\hat{q}_i$ and $\hat{p}_i$ represent the coordinate and the momentum of the two vibrations, while $\hat{\rho}_i$ is the ionicity relative to each branch. Exploiting symmetry, the two molecular coordinates can be combined to get a symmetric ($q_+ = (q_1 + q_2)/\sqrt{2}$) and an antisymmetric ($q_- = (q_1 - q_2)/\sqrt{2}$) coordinate, and the relevant Hamiltonian reads:

$$H_{vib} = -\sqrt{\varepsilon_{sp}}\omega\hat{q}_+\hat{\rho} - \sqrt{\varepsilon_{sp}}\omega\hat{q}_-\hat{\delta} + \frac{1}{2}(\omega^2\hat{q}_+^2 + \hat{p}_+^2) + \frac{1}{2}(\omega^2\hat{q}_-^2 + \hat{p}_-^2) \tag{1.28}$$

Polar solvation is included in the picture following the same approach originally developed for dipolar systems. For bent molecules two components of the reaction field, F_x and F_y, must be introduced that reduce to a single component, Fx, for linear molecules (α=0). The relevant Hamiltonian reads:

$$H_{or} = -\hat{\mu}_x F_x - \hat{\mu}_y F_y + \frac{\mu_0^2}{4\varepsilon_{or}}(F_x^2 + F_y^2) \tag{1.29}$$

The (F_x, F_y)-dependent Hamiltonian can be written on the basis obtained as the direct product of the three electronic basis states times the eigenstates of the two harmonic oscillators associated to q_+ and q_- with large enough M as to ensure convergence of the relevant results. Numerical diagonalization of the resulting matrix (total dimension

$3M^2$) leads to numerically exact non-adiabatic eigenstates. The calculation is repeated on a grid of (F_x, F_y) values to get (F_x, F_y)-dependent eigenstates and, weighting each microstate according to the Boltzaman distribution, linear and nonlinear optical spectra can be calculated.

The vibrational Hamiltonian of eq. 1.28 shows that $\hat{q}_-$ is coupled to the antisymmetric δ, which mixes $|Z_+\rangle$ with $|Z_-\rangle$: oscillations along q_-, driving an unbalance of charge distribution, are responsible for symmetry breaking phenomena with relevant consequences in the optical spectra of linear quadrupolar dyes, further supported by the reaction field (F_x), that is also coupled to $\hat{\delta}$ operator [36].

Symmetry-breaking in quadrupolar dyes has been extensively discussed by F. Terenziani and A. Painelli [36]. In the adiabatic approximation, the PESs are functions of the two vibrational coordinates q_+ and q_-. Stable states with respect to symmetry breaking show PES with a displacement just along the q_+ coordinate: the single minimum is located at $q_- = 0$ and $q_+ = \sqrt{\varepsilon_{sp}}\langle\rho\rangle/\omega$ (where $\langle\rho\rangle$ is the expectation value of the $\hat{\rho}$ in the relevant state). By contrast, states undergoing symmetry-breaking show a double minimum at finite and opposite q_- values ($q_- = \pm\sqrt{\varepsilon_{sp}}\langle\delta\rangle/\omega$) separated by a saddle point at $q_- = 0$. Analizing the structures of the PESs, the phase diagram reported in Figure 1.4 is obtained, as a function of ground state ionicity (ρ) and of the vibrational relaxation energy (ε_{sp}). Three different regions can be recognized:
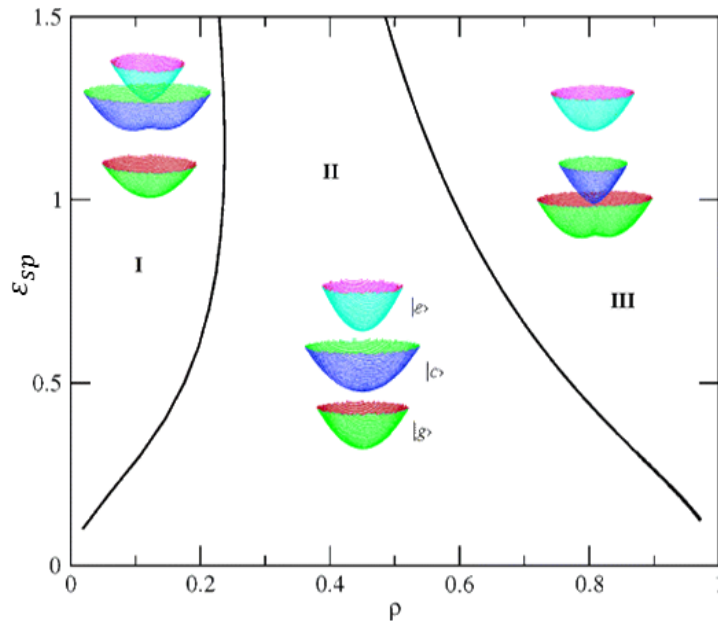

FIGURE 1.4: *Phase diagram for linear quadrupolar chromophores, describing the stability of different states as function of ρ and ε_{sp} in τ unit. Region I: stable ground state and bistable first excited state; Region II: all PES have a single minimum; Region III: bistable ground state.*

- **Class I** describes dyes where symmetry breaking is expected in the first excited state. Chromophores belonging to this class have a nondipolar $|g\rangle$ and $|e\rangle$ while $|c\rangle$ is polar; several dyes are known for Class I, for example fluorene- [36] and biphenyl- [52] based dyes.

- **Class II** includes dyes not undergoing symmetry-breaking, like squaraine dyes.

- **Class III** describes systems undergoing symmetry-breaking in the ground state, like cyanine dyes.

Symmetry breaking gives rise to important consequences in spectral properties of linear quadrupolar molecules. The presence of polar states, originated by symmetry breaking in the first excited state or in the ground state, leads to solvatochromic behavior. Specifically, since absorption is a vertical process no solvatochromic effects are expected in absorption process neither in Class I and II dyes; on the contrary, strong positive fluorescence solvatochromism is expected for Class I dyes: after absorption the system relaxes towards one of the two minima giving rise a fluorescence relaxed *polar* state. For dyes of Class III a strong inverse solvatochromism is predicted only in absorption.

1.2.3 Four-state model for octupolar dyes

In the essential-state framework, octupolar dyes, AD_3 or DA_3, are described in terms of four states, $|N\rangle$ and the three degenerate zwitterionic structures, $(|Z_1\rangle, |Z_2\rangle$ and $|Z_3\rangle)$, where the charge is displaced along one of the three molecular arms. The energy difference between $|N\rangle$ and the three charge-separated states is $2z$, and the three zwitterionic forms are mixed with the neutral one by the charge-transfer integral, $-\tau$. On this basis set, the following operators are conveniently defined:

$$\hat{\rho} = \begin{pmatrix} 0 & 0 & 0 & 0 \\ 0 & 1 & 0 & 0 \\ 0 & 0 & 1 & 0 \\ 0 & 0 & 0 & 1 \end{pmatrix} \tag{1.30}$$

$$\hat{\sigma} = \begin{pmatrix} 0 & 1 & 1 & 1 \\ 1 & 0 & 0 & 0 \\ 1 & 0 & 0 & 0 \\ 1 & 0 & 0 & 0 \end{pmatrix} \tag{1.31}$$

$$\hat{\delta}_1 = \begin{pmatrix} 0 & 0 & 0 & 0 \\ 0 & 2 & 0 & 0 \\ 0 & 0 & -1 & 0 \\ 0 & 0 & 0 & -1 \end{pmatrix} \tag{1.32}$$

$$\hat{\delta}_2 = \begin{pmatrix} 0 & 0 & 0 & 0 \\ 0 & 0 & 0 & 0 \\ 0 & 0 & 1 & 0 \\ 0 & 0 & 0 & -1 \end{pmatrix} \tag{1.33}$$

Exploiting the C_3 symmetry, we find two totally-symmetric (A-type) wavefunctions, $|A_1\rangle = |N\rangle$ and $|A_2\rangle = 1/\sqrt{3}(|Z_1\rangle + |Z_2\rangle + |Z_3\rangle)$, and two degenerate (E-symmetry) states, $|E_1\rangle = 1/\sqrt{6}(2|Z_1\rangle - |Z_2\rangle - |Z_3\rangle)$ and $|E_2\rangle = 1/\sqrt{2}(|Z_2\rangle - |Z_3\rangle)$. On this basis, the Hamiltonian mixes the A-symmetry states, giving the ground ($|g\rangle$) and the highest-energy excited state ($|e\rangle$) while the two E-states stay unmixed. The previous operators (1.30, 1.31, 1.32 and 1.33) in the symmetrized basis are:

$$\hat{\rho} = \begin{pmatrix} 0 & 0 & 0 & 0 \\ 0 & 1 & 0 & 0 \\ 0 & 0 & 1 & 0 \\ 0 & 0 & 0 & 1 \end{pmatrix} \tag{1.34}$$

$$\hat{\sigma} = \sqrt{3} \begin{pmatrix} 0 & 1 & 0 & 0 \\ 1 & 0 & 0 & 0 \\ 0 & 0 & 0 & 0 \\ 0 & 0 & 0 & 0 \end{pmatrix} \tag{1.35}$$

$$\hat{\delta}_1 = \sqrt{2} \begin{pmatrix} 0 & 0 & 0 & 0 \\ 0 & 0 & -1 & 0 \\ 0 & -1 & \frac{1}{\sqrt{2}} & 0 \\ 0 & 0 & 0 & -\frac{1}{\sqrt{2}} \end{pmatrix} \tag{1.36}$$

$$\hat{\delta}_2 = \frac{1}{\sqrt{3}} \begin{pmatrix} 0 & 0 & 0 & 0 \\ 0 & 0 & 0 & -\sqrt{2} \\ 0 & 0 & 0 & -1 \\ 0 & -\sqrt{2} & -1 & 0 \end{pmatrix} \tag{1.37}$$

The electronic Hamiltonian written in the symmetrized basis reads:

$$H_{el} = 2z\hat{\rho} - \tau\hat{\sigma} \tag{1.38}$$

Two dipole moments operators are defined, along the x- and y-direction (see Figure 1.5 for the reference system):

$$\begin{aligned}
\hat{\mu}_x &= \frac{1}{2}\mu_0\hat{\delta}_1 \\
\hat{\mu}_y &= \frac{\sqrt{3}}{2}\mu_0\hat{\delta}_2
\end{aligned} \tag{1.39}$$

where μ_0 is the magnitude of the dipole moment of each of $\mathrm{D^+A^-}$ branches.

The eigenstates of the Hamiltonian in eq. 1.38 are:

$$\begin{aligned}
|g\rangle &= \sqrt{1-\rho}|A_1\rangle + \sqrt{\rho}|A_2\rangle \\
|c_1\rangle &= |E_1\rangle \\
|c_2\rangle &= |E_2\rangle \\
|e\rangle &= \sqrt{\rho}|A_1\rangle - \sqrt{1-\rho}|A_2\rangle
\end{aligned} \tag{1.40}$$

where ρ is the ground state expectation value of the operator $\hat{\rho}$ (eq. 1.34), and represents the weight of the zwitterionic states in the ground state. ρ is fixed by the model parameters z and τ as follows:

$$\rho = \frac{1}{2}\left(1 - \frac{z}{\sqrt{z^2 + 3\tau^2}}\right) \tag{1.41}$$

The permanent dipole moments of $|g\rangle$ and $|e\rangle$ are both zero, while $|c_1\rangle$ and $|c_2\rangle$ have non-vanishing components along x. As summarized in Figure 1.5, the OPA transition from the ground state $|g\rangle$ is allowed towards the two-degenerate states, while $|e\rangle$ is a dark state; the TPA transitions from the $|g\rangle$ towards $|c_1\rangle/|c_2\rangle$ and to $|e\rangle$ state are allowed though the former is weak.
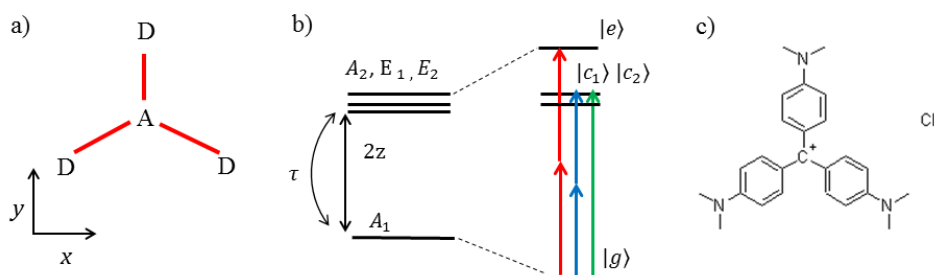

FIGURE 1.5: *Panel a:schematic representation of the octupolar dyes and their orientation in the (x,y) plane. Panel b: four-state model for octupolar chromophores on the symmetrized basis and relevant electronic states. Panel c: chemical structure of Crystal Violet (CV).*

The electronic model is now extended to account for molecular vibrations. Three vibrational coordinates (q_1, q_2, q_3), one for each molecular arms, are introduced. They are equivalent by symmetry and they are characterized by the same frequency ω and by the same relaxation energy ε_{sp}. The symmetry adapted vibrational coordinates are:

$$\hat{q}_A = \frac{1}{\sqrt{3}}(\hat{q}_1 + \hat{q}_2 + \hat{q}_3) \tag{1.42}$$

$$\hat{q}_{E_1} = \frac{1}{\sqrt{6}}(2\hat{q}_1 - \hat{q}_2 - \hat{q}_3) \tag{1.43}$$

$$\hat{q}_{E_2} = \frac{1}{\sqrt{2}}(\hat{q}_2 - \hat{q}_3) \tag{1.44}$$

where $\hat{q}_A$ describes a totally symmetric deformation, while $\hat{q}_{E_1}$ and $\hat{q}_{E_2}$ have E-symmetry.

The vibrational Hamiltonian reads:

$$H_{vib} = -\sqrt{\frac{2\epsilon_{sp}}{3}}\omega\hat{q}_A\hat{\rho} - \sqrt{\frac{\epsilon_{sp}}{3}}\omega\hat{q}_{E_1}\hat{\delta}_1 - \sqrt{\epsilon_{sp}}\omega\hat{q}_{E_2}\hat{\delta}_2 \tag{1.45}$$
$$+\frac{1}{2}(\omega^2\hat{q}_A^2 + \hat{p}_A^2) + \frac{1}{2}(\omega^2\hat{q}_{E_1}^2 + \hat{p}_{E_1}^2) + \frac{1}{2}(\omega^2\hat{q}_{E_2}^2 + \hat{p}_{E_2}^2)$$

where the operators $\hat{p}_A$, $\hat{p}_{E_1}$ and $\hat{p}_{E_2}$ represent the conjugate momenta of the relevant vibrational coordinate.

Following the same procedure adopted for quadrupolar dyes, the total Hamiltonian is solved in the adiabatic approximation to get relevant PESs. In Figure 1.6 we report the potential energy surface along (q_{E_1}, q_{E_2}) keeping the q_A coordinate at its equilibrium value. The PESs relevant to c_1 and c_2 show the typical structure of a conical intersection with the two states exactly degenerate only at $(q_{E_1}, q_{E_2} = 0, 0)$ and the lowest surface developing three equivalent minima along the directions of the three molecular branches. In close analogy with the case of quadrupolar dyes, we classify octupolar chromophores as belonging to Class I when having a stable ground state and a multistable first excited state, and to Class III when having a multistable ground state. In octupolar chromophores Class II is not present: symmetry-preserving octupoles do not exist. Class I largely dominates the phase diagram of octupolar dyes.

The picture emerging from Figure 1.6 is in line with available experimental data [53, 53–55]. In fact, known octupolar dyes do not show major solvatochromic effects in absorption spectra, in agreement with their non-polar ground state; at variance, their fluorescence band exhibits a large bathochromic shift with increasing solvent polarity.

The solute-solvent interaction is introduced in the framework of the reaction-field approach. Treating the solvent as an elastic medium, two orientational components for the
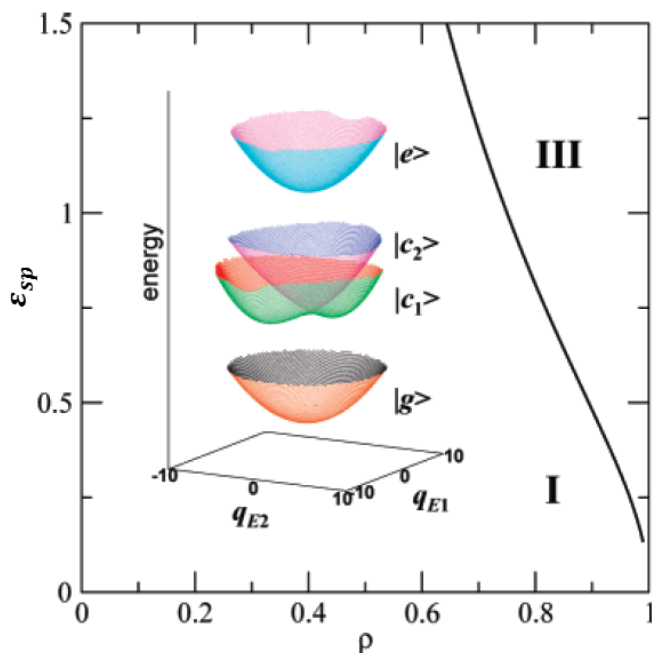
FIGURE 1.6: *Phase diagram for octupolar chromophores, describing the stability of different states as function of ρ and ε_{sp}; Region I corresponds to stable $|g\rangle$ and $|e\rangle$ and multistable $|c_1\rangle$ state; Region III have both ground and $|c_1\rangle$ multistable PESs.*

reaction field are considered, F_x and F_y. The Hamiltonian relevant to solvation reads:

$$H_{or} = -\hat{\mu}_x F_x - \hat{\mu}_y F_y + \frac{\mu_0^2}{4\varepsilon_{or}}(F_x^2 + F_y^2) \tag{1.46}$$

To attack the problem of optical spectra in polar solvents, the total Hamiltonian, $(\text{H}_{ele} + \text{H}_{vib} + \text{H}_{or})$ is diagonalized for a grid of (F_x, F_y)-values, and non-adiabatic spectra are calculated for each value of (F_x, F_y). The full spectra, accounting for polar solvation, are finally obtained summing up the spectra calculated at different (F_x, F_y), each spectrum being weighted for the relevant (ground or excited state) Boltzmann distribution.

A prototypical example of octupolar dye is Crystal Violet (CV), as shown in Figure 1.5, whose linear and nonlinear spectral properties has been extensively investigated [16].

1.3   The Brilliant Green case

Having summarized essential-state models as applied to the different classes of dyes, here we address the case of Brilliant Green (BG), studied in collaboration with the group of Prof. W. Wenseellers (Antwerp University) [17]. BG belongs to triarylmethane class and it combines the large NLO responses typical of multibranched CT dye with an optical response sensible to the environment, making it good candidate as biological marker

[56]. BG is very weakly fluorescent but its fluorescence quantum yield increases by up to six orders of magnitude when bound to biomolecular hosts or when dissolved in a viscous solvent [57–59]. BG, shown in Figure 1.7, is a cationic molecule, very similar to CV, the parent compound with octupolar symmetry discussed in previous Section, but with a lower symmetry, due to the lack of the amino-group in one of the three arms.
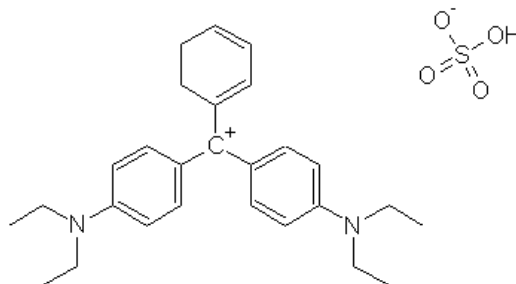

FIGURE 1.7: *Chemical structure of BG dye.*

1.3.1 Experimental data

The experimental investigation of BG is made in collaboration with the group of W. Wenseleers of the University of Antwerp. Absorption, fluorescence and fluorescence anisotropy were collected in our group; HRS and pump-probe spectra were measured by the group of Antwerp.

Brilliant Green was purchased from Sigma Aldrich and used without further purification. Absorption spectra are recorded on a Perkin Elmer Lambda 650 UV-Vis spectrometer. Fluorescence and fluorescence anisotropy (emission and excitation) spectra were collected on a Fluoromax-3 Horiba Jobin-Yvon spectrofluorometer equipped with a Xenon lamp, as the excitation source, and excitation and emission Glan-Thompson automatic polarizers for anisotropy measurements (single-channel L format). Spectra were collected in chloroform (CHCl$_3$, Sigma-Aldrich, > 99.0), tetrahydrofuran (THF, Sigma-Aldrich, $> 99.0\%$), dichloromethane (CH$_2$Cl$_2$, Sigma-Aldrich, $> 99.0\%$), 1,2-propandiol (propylen glycole,Sigma-Aldrich, $> 99.0\%$), glycerol (Sigma-Aldrich, $> 99.0\%$) and dimethyl sulfoxide (DMSO, Sigma-Aldrich, $> 99.0\%$).

The absorption spectrum of BG, collected in CHCl$_3$ and reported in Figure 1.8, exhibits three main bands: a very intense transition at 630 nm (S0$\longrightarrow$S1) with a shoulder at 587 nm, and two weaker transitions at 430 nm and 321 nm (S0$\longrightarrow$S2) and (S0$\longrightarrow$S3), respectively. Absorption spectra are marginally affected by solvent polarity, as observed in Figure 1.9, showing a small broadening with increasing solvent polarity. The molar

extinction coefficient measured at 630 nm in $CHCl_3$ is 112800 $M^{-1}cm^{-1}$. BG emission is not detectabled at room temperature in non-viscous solvents but its fluorescence quantum yield increases in viscous or glassy solvents, as shown in Figure 1.10.
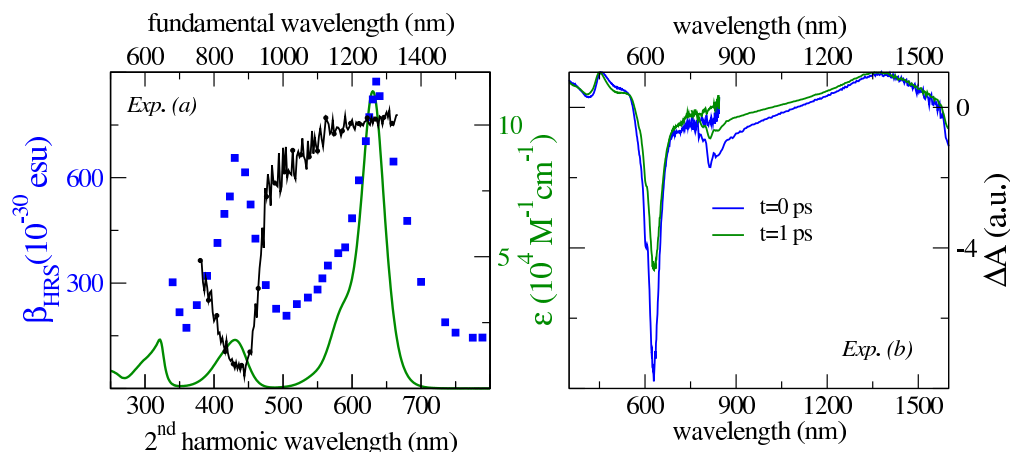
FIGURE 1.8: *Experimental data: panel (a) Absorption spectrum in CHCl$_3$ (green), HRS data in CHCl$_3$ (blue squares), fluorescence excitation anisotropy spectrum (black) detected at 675 nm; panel (b) unpolarized pump-probe spectra collected in CHCl$_3$ at different delay times; the pump beam is centered at 600 nm using UV and NIR probes.*
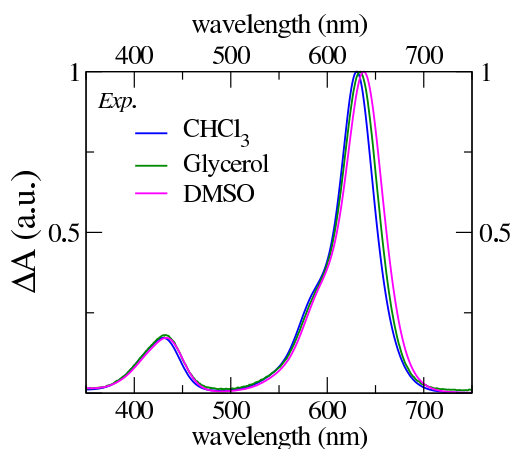
FIGURE 1.9: *Experimental linear absorption spectra of BG in different solvents.*

Figure 1.10 shows fluorescence and fluorescence excitation spectra recorded in glassy propylene glycol at 200 K: at this temperature the inhomogenous broadening due to polar solvation is reduced and the excitation spectrum shows a more resolved vibronic structure than the absorption spectrum at room temperature. The emission spectrum shows a single broad band at 662 nm. At variance with ref. [60] and [61], the emission from S2 state is not observed.

Excitation anisotropy (panel (a) in Figure 1.10) ranges from -0.2 (the minimum value for anisotropy, corresponding to perpendicular transition dipole moments for the absorption

and emission processes) within the S2 band and increases up to 0.4 (the maximum value for anisotropy, corresponding to parallel transition dipole moments for the absorption and emission processes) in the S1 band. Similar information is obtained from fluorescence emission anisotropy spectra (panel (b) Figure 1.10): when exciting within S1, the anisotropy is close to 0.4, while it decreases down to -0.2 when exciting into S2.
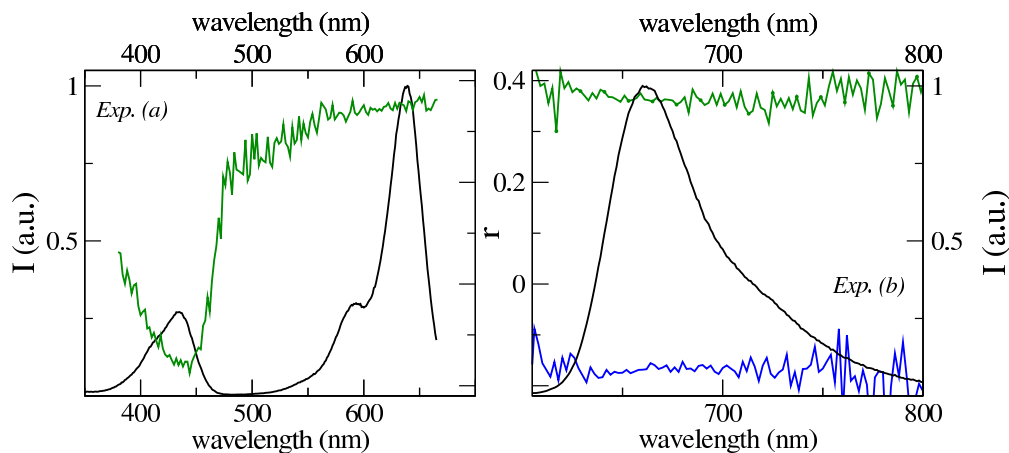
FIGURE 1.10: *Top: experimental data, BG in glassy propylene-glycol at 200K; (a) fluorescence excitation spectrum (black), fluorescence excitation anisotropy spectrum (green) detected at 675 nm; (b) fluorescence spectrum (black), fluorescence anisotropy spectrum obtained upon excitation at 434 nm (blue) and 595 nm (green).*

Two main bands are seen in the HRS spectrum in Figure 1.8, clearly corresponding to the S0$\longrightarrow$S1 and S0$\longrightarrow$S2 bands in the absorption spectrum. A hint of a third band S0$\longrightarrow$S3 is seen in the increase of the HRS signal, but unfortunately reliable HRS data could not be collected at shorter wavelengths. The lowest-energy HRS band is the most intense HRS feature and shows a clear vibronic structure, being slightly red-shifted with respect to the corresponding linear absorption band [16, 62]. The two main bands observed in the HRS spectrum have similar intensity, resulting in a very different spectroscopic profile with respect to the linear absorption spectrum, where instead the S0$\longrightarrow$S1 largely dominates the spectrum.

In line with the minor dependence of the spectral properties of BG on solvent polarity, pump-probe spectra of BG in Figure 1.8 show a minor dependence on the delay time, apart from decrease of the intensity of the photoinduced signal due to the re-equilibration of the system after excitation. The pump-probe spectrum exhibits two positive signals attributed to excited state absorption (ESA): a broad band centered at 1354 nm, attributed to S1$\longrightarrow$S2, and a smaller feature at 455 nm, corresponding to the transition from S1 to some higher-energy excited state. The VIS region of the spectrum is dominated by an intense negative signal at 630 nm with a partly resolved shoulder in the high-energy side, ascribed to the superposition of the negative signals due to S0$\longrightarrow$S1 photobleaching (PB) and S1$\longrightarrow$S0 stimulated emission (SE). In the same region, the

S0⟶S3 transition should give rise to a positive ESA signal that is probably hidden by the superimposed negative PB and SE signals. Finally a negative feature at 430 nm is ascribed to the S0⟶S2 PB.

1.3.2   The essential-state model for BG

BG is a substituted triphenylmethyl carbocation dye, closely related to CV but with a lowered symmetry: removing the amino group, one of the three arms is made a poor donor. In a model for a perfect octupolar dye (Section 1.2.3), the lowest optical transition is towards two degenerate bright states ($|g\rangle \longrightarrow |c_1\rangle$, $|g\rangle \longrightarrow |c_2\rangle$) that are also responsible for an intense HRS signal and a comparatively weak TPA signal. The third excited state $|e\rangle$, at higher energy, is a dark state, and appears with a large intensity in TPA spectra. Indeed, vibrational coupling and symmetry-lowering due to polar solvation relax the symmetry rules, and a tiny signal is seen in OPA and HRS at the frequency of the dark state. In BG, the appearance of a secondary band in the linear absorption spectrum to the blue of the main band marks the reduced symmetry of BG with respect to CV: the two $|g\rangle \longrightarrow |c_1\rangle$, $|g\rangle \longrightarrow |c_2\rangle$ transitions loose their degeneracy giving rise to OPA-, HRS- and TPA- bands. In addition the third excited states appears with a weak intensity in OPA spectrum.

The different optical features of BG respect to CV can be qualitatively rationalized based on simple perturbative arguments. Specifically, we adopt a purely *electronic* model for an octupolar dye with the same model parameters as for CV, τ=0.91 eV, Γ=0.05 eV, μ_0=18.5 D and $2z$=0.48 eV, as to implicitly account for red-shift of the spectra due to electron-vibration coupling; then we first reproduce the qualitative BG optical features varying the energy of the CT along the asymmetric arm from $2z$ (as in the perfect octupolar system) to $2(z + \Delta z)$. Results are summarized in Figure 1.11.

As expected, the degeneracy of the two bright states of the perfect octupole is lost. Accordingly, two transitions appear, one slightly red-shifted with respect to the octupole and a second one more markedly shifted to the blue, in line with BG spectra. The corresponding peaks dominate OPA and HRS spectra. The dark state in CV, dominating the TPA spectrum, moves to the blue with increasing Δz, and for $\Delta z > 0.4$ eV it enters in resonance and the TPA spectrum is obscured by the OPA resonance. In the same region a resonance enhancement is clearly seen in HRS, with the intensity of the relevant peak increasing by orders of magnitude when close to resonance. Of course, when Δz becomes very large we reach the limiting case of a bent quadrupolar molecule, where only three states are relevant, since the fourth resonant state goes too high in energy to
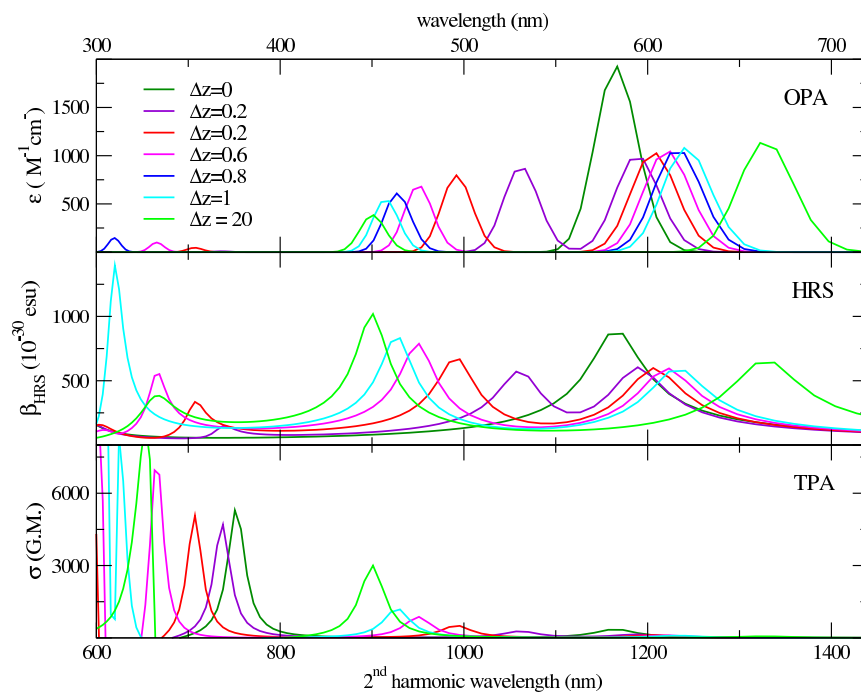
FIGURE 1.11: *OPA, HRS and TPA spectra calculated for a purely electronic model of a distorted octupolar molecule. The dark green line shows results relevant to CV, a perfect octupolar dye, with $\tau=0.91$ eV, $\Gamma=0.05$ eV, $\mu_0=18.5$ D and $2z=0.48$ eV. The light green line refers to a bent quadrupolar dye, corresponding to the $\Delta z \longrightarrow \infty$ limit of the distorted octupolar dye. Other colored lines refer to intermediate cases with Δz increasing from 0.2 to 1eV (see caption).*

be relevant. In this limit, the signal seen in HRS at 670 nm is just the overtone of the main peak at 1340 nm.

Quite irrespective of the fine tuning of model parameters, we are not able to reproduce the relative intensity of the two main OPA and HRS bands and their position. More generally, we are not able to obtain a satisfactorily fit of the large amount of available spectra for BG. Therefore, we conclude that a distorted octupolar model does not apply to BG.

A clue towards a successful model is offered by chemical intuition: in BG, the unsubstituted benzene will not act as a poor donor, rather it can act as a weak acceptor. In addition, the broad and structureless bandshape of the second OPA transition, suggests the involvement of a highly polar state. Therefore we introduce the model sketched in Figure 1.12, formally analogous to a four-state model recently proposed for cyanine dyes [15].
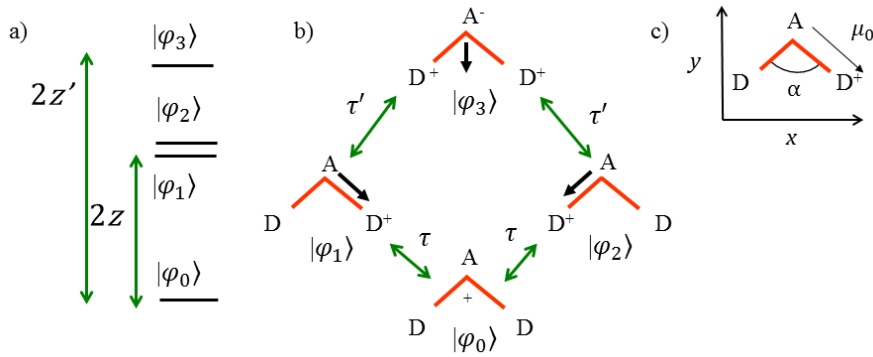
FIGURE 1.12: *The essential-state electronic model for BG; (a) the energy of the four resonating structures; (b) the four resonating structures; the green arrows connects states mixed by τ and τ' matrix elements, the black arrows close to φ_1, φ_2 and φ_3 show relevant permanent dipole moments (φ_0 has a vanishing dipole moment); (c) the orientation of the molecule in the (x,y) plane.*

The electronic model for BG is therefore defined as a 4x4 Hamiltonian matrix:

$$H_{el} = \begin{pmatrix} 0 & -\tau & -\tau & 0 \\ -\tau & 2z & 0 & -\tau' \\ -\tau & 0 & 2z & -\tau' \\ 0 & -\tau' & -\tau' & 2z' \end{pmatrix} \tag{1.47}$$

where the physical meaning of the model parameters is illustrated in Figure 1.12.

Being interested in optical spectra, the dipole moment operator must be defined, a non-trivial task for a dye with a net charge. Following the successful approach adopted for CV, we expand the charge distribution in terms of monopolar and dipolar charges located in the central C atom [16]. The monopole charge stays fixed in all states and becomes irrelevant in the subsequent discussion. The dipole vanishes in state φ_0; φ_1 and φ_2 have a permanent dipole of magnitude μ_0 along the first or second molecular arm (compare with Figure 1.12) and φ_3 has a permanent dipole equal to the vectorial sum of the dipoles associated with φ_1 and φ_2. In line with the Mulliken approximation, we neglect all off diagonal elements of the dipole moment with respect to μ_0, so that the operators associated with the x and y components of the dipole moment read:

$$\mu_x = \mu_0 \sin\left(\frac{\alpha}{2}\right) \begin{pmatrix} 0 & 0 & 0 & 0 \\ 0 & 1 & 0 & 0 \\ 0 & 0 & -1 & 0 \\ 0 & 0 & 0 & 0 \end{pmatrix} \tag{1.48}$$

$$\mu_y = \mu_0 \cos\left(\frac{\alpha}{2}\right) \begin{pmatrix} 0 & 0 & 0 & 0 \\ 0 & 1 & 0 & 0 \\ 0 & 0 & 1 & 0 \\ 0 & 0 & 0 & 2 \end{pmatrix} \tag{1.49}$$

Two symmetry-equivalent effective vibrational coordinates, q_1 and q_2, are introduced to account for the structural reorganization occurring following the CT along the two molecular arms. The electron-vibration coupling is introduced accounting for a variation of the equilibrium geometry: setting the origin of the coordinates at the equilibrium position for the $|\varphi_0\rangle$ state, the PESs for $|\varphi_1\rangle$ and $|\varphi_2\rangle$ are displaced along q_1 and q_2, respectively, while $|\varphi_3\rangle$ is displaced along both q_1 and q_2, with the strength of the coupling fixed by the vibrational relaxation energy, ε_{sp} [15]. Solvation effects are introduced in the same framework adopted for three states and four states model reaction-field approach.

The total Hamiltonian, accounting for both electron-vibration coupling and for polar solvation reads:

$$H_{tot} = \begin{pmatrix} 0 & -\tau & -\tau & 0 \\ -\tau & 2z + \omega\sqrt{2\varepsilon_{sp}}q_1 & 0 & -\tau' \\ -\tau & 0 & 2z + \omega\sqrt{2\varepsilon_{sp}}q_2 & -\tau' \\ 0 & -\tau' & -\tau' & 2z' + \omega\sqrt{2\varepsilon_{sp}}q_1 + \omega\sqrt{2\varepsilon_s}q_2 \end{pmatrix}$$

$$+ \frac{1}{2}\sum_{n=1,2}(p_n^2 + \omega^2 q_n^2) - \mu_x F_x - \mu_y F_y + \frac{\mu_0^2(F_x^2 + F_y^2)}{4\varepsilon_{or}}$$

$$\tag{1.50}$$

where the matrix represents the electronic Hamiltonian with q_1- and q_2- dependent diagonal energies, the third term describes the harmonic oscillators associated with q_1 and q_2, p_1 and p_2 being the conjugated momenta. The last three terms describe polar solvation, where F_x and F_y are the two in-plane components of the orientational reaction field, coupled to the relevant components of the dipole moment operator, defined in eq. 1.48 and 1.49. The very last term is the elastic energy associated with the orientational field, where $\langle F_{or}\rangle^2 = \langle F_x\rangle^2 + \langle F_y\rangle^2$ and ε_{or}, the solvation relaxation energy, increases with solvent polarity [30].

Since F_{or} enters the problem as a classical variable, the Hamiltonian in eq. 1.50 can be diagonalized at fixed F_x and F_y. The (F_x, F_y)-dependent Hamiltonian can be written on the basis obtained as the direct product of the four electronic basis states times the eigenstates of the two harmonic oscillators associated to q_1 and q_2 (trunctaed to M=10 states). Numerical diagonalization of the resulting matrix (total dimension $4M^2$) leads

to numerically exact non-adiabatic eigenstates. The calculation is repeated on a grid of (F_x, F_y) values to get (F_x, F_y)-dependent eigenstates. These eigenstates can then be used to calculate linear and nonlinear optical spectra, using standard sum-over-state expressions that are defined by transition energies and dipole moments. Explicit expressions used for the calculation of absorption, fluorescence and fluorescence anisotropy and TPA can be found in the Appendix B. The description of the calculations of the pump-probe spectra at two different limiting time is offered in the following Section.

1.3.3 The calculation of pump-probe spectra

In a typical pump-probe experiment, a pump pulse creates an excited state population in the system, which is interrogated by a delayed probe pulse. The pump pulse is simulated, in this work, as a Gaussian beam with full width at half maximum of 0.03 eV, as shown in Figure 1.13.
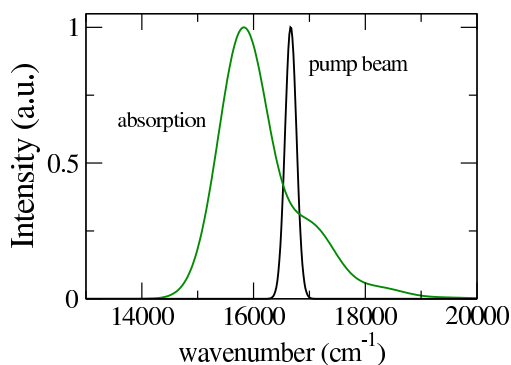
FIGURE 1.13: *Spectral profile of the pump used for the calculation of the pump-probe spectra and absorption profile (S0⟶S1) of BG in CHCl$_3$.*

Due to the finite spectral width of the pump, only the vibronic excited states resonant with its spectral profile can be populated. After photoexcitation, vibrational degrees of freedom relax almost instantaneously with respect to the slower solvation time scale. For this reason, we can separate vibrational and solvation dynamics, assuming that solvent relaxation starts once the vibrational relaxation is accomplished.

Specifically, we calculate the pump-probe spectrum in two limiting cases: the zero solvation time, describing a system with a complete relaxation of vibrational coordinates but unrelaxed solvent, and the infinite time, referring to the fully relaxed vibrational and solvent coordinates, but without accounting for the depopulation of the electronic state. At zero solvation time, the vertical occupation probability of the vibrationally cooled excited state for each value of the reaction field, $d^{ex,t=0}(F_x, F_y)$, is given by the ground state probability distribution of the reaction field, $d^{gs,t=0}(F_x, F_y)$, multiplied

by the absorbance of the sample generated by the specific pump profile, $\delta_{pump}(\omega)$, as to account for the finite width of the pump pulse. The population of the excited state evolves to adapt to the new reaction field generated by the excited dipole moment: at the effective infinite time, the occupation probability of the excited state for each value of the reaction field, $d^{ex,t=\infty}\,(F_x, F_y)$, is described by the excited state distribution of the reaction field (normalized as to preserve the initial area, not to introduce any spurious depopulation effect). The resulting distributions are reported in Figure 1.14. In the same Figure, the evolution of the ground state population is shown: at zero time, it is proportional to $d^{gs,t=0}\,(F_x, F_y)$ multiplied with the population remained in the ground state after the pulse excitation; after few picoseconds, $d^{gs,t=\infty}\,(F_x, F_y)$ recovers its equilibrium form.
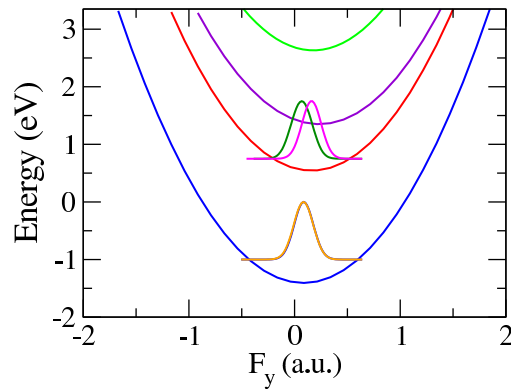
FIGURE 1.14: *Schematic view of the potential energy surfaces relevant to the four electronic states and distribution of reaction field relevant to the calculated pump-probe spectrum; the ground state distribution of reaction field at t=0 (orange line) is superimposed to the corresponding ground state PES; no appreciable difference is observed between ground state distribution at t=0 ps and at $t = \infty$ (blue line); the excited state distribution of reaction field at t=0 ps (green line) and $t = \infty$ (magenta line) is superimposed to corresponding excited state PES.*

Differential absorption pump-probe spectra are calculated as the sum of four contributions:

$$\Delta A(\omega, t) = \sum_{F_x, F_y} ESA(\omega)d^{ex,t}(F_x, F_y) + A(\omega)d^{gs,t}(F_x, F_y) + \tag{1.51}$$
$$-A(\omega)d^{gs,t=0}(F_x, F_y) - SE(\omega)d^{gs,t}(F_x, F_y)$$

where ω is the probe frquency, $d^{ex,t}(F_x, F_y)$ and $d^{gs,t}(F_x, F_y)$ are the excited state and the ground state population, respectively, at the delay time t (either 0 or infinite in the present treatment), and $A(\omega)d^{gs,t=0}(F_x, F_y)$ is the absorbance induced by the specific pump pulse. The $ESA(\omega)$ contribution takes into account all the transitions from the fluorescent state to all higher-energy eigenstates; $SE(\omega)$ is computed summing over all the eigenstates lying lower in energy than the fluorescent state; the photobleaching

$(A(\omega)d^{gs,t}F_x, F_y)$ - $A(\omega)d^{gs,t=0}(F_x, F_y))$ accounts for the reduced absorbance from the ground state due to its pump-induced depletion.

1.3.4   Discussion

For the BG model proposed here, the four energies in the electronic Hamiltonian of eq. 1.47, μ_0 and α of eqs. 1.48 and 1.49, define the electronic problem, while ω and ε_{sp} define the vibrational model. These molecular model parameters and the additional parameter Γ, the intrinsic bandwidth of each vibronic line in the calculation of optical spectra, are maintained fixed, irrespective of the solvent, while a last parameter, the solvent relaxation energy ε_{or}, is tuned to account for the solvent polarity.

The success of the proposed model for BG then clearly emerges from Figure 1.15 where calculated and experimental spectra are shown together as to best appreciate the overall quality of the agreement. All spectra in Figure 1.15, including linear absorption, HRS and pump-probe spectra were obtained using the 9 molecular parameters in Table 1.1; we fixed α=119° based on the results of the optimization of ground state geometry at DFT level (CAM-B3LYP/6-31+G*) with PCM model (chloroform) and fixing ε_{or}= 0.16 eV for CHCl$_3$.

TABLE 1.1: *Molecular parameters for BG; all energies are in eV;*

$2z$	$2z'$	τ	τ'	ω	ε_{sp}	$\mu_0(D)$	α	Γ
0.37	1.1	1.15	0.43	0.15	0.37	16.5	119°	0.06

The model reproduces very well the linear absorption spectra, including their minor solvent dependence, as shown in Figures 1.15 and 1.16. The main discrepancy concerns the highest energy feature at 321 nm. This transition is also observed in CV [16], suggesting the presence of a localized excitation that is clearly beyond the scope of essential-state models.

A similar quality of the agreement is observed for excitation anisotropy and HRS spectra in Figures 1.15 and 1.17, respectively. The model quite naturally reproduces the different relative intensity of the first and second peak in linear absorption and HRS as well as the bandshapes. Again, the calculated spectrum reproduces well the shape and relative intensities of the two lowest bands. As for the absolute intensity, calculated spectra are less intense by a factor of three with respect to experimental spectra. Indeed, calculated HRS spectra are most often underestimated by a factor of 3 with respect to experimental data [16], shedding doubts on the absolute calibration of HRS data.

As for the pump-probe experiment, the $t = \infty$ spectrum should be compared with long-time pump-probe signal, keeping in mind that, for the sake of simplicity, we do not
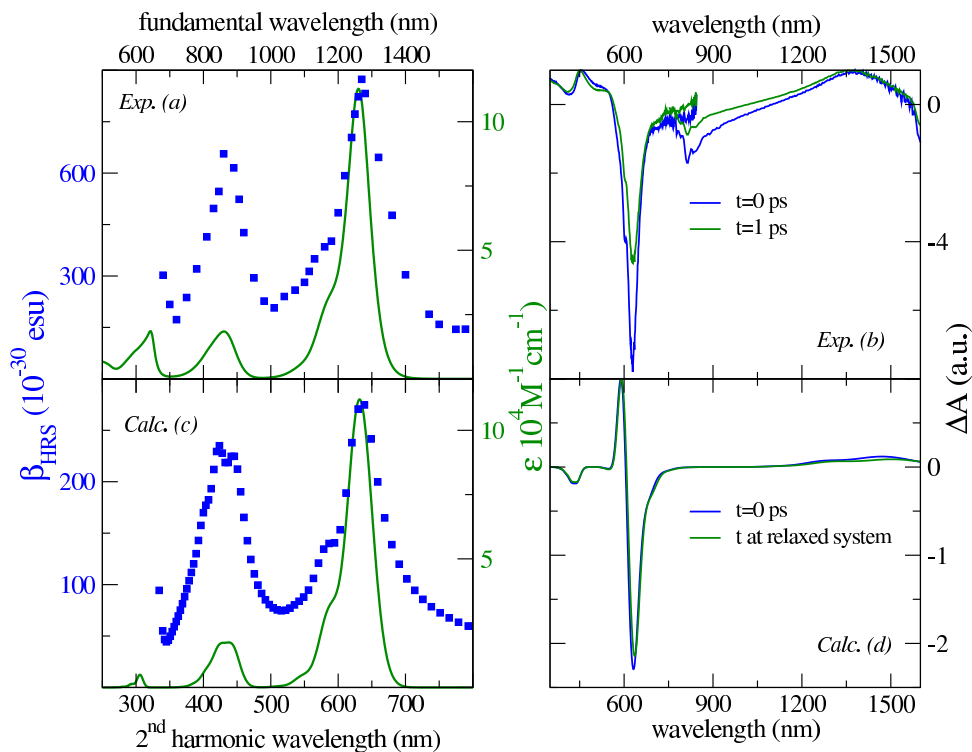
FIGURE 1.15: *Experimental data: (a) Absorption spectrum in CHCl₃ (green), HRS data in CHCl₃ (blue squares); (b) unpolarized pump-probe spectra collected in CHCl₃ at different delay times; the pump beam is centered at 600 nm using UV and NIR probes. Bottom: Calculated spectra (molecular parameters in Table 1); (c) Absorption spectrum (green), HRS spectrum (blue squares) in CHCl₃ (ε_{or} = 0.16 eV); (d) Pump-probe spectrum in CHCl₃ (ε_{or} = 0.16 eV) calculated at zero solvation time and for the fully relaxed system (see text). The adopted spectral profile of the pump beam is shown in Figure 1.13.*

explicitly account for the depopulation of the photoexcited states. Indeed, the pump-probe spectra calculated at $t = 0$ and $t = \infty$ are only marginally different, in line with the experimental result, and with the general observation of minor solvent effects in spectral properties of BG. Going in more detail, the low-energy ESA signal and the negative feature ascribed to PB are well reproduced in calculated spectra. The most significant discrepancy is observed for the narrow ESA contribution at 590 nm (corresponding to the $S1 \longrightarrow S3$ transition) that is not clearly recognizable in the experimental spectra. A problem could be a partial superposition with the bleaching signal, but we underline that, as for the linear absorption, S3 state is partially overlapped (mixed) with some local excited state. In good agreement with experimental data, the time evolution has minor effects on the pump-probe spectrum: just a slight redshift is observed in the calculated ESA signal at low energy. The relative intensity of the bands is not addressed, since spectra have been collected using different probes and different conditions depending on the wavelength of interest.
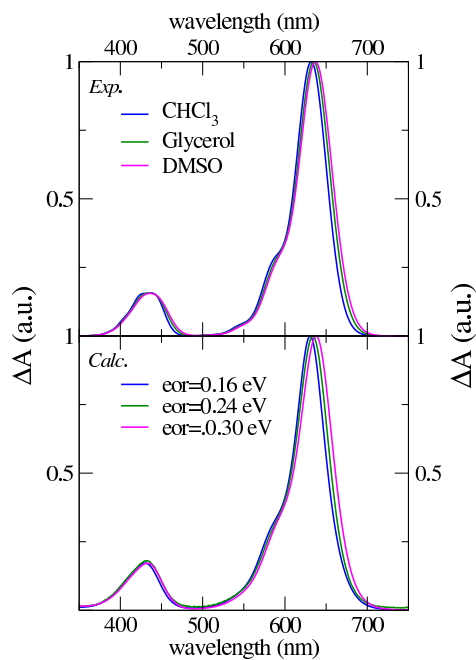
FIGURE 1.16: *Experimental (top) and calculated (bottom) OPA spectra of BG in different solvents.*

To complete the analysis we shortly address TPA spectra, available in a narrow spectral region around 3 eV (631 nm) for glycerol solutions [11], and in a wider spectral range for acetonitrile solution [63] [64]. The gross features of the TPA spectra are well reproduced by the calculated spectra in Figure 1.18, where two bands are recognized, corresponding to the S0⟶S1 and S0⟶S2 transitions. The intensity ratio of the two bands, roughly 1:8 is in line with the experimental data, even if calculated spectra are a factor of two less intense than experimental spectra and somewhat broader.
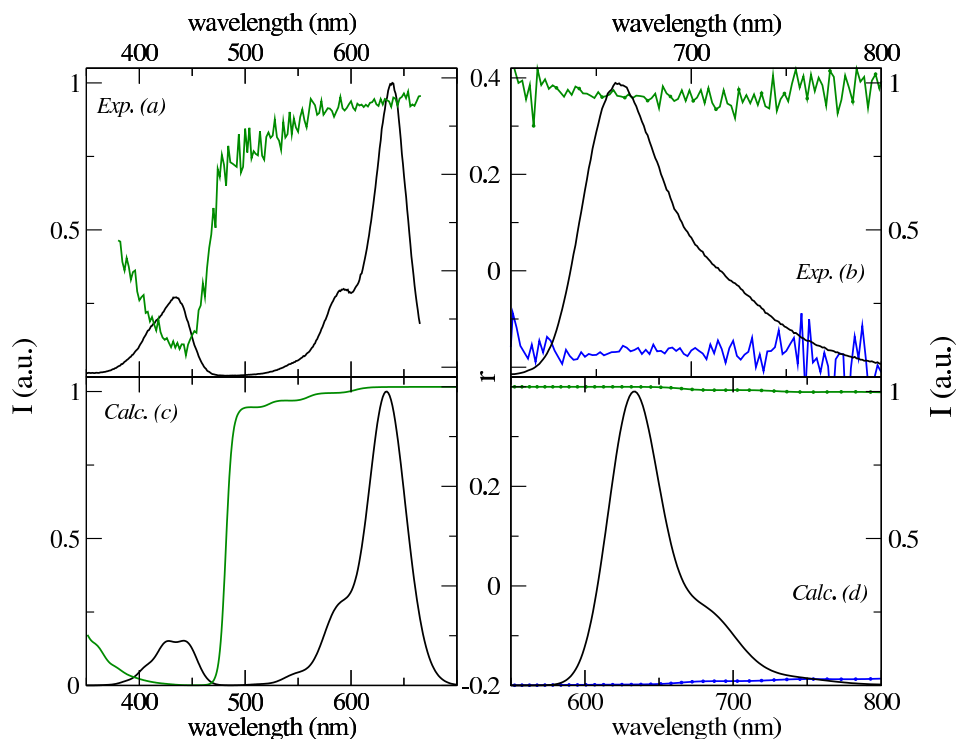
FIGURE 1.17: *Top: Experimental data, BG in glassy propylene-glycol at 200K; (a) fluorescence excitation spectrum detected at 675 nm and fluroscence excitation anisotropy obtained by detecting at 675 nm (green line); (b) florescence spectrum (black) and fluorescence anisotropy spectra obtained upon excitation at 434 nm (blue) and 595 nm (green). Bottom: Calculated spectra (c) fluorescence excitation spectrum obtained for 643 nm (black line) and fluroscence excitation anisotropy obtained by detecting at 643 nm (green line); (d) fluorescence spectrum (black) and fluorescence anisotropy spectra obtained upon excitation at 433 nm (blue) and 588 nm (green). The excitation wavelengths for calculated spectra were chosen as to best simulate the spectral position of experimental spectra.*
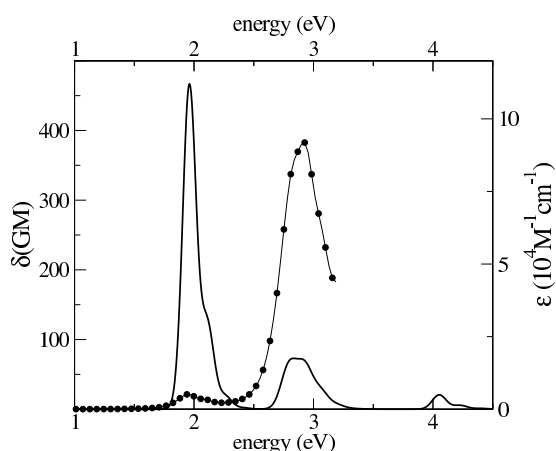
FIGURE 1.18: *Calculated TPA spectrum (black line with circles) compared with the linear absorption spectrum (black line) in glycerol (ε_{or}=0.18 eV).*

In this work, we have demonstrated that the definition of the diabatic states is not a trivial task for multi-branched chromophores and extensive comparison with experiment is crucial to validate the choice of the electronic diabatic basis states. Without a proper model, there is no way to fully understand the photophysical properties of a given dye and in this perspective, chemical/physical intuition can help to address towards the most relevant resonating structures among a wide spectra of potential states. Once a proper model is defined however we obtain a powerful tool: with few parameters, a large amount of photophysical properties of a given dye can be *quantitatively* estimated. In the present case, with nine parameters we are able to reproduce absorption spectra collected in several solvents, fluorescence and fluorescence anisotropy spectra, HRS and TPA spectra as well as time-resolved pump-probe spectra. Finally, the present model can be applied to other dyes of similar structure, allowing for a rationalization and systematization of the large and variegated group or organic dyes into families of systems that share the same basic physics. In this perspective, essential-state model offers a valid alternative to quantum-chemical calculations to understand the families of tripheylmethane dyes: S. Rafiq *et al.* report a computational study of Malachite Green, closely related to BG but with N,N-dimethyl substituted phenyl rings instead of N,N-ethyl groups. TD-DFT (B3LYP/ 6-31+g(d,p)) are not able to reproduce neither the absolute energy of the two lowest transition bands nor the relative transition energy: the S0$\longrightarrow$S1 and S0$\longrightarrow$S1 are overestimated, respectively, by 0.53 eV and 0.16 eV giving rise to a relative difference about twice the experimental data [65].

1.4   Vibrational coherences of charge transfer dyes

In this Section, we extend the essential-state machinery to investigate the early-stage dynamics of coherent states generated upon ultrafast (coherent) excitation that allows the direct observation of vibrational coherences. The capability to create coherent states opens the possibility of controlling the excited state vibrations and the photoinduced molecular dynamics: through ultrafast spectroscopy, an impulsive pump excites the system to an electronic state, whose subsequent oscillations can be picked up by a delayed probe. The instantaneous frequency and amplitude of these oscillations give the possibility to investigate the structural and electronic changes of excited molecules. To understand these complex phenomena, non-adiabatic dynamics is crucial [66–70] since the adiabatic separation of electronic and vibrational degrees of freedom blurs when several electronic states are close in energy. Several approximation schemes have been proposed to deal with the complex dynamics of systems undergoing photoinduced reactions, photoisomerization, etc. The problem becomes particularly delicate if relaxation is added to the picture, as needed to describe decay pathways after photoexcitation.

An accurate picture of the systems of interest is obtained implementing non-adiabatic dynamics based on the description of excited states derived from quantum-chemical calculations, ranging from comparatively simple semiempirical approaches to more refined first-principle or ab initio results. Several electronic states and several vibrational modes are usually involved, making the resulting picture fairly complex and asking for refined and advanced computational strategies.

By contrast, as discussed above, essential-state models, relying on an oversimplified picture of the molecular electronic structure in terms of few electronic diabatic states and only accounting for a minimal set of vibrational coordinates, can be written in the non-adiabatic approximation: brute-force numerical diagonalization of the non-adiabatic Hamiltonian is possible. The non-adiabatic approach of essential-state model has been adopted to investigate the real-time vibrations in dyes, whose excited state PES clearly shows dramatic symmetry-breaking effects, as quadrupolar Class I chromophores [36]; in order to underline the peculiar dynamics of Class I dyes as well as the efficiency of the model, a comparison with systems characterized by stable PESs, is offered. Specifically, a polar dye and a quadrupolar dye belonging to Class II have been selected [18].

1.4.1   Essential-state models for dipolar and quadrupolar dyes at work

In this Section we introduce the three CT dyes for which an ultrafast experiment has been simulated. In particular, Phenol Blue (P1) has been chosen as prototypical polar dye; among quadrupolar dye, squaraine (Q1) and fluorene (Q2) belonging to Class II and Class I, respectively have been selected. The three CT dyes under investigation are reported in Figure 1.19. All chromophores have been parameterized in the framework of essential-state models several years ago [36, 48, 71]. The dipolar dye is modeled adopting the two-state description presented in Section 1.2.1, while three-state model is adopted for quadrupolar dyes (Section 1.2.2). Molecular parameters for the three dyes are summarized in Table 1.2.

TABLE 1.2: *Molecular parameters for the three dyes of interest; all energies are in eV;*

Dye	z	$-\tau$	ε_{sp}	ω	Γ
P1	0.7	1	0.42	0.2	0.2
Q1	0.28	1.2	0.16	0.16	0.05
Q2	1.5	0.6	0.3	0.16	0.08

Phenol blue, also known as dimethylindoaniline, is an interesting chromophore for NLO applications due to a large first hyperpolarizability. P1 is a non fluorescent dye showing absorption solvatochromic effect: the absoprtion band moves by 950 cm^{-1} passing from
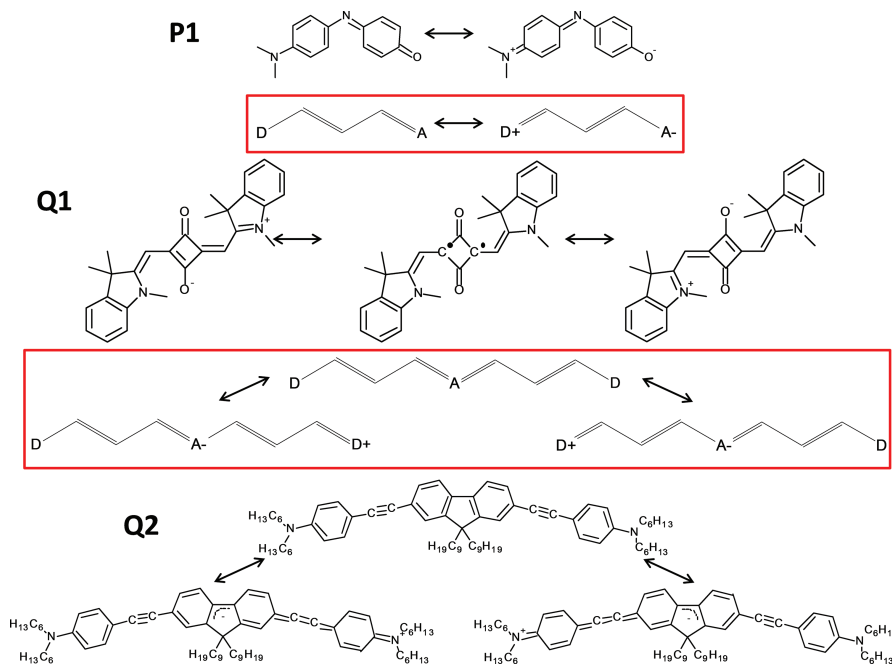
FIGURE 1.19: *Resonating structures of the three investigated molecules. In the red boxes, the two/three electronic states are schematized for polar/quadrupolar dyes.*

tetrachlorocarbone to chloroform. Essential-state model is also applied to investigate vibrational spectroscopy: a large softening of the vibrational (IR and Raman) frequencies increasing the solvent polarity are predicted in virtue of a large linear *e-ph* coupling [48, 71].

The squaraine-based chromophore, with intermediate quadrupolar character (Class II) is characterized by a large mixing betweeen the neutral and charge-separated states that allows a sizable energy splitting between all relevant states. In addition, the intermediate ρ value makes squaraine based dyes extensively studied in the literature for their high two photon response, due to the pre-resonance effects with OPA transition. Due to the non-polarity of relevant states, no solvatochromic effect is observed neither in absorption nor in fluorescence [36].

Q2, a prototypical Class I dye, is characterized by two external electron donor amino groups and a central fluorene core as an electron acceptor moiety. Spectral properties are qualitatively different with respect to the previous compound. Absorption spectra are only marginally affected by the solvent polarity: only inhomogeneous broadening is observed increasing the solvent polarity; by variance, this dye shows a markable fluorescence solvatochromism: increasing the solvent polarity from toluene to acetonitrile, the emission band is red-shifted by $\sim$3700 cm^{-1}. This feature can be explained in terms of symmetry breaking in the OPA excited state: indeed, the OPA excited state in Class I dye shows two minima (see Figure 1.4) and after vertical excitation, the system relaxes

towards one of those, leading to a *polar* relaxed excited state whose energy is stabilized increasing the solvent polarity. The absorption spectra calculated for the three dyes in absence of solvent are shown in Figure 1.20.
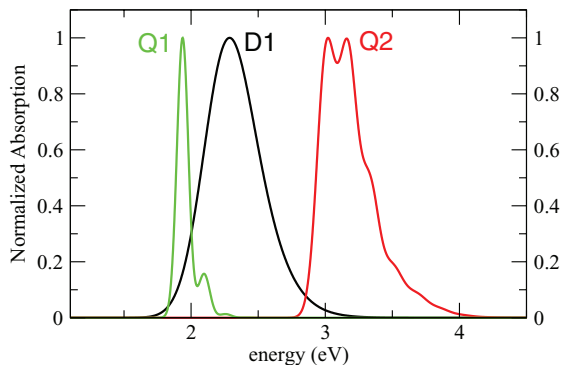
FIGURE 1.20: *Calculated absorption spectra for the three dyes in a non-polar solvent (ε_{or} = 0). Model parameters are listed in Table 1.2.*

1.4.2 Excitations and pump-probe spectra

Ultrafast excitation with pulse duration shorter than a vibrational period generates vibrationally coherent excitations, whose dynamics is responsible for characteristic oscillations in the transient absorption signals, giving real-time information about vibrational motion. These coherent oscillations are well understood and are usually successfully modeled based on the *adiabatic approximation* and assuming *harmonic PES* [72–76]. In the *adiabatic approximation*, the ground state is the product of the ground electronic wavefunction times the vibrational wavefunction. In the *harmonic approximation* and low-temperature limit, the ground state vibrational wavefunction is χ_0, the lowest eigenstate of the relevant oscillator (assuming to consider a diatomic molecule). As it is well known, χ_0 describes a coherent state.

The Condon approximation leads to the simplest description of impulsive excitation: if electronic transition dipole moments are assumed independent on vibrational coordinates, the ultrafast excitation simply transfers the vibrational coherent state into the excited state PES, creating a (non-equilibrium) coherent wavepacket. The motion of a coherent wavepacket on a harmonic PES preserves its coherence and its dynamics can be described as the dynamics of a classical particle on a harmonic potential [77]: the wavepacket starts oscillating around the displaced minimum in the excited state PES, giving rise to typical oscillations in the photoinduced signal. Pump-probe spectra induced by ultrafast excitation then give us the opportunity to monitor vibrational dynamics in real-time.

This simple picture is very useful to understand the basic physics of coherent oscillations, and most often leads to accurate results. However, it is based on several approximations that, as discussed above, cannot apply to the excited state dynamics of dyes undergoing symmetry breaking, like Class I quadrupolar dyes. Indeed as discussed in Section 1.2.2, due to the low quadrupolar character of the ground state, the two excited states are quasi-degenerate giving rise to a double-minima first excited state PES: both the adiabatic and the harmonic are doomed to fail in this case. We therefore exploit the essential-state models to obtain a truly non-adiabatic approach to the description of coherent oscillations in systems undergoing symmetry breaking in the excited state.

To start with, and to get confidence on the proposed approach, we discuss dyes in non-polar solvents ($\varepsilon_{or}= 0$). The diagonalization of the Hamiltonian matrix written on the non-adiabatic basis leads to the (numerically exact) vibronic eigenstates, ψ_k and to relevant transition energies. At time zero, an ideal instantaneous light pulse excites the system from the ground state to a coherent state [78], φ, expressed as a linear combination of the exact vibronic eigenstates:

$$|\varphi(0)\rangle \propto \sum_{k=2}^{m} \mu_{k \leftarrow 1}|\psi_k\rangle \propto \sum_{k=2}^{m} \delta_{k \leftarrow 1}|\psi_k\rangle \tag{1.52}$$

where the sum runs over all the vibronic excited eigenstates, ψ_k, of the non-adiabatic Hamiltonian and $\mu_{k \leftarrow 1}$ is the transition dipole moment from the ground state, ψ_1, to the kth state. We underline that the ψ_k are *truly vibronic* (non-adiabatic) eigenstates, obtained as linear combination of the basis states, that by themselves are expressed as products of electronic and vibrational basis states. The transition dipole moments are therefore the true (fully non-adiabatic) transition dipole moments associated with (numerically exact) vibronic eigenstates.

In systems where the adiabatic approximation works well, the electronic and vibrational problems effectively factorize and the adiabatic wavefunctions are a good approximation of vibronic eigenstates. In these conditions, it is useful to distinguish two different kinds of excitations:

- *purely vibrational excitations*, where the system is driven from the ground state (product of the electronic ground state wavefunction and the ground state vibrational wavefunction) to a state where only the vibrational state is changed;

- *electronic excitations*, where the system is driven from the ground state towards an excited state with a different electronic wavefunction (and most often a different vibrational wavefunction).

In both cases, the relevant transition dipole moment, $\mu_{k\leftarrow 1}$ is calculated by first integrating over the electronic wavefunction, to get q-dependent electronic dipole moments. For vibrational transitions, the permanent molecular dipole moment for the electronic ground state is expanded on the vibrational coordinates, and the linear term accounts for the vibrational intensities of fundamental modes. For electronic excitations, the electronic transition dipole moment is similarly expanded with respect to q: the zeroth order (constant) term accounts for the Condon intensity of the electronic transition, and the linear term accounts for Herzberg-Teller contributions. As expected on physical grounds, purely vibrational excited states, having small transition dipole moments, contribute marginally to the coherent state in eq. 1.52, that is instead largely dominated by optically allowed states, showing sizable $\mu_{k\leftarrow 1}$. As discussed above, in the Condon approximation the transition dipole moment is independent of the vibrational coordinates, and the coherent state $|\varphi(0)\rangle$, can be written as the product of an electronic excited state times the ground state vibrational wavefunction (the coherent ground state of the harmonic oscillator).

We will not impose either the adiabatic or the Condon approximation, but we will show in the following that the Condon approximation works well to describe the generation of the coherent state $|\varphi(0)\rangle$, but not its dynamics. The exact quantum dynamics of the coherent state is calculated as follows:

$$|\varphi(t)\rangle = \sum_{k=2}^{m} \mu_{k\leftarrow 1} e^{-i\omega_{k\leftarrow 1}t}|\psi_k\rangle \propto \sum_{k=2}^{m} \delta_{k\leftarrow 1} e^{-i\omega_{k\leftarrow 1}t}|\psi_k\rangle \qquad (1.53)$$

where $\omega_{k\leftarrow 1}$ is the frequency of the kth excitation from the ground state. Being interested in the early-stage dynamics, we will not introduce any dissipation term. In these conditions, the energy of the coherent state is independent of time

$$E_\varphi = \sum_{k=2}^{m} |\mu_{k\leftarrow 1}|^2 \varepsilon_k \qquad (1.54)$$

where ε_k is the kth eigenvalue.

In the typical experiment, the temporal evolution of the coherent excitation is monitored measuring the time-dependence of the differential absorbance

$$\Delta A(t,\omega) = A(t,\omega) - A_0(\omega) \qquad (1.55)$$

where $A_0(\omega)$ is the frequency-dependent steady-state absorbance and A(t,ω) is the time-frequency-dependent absorbance of the system after the ultrafast excitation. Three

processes contribute to ΔA:

$$
\begin{aligned}
\Delta A(t,\omega) \quad \propto \quad & \omega \sum_{k>\varphi(t)}^{m} |\mu_{k\leftarrow\varphi(t)}|^2 I(\omega - \omega_{k\leftarrow\varphi(t)}) \\
& -\omega \sum_{k=1}^{\varphi(t)-1} |\mu_{k\leftarrow\varphi(t)}|^2 I(\omega - \omega_{k\leftarrow\varphi(t)}) \\
& -\omega \sum_{k=2}^{m} |\mu_{k\leftarrow 1}|^2 I(\omega - \omega_{k\leftarrow 1}) \qquad (1.56)
\end{aligned}
$$

The first term (positive sign) describes the absorption from the coherent state to all higher-energy eigenstates, $\omega_{k\leftarrow\varphi(t)} = (\varepsilon_k - E_\varphi)/\hbar$ measuring the relevant transition frequency. The second term (negative sign) is the stimulated emission from the coherent state: the sum runs now over eigenstates lying lower in energy than the coherent state. Finally, the third term (negative sign) accounts for the bleaching of the absorption, as due to the depopulation of the ground state induced by the pump: the sum runs, in this case, over all excited states. In all the three terms above, $I(\omega)$ is the Gaussian bandshape (with half width at half maximum Γ) assigned to each transition. Exactly the same treatment applies to the case of polar solvents, $\varepsilon_{or} > 0$, but the calculation is repeated for different values of the effective solvation coordinate and then summing up relevant spectra weighted by the Boltzmann distribution relevant to the ground state energy, as discussed in Section 1.2.1.

1.4.2.1 Vibrational coherences in dipolar dyes

In this Section, we focus attention on transient absorption spectra and their temporal evolution as calculated for P1, the prototypical polar dye. We start our discussion with spectra calculated for non-polar solvents ($\varepsilon_{or} = 0$) and we refer to Figure 1.21.
In panel (a) we report the differential absorbance calculated as a function of time delay and probe frequency. As we can observe from the color map, the signal is always negative: in fact, a two-state model cannot address photoinduced absorption from the single excited state considered. Panel (c) describes ΔA as a function of probe energy at two different delay time. Coherent oscillations at fixed probe energy are reported in panel (b) and direct information about vibrational frequencies is obtained via Fourier Transform (FT) and shown in panel (d). The FT signal (continuous line or dashed line) clearly reports a single band at 0.21 eV. This energy corresponds to the vibrational frequency relevant to the excited state PES which is expected to be somewhat higher than the reference frequency [30]. As mentioned above, we do not introduce any source of friction or relaxation in our model, so that calculated coherent oscillations are not damped. The width of the FT-signal is therefore related to the finite width of the temporal window
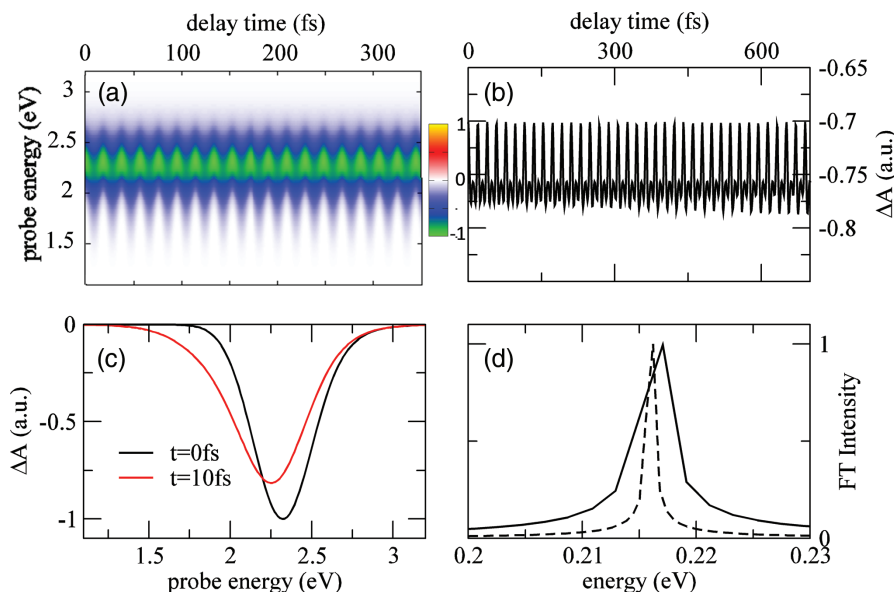
FIGURE 1.21: *Calculated spectra for P1 in a non-polar solvent ($\varepsilon_{or} = 0$). Panel (a): 2D map of pump-probe spectrum as a function of time delay and probe energy. Panel (b): Pump-probe signal as a function of time, calculated for probe energy fixed at 2.17 eV. Panel (c): Pump-probe spectrum calculated at two different times after pump excitation (t=0 fs and t=13 fs). Panel (d): Normalized Fourier transform magnitude spectrum of the pump-probe signal in panel (b). Continuous line: temporal windows of 2 ps; dashed line: temporal window of 7 ps.*

used for integration: this is clearly demonstrated comparing the FT spectra obtained from the oscillating signal in panel (b), working on temporal windows of 2 and 7 ps (continuous and dashed lines) respectively. Panel (c) shows ΔA as a function of probe energy at two different delay time.

Several new features appear in a polar solvent, as summarized in Figure 1.22. First of all, in panel (c) we can observe that the peak in the pump-probe spectrum is red shifted respect to the signal in apolar solvent, due to the normal positive solvatochromism characterizing optical spectra of dipolar dye [48, 71]. Similarly, one observes that the excited state vibrational frequency becomes higher (see Figure 1.22, panel (d), to be compared with Figure 1.21, panel (d)). More interesting is the behavior of the ΔA signal shown as a function of time in panel (b): in fact, at variance with the previous results obtained in non-polar solvents, a damping of the oscillations is clearly observed in polar solvents. The observed damping of the oscillations is a pure-dephasing effect, due to disorder (inhomogeneous broadening) induced by solvent polarity. In fact, in polar solvents, each solute molecule is surrounded by solvent molecules that, due to thermal disorder, generate slightly different values of the local reaction field. The (polarizable) solute molecule responds to the reaction field readjusting its charge distribution. Each solute molecule is therefore characterized by a specific value of ρ and, due to the coupling between electrons and vibrations, by a (slightly) different vibrational frequency. The observed
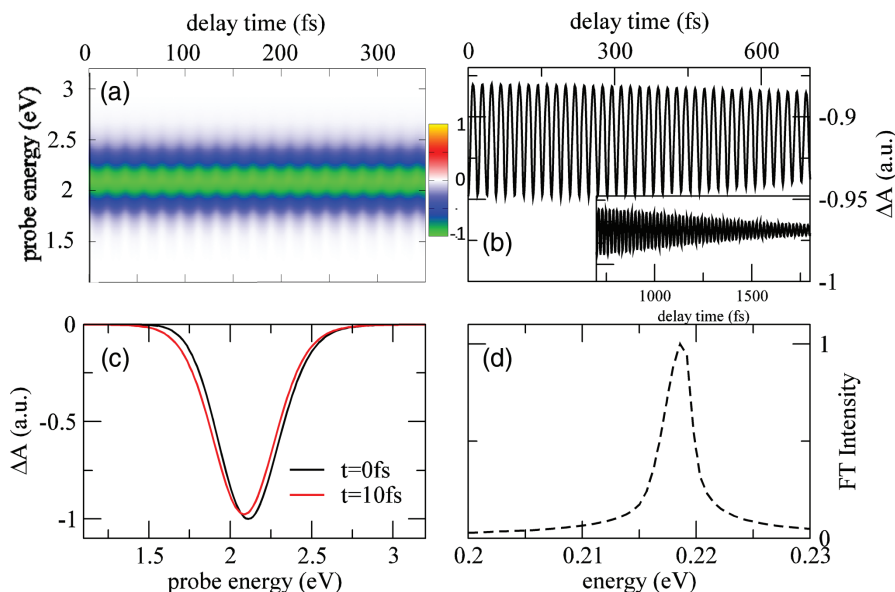
FIGURE 1.22: *Calculated spectra for P1 in a polar solvent ($\varepsilon_{or} = 0.7\,eV$). Panel (a): 2D map of pump-probe spectrum as a function of time delay and probe energy. Panel (b): Pump-probe signal as a function of time calculated for probe energy fixed at 2.17 eV. Panel (c): Pump-probe spectrum calculated at two different times after pump excitation (t=0 fs and t=10 fs). Panel (d): Normalized Fourier transform magnitude spectrum of the pump-probe signal in panel (b).*

oscillations are then the sum of signals oscillating at slightly different frequencies: the inhomogeneity shows up with a damping of the oscillations and a broadening of the relevant Fourier transform spectrum (see Figure 1.22, panel (d)).

Photoselection is another phenomenon originating interesting spectral effects in polar solvents. At each frequency of the probe beam, in fact, different molecules (i.e., molecules experiencing slightly different values of the solvent reaction field, as a result of thermal disorder) contribute by different amounts to the observed signal. Since each group of molecules is characterized by a slightly different vibrational frequency, the observed frequency of the coherent oscillation shows a small dispersion with the frequency of the probe beam, as sketched in Figure 1.23.

This information is collected in the color map in Figure 1.23, where the magnitude spectrum obtained from the FT of the pump-probe signal is reported as a function of the probe energy in a 2D plot: the position of the maximum of the FT spectrum changes with the probe energy, especially when the probe wavelength falls in the blue side of the absorption and emission band. This effect is analogous to the dispersion of the vibrational frequency in resonant Raman spectra while changing the excitation laser wavelength [48, 71, 79].
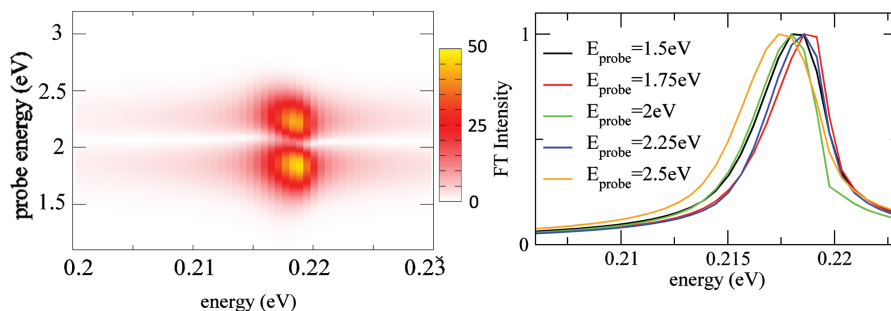
FIGURE 1.23: *Fourier transform spectra calculated for P1 in a polar solvent (ε_{or}=0.7 eV). Left panel: 2D plot of the magnitude spectrum obtained from the FT of the pump-probe signal. Right panel: Normalized Fourier transform magnitude spectrum of the pump-probe signal for selected probe energies.*

1.4.2.2 Vibrational coherences in quadrupolar dyes

We now turn attention to quadrupolar dyes. In Figure 1.24 are summarized results obtained for the squaraine dye Q1.

FIGURE 1.24: *Calculated spectra for Q1 in a non-polar solvent ($\varepsilon_{or} = 0$). Panel (a): 2D map of pump-probe spectrum as a function of time delay and probe energy. Panel (b): Pump-probe signal as a function of time, calculated for probe energy fixed at 2.17 eV. Panel (c): Pump-probe spectrum calculated at two different times after pump excitation (t=0 fs and t=13 fs. Panel (d): Normalized Fourier transform magnitude spectrum of the pump-probe signal in panel (b). Continuous line: temporal windows of 2 ps; dashed line: temporal window of 7 ps.*

As shown in panel (c), the differential absorption signal is negative in the region 1.8-2.0 eV, where stimulated emission and absorption bleaching occur, but is positive at lower energies, where excited state absorption (from the first to the second excited state) dominates. This is in line with the behavior of squaraine-based dyes, or more generally

of Class II quadrupolar dyes ($\rho \sim 0.5$), characterized by an excitation spectrum where the first excited state (OPA) approximately lies half-way between the ground and the second excited state (TPA). As for P1, the transient signal shows a clean coherent oscillation, whose frequency is independent of the probe energy (either in the positive or negative ΔA region, as shown in Figure 1.24, panel (b)) and the relevant FT shows a single peak located at the same frequency (0.16 eV) assigned to the unperturbed harmonic oscillator. Due to the large mixing character in the squaraine dyes and, more generally, in Class II dyes, the large energy separation among electronic states are not prone to symmetry breaking and relevant PES are well-behaved, showing a single minimum and a roughly parabolic shape. Since excited states preserve the molecular symmetry, all PES are aligned along the q_- coordinate, being only displaced along q_+. As a result, after coherent excitation, the system oscillates according to the first excited state PES but only along the symmetric q_+ coordinate. Since the first excited state is the pure (unmixed) zwitterionic state Z_-, its curvature along either q_+ or q_- is not affected by the electron-vibration coupling and we observe oscillations at the frequency of the unperturbed oscillator (0.16 eV, compare with Table 1.2).

More interesting is the behavior of Q2, a Class I quadrupolar dye undergoing symmetry breaking in the excited state (see Figure 1.4). Relevant spectra calculated in a non-polar solvent are reported in Figure 1.25.
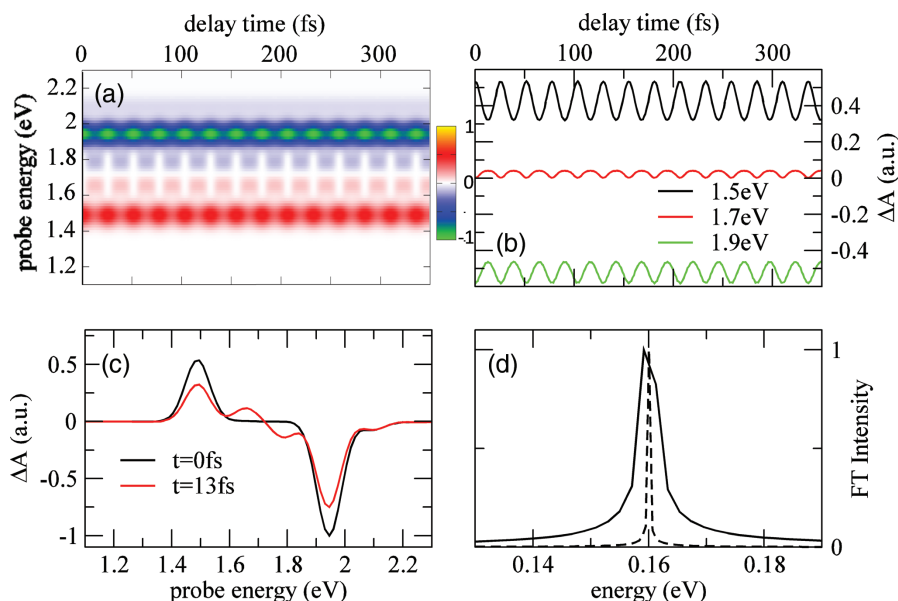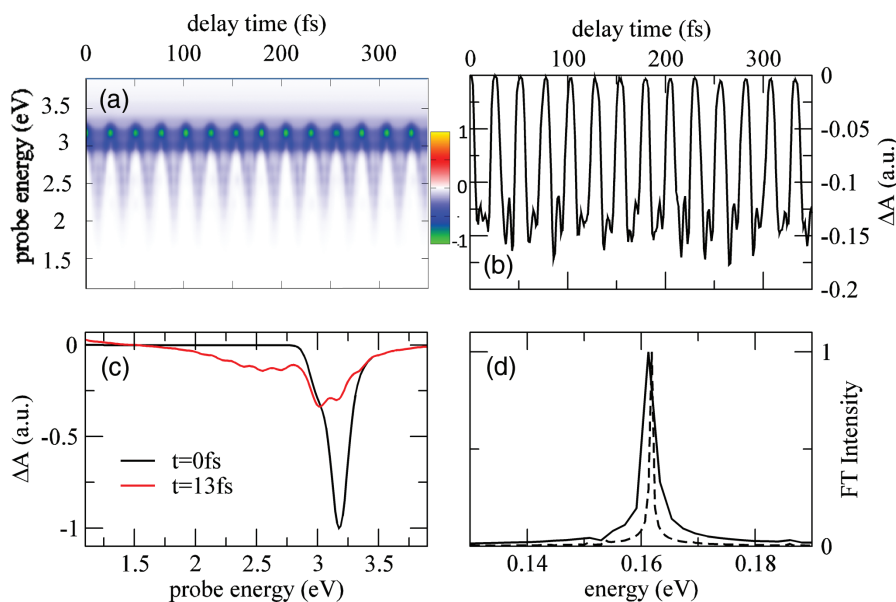

FIGURE 1.25: *Calculated spectra for Q2 in a non-polar solvent ($\varepsilon_{or} = 0$). Panel (a): 2D map of pump-probe spectrum as a function of time delay and probe energy. Panel (b): Pump-probe signal as a function of time, calculated for probe energy fixed at 2.17 eV. Panel (c): Pump-probe spectrum calculated at two different times after pump excitation (t=0 fs and t=13 fs. Panel (d): Normalized Fourier transform magnitude spectrum of the pump-probe signal in panel (b). Continuous line: temporal windows of 2 ps; dashed line: temporal window of 7 ps.*

The energy difference between the two excited states is rather small in Class I dyes, due to the small quadrupolar character, and therefore the contribution to the ΔA signal due to excited state absorption is located outside the spectral region shown in the Figure 1.25. The oscillating signal is clearly dominated by a single frequency, even if some *noise* appears, suggesting the contribution of some additional frequencies. Indeed, the FT spectrum in panel (d) shows a slightly asymmetric single main peak, and some small additional features. The relative simplicity of the oscillating signal and of the corresponding FT contrast sharply with the complex shape of the excited state PES, with its well pronounced two minima.

To understand the behavior of the system after coherent excitation, we have calculated the evolution of (the square modulus of) the wavefunction on the (q_-, q_+) plane. Specifically, for quadrupolar chromophores, the k-th eigenstate is expressed as follows:

$$|\varphi_k\rangle = \sum_{i,m,m} c_{imn}|\phi_i\rangle|m\rangle|n\rangle \tag{1.57}$$

where $|\phi_i\rangle$ represents the i-electronic basis state and $|m\rangle, |n\rangle$ are the eigenstates of two independent harmonic oscillators. In the (q_+, q_-) space, the eigenstate in eq. 1.57 reads:

$$|\varphi_k(q_+, q_-)\rangle = \sum_{i,m,m} c_{imn}|\phi_i\rangle\chi_m(q_+)\chi_n(q) \tag{1.58}$$

where $\chi_m(q_+)$ and $\chi_n(q_-)$ are the m, n eigenstates of the relevant harmonic oscillators. The integration over the electronic coordinates gives the probability density in the (q_+, q_-) space:

$$P_k(q_+, q_-) = \sum_i \sum_{m,n} \sum_{k,l} c_{imn}^* c_{ikl} \chi_m(q_+)\chi_n(q_-)\chi_l(q_+)\chi_k(q_-) \tag{1.59}$$

Figure 1.26 shows the evolution on the (q_-, q_+) plane of (the square modulus of) the wavefunction for the two quadrupolar dyes. In each panel of Figure 1.26, the color map shows the squared modulus of the wavefunction, while the information on the ground- and first-excited state (adiabatic) PES is given by the isolines drawn as black and green lines, respectively. The double minimum in the excited state PES is a signature of symmetry breaking in Q2. At t = 0 the coherently excited wavefunction has approximately the same shape as the ground state wavefunction (the Condon approximation works very well) and is centered around the minimum of the ground state PES.

For Q1, and more in general, for Class II dyes, the excited state PES is only displaced along the q_+ coordinate: after coherent excitation the wavefunction oscillates (basically
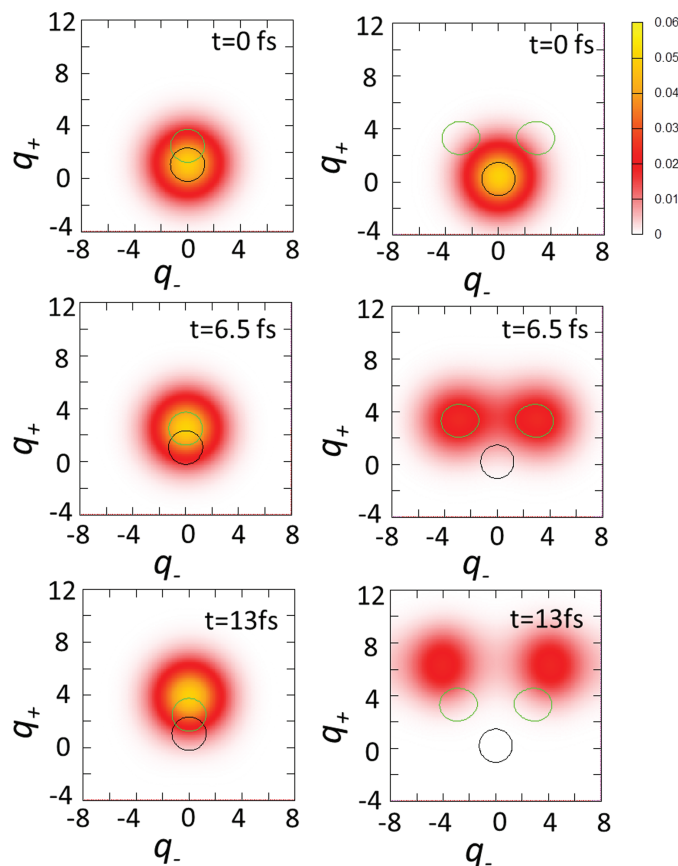
FIGURE 1.26: *Probability of the coherent wavepacket in the (q_+, q_-) space for Q1 (left) and Q2 (right).*

maintaining constant shape) back and forth around the minimum of the excited state PES, with a frequency coincident with the curvature of the excited state PES along q_+.

For Q2, the motion after coherent excitation is more complex and interesting: the wavefunction starts moving along q_+, but it splits in two (equivalent) components moving towards the two equivalent minima and then goes back almost retracing the forward path. The motion represents a direct observation of a *dynamical Jahn-Teller effect*: the system has a broken-symmetry PES yet it dynamically recovers the symmetry during the motion. Basically, the only relevant oscillations are those along q_+ and the complexity of the bistable excited state PES only shows up with some *noise* and a deviation of the main frequency from the reference frequency.

Solvent polarity has marginal effects on the spectral properties of squaraine dyes, and this holds true for coherent oscillations as well, as shown in the left panel in Figure 1.27. For systems undergoing symmetry breaking in the excited state, instead polar solvation is important. We underline that, due to the very short time involved in the typical experiment, we do not allow the solvent to relax after photoexcitation. However, thermal disorder introduces pure-dephasing (inhomogeneous broadening) effects. For Class II

molecules (like Q1), the presence of a finite reaction field has marginal effects on the PES. For Q2, instead, the excited state PES is strongly affected by the reaction field, leading to a largely asymmetric motion: after coherent photoexcitation, the wavefunction oscillates both along q_+ and q_- driven by a strongly asymmetric and anharmonic PES: the FT of the oscillating signal clearly shows two frequencies, associated to the oscillations along q_+ and q_-, as well as a wide broadening.
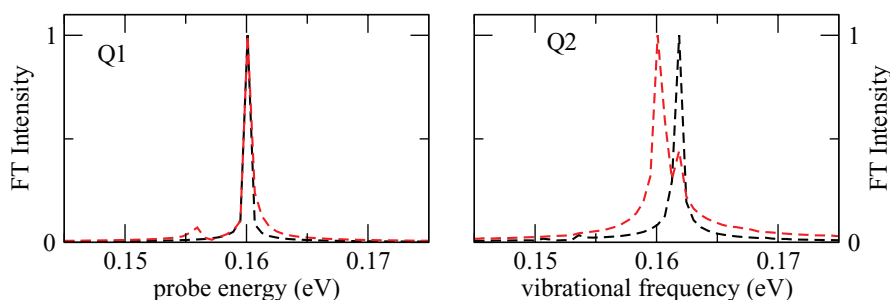
FIGURE 1.27: *Normalized FT magnitude spectra calculated for Q1 (left) and Q2 (right) in a non-polar solvent ($\varepsilon = 0$,, black line) and a polar solvent ($\varepsilon_{or} = 0.25$, red line). The total delay time for the FT is 7 ps. The probe energy is 1.94 eV and 2.17 eV for Q1 and Q2, respectively.*

The picture emerging from all those observations is the following. In the polar dye (P1) and the *well-behaved* quadrupolar dye belonging to Class II (Q1), the excited states are fairly well separated in energy and the adiabatic approximation works well. The Condon approximation and the harmonic approximation seem similarly robust.

When dealing with a Class I quadrupolar dye (Q2), the situation is different due to the presence of two almost degenerate excited states that give rise, in the adiabatic approximation, to a broken-symmetry (two-minima) PES. The Condon approximation stays essentially valid but, to calculate the dynamics after coherent excitation, one must relax both the harmonic and the adiabatic approximation. The results of non-adiabatic calculation support a complex motion on the excited state PES, with the wavefunction that symmetrically splits to explore the two degenerate minima and refocusing back periodically. As expected in a dynamic Jahn-Teller system, the symmetry is broken at the adiabatic level (the PES shows two minima) but it is regained dynamically, with the system exploring both minima. Medium effects and in particular polar solvation enter the model quite naturally. Of course, the solvent dynamics is irrelevant on the time scales of an ultrafast pump-probe experiment. However, polar solvation introduces thermal disorder and hence inhomogeneous broadening in the spectra and some new features in the transient absorption signals: for polar dyes, a dispersion of the frequency of coherent oscillations with the probe frequency; for Class II quadrupolar dyes, very small features due to solvent-induced symmetry lowering. The role of polar solvation has instead disruptive effects in Class I quadrupolar dyes, where finite reaction-field

values effectively remove the degeneracy between the two minima in the excited state PES, lowering the symmetry and leading to an asymmetric motion and the consequent activation of both symmetric and antisymmetric vibrations.

1.5   Conclusion

In this Chapter theoretical methods based on the essential-state strategy were presented. In the first Sections, a briefly *review* of the different model developed to describe CT molecules of different symmetry was offered. The specific contribute of this thesis is provided in Section 1.3 and 1.4.

In Section 1.3, the razionalization of linear and nonlinear optical properties of Brilliant Green confirms that essential-state models are tractable and reliable tools to describe low-energy spectral properties of CT chromophore. We demonstrate that the definition of the diabatic states is not a trivial task for multi-branched chromophores and that without the proper and physically relevant choice of the electronic basis set, there is no way to reproduce the photophysical properties of a given dye. Once a proper model is defined, with few parameters, we were able to reproduce linear, nonlinear and pump probe spectra, offering therefore a reliable alternative to quantum-chemical calculations to understand the families of tripheylmethane dyes.

In Section 1.4, we demonstrated that the same models can describe time-resolved spectral properties and specifically coherent oscillations measured in pump-probe spectra with ultrafast excitation. At variance with common approaches to the problem, based on the adiabatic and (most often) harmonic approximation, essential-state models allow to attack the calculation in a genuinely non-adiabatic approach, so that reliable results can also be obtained for critical cases, where the coherent excitation drives the system towards degenerate or almost degenerate and/or bistable excited states and the adiabatic approximation fails. The fully non-adiabatic treatment of coupled electronic and vibrational motion allows for a reliable description of the dynamics of these intriguing systems, such as quadrupolar dyes showing a multistable, broken-symmetry excited state.

Chapter 2

Mixed-stack charge transfer salts

*"Measure what is measurable, and
make measurable what is not so"*
-Galileo Galilei

2.1 Introduction

Charge transfer (CT) crystals represent a wide class of organic molecular materials formed by planar π- conjugated molecules with electron donor (D) and electron acceptor (A) character. Due to the directionality of the CT interactions between the frontier orbitals, the molecules arrange themselves in *quasi-one* dimensional stacks. Different stacking geometries are possible and CT crystals are conveniently classified as *segregated-stack* CT crystals, when each stack is made up by the same molecule (...DDDD... or ...AAAA...) and *mixed-stack* CT crystals, in which D and A units pack in an alternating DADADADA pattern. In the present Thesis, we will focus the attention on mixed stacks systems.

In mixed stack CT salts, intermolecular distances along the stack imply sizeable overlap between frontier orbitals, leading to delocalized electrons along the stack. Large interstack distances exclude electron delocalization in other directions. Electrons are therefore delocalized in 1D and different stacks interact mainly via electrostatic interactions. The charge delocalization and the inequivalence of D and A sites cause a CT between D and A; the resulting stack can be described as $D^{+\rho}A^{-\rho}D^{+\rho}A^{-\rho}$ where ρ is the fractional molecular ionicity. The large majority of mixed stack CT crystals have a largely neutral (N) ground state, with $\rho < 0.1$. The number of largely ionic systems (I, $\rho > 0.9$) is modest and even rarer are systems with intermediate ionicity [80].
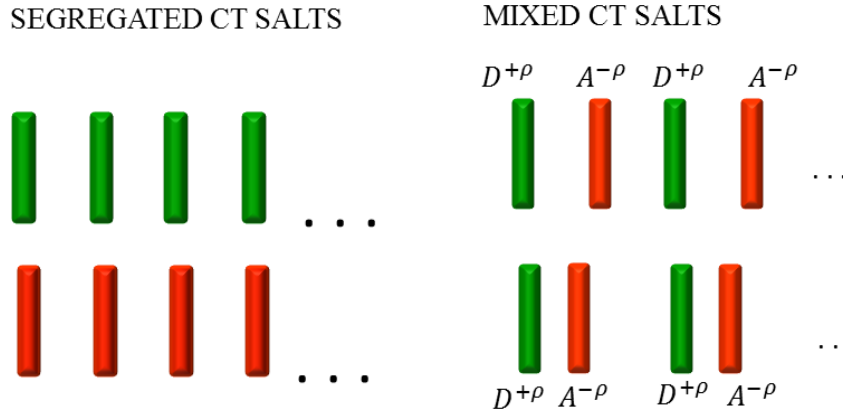
FIGURE 2.1: *A schematic representation of the segregated CT salts (left) and mixed CT salts (right); the latter is represented in the regular N phase (top) and in the dimerized I phase (bottom).*

As originally recognized by McConnell, the N/I nature of the ground state depends on the balance between the electrostatic potential energy (Madelung energy, M) and the energy cost for the charge transfer (ionization energy of a DA pair, $I_D - E_A$, where I_D is the ionization energy for D and E_A is the electronic affinity for A) [81]. Specifically, a N crystal is expected for $I_D - E_A > M$, while I salts are expected for $I_D - E_A < M$. More interesting are systems where $I_D - E_A \approx M$, for which, by varying external conditions (decreasing temperature, increasing pressure), the N-I boundary can be crossed yielding the neutral-ionic phase transition (NIT). In these systems, the lattice contraction due to increased pressure or reduced temperature lead to an increase of the Madelung energy driving the system from the N to the I phase [82, 83].

The first observations of pressure and temperature induced NITs were reported for tetrathiafulvalene-chloranil (TTF-CA) by Torrance *et al.* in 1981 [84, 85]. From the frequency of the infrared active vibrations, the average ionicity ρ was estimated: ~ 0.3 at room temperature that becomes ~ 0.6 below 81 K [84]. This discovery triggered intense experimental and theoretical investigations, and several systems with either continuous and discontinuous NIT have been reported in literature [80].

Irrespective of its nature, the phase transition is always accompanied by stack dimerization [83, 86]. Indeed in the I phase mixed stack CT crystals are unstable towards dimerization. The dimerization is related to a generalized Peierls instability, due to the coupling of the lattice to both charge (electronic Peierls instability of 1D metals) and spin (spin Peierls instability of S=1/2 Heisenberg chains) degrees of freedom. The reduced symmetry of the dimerized stack may lead to a ferroelectric phase, at least if the dimerized polar chains properly order in 3D. The I phase in TTF-CA is ferroelectric [87, 88], but the I phase of DMTTF-CA shows an antiferroelectric packing [89].

Mixed stack CT crystals are among the most promising materials for organic ferro-electrics [22] and possibly multiferroics [21, 23]. Renewed interest on NIT has recently been prompted by the discovery of photoinduced NIT, shifting both experimentalists [19, 90] and theoreticians [91] focus on the dynamic aspect of the transition.

2.2 The phenomenology of NIT

In this Section we shortly summarize some of the most interesting experimental findings for mixed-stack CT salts. Specifically we discuss some of the anomalous features observed in vibrational spectra and in diffuse X-ray scattering, focusing on TTF-CA [85, 92, 93] and DMTTF-CA [94] (Figure 2.2), two examples of MS-CT crystal, showing a discontinuous and a continuous NIT, respectively.
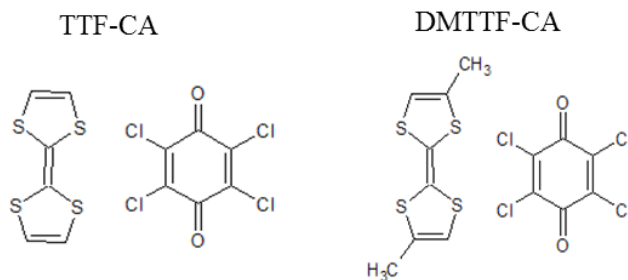
FIGURE 2.2: *Molecular structure of TTF-CA and DMTTF-CA.*

Vibrational spectra of MS-CT crystals are extremely informative and have been extensively investigated [95]. Specifically, the frequency of non-totally symmetric modes linearly scales with the charge residing on the molecular site and for most D and A molecules a few charge-sensitive modes have been recognized that can be safely used to evaluate the molecular ionicity, via a linear interpolation between the known frequencies of the neutral and fully ionic molecule [96].

Totally symmetric molecular vibrations of the D and A molecules show a more interesting behavior due to the coupling with delocalized electrons. Totally symmetric molecular modes in fact modulate orbital energies, i.e. modulate the on-site energy of the Hubbard model (Holstein coupling [95]). This leads to important spectroscopic consequencies. In particular the frequencies of totally symmetric modes are softened as a result of the coupling with delocalized electrons, an effect that becomes more important for systems of intermediate ionicities. The effect is clearly seen in Figure 2.3, where the black lines show Raman spectra of DMTTF-CA crystals at different temperatures [94]. When temperature decreases from ambient conditions towards T_c, the ionicity of the crystal increases from 0.18 to 0.43 [94] and the two totally symmetric modes seen in the Raman

spectra (around 950 cm^{-1} and 1400 cm^{-1}) show a well pronounced softening.
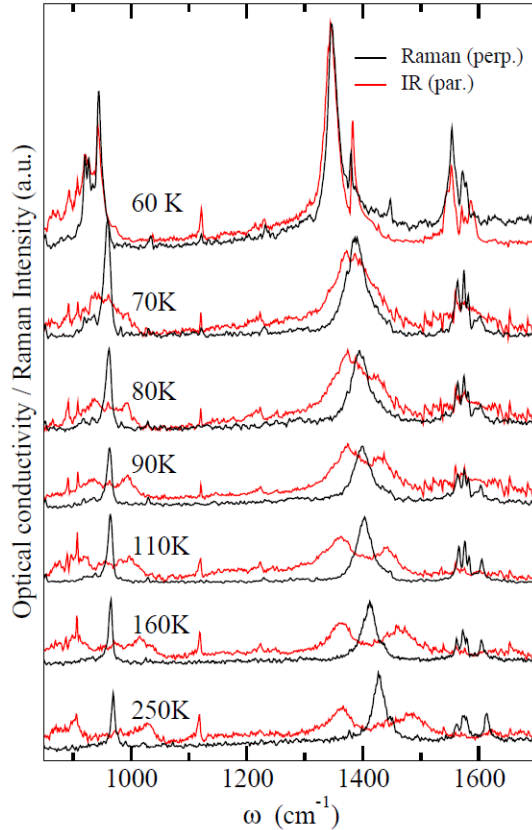
FIGURE 2.3: *Temperature dependence of DMTTF-CA Raman spectra (black lines) and IR conductivity spectra polarized parallel to the stack axis (red lines).*

The totally symmetric modes, IR inactive in the regular stack, acquire a huge intensity in the dimerized phase, due to vibronic coupling [95]. Indeed the appearance of relevant *vibronic bands* in mid-IR spectra is used as an evidence of dimerization [95, 97]. In Figure 2.3 vibronic bands are clearly seen in the low-T phase (T < 70K). However, even at higher temperatures, some strange features are seen in infrared spectra. Specifically, pairs of broad IR bands are observed close to the Raman bands and more precisely one peak is seen to the red of the Raman bands and another to the blue-side. These *side bands* approach each other when temperature is lowered towards T_c and finally coalesce in a single band, superimposed to the Raman band in the I dimerized phase.

The physical origin of these bands was initially ascribed by Tokura group [98] to local defects, called charge transfer exciton strings (LR-CT). Indeed these bands have a much simpler explanation: the *side-bands* can be safely assigned to combination modes of the totalsymmetric Raman band with the lattice-mode that drives the dimerization [92, 94]. The IR-active dimerization mode has the proper symmetry to give IR-active combination band with the Raman mode. Moreover its softening at the NIT explains the fact that

the two *side-bands* approach each other when the system is driven towards NIT. The appearance of intense combination bands demonstrates the large anharmonicity of the system close to NIT, that also shows up with the appearance of an overtone of the dimerization mode in low-frequency Raman spectra [99]. A theoretical approach to vibrational spectra of MS-CT crystals has been recently proposed, that fully accounts for the observed features [99].

Direct experimental identification and characterization of the Peierls mode and of its role in the NIT proved difficult. Analysis of the far-infrared reflectivity measurements on TTF-CA (reported in Figure 2.4) performed by Girlando and coworkers suggests that the Peierls mode is a superposition of several phonons, all coupled to the CT electrons [93]. This effective mode softens upon approaching NIT in quantitative agreement with the mid-IR spectra.
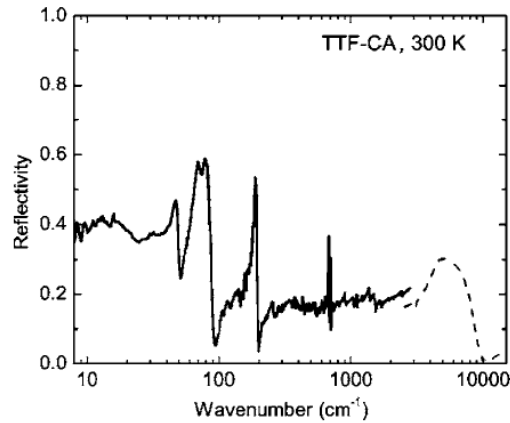
FIGURE 2.4: *Experimental reflectivity of TTF-CA at T=300 K with the polarization parallel to the a direction with logarithmic scale for the frequencies; the spectral region above 3000 cm^{-1} is taken from Ref. [97].*

Buron Le-Cointe, Collet *et al.* [100, 101] investigated TTF-CA and DMTTF-CA through X-ray diffuse scattering at ambient pressure and observed strong peaks in the signal upon approaching NIT. Results for TTF-CA are shown in Figure 2.5, where the spatial dependence of the diffuse intensity in the reciprocal space at 84 K is presented. TTF-CA exhibits an intense X-ray signal in the (b^*, c^*) planes of the reciprocal space around Bragg reflections with integer values of the Miller index h. These anomalies in the diffuse X-ray scattering signal were again ascribed to charge transfer exciton strings (LR-CT) [100, 101]. Indeed, these anomalies are again due to the strong electron-phonon coupling $(e - ph)$ and can be quantitatively explained in terms of the soft behavior of the dimerization mode [102].

Electron-phonon coupling has enormous effects on the physics of MS-CT crystals that
appear not only in their vibrational spectra and diffuse X-ray spectra. The anomalous
large dielectric peak, appearing close to NIT for TTF-CA and related systems, is a man-
ifestation of *e-ph* coupling and is quantitatively reproduced using the Peierls-Hubbard
model and the Berry phase formulation of polarization dielectric [103, 104].
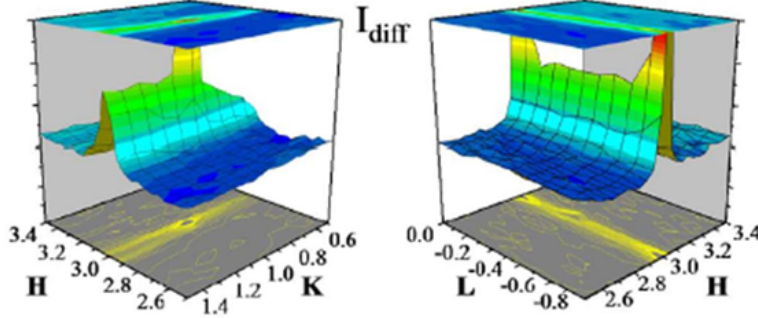
FIGURE 2.5: *Diffuse scattering intensity at 84 K around (3 1 1) in the (a^*, b^*) (left)
and (a^*, c^*) (right) planes in TTF-CA crystal.*

2.3 Models, methods, approximation

2.3.1 Modified Hubbard model (MHM)

The rich and variegated physics of MS-CT salts can be described by a half-filled 1D
Hubbard model accounting for the inequivalence of lattice sites and for 3D Coulomb
interactions. The *modified* Hubbard Hamiltonian reads:

$$H_{el} = \Delta \sum_{i=1}^{N_s} (-1)^i \hat{n}_i + \frac{U}{2} \sum_{i=1}^{N_s} \hat{n}_i \hat{n}_{i+1} - \sum_{i=1}^{N_s} \sum_{\sigma=\alpha}^{\beta} t_i (\hat{a}_{i,\sigma}^{\dagger} \hat{a}_{i+1,\sigma} + H.c.) + \sum_{i,j}^{3D} V_{ij} \hat{\rho}_i \hat{\rho}_j \quad (2.1)$$

where the simple sums run on the N_s number of sites on the 1D stack, while the last
double sum runs on all sites in the 3D crystal. The operator $\hat{a}_i^{\dagger}(\hat{a}_i)$ creates (annhilates)
an electron with spin σ on site i; $\hat{n}_i = \hat{a}_i^{\dagger} \hat{a}_i$ is the occupation-number operator. The
operators $\hat{\rho}_i = 2 - \hat{n}_i$ and $\hat{\rho}_i = \hat{n}_i$ measure the charge on odd (D) and on even (A) sites,
respectively. Several energies enter the Hamiltonian:

- 2Δ represents the energy difference between the donor's HOMO and the acceptor's
  LUMO;

- U represents the on-site electron-electron repulsion and it is set $U \geq 0$ at each
  doubly-occupied sites;

- t_i is the nearest-neighbor interactions between i and $i{+}1$;

- $V_{i,j}$ measures the electrostatic interactions between fully ionized molecules on i and j sites.

The average charge transferred from D to A is measured by the ionicity operator, defined as:

$$\hat{\rho} = \frac{1}{N_s} \sum_{i=1}^{N_s} \hat{\rho}_i \tag{2.2}$$

If we focus on the two first parameters and we consider an isolated DA pair, there are three different charge distributions, as sketched in the Figure 2.6. The neutral DA configuration has a $U - 2\Delta$ energy; the ionic state, D^+A^-, represents the zero of energy; finally, the doubly ionized state $D^{2+}A^{2-}$ has $U + 2\Delta$ energy. The doubly ionized state
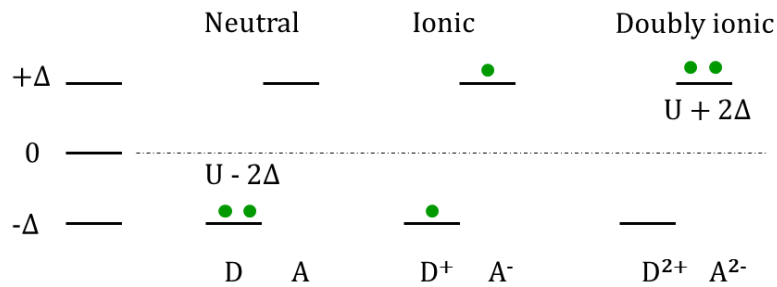
FIGURE 2.6: *Possible electron distributions for an isolated DA pair.*

$D^{+2}A^{-2}$ is very high in energy and since we are interested in the low-energy physics of the system, it can be safely disregarded. This is easily enforced by setting Δ, $U \to \infty$ while maintening their difference, Γ finite; specifically, $2\Gamma = 2\Delta - U = I_D - E_A$.

2.3.2 Electrostatic interactions: the mean-field approximation

Accounting for electrostatic interactions is difficult mainly because of their 3D nature. Exact diagonalization of the Hubbard Hamiltonian on 3D lattices is not possible, so we adopt a *mean-field approximation (mf)* for interstack interactions [82, 83]. Indeed the problem can be recast into an Hamiltonian that treats electrostatic interactions exactly within a stack, then, accounting for interstack interactions within mean field. Most often, all electrostatic interactions are treated in mf. Specifically, one consider the crystal as a collection of DA pairs and explicitly accounts for electrostatic interactions within each DA pair. As a result, $2\Gamma = 2\Delta - U = I_D - E_A$, measuring the energy required for the ionization of a single pair, is renormalized to $2\Gamma = 2\Delta - U - V = I_D - E_A - V$,

where V is the absolute value of the electrostatic interaction between D^+ and A^- within a pair (for historical reasons, here attractive electrostatic interactions are positive and repulsive negative). All other intermolecular electrostatic interactions are treated in mean field, neglecting in the above Hamiltonian all terms containing squares of the deviation operators $\hat{\rho}_i - \rho$, where ρ is the average value of ρ_i. The *mf* Hamiltonian becomes [82, 104]:

$$H_{el} = (\Gamma - \varepsilon_c \rho) \sum_{i=1}^{N_s} (-1)^i \hat{n}_i - \sum_{i,\sigma} (\hat{a}_{i,\sigma}^\dagger \hat{a}_{i+1,\sigma} + H.c.) + \frac{N_s}{2} \varepsilon_c \rho^2 - N_s \varepsilon_c \rho \qquad (2.3)$$

where $\varepsilon_c = (2M - V)$ measures the strength of electrostatic interactions with

$$M = \frac{1}{N_s} \sum_{i,j}^{N_s} V_{i,j}, \qquad (2.4)$$

measuring the Madelung energy of a lattice composed of fully ionized D^+ and A^- molecules. For a given ρ, the last two terms in eq. 2.3 are constant and, therefore, irrelevant in the solution of the Hamiltonian. Therefore, in the *mf* treatment, the electrostatic interactions enter as a self-consistent renormalization of Γ [82]. The mean field treatment for electrostatic interactions leads reliable results when compared with exact diagonalization of stacks with V_{ij} restricted to 1D [83, 86].

2.3.3 Lattice phonons and molecular vibrations

Only phonons at the center of the Brillouin zone are relevant to spectroscopy, and, for MS-CT salt, the dimerization mode is a $k = 0$ mode. Therefore we limit attention to $k = 0$ lattice mode and molecular vibrations. As for the *lattice phonon*, we only account for the dimerization (*Peierls*) mode, x_P, describing the rigid motion of the D and A sublattices in anti-phase. The coupling to the electronic system derives from the modulation of the hopping integral due to the variation of the intermolecolar distances. In the hypothesis of linear coupling:

$$t_i = t + \gamma(x_i - x_{i+1}) = t(1 + (-1)^i \delta) \qquad (2.5)$$

A harmonic lattice and linear electron-phonon coupling can be used to describe the *Peierls mode*; the former is equal to:

$$V_{vib} = \frac{K}{2} x^2{}_P = \frac{N_s}{2\varepsilon_d} \delta^2 \qquad (2.6)$$

where K is the harmonic force constant of the lattice mode and $\varepsilon_d = \dfrac{K}{4\gamma^2}$ is the lattice relaxation energy.

Regarding the *electron-molecular vibration coupling*, we introduce a generic totally symmetric vibrational mode to describe the variation of the molecular geometry along the symmetric coordinate, occurring upon ionization. In fact, as Rice noticed for segregated stacks, upon ionization, D and A molecules relax along totally symmetric vibrational coordinates [105]. The *Holstein coupling* enters the Hamiltonian with a modulation of Γ and an elastic energy defined in terms of the corresponding relaxation energy, sometimes called the small-polaron binding energy, ε_{sp}. Defining q as the effective dimensionless coordinate the total Hamiltonian in units with $t = 1$ reads [82]:

$$H_{el} = (\Gamma - \varepsilon_c \rho + q) \sum_{i=1}^{N_s} (-1)^i \hat{n}_i - \sum_{i,\sigma} [1 + (-1)^i \delta](\hat{a}_{i,\sigma}^\dagger \hat{a}_{i+1,\sigma} + H.c.)$$
$$+ \frac{N_s}{2} \varepsilon_c \rho^2 - N_s \varepsilon_c \rho + \frac{N_s}{2\varepsilon_{sp}} q^2 + \frac{N_s}{2\varepsilon_d} \delta^2 \tag{2.7}$$

2.3.4 The solution of the electronic problem

The Hamiltonian in eq. 2.7 is a typical adiabatic Hamiltonian. The relevant electronic Hamiltonian can be solved for fixed q and δ. Neglecting constant terms, the electronic Hamiltonian reduces to:

$$H_{el} = \Gamma_{eff} \sum_{i=1}^{N_s} (-1)^i \hat{n}_i - \sum_{i,\sigma} [1 + (-1)^i \delta](\hat{a}_{i,\sigma}^\dagger \hat{a}_{i+1,\sigma} + H.c.) \tag{2.8}$$

and depends on just two terms Γ_{eff} and δ, with

$$\Gamma_{eff} = \Gamma - \varepsilon_c \rho + q \tag{2.9}$$

This Hamiltonian can be diagonalized numerically on cluster of N sites. Specifically, the diagrammatic valence bond (DVB), an implementation of the valence bond method developed by Soos and Ramasesha for quantum-cell models [106] was adopted to calculate the ground state properties of systems with a finite number of sites (up to 16) and periodic boundary conditions. Once the ground state energy and ionicity are calculated as a function of Γ_{eff}, eq. 2.9 is used to calculate the energy as a function of δ and q, fixed all other model parameters [82]. Figure 2.7 shows the resulting adiabatic potential energy surfaces, PES, calculated for the model parameters reported in the caption, and for three different V values [82]. The PES in the top panel describes a stable neutral

state with a single minimum located at $\delta_0 = 0$. The PES in the bottom panel, instead, is representative for an ionic stack, which is unconditionally unstable to dimerization, and therefore, develops two equivalent minima at $\pm\delta$, corresponding to I dimerized phases with opposite polarization. In the central panel, a bistable PES is shown, characterized by three minima; one of them describes a N regular phase (δ=0) coexisting with an ionic dimerized phase, described by the two equivalent minima at $\pm\delta$. The PES in Figure 2.7 clearly describes a discontinuous NIT, where the system goes from a N regular phase to an I dimerized phase with an abrupt jump pointed out by the bistable behavior.
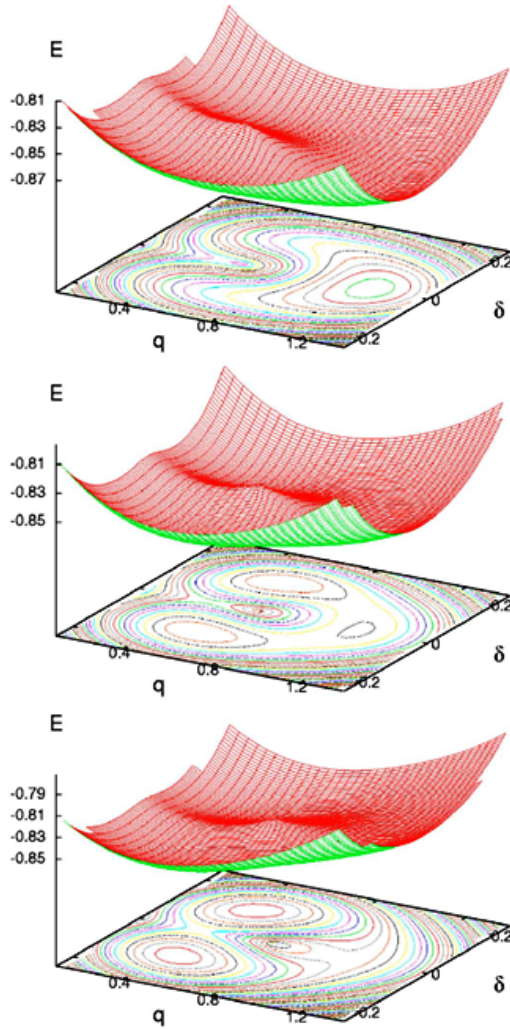
FIGURE 2.7: *The PESs relevant to the system with ε_d=0.28, ε_{sp}=1.8, M=1.4 and Γ=0.5 calculated for V=2.26 (upper panel), V=2.34 (central panel) and V=2.42 (bottom panel)* [82].

The nature of the phase transition can be easily modified by changing the parameters of the electronic Hamiltonian. Figure 2.8 shows the relevant PESs for the same parameters of Figure 2.7 but with a smaller Madelung energy ($M = 1.1$, see the caption). In this

case the transition is *continuous* and the dimerization starts on the N side at $\rho \sim 0.4$.
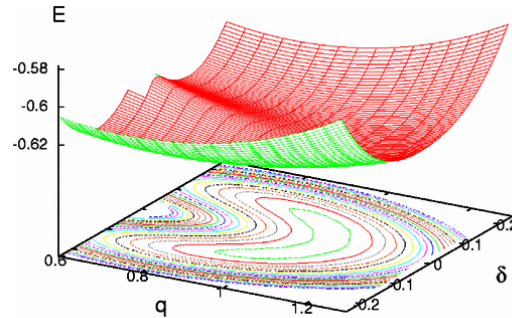
FIGURE 2.8: *The PES relevant to the system in Figure 2.7 but with M=1.1 calculated for V=2.94 [82].*

Figures 2.7 and 2.8 allow us to remark some important concepts. First, in mixed CT crystals, coupling to both *lattice phonons* and *molecular vibrations* is amplified near the phase transition, as confirmed by the largely anharmonic PES in Figure 2.7. Both Peierls and Holstein vibrations enter the Hamiltonian as purely harmonic (see eq. 2.7), and therefore the anharmonicity is totally due to the coupling to the electronic system. Second, the nature of the transition is governed by the competition between a *discontinuous* crossover, coupled to on-site vibrations, and a *continuous dimerization* transition, driven by Peierls phonon. When moving from the N to the I phase, the coupling to delocalized electrons causes a decrease of the curvature of the PES along the δ direction so that a softening of the Peierls mode develops in any case. But, in a system with large enough M and ε_{sp}, a *discontinuous* NIT occurs *before* the complete softening of the Peierls mode. This is the case of Figure 2.7, where a discontinuous NIT takes place, accompanied by lattice dimerization. On the opposite, when ε_{sp} and M are small, a complete lattice softening of the Peierls mode drives the lattice dimerization. The minima of the PES in Figures 2.7 and 2.8 define the equilibrium positions for q and δ.

Much information about NIT can be gained working on regular stacks. For these systems, the purely electronic Hamiltonian is defined in terms of a single dimensionless parameter Γ_{eff}. The universal curve relating ρ to Γ_{eff} for a regular chain is known since 1986 [86] and is reported in Figure 2.9. The $\rho(\Gamma_{eff})$ curve is characterized by a sigmoid shape pointing to a continuous evolution of ρ: NIT is located in correspondence of the maximum slope at $\Gamma(\rho_c = 0.63)$.

Eq. 2.9 allows us to extract information about the role of Coulomb interactions and molecular vibrations on ground state properties of mixed stack CT crystals. In particular, the *Hellmann-Feynman* theorem allows us to relate the equilibrium value of the
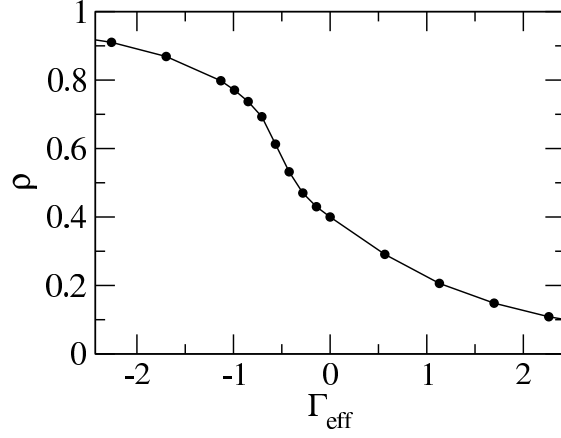
FIGURE 2.9: *The black line shows the $\rho(\Gamma_{eff})$ curve calculated for an infinite chain. All energies are shown in units with $t = 1$.*
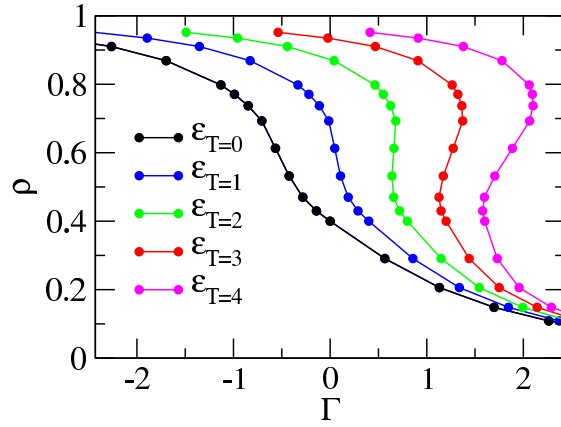
FIGURE 2.10: *$\rho(\Gamma)$ curves obtained from the $\rho(\Gamma_{eff})$ curve (see eq. 2.12) in the mean field approximation for the different ε_T values shown in the legend and $\varepsilon_{sp} = 0$. All energies are shown in units with $t = 1$.*

vibrational coordinate, q_{eq}, to the ground state charge distribution ρ by:

$$\left(\frac{\partial E}{\partial q}\right)_{eq} = \sum_{even,i}^{N_s} (-1)^i \langle \rho \rangle + \sum_{odd,i}^{N_s} (-1)^i (2 - \langle \rho \rangle) + \frac{N_s q_{eq}}{\varepsilon_{sp}} = (\langle \rho \rangle - 1) + \frac{q_{eq}}{\varepsilon_{sp}} = 0 \quad (2.10)$$

so that

$$q_{eq} = \varepsilon_{sp}(1 - \langle \rho \rangle) = \varepsilon_{sp}(1 - \rho) \qquad (2.11)$$

For fixed ε_c and ε_{sp} we can therefore calculate, from each point in the $\rho(\Gamma_{eff})$ curve the corresponding $\rho(\Gamma)$ point, simply using the expression

$$\Gamma = \Gamma_{eff} - \varepsilon_{sp} + \rho(\varepsilon_{sp} + \varepsilon_c) = \Gamma_{eff} - \varepsilon_{sp} + \rho\varepsilon_T \qquad (2.12)$$

and

$$\varepsilon_T = \varepsilon_c + \varepsilon_{sp} \tag{2.13}$$

The coloured lines in Figure 2.10 show the $\rho(\Gamma)$ curves calculated for different ε_T values. The slope of the curves increases fast with ε_T and, for $\varepsilon_T > 3t$, the curves acquire the typical S-shape behavior that signals the occurrence of a discontinuous phase transition and the $\rho(\Gamma)$ function is no longer single valued. The portion of the curve with a positive slope in fact corresponds to unstable states [86].

2.4 State of art of TTF-CA, TTF-2,5Cl$_2$BQ and perylene-TCNQ

In this Section, we illustrate how microscopic parameters of the MHM can be extracted from experimental data. Specifically, the hopping integral (t), the degree of ionicity (ρ) and the small polaron binding (ε_{sp}) can be estimated, following the method proposed by A. Girlando and A. Painelli [107]. As discussed above, ρ, the degree of ionicity, can be extracted from vibrational spectra assuming a linear dependence of the vibrational frequency of non coupled molecular vibrations (i.e. of non-totally symmetric molecular modes) on the molecular charge. Electronic spectra offer the opportunity to estimate both ρ and t, since the frequency (ω_{CT}) and the oscillator strength (f_{CT}) of the CT transition essentially depend on these two parameters [108]. The small polaron binding energy is a molecular parameter that can be extracted from the analysis of spectroscopic properties of segregated stack systems based on relevant molecules [95]. Based on these values, the softening of totally symmetric modes leads to an estimation of the electronic response to the vibrational perturbation allowing for an indirect estimation of ε_{sp}.
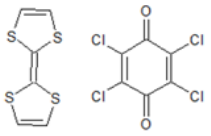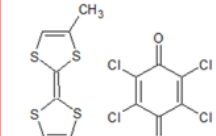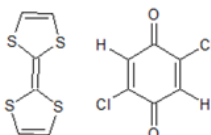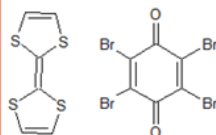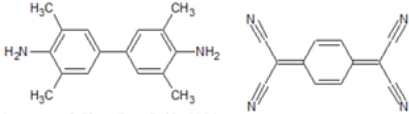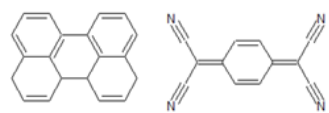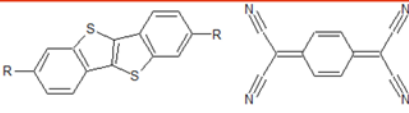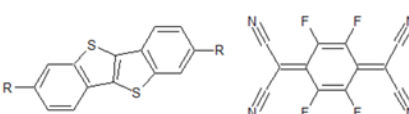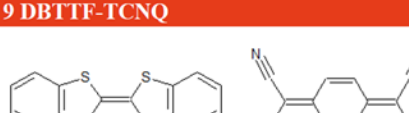
In Table 2.1, microscopic parameters for TTF-CA, TTF-2,5Cl$_2$BQ and perylene-TCNQ are summarized. TTF-CA and TTF-2,5Cl$_2$BQ parameters were extracted by A. Girlando and A. Painelli, adopting the methods proposed above. Instead, perylene-TCNQ parameters are estimated by Ida *et al.* from reflectance data [109] based on the numerical results of A. Painelli and A. Girlando [108]. The Madelung energy has been estimated in the hypothesis of a fully ionic system using the atomic charge distribution computed at CNDO/2 and MNDO level for D and A [107, 109].

TABLE 2.1: *Microscopic parameters of TTF-CA, TTF-2,5Cl$_2$BQ and perylene-TCNQ at ambient conditions; parameters for the two first salts are taken from reference [107] and for perylene-TCNQ from [109]; in the second row the difference between the ionization energy of D and the electron affinity of A is reported; all energies are reported in eV;*

System	$I_D - E_A$	ρ	t	ε_{sp}	V	M
1 TTF-CA	4.08	0.21	0.21	0.37	2.77	3.87
3 TTF-2,5ClBQ	4.28	0.18	0.22	0.31	2.90	3.96
6 perylene-TCNQ	4.2	0.10-0.11	0.25	-	2.46	3.01

2.5   Microscopic model parameters from DFT calculations

Extracting model parameters from experimental data requires a large amount of data that are often not readily available. Therefore it is important to define reliable first-principle approaches to parametrize the model Hamiltonian. We follow a method recently proposed by G. D'Avino *et al.* and apply it to the large set of MS-CT crystals, listed in Figure 2.11, selected based on the availability of crystallographic data and to cover the whole spectrum of ionicities and behavior.

1 TTF-CA

a =7.411Å
b=7.621 Å
c=14.571 Å
α=90°
β=99.20°
γ=90°
V=812.37 Å³
P21/n

Mayerle et al. Act. Crys. B, 35, 1979;

2 DMTTF-CA

a =7.678 Å
b=8.521 Å
c=7.285 Å
α=103.99°
β=91.91°
γ=95.9°
V=459.397 Å³
P1

Horiuchi et al. Science 299, 2003;

3 TTF-2,5Cl2BQ

a =7.935 Å
b=7.216 Å
c=6.844 Å
α=106.94°
β=97.58°
γ=93.66°
V=369.43 Å³
P1

Girlando et al. J. Chem. Phys. 98, 1993;

4 TTF-BA

a =8.390 Å
b=8.699 Å
c=11.630 Å
α=93.6°
β=97.17°
γ=91.92°
V=839.88 Å³
P1

Garcia et al. Phys. Rev. B. 72, 2005;

5 TMB-TCNQ

a = 6.748 Å   α= 90°
b= 21.891 Å   β= 100.23°
c= 8.1279 Å   γ=90°
V=1181.59 Å³ P21/n

Iwasa et al. Phys. Rev. B 42, 1990;

6 perylene-TCNQ

a = 7.201 Å   α=90°
b= 10.839 Å   β= 90.32°
c= 14.475 Å   γ=90°
V=1129.8 Å³   P21/c

Ida et al. J. Chem. Phys. 91, 1989;

7 BT-TCNQ

a = 7.1901 Å   α= 96.27°
b= 7.7142 Å   β= 93.17°
c= 19.851 Å   γ=106.51°
V=1045.03 Å³ P1

Méndez et al. Ang. Chem. Int. 52, 2013;   R=C₁₀H₂₁

8 BT-F4TCNQ

a = 7.0715 Å   α= 97.72°
b= 8.0773 Å   β= 94.05°
c= 19.8477 Å   γ=107.85°
V=1061.78 Å³ P1

Méndez et al. Ang. Chem. Int. 52, 2013;   R=C₁₀H₂₁

9 DBTTF-TCNQ

a = 9.215 Å   α= 113.32°
b= 10.644 Å   β= 122.28°
c= 7.734 Å   γ=67.66°
V=574.882 Å³ P1

Emge et al. Mol. Cryst. Liq. Cryst. 87, 1982;

10 TMPD-TCNQ

a = 9.880 Å   α= 90°
b= 12.710 Å   β= 97.33°
c= 7.720 Å   γ=90°
V=961.515 Å³ C2/m

Girlando et al. Mol. Cryst. Liq. Cryst. 112, 1984;

FIGURE 2.11: *Chemical structure of the family of MS-CT salts theoretically investigated; for each compound cell parameters and reference paper are reported.*

2.5.1 Calculations on a DA pair: towards the first-principle estimate of Γ and t

The Hubbard Hamiltonian for a DA pair is described on the basis of four basis states, each of them accounting for a different electronic configuration:

$$\Phi_0 = [\psi_d(1)\psi_d(2)][\alpha(1)\beta(2) - \alpha(2)\beta(1)]$$

$$\Phi_1 = [\psi_d(1)\psi_a(2) + \psi_d(2)\psi_a(1)][\alpha(1)\beta(2) - \alpha(2)\beta(1)]$$

$$\Phi_2 = [\psi_d(1)\psi_a(2) - \psi_d(2)\psi_a(1)][\alpha(1)\beta(2) + \alpha(2)\beta(1)]$$

$$\Phi_3 = [\psi_d(1)\psi_a(2)][\alpha(1)\alpha(2)]$$

$$\Phi_4 = [\psi_d(1)\psi_a(2)][\beta(1)\beta(2)]$$

where Φ_0 is the singlet neutral basis state, while the others represent the ionic basis states; among them, Φ_2, Φ_3, Φ_4 are the components of the triplet function and Φ_1 is the singlet ionic function. Triplet states stay unmixed and the Hamiltonian for the singlet subspace reads:

$$H = \begin{pmatrix} z_1 & -\sqrt{2}t \\ -\sqrt{2}t & z_2 \end{pmatrix} \tag{2.14}$$

or

$$H = \begin{pmatrix} 0 & -\sqrt{2}t \\ -\sqrt{2}t & 2\Gamma \end{pmatrix} \tag{2.15}$$

where $2\Gamma = z_2 - z_1$; the two singlet basis functions factorize into the two electronic states Ψ_g and Ψ_e, defined in 2.16 and 2.17, respectively:

$$\Psi_g = \sqrt{1 - \rho_S}|\Phi_0\rangle + \sqrt{\rho_S}|\Phi_1\rangle \tag{2.16}$$

$$\Psi_e = \sqrt{\rho_S}|\Phi_0\rangle - \sqrt{1 - \rho_S}|\Phi_1\rangle \tag{2.17}$$

where ρ_S, the degree of ionicity in singlet dimeric system, is expressed as:

$$\rho_S = \frac{1}{2}\left(1 - \frac{\Gamma}{\sqrt{\Gamma^2 + 2t^2}}\right) \tag{2.18}$$

The components of the triplet function correspond to fully ionic states.

The ground state energy is:

$$E_S = z_1 + \Gamma - \sqrt{\Gamma^2 + 2t^2} \tag{2.19}$$

and the singlet-triplet gap reads:

$$\Delta_{ST} = \Gamma + \sqrt{\Gamma^2 + 2t^2} \tag{2.20}$$

A scheme of the energies of the basis states and of the eigenstates of the dimer Hamiltonian is reported in Figure 2.12
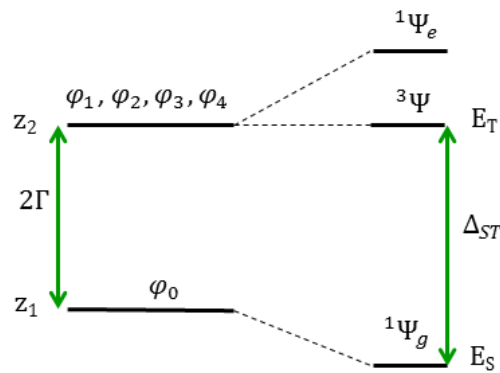
FIGURE 2.12: *Schematic representation of the two states model.*

Quantum chemical calculations on an isolated DA pair in the crystallographic geometry give access to E_S and E_T, the energies of the lowest eigenstates for the DA pair with singlet and triplet multiplicity, and hence to Δ_{ST}. Another quantity is needed however

to extract model parameters. In **Method A** we access z_1 by summing up the ground state energies of isolated (neutral) D and A molecules. Equations 2.19 and 2.20 can then be used to estimate Γ and t. This method, that has the advantage of only relying on energies and not on wavefunctions, is however affected by large errors due to the neglect of dispersion forces in the estimatation of z_1.

An alternative approach **Method B** relies, instead, on the calculation of the degree of CT, ρ_S, from the charge distribution calculated for the singlet ground state of the isolated DA pair. Γ and t are therefore estimated from ρ_S and Δ_{ST} as follows:

$$t = \Delta_{ST}\sqrt{\frac{\rho_S}{2(1-\rho_S)}} \tag{2.21}$$

$$\Gamma = t\frac{1-2\rho_S}{\sqrt{2\rho_S(1-\rho_S)}} \tag{2.22}$$

2.5.2   Calculations on DA pairs

For the selected systems in Figure 2.11, we extract relevant DA pairs, as illustrated in Figure 2.13, and on these structures we perform DFT calculations. The same calculations are also run on isolated D and A molecules and D^+ and A^- ions, maintaining the crystal geometry. For the calculation of vibrational relaxation energies, calculations on isolated species at optimized geometry are performed, as discussed in Section 2.5.3.

1 TTF-CA

Mayerle et al. Act. Crys. B 35, 1979;

2 DMTTF-CA

Horiuchi et al. Science 299, 2003;

3 TTF-2,5Cl2BQ

Girlando et al. J. Chem. Phys. 98, 1993;

4 TTF-BA

4a

4b

Garcia et al. Phys. Rev. B. 72, 2005;

5 TMB-TCNQ

Iwasa et al. Phys. Rev. B 42, 1990;

6 perylene-TCNQ

Ida et al. J. Chem. Phys. 91, 1989;

7 BT-TCNQ

Méndez et al. Ang. Chem. Int. 52, 2013;

8 BT-F4TCNQ
Méndez et al. Ang. Chem. Int. 52, 2013;

9 DBTTF-TCNQ
Emge et al. Mol. Cryst. Liq. Cryst. 87, 1982;

10 TMPD-TCNQ
Girlando et al. Mol. Cryst. Liq. Cryst. 112, 1984;

11 TMB-CA
Castagnetti et al. private communication;

12 N,N,N',N'-TMB-CA
Yakushi et al. Acta Crys. B 29, 1973;

13 ClMePD-DMeDCNQI
13a
13b
Bewick et al. J. Chem. Phys. 122, 2005;

FIGURE 2.13: *Selected dimer(s) along crystallographic axis (a,b,c respectively) for each MS-CT salts theoretically investigated.*

For most salts, the crystal is built based on repetition of a single DA pair. TTF-BA represents a notable exception, being characterized by two mutually orthogonal and non-equivalent stacks [110]. In this case, two different TTF-BA pairs, *4a* and *4b* TTF-BA are selected, as shown in Figure 2.13. In the disordered ClMePD-DMeDCNQI crystal (13) the chlorine atom and the methyl group have 1:1 occupancy at each site [111], originating two inequivalent pairs, called *13a* and *13b*. In either case the typical C-Cl distance (1.71 Å) is used. When the position of H atoms is not explicitly given in the crystallographic structure, they are added manually and their position is optimized at PM7 level (MOPAC package [112] [113]).

All calculations are performed at DFT level (Gaussian 09 package [114]), using the UωB97XD hybrid functional. This functional, in virtue of the range-separated treatment of the Coulomb operator and of the inclusion of dispersion correction, is one of the most reliable for the study of the intermolecular CT phenomena [115]. The basis set 6-31+G* has been chosen to include both anisotropic distribution and electron distribution far away from the nuclei (important for lone pairs systems and anions).

Table 2.2 collects the energies calculated for the lowest singlet and triplet eigenstates for the DA pairs, E_S and E_T, respectively, as well as z_1 estimated as the sum of the ground state energies of the isolated (neutral) D and A molecules.

TABLE 2.2: *Singlet and triplet energies for the selected dimers and z_1 calculated as the sum of the ground state energies of not interacting D and A; all energies are measured in eV;*

System	E_S	E_T	z_1
1 TTF-CA	-110'008.190	-110'007.202	-110'007.624
2 DMTTF-CA	-112'158.706	-112'157.819	-112'158.191
3 TTF-2,5,Cl$_2$BQ	-85'007.553	-85'006.348	-85'007.037
4a TTF-BA	-339'848.881	-339'848.608	-339'847.999
4b TTF-CA	-339'849.040	-339'848.621	-339'848.119
5 TMB-TCNQ	-38'344.988	-38'344.289	-38'343.676
6 perylene-TCNQ	-39'381.349	-39'380.178	-39'380.327
7 BT-TCNQ	-76'139.606	-76'138.011	-76'138.513
8 BT-F4TCNQ	-86'938.307	-86'937.089	-86'937.035
9 DBTTF-TCNQ	-76'431.683	-76'430.944	-76'430.864
10 TMPDTCNQ	-32'064.535	-32'064.885	-32'063.813
11 TMB-CA	-80'280.816	-80'279.652	-80'279.846
12 N,N,N"-TMB-CA	-80'289.735	-80'287.852	-80'288.951
13a ClMePD-DMeDCNQI	-39'352.860	-39'351.975	-39'352.024
13b ClMePD-DMeDCNQI	-39'352.835	-39'351.933	-39'352.006

We notice that for 5 and 9 we obtain $E_T < z_1$, making it impossible to estimate model parameters according to **Method A**. This discrepancy is ascribed to the neglect of

dispersion energies in the z_1 estimation. The results in Table 2.2 allow to estimate model parameters (Γ and t) based on **Method A**. Results are collected in Table 2.3. The estimated t are fairly large. Indeed we believe that **Method A**, only relying on energies, is not very accurate due to the neglect of dispersion forces in the calculation of z_1. Moreover in TMPD-TCNQ (system number 10) $E_T < E_S$, a result that cannot be reconciled with the proposed model. Accordingly we cannot estimate model parameters for TMPD-TCNQ following either Method A or B.

TABLE 2.3: ***Method A*** *results:* Γ *and* t, *both reported in eV;*

Method A		
System	Γ	t
1 TTF-CA	0.211	0.529
2 DMTTF-CA	0.186	0.478
3 TTF-2,5,Cl$_2$BQ	0.345	0.558
4a TTF-BA	-0.304	0.347
4b TTF-BA	-0.251	0.439
5 TMB-TCNQ	—	—
6 perylene-TCNQ	0.075	0.774
7 BT-TCNQ	0.251	0.934
8 BT-F4TCNQ	-0.027	0.880
9 DBTTF-TCNQ	—	—
10 TMPDTCNQ	—	—
11 TMB-CA	0.097	0.751
12 N,N,N',N'-TMB-CA	0.550	0.860
13a ClMePD-DMeDCNQI	0.024	0.608
13b ClMePD-DMeDCNQI	0.036	0.612

To address **Method B** we do not rely on z_1, but we need estimation of the ground state ionicity in the dimer. Table 2.4 reports the results obtained for the different DA pairs. Specifically, ρ is calculated summing up the atomic charges in the D molecule (those on A are equal and opposite). Two different choices have been made for the calculation of atomic charges. The Hirshfeld (HIRS) charges should be the most appropriate way to address charge distribution [116]. For the sake of comparison, we also list results obtained from electrostatic potential charges (ESP) [117]. In the same Table we also show the ionicity of the triplet state, ρ_T estimated from the charge distribution in the lowest triplet state of the isolated DA pair. This quantity does not enter the expressions for the estimation of microscopic model parameters, but is an important parameter to verify the quality of the proposed approach. In fact, if the dimer model holds true, we expect $\rho_T = 1$: large deviation from this limiting value suggests a poor reliability of the approach.

TABLE 2.4: *Distribution of charge in singlet (ρ_S) and triplet (ρ_T) state calculated for all dimers investigated using two different charges schemes: Hirshfeld charges (HIRS) and electrostatic ones (ESP);*

System	$\rho_{S,HIRS}$	$\rho_{S,ESP}$	$\rho_{T,HIRS}$	$\rho_{T,ESP}$
1 TTF-CA	0.091	0.095	0.867	0.787
2 DMTTF-CA	0.097	0.120	0.864	0.801
3 TTF-2,5,Cl$_2$BQ	0.097	0.081	0.887	0.792
4a TTF-BA	0.121	0.089	0.946	0.813
4b TTF-CA	0.128	0.079	0.947	0.810
5 TMB-TCNQ	0.169	0.267	0.820	0.854
6 perylene-TCNQ	0.109	0.155	0.867	0.823
7 BT-TCNQ	0.046	0.127	0.736	0.710
8 BT-F4TCNQ	0.064	0.121	0.880	0.809
9 DBTTF-TCNQ	0.155	0.157	0.860	0.780
10 TMPDTCNQ	0.244	0.309	0.813	0.862
11 TMB-CA	0.087	0.219	0.81	0.850
12 N,N,N',N'-TMB-CA	0.070	0.131	0.841	0.861
13a ClMePD-DMeDCNQI	0.219	0.212	0.868	0.810
13b ClMePD-DMeDCNQI	0.219	0.200	0.878	0.817

According to Table 2.4, the ionicities calculated in either scheme are very similar for TTF-CA, TTF-2,5Cl$_2$BQ, DBTTF-TCNQ and ClMePD-DMeDCNQI, while more generally ESP overestimates the singlet ρ with respect to HIRS. In all systems we obtain $\rho_T \sim 1$ supporting the dimer model.

Data in Tables 2.2 and 2.4 can be used to extract model parameters according to **Method B**. Results are reported in Table 2.5 that compares Γ and t estimates obtained using both Hirshfeld and electrostatic charges. The estimated t in Table 2.5 obtained used either HIRS or ESP charges are in reasonable agreement with available estimates of charge transfer integral in mixed-stack CT crystals [97, 109]. For both set of charges, TTF-BA has by far the smallest hopping integral: the low electron kinetic energy favors electron localization so that TTF-BA is expected either largely neutral or largely ionic. Indeed TTF-BA is a largely ionic system with $\rho \sim 0.95$ [110]. The largest hopping integral is found for N,N,N',N'-TMB-CA. For most systems the hopping integrals evaluated based on HIRS or ESP charges are similar, except for BT-TCNQ, BT-F$_4$TCNQ, TMB-CA and N,N,N',N'-TMB-CA. Apparently the estimate obtained based on ESP charges for BT-TCNQ and BT-F$_4$TCNQ aggree well with previous estimates, $t \sim 0.4$-0.6 obtained by Méndez *et al.* [118]. The hopping integral estimated for TTF-CA agrees quantitatively with current estimates ($t \sim 0.21$ eV, see Table 2.1) [107].

Regarding TTF-2,5Cl$_2$BQ, a larger hopping integral than for TTF-CA is expected, based on the shorter intermolecular distances [107] (see Table 2.1), in line with our results. The mixing integral predicted by Hirshfeld charges in perylene-TCNQ matches exactly

TABLE 2.5: Γ, t and ΔG parameters derived through **Method B** adopting Hirshfeld charges (first three columns) and ESP charges (last three columns).

	Method B					
	Hirshfeld charges			ESP charges		
System	ρ(HIRS)	Γ	t	ρ(ESP)	Γ	t
1 TTF-CA	0.091	0.445	0.221	0.095	0.442	0.226
2 DMTTF-CA	0.097	0.396	0.206	0.120	0.383	0.232
3 TTF-2,5,Cl$_2$BQ	0.097	0.538	0.279	0.081	0.549	0.253
4a TTF-BA	0.121	0.118	0.072	0.089	0.123	0.060
4b TTF-BA	0.128	0.178	0.113	0.079	0.191	0.087
5 TMB-TCNQ	0.169	0.278	0.223	0.267	0.222	0.298
6 perylene-TCNQ	0.109	0.514	0.290	0.155	0.478	0.355
7 BT-TCNQ	0.046	0.759	0.248	0.127	0.681	0.430
8 BT-F4TCNQ	0.064	0.567	0.225	0.121	0.525	0.319
9 DBTTF-TCNQ	0.155	0.302	0.224	0.157	0.301	0.226
10 TMPDTCNQ	0.243	-	-	0.309	-	-
11 TMB-CA	0.087	0.526	0.254	0.219	0.419	0.436
12 N,N,N',N'-TMB-CA	0.070	0.871	0.365	0.131	0.800	0.517
13a ClMePD-DMeDCNQI	0.219	0.318	0.331	0.212	0.323	0.325
13b ClMePD-DMeDCNQI	0.219	0.325	0.338	0.200	0.338	0.319

with Ida's results, as shown in Table 2.1. In addition, Bewick *et al.* predict a mixing integral equal to 0.25 eV for ClMePD-DMeDCNQI [119]: with both approaches, we get comparable results. By contrast, present estimates of t for DBTTF-TCNQ are somewhat smaller than Zhu's computed value $t \sim 0.70$ eV [120].

2.5.3 Calculation of the small polaron binding energy

The small polaron binding energy, ε_{sp}, measures the sum of the relaxation energies of the two isolated molecules, associated with the geometrical relaxation following the D to D$^+$ and A to A$^-$ processes, as sketched in Figure 2.14. The relaxation energy is then evaluated within the Adiabatic Potential approach (AP) as the reorganization energy in the charged states for the two isolated molecules. Calculations on the neutral and ionic isolated D and A species are executed at UωB97XD/6-31+G* level of theory in gas phase. Results are reported in Table 2.6.

Previous estimates of relaxation energies in Ref. [83] were obtained analyzing spectral properties of CT crystals with a segregated stack motif (indeed vibrational relaxation energies are molecular parameters and hence transferable among different systems composed of the same molecular units). Authors have estimated $0.11 < \varepsilon_{sp} < 0.40$ eV. Actually, DFT calculations in gas phase suggest somewhat larger small-polaron binding, spanning a range of 0.30-0.82 eV. Among the studied systems ClMePDMeDCNQI is
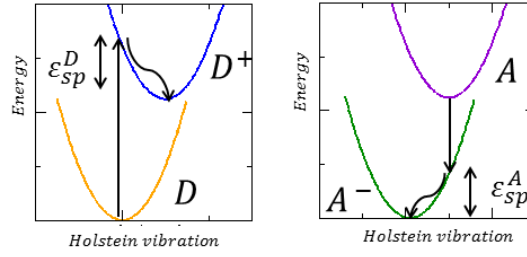
FIGURE 2.14: *Schematic representation of the potential energy of the neutral and charged state of D and A; specifically for D(A) the cation (anion) is considered. The relaxation energy is calculated as the difference between the energy of the charged state at optimized neutral geometry minus the energy of the optimized charged state.*

TABLE 2.6: *Relaxation energies for salts under investigation;*

System	ε_{sp} (eV)
1 TTF-CA	0.47
2 DMTTF-CA	0.49
3 TTF-2,5,Cl$_2$BQ	0.49
4 TTF-BA	0.45
5 TMB-TCNQ	0.60
6 perylene-TCNQ	0.31
7 BT-TCNQ	0.36
8 BT-F4TCNQ	0.36
9 DBTTF-TCNQ	0.36
10 TMPD-TCNQ	0.65
11 TMB-CA	0.70
12 N,N,N',N'-TMB-CA	0.58
13 ClMePD-DMeDCNQI	0.82

the softest crystal, while perylene-TCNQ is the hardest one. The relaxation energy estimated for TTF-2,5Cl$_2$BQ is lower than that in TTF-CA, at variance with the previous parametrization (Table 2.1) [83].

2.5.4   Calculation of electrostatic interactions

As mentioned in Section 2.3.2, in the mf, intersite electrostatic interactions enter the problem in terms of a single parameter $\varepsilon_c = (2M - V)$ where M is the Madelung energy (see eq. 2.4) and V the interaction between D and A species in a single pair [82]. The Madelung energy can be estimated as the difference between the sum of electrostatic interactions in a lattice of fully ionized D$^+$ and A$^-$ sites (M_I) minus the same energy calculated in a lattice of neutral D and A species (M_N), $M = M_I - M_N$ [42]. The two

basic interactions are defined as

$$M_{N/I} = \frac{1}{N_s} \sum_{i,j} V_{i,j}^{N/I} \qquad\qquad (2.23)$$

corresponding to the Madelung energy for a crystal of fully ionic (I) or fully neutral (N) molecules, with the sum running on the 3D lattice, N_s counting the number of sites and $V_{i,j}^{N/I}$ measuring the electrostatic interactions between i and j sites in the 3D cluster. For historical reasons, we use a convention so that a positive (negative) $V_{i,j}$ refers to attractive (repulsive) interactions, so that V is always positive.

The $V_{i,j}^{N/I}$ are calculated as sum of electrostatic interactions among point atomic charges located at the crystallographic positions for the neutral and ionic D and A isolated species [42]. The crystallographic data give information about the atomic positions, whereas atomic charges are calculated at ωB97XD/6-31+G* level of theory in the ESP scheme, as the most appropriate to simulate the electrostatic potential [117].

The sum in eq. 2.23 run on the infinite 3D crystal: we calculate $M_{N/I}$ for spherical clusters of increasing radius constructed out of the crystalline structure (see Figure 2.15 for an example) and we increase the size of the cluster until convergence. The codes to calculate Madelung energies were kindly provided by G. D'Avino. Results are summarized in Table 2.7. For TTF-BA compound and ClMeDMeDCNQI, the Madelung energy is calculated considering just the charge distribution of units a.
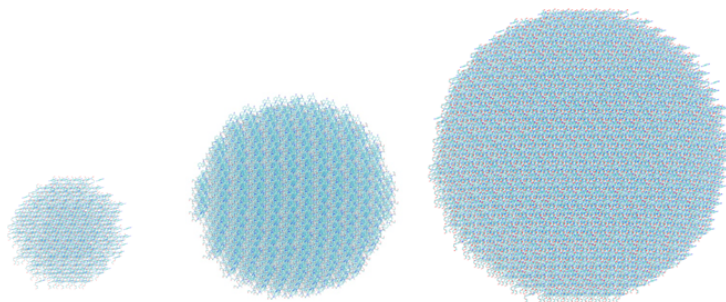
FIGURE 2.15: *Spherical clusters with different radius for TTF-CA crystals; from left: radius values 40, 70, 100 Å.*

The nearest-neighbor interaction V is estimated as the difference between the electrostatic interaction calculated for a $D^+ A^-$ pair (V_I) minus the same interaction calculated for a neutral DA pair (V_N) [121]. Table 2.8 reports relevant results.

The current estimate of $V = 2.53$ eV is in good agreement with the literature data, $V = 2.77$ eV calculated for TTF-CA [107]. The shorter intermolecular distances in

TABLE 2.7: *Madelung energy extrapolated for an infinite crystal;*

System	M (eV)	M_{ionic} (eV)	$M_{neutral}$ (eV)
1 TTF-CA	1.654	1.752	0.140
2 DMTTF-CA	1.197	1.391	0.193
3 TTF-2,5,Cl$_2$BQ	1.314	1.517	0.203
4 TTF-BA	1.456	1.473	0.019
5 TMB-TCNQ	1.325	1.712	0.386
6 perylene-TCNQ	1.035	1.242	0.207
7 BT-TCNQ	1.002	1.220	0.218
8 BT-F4TCNQ	0.952	1.191	0.240
9 DBTTF-TCNQ	1.038	1.320	0.282
10 TMPDTCNQ	1.132	1.248	0.108
11 TMB-CA	1.602	1.843	0.217
12 N,N,N',N'-TMB-CA	1.011	1.113	0.102
13 ClMePD-DMeDCNQI	1.259	1.661	0.403

TABLE 2.8: *Nearest-neighbor electrostatic interactions;*

System	V	V_I	V_N
1 TTF-CA	2.533	2.593	0.059
2 DMTTF-CA	2.414	2.476	0.062
3 TTF-2,5,Cl$_2$BQ	2.578	2.626	0.048
4a TTF-BA	2.355	2.392	0.037
4b TTF-BA	2.624	2.660	0.036
5 TMB-TCNQ	2.029	2.291	0.263
6 perylene-TCNQ	2.055	2.210	0.155
7 BT-TCNQ	2.004	2.161	0.157
8 BT-F4TCNQ	1.887	2.103	0.216
9 DBTTF-TCNQ	2.008	2.103	0.095
10 TMPDTCNQ	2.370	2.387	0.018
11 TMB-CA	2.290	2.416	0.126
12 N,N,N'N'-TMB-CA	2.258	2.281	0.023
13a ClMePD-DMeDCNQI	2.465	2.579	0.114
13b ClMePD-DMeDCNQI	2.435	2.563	0.128

TTF-2,5Cl$_2$BQ with respect to TTF-CA suggest a larger V, as confirmed by our results. Similarly, we can explain the different results observed in the two dimeric units in TTF-BA, in which the second one presents shortest intermolecular distances. Intermolecular distances cannot be invoked to explain the smaller V observed in DMTTF-CA respect to TTF-CA or that in BT-F4TCNQ respect to BT-TCNQ. In the systems with substituents, the charge distribution is delocalized among a larger number of atoms diluting interactions respect to unsubstituted ones.

The large M value in TTF-CA can be ascribed to the presence of attractive electrostatic *intra-* and *inter-* chain interactions, along a axis and c axis, respectively (see

Figure 2.19). Specifically, in the monoclinic TTF-CA, we observe short C-H--→O and S←--Cl distances between D and A molecules of different stacks, that play an important role favoring attractive electrostatic interchain interactions [122]. Both interactions are also observed in DMTTF-CA, while, in TTF-2,5Cl$_2$BQ C-H--→O as well as Cl←--H attractive contacts are presents. On this basis one could expect for these systems a comparable Madelung energy as for TTF-CA. Instead, weaker Madelung energy is predicted for both (respect to TTF-CA). However in TTF-2,5Cl$_2$BQ and in DMTTF-CA, the triclinic structure with only one DA pair per unit cell, induces unfavorable inter-stack D^+D^+ and A^-A^- Coulomb interactions in the bc plane, as shown in Figure 2.16 possibly justifying the obtained results.

TTF-2,5Cl$_2$BQ   DMTTF-CA
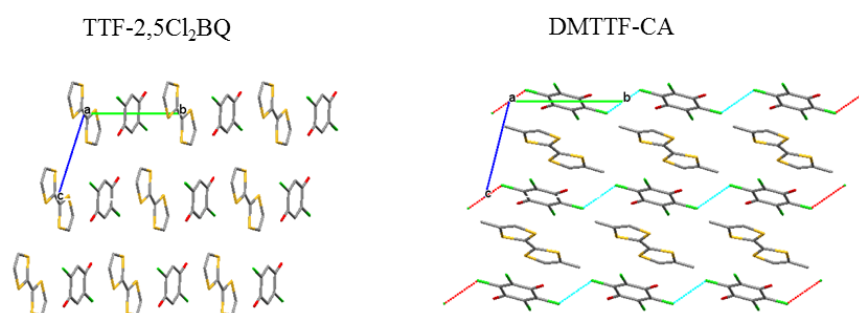
FIGURE 2.16: *TTF-2,5Cl$_2$BQ and DMTTF-CA in the bc plane; hydrogen atoms are omitted for clarity.*

TMB-TCNQ and perylene-TCNQ, report both *inter-* and *intra-* stack N-H closest contacts, as shown in Figure 2.17; in addition, in perylene-TCNQ, the copresence of donor-donor and acceptor-acceptor interactions along b axis (Figure 2.19) contributes to decrease the Madelung energy respect to TMB-TCNQ; a similar rearrangement is observed in DBTTF-TCNQ and in TMPD-TCNQ. Specifically, in the former, both *inter-* N-H and *intra*-stack C-S interactions (see Figure 2.17) are found togheter with the adjacent (and slightly glided) D-D and A-A in the ac plane (Figure 2.19); in addition, since the cell volume in DBTTF-TCNQ is about the half respect the perylene-based salt (Figure 2.11), we hypothesize that the D-D and A-A repulsions contribute much more, suggesting therefore a smaller value of ε_c respect to perylene-TCNQ.

In TMPD-TCNQ, adjacent donor-donor moieites are observed along a and b axis and acceptor-acceptor interaction are found just along the a direction. This packing can be invoked to explain the smaller value of Madelung energy in TMPD-TCNQ respect the TMB counterpart.

As expected, BT-TCNQ and BT-F$_4$TCNQ show the smallest Madelung energies due to the steric hindrance of chains which block attractive intrastack interactions. In addition,
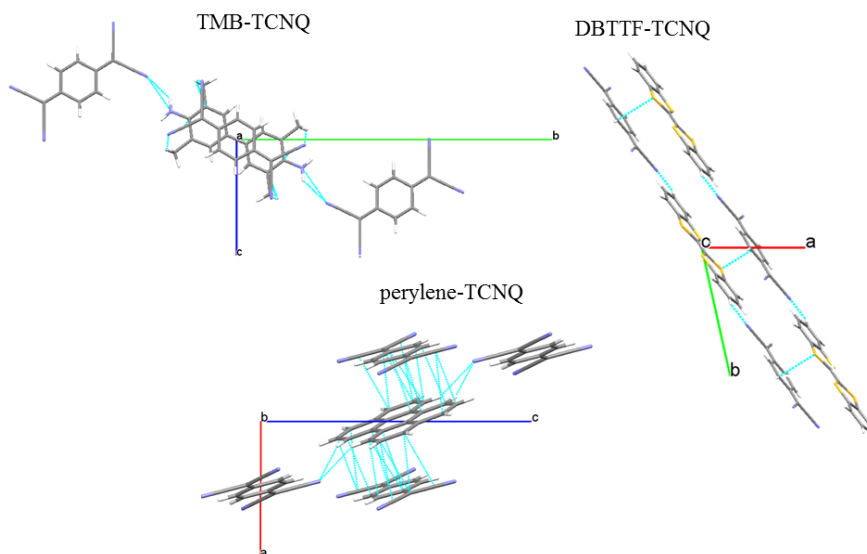
FIGURE 2.17: *TMB-TCNQ, DBTTF-TCNQ and perylene-TCNQ packing in which inter- and intra- stack close contacts are shown (cyan line) along a,c and b axis respectively.*

it is surprisingly that BT-TCNQ is characterized by a zero value of ε_c, indicating a very short range of intermolecular Coulombian interactions.

As reported in Figure 2.18, *inter-* and *intra-* chain interactions are involved in TMB-CA, where each acceptor attractively interacts with two donors, owning to the same stack and with other two donors of different stacks; on the other hand, in N,N,N',N'-TMB-CA, just intrachain interactions are observed: each acceptor is involved in attractive interactions with only two donors and in repulsive Cl-Cl interactions with two other acceptor units. This rearrangement can explain the smaller Madelung energy computed.
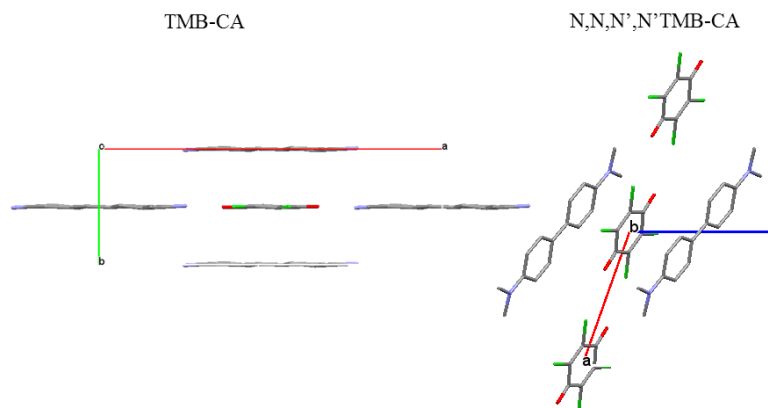
FIGURE 2.18: *TMB-CA and N,N,N',N'-TMB-CA packing in which the close contacts betweeen each acceptor are shown along c and b axis, respectively; hydrogen atoms are omitted for clarity.*

Data in Tables 2.7 and 2.8 allow to estimate the main parameter entering the mf description of electrostatic interactions, $\varepsilon_c = (2M - V)$; then, combining ε_c with ε_{sp} (Table 2.6) we can access to ε_T (see eq. 2.13). Results are listed in Table 2.9.

TABLE 2.9: ε_c (eV), ε_T (eV), ε_c/t and ε_T/t;

System	ε_c	ε_T	$\frac{\varepsilon_c}{t}$	$\frac{\varepsilon_T}{t}$
1 TTF-CA	0.77	1.25	3.50	5.63
2 DMTTF-CA	-0.02	0.47	-0.10	2.29
3 TTF-2,5,Cl$_2$BQ	0.54	0.18	0.49	1.93
4a TTF-BA	0.56	1.01	7.77	14.0
4b TTF-BA	0.29	0.74	2.54	6.51
5 TMB-TCNQ	0.62	1.22	2.79	5.48
6 perylene-TCNQ	0.01	0.33	0.05	1.12
7 BT-TCNQ	0	0.36	0	1.45
8 BT-TCNQF4	0.02	0.38	0.08	1.67
9 DBTTF-TCNQ	0.07	0.43	0.30	1.91
10 TMPDTCNQ	-0.11	0.55	-	-
11 TMB-CA	0.91	1.61	3.60	6.36
12 N,N,N',N'-TMB-CA	-0.24	0.34	-0.65	0.94
13a ClMePD-DMeDCNQI	0.05	0.88	0.16	2.63
13b ClMePD-DMeDCNQI	0.08	0.90	0.25	2.67

A first observation of Table 2.9 concerns the three systems, DMTTF-CA, TMPD-TCNQ and N,N,N',N'-TMB-CA, showing negative (repulsive in our convention) ε_c values. Indeed ε_c is always positive for a single DA chain: negative values imply strong repulsive interchain interactions as to override the positive (attractive) intrachain interactions. BT-TCNQ is characterized by a zero value of ε_c, indicating a very short range of intermolecular Coulombian interactions.

1 TTF-CA

Mayerle et al. Act. Crys. B 35, 1979;

2 DMTTF-CA

Horiuchi et al. Science 299, 2003;

3 TTF-2,5Cl2BQ

Girlando et al. J. Chem. Phys. 98, 1993;

4 TTF-BA

Garcia et al. Phys. Rev. B. 72, 2005;

5 TMB-TCNQ

Iwasa et al. Phys. Rev. B 42, 1990;

6 perylene-TCNQ

Ida et al. J. Chem. Phys. 91, 1989;

7 BT-TCNQ

Méndez et al. Ang. Chem. Int. 52, 2013;

8 BT-F4TCNQ

Méndez et al. Ang. Chem. Int. 52, 2013;

9 DBTTF-TCNQ

Emge et al. Mol. Cryst. Liq. Cryst. 87, 1982;

10 TMPD-TCNQ

Girlando et al. Mol. Cryst. Liq. Cryst. 112, 1984;
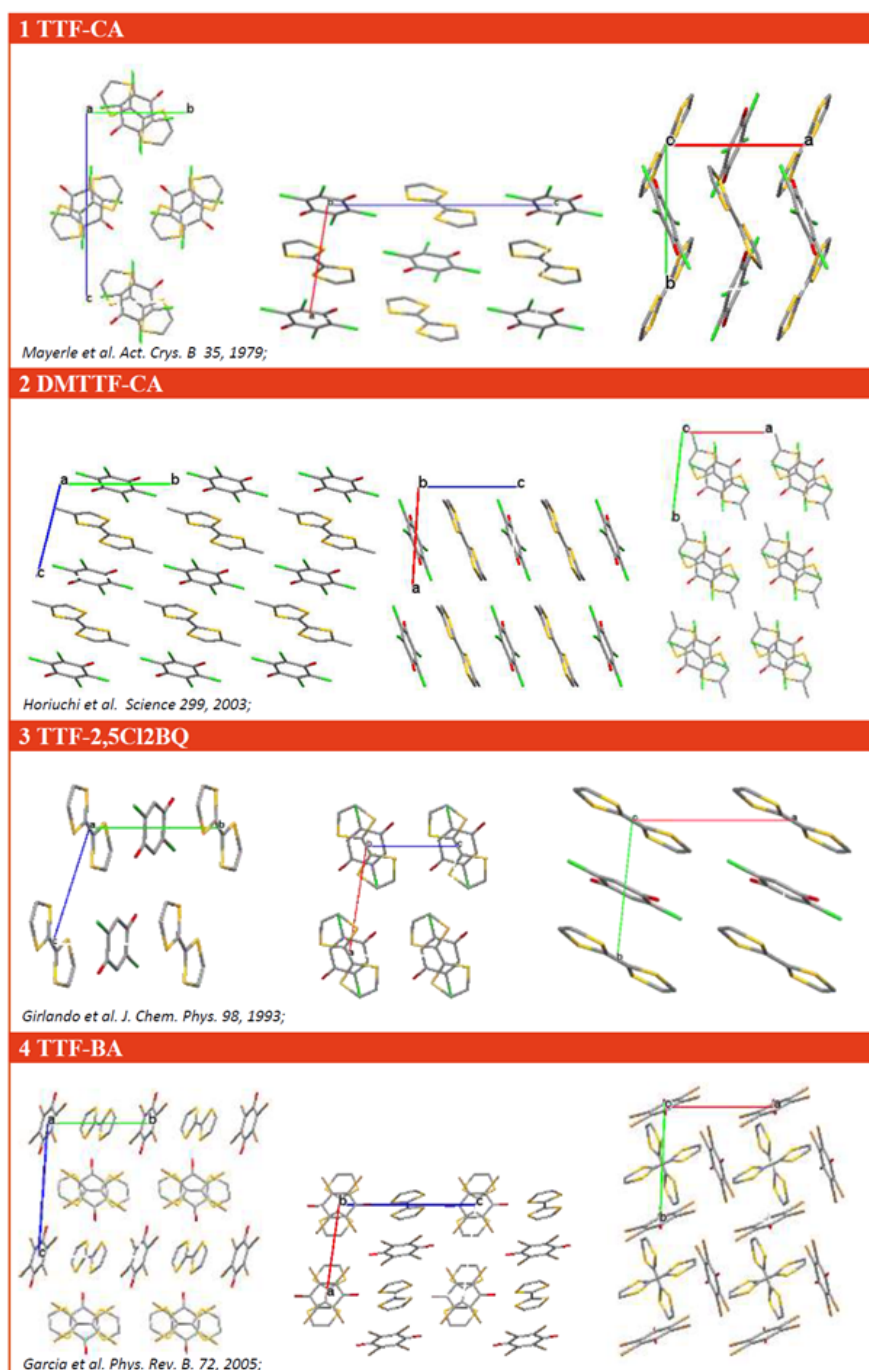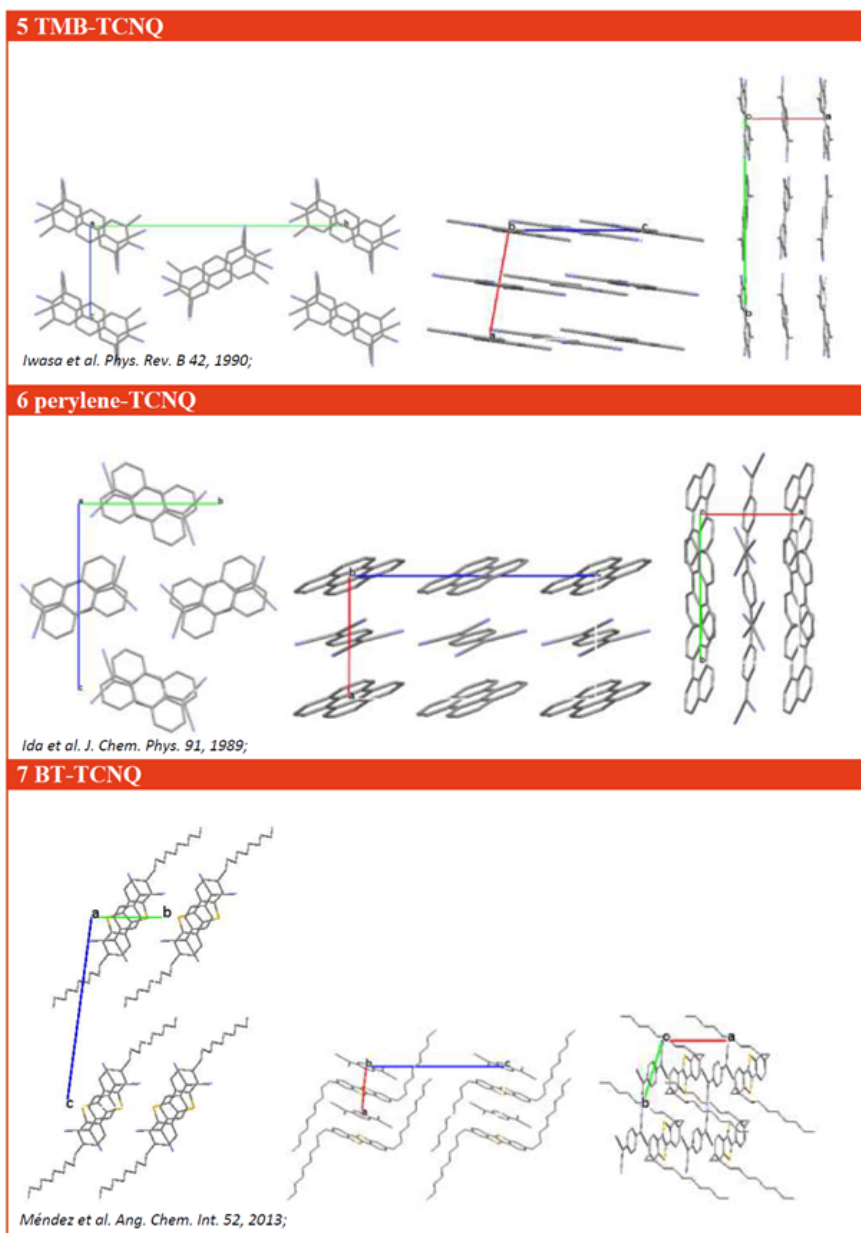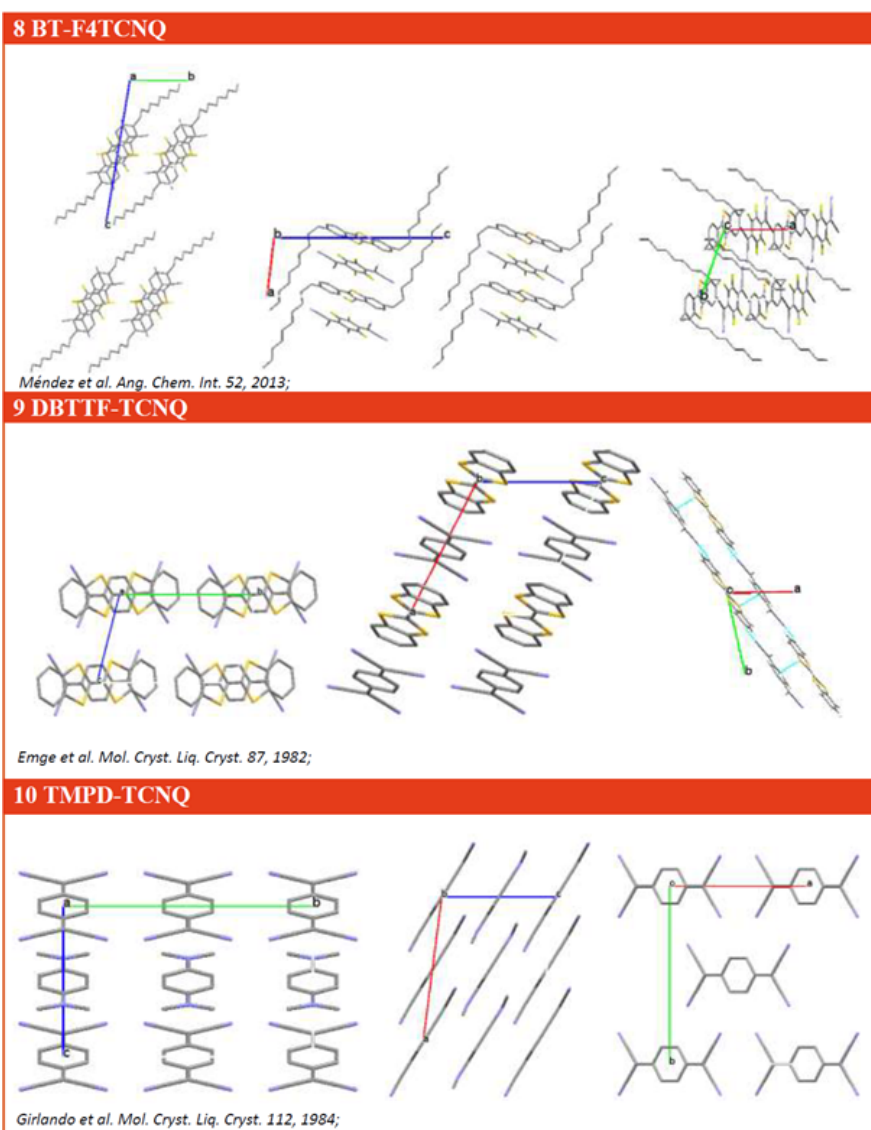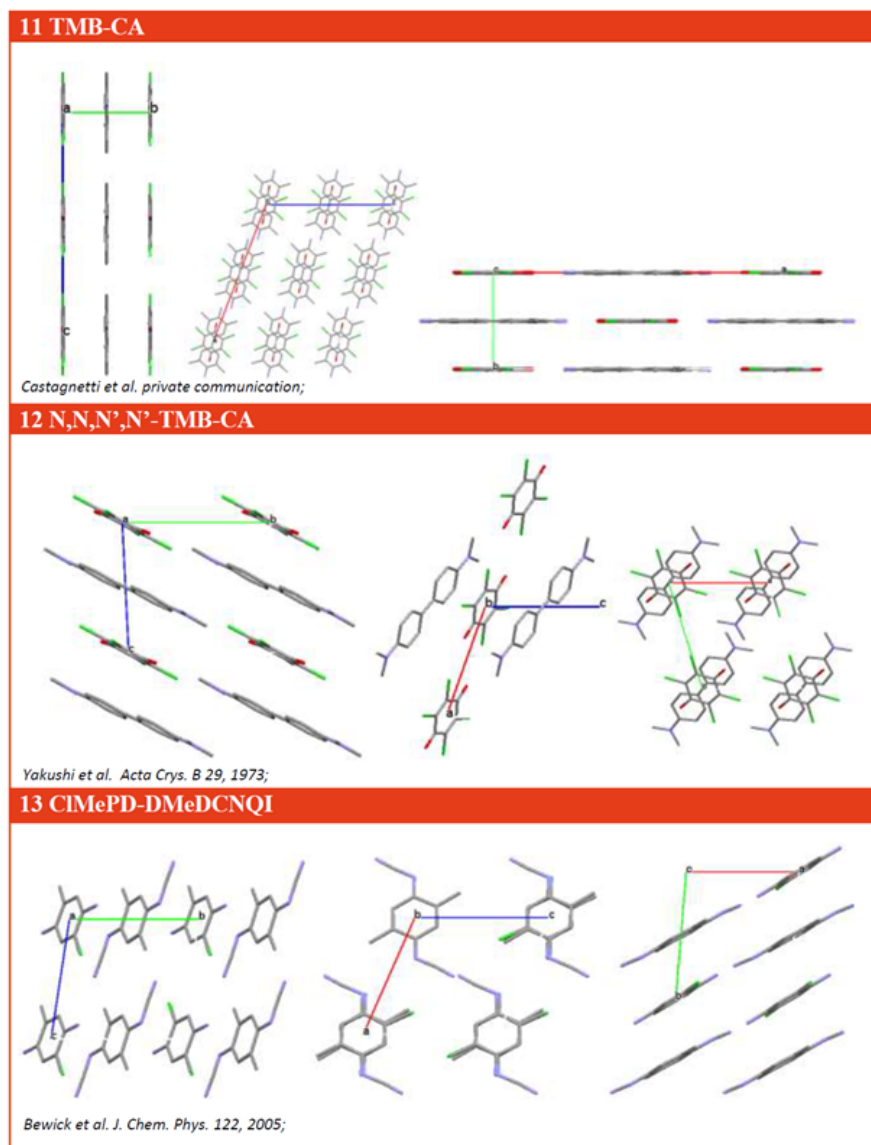
FIGURE 2.19: *Crystal packing along crystallographic axis for each MS-CT compounds investigated; hydrogen atoms are omitted for clarity.*

2.5.5 Ground state properties of MS-CT salts from DFT

We now have all parameters needed for a mean-field description of the ground state properties of our systems. Using eq. 2.12 we can now extract out of the *universal curve* $\rho(\Gamma_{eff})$ in Figure 2.9, the $\rho(\Gamma)$ curves relevant to the systems at hand, as shown in Figure 2.20.
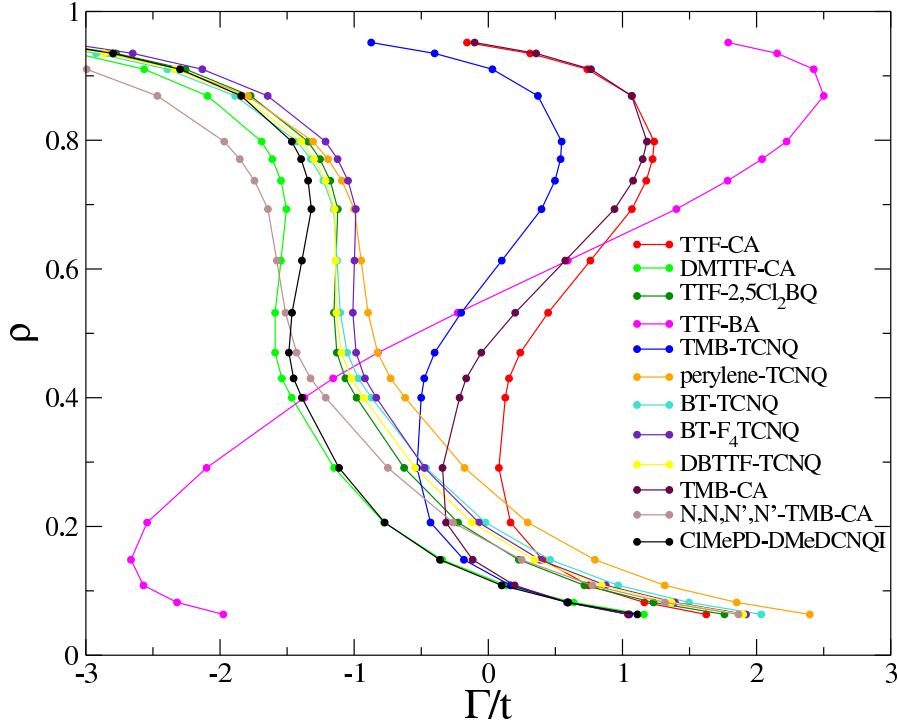
FIGURE 2.20: *Degree of ionicity as function of Γ in t unit calculated for each salt based on model parameters estimated in this work.*

The scenario emerging from Fig. 2.20 is very variegated and three different trends can be observed:

1. perylene-TCNQ (orange), N,N,N',N'-TMB-CA (grey), DBTTF-TCNQ (yellow), BT-TCNQ (cyano), BT-F$_4$TCNQ (violet) and TTF-2,5Cl$_{2,5}$BQ (dark green) are characterized by a fairly modest steepness of the curve pointing to a *continuous* or almost continuous behavior;

2. TTF-CA (red), TMB-TCNQ (blue), TMB-CA (brown), DMTTF-CA (light green) and ClMePD-DMeDCNQI (black) show a well evident S-shaped $\rho(\Gamma)$ curve pointing to a *discontinuous* behavior;

3. in TTF-BA (magenta) the curve points to an *extremely discontinuous* behavior with region of stability limited to just fully N ($\rho < 0.1$) or fully I ($\rho > 0.9$) states.

The observed behavior is fully dominated by the ε_T/t ratio, reported in Table 2.9, as already discussed in Section 2.3.4. Specifically, according to Figure 2.10, a continuous behavior is predicted for perylene-TCNQ, N,N,N',N'-TMB-CA, DBTTF-TCNQ, BT-TCNQ, BT-F_4TCNQ and TTF-2,5$Cl_{2,5}$BQ since they are characterized by $\varepsilon_T/t < 2$: in this case, neither intersite interactions nor molecular vibrations are large enough to overcome the effect of the integral hopping, giving rise a second-order phase transition. By contrast, in TTF-CA, TMB-TCNQ and TMB-CA, $\varepsilon_T/t > 3$ signals a discontinuous phase transition: the $\rho(\Gamma/t)$ function is no longer single valued and two stable states corresponding to the curve with positive slope can be found. Moreover, Tables 2.6 and 2.9 allow to discriminate the main contribution to the discontinuous transition between ε_c and ε_{sp}. In particular, we can state that in TTF-CA, intersite interactions play the major role, while the discontinuous behavior in TMB-TCNQ stems mainly from the significant relaxation energy of the Holstein mode. Finally, both contributions play an important role in TMB-CA.

DMTTF-CA and ClMePD-DMeDCNI show continuous or weakly discontinuous $\rho(\Gamma/t)$ curve as due to the intermediate value of ε_T/t ($2< \varepsilon_T/t <3$) respect with the previous cases. We can attribute such behavior in ClMePD-DMeDCNQI to the competition between the significant molecular relaxation energy and relatively large hopping integral; while in DMTTF-CA the repulsive intersite interactions are the main responsible.

The $\rho(\Gamma)$ curve in TTF-BA is completely different; in this case the large ε_T/t ratio is due to the very small hopping integral predicted: for this salt, only largely neutral ($\rho < 0.1$) or largely ionic states ($\rho > 0.9$) are accessible with a very large bistability.

A more detailed comparison would include the estimate of ρ from Γ and t reported in Table 2.5. Indeed, the calculated Γ/t allows to estimate from the curves in Figure 2.20 the relevant ρ values, as reported in Table 2.10.
The results however point to underestimated ionicities if compared with experimental values (see fourth column in Table 2.10). This can be ascribed to several problems. We exclude a role of adopted functional: Γ values obtained by D'Avino *et al.* for TTF-CA through CAMB3LYP and M06HF are similar [24]. One problem arises from the fact that all calculations are performed in gas phase, then leading to an overestimation of Γ. To correct for this contribution we mimic the environment repeating the calculation on a TTF-CA pair in cyclohexane. This leads to a stabilization of both neutral singlet and triplet states, with a decrease of Δ_{ST} down to 0.3 eV. **Method B** gives a Γ and an hopping integral values amounting to 0.306 eV and 0.162 eV respectively; then adopting the new value of Γ in t unit, we estimate the degree of ionicity in the crystal $\rho_{calc} \sim 0.03$ that does not improve appreciably over the previous result. For TTF-CA D'Avino *et al.* estimated the polarizability correction to Γ of the order of 0.2 eV. [24]. Again the

TABLE 2.10: ρ_{calc} *is extracted from data plotted in Figure 2.9 using* Γ *and t computed by Method B (see Tables 2.5) in comparison with* ρ_{exp};

System	Γ/t	ρ_{calc}	ρ_{exp}	Ref.
1 TTF-CA	2.014	0.06	0.24	[107]
2 DMTTF-CA	1.922	0.06	0.18	[94]
3 TTF-2,5,Cl2BQ	1.928	0.06	0.18	[107]
4 TTF-BA	1.607	0.04	1	[80]
5 TMB-TCNQ	1.247	0.06	0.5-0.6	[123]
6 perylene-TCNQ	1.772	0.09	0.10-0.11	[109]
7 BT-TCNQ	3.060	0.05	0.1	[118]
8 BT-TCNQF4	2.520	0.05	0.1	[118]
9 DBTTF-TCNQ	1.348	0.08	0.2	-
10 TMPD-TCNQ	-	-	1	[80]
11 TMB-CA	2.071	0.05	0.14	[124]
12 N,N,N',N'-TMB-CA	2.386	0.06	-	-
13 ClMePD-DMeDCNQI	0.961	0.07	0.35-0.58	[111]

correction does not qualitatively improve the result. However, due to the much smaller t, a correction of the similar order of magnitude would bring TTF-BA into the ionic phase. Further analysis of this point is in order.

2.6   Discussion

While the estimate of Γ is not successful, the overall scenario offered by the curves $\rho(\Gamma)$ in Figure 2.20 leads to a reasonable picture. The S-shaped curves of TTF-CA, TMB-TCNQ and TMB-CA clearly predict a *discontinuous* transition in agreement with available experimental data. In particular TTF-CA is the first MS-CT undergoing a discontinuous NIT [125]: on cooling below T_c=81 K in fact an abrupt jump from a largely neutral ($\rho \sim 0.3$) to a largely ionic ($\rho \sim 0.6$) ground state is observed, as shown in Figure 2.21 [126]. Iwasa *et al.* report a first-order NIT for TMB-TCNQ, signaled by an abrupt jump in the magnetic susceptibility and a stack dimerization at low temperature [123]. The ionicity jump in TMB-TCNQ ($\sim$0.1) is smaller than in TTF-CA ($\sim$0.3). Preliminary low-temperature measurements on TMB-CA do not show a temperature-induced phase transitions. Additional studies are planned in order to see if a phase transition may be induced in this system by increasing pressure.

DMTTF-CA and ClMePD-DMeDCNQI show *continuous* or weakly discontinuous $\rho(\Gamma)$ curve as due to the rather small ε_T/t value. Indeed for DMTTF-CA, Ranzieri *et al.* report a Peierls transition accompanied by a continuous variation of ionicity, and the system dimerizes before reaching the I phase ($\rho \sim 0.43$ at 20K, see Figure 2.21). On the other hand, ClMePD-DMEDCNQI undergoes to a continuous temperature-induced NIT
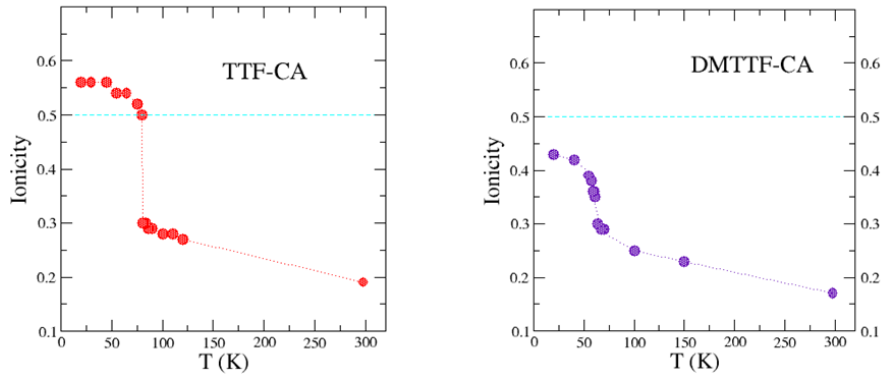
FIGURE 2.21:   *Temperature dependence of ionicity in TTF-CA (left panel) and DMTTF-CA (right panel), estimated from the frequency of the carbonyl stretching.*

at ambient pressure: IR absorption spectra suggest a continuous change in ionicity at around 200K. The ionicity estimated from the C=C stretching frequency of the acceptor goes from 0.3 at room temperature to 0.6 in the ionic phase. The continuous or almost continuous phase transition is confirmed by the very small hysteresis observed [111].

For TTF-2,5Cl$_2$BQ,DBTTF-TCNQ, BT-TCNQ, BT-F$_4$TCNQ and N,N,N',N'-TMB-TCNQ and perylene TCNQ the curves in Figure 2.20 clearly indicate a *continuous* change of ionicity. The data available for TTF-2,5Cl$_2$BQ and perylene-TCNQ confirm these results.

TTF-2,5Cl$_2$BQ has been investigated by A. Girlando *et al.* [107]. TTF-2,5Cl$_2$BQ does not undergo a T-induced NIT, but a continuous pressure-induced NIT is observed [107]. The different behavior in the two complexes has been discussed by Girlando *et al.* in terms of the more competitive role of CT integral respect to the Madelung energy in TTF-2,5Cl$_2$BQ, in agreement with our result. In fact, a ε_c/t amounting to 0.18 is obtained for TTF-2,5Cl$_2$BQ while a larger value (3.50) is predicted for TTF-CA.

For perylene-TCNQ there is no evidence of NIT neither upon lowering temperature nor increasing pressure (up to 27 Kbar) [109]. The different behavior respect to TTF-CA was justified based on the larger hopping integral and the smaller Madelung energy [109]. Our results confirm this picture.

The extreme discontinuity predicted for TTF-BA stems from the very small hopping integral calculated for this system: only largely neutral ($\rho < 0.1$) or largely ionic states ($\rho > 0.9$) are accessible with a very large bistability. Indeed TTF-BA shows a largely ionic ground state ($\rho \sim 0.95$) [110, 127].

These results reveal the strength of this relatively simple method that is able to reproduce not only some relevant microscopic parameters of the MHM, but also gives a wide picture

of ground state properties, revealing the nature of the NIT transition. It is surprising that the pertinence of such model is not confined to some crystals but is extended to a large family of MS-CT crystals.

2.7 Conclusion

In this Chapter, MS-CT crystals are presented. In Section 2.2 we have summarized the most interesting experimental features observed in MS-CT compounds. Then in Section 2.3, the *modified* Hubbard model accounting for *Peierls coupling* to lattice phonons and *Holstein coupling* to molecular vibrations, that successfully treats the rich physics governing the phase transition, is extensively described. The specific contribution of this Thesis is provided in Section 2.5, where we extract model parameters for MS CT salts from DFT calculations on DA pairs.

The method has been applied to a large family of MS-CT salts covering a wide spectrum of ionicities. DFT calculations (UωB97XD/6-31+G*) in gas phase are performed on the relevant DA pair and on the corresponding isolated moieties, both at crystallographic and optimized geometry. Among selected salts, only TMPD-CA cannot be parametrized since it doesn't fit the electronic model: the triplet state is in fact calculated as more stable than the singlet state.

The extensive comparison of our calculated parameters with the same parameters previously extracted from experimental data, when available, is a valid proof of the robustness of the present approach in the description of MS-CT crystals. The strength of the method is best represented by the calculation of $\rho(\Gamma)$ curves: from a *qualitative point of view*, the present model gets insight into the extremely complex behavior of the NIT in MS-CT salts. The pertinence is not confined to one salt but is expanded to a large group of MS-CT salts for which experimental data are available. In addition, for some compounds our results offer a prediction of experimental evidences and should encourage further experimental work to investigate the dependence of ionicity from pressure and temperature. In this perspective, the present model has demonstrated to be a reliable and powerful tool for experimentalists: measurements in very extreme conditions (low temperatures and high pressure) are very demanding. Once the crystallographic structure is known, the model offers an excellent *qualitative* screening to discriminate systems that can undergo to first- or to second-order transition, as well as, to discriminate the more competitive effect in the entangling between electronic and vibrational degrees of freedom. The model underestimates the ionicity, most probably due to an overestimate of Γ. Further investigation has to be carried out in order to obtain reliable ρ estimation.

The proposed approach offers a valid alternative to DFT calculations on periodic systems, which perform poorly in situations involving strong electron correlation effects [128], often predicting results that are not only quantitatively but also qualitatively inconsistent. Such failure has been attributed by Cohen *et al.* to the inability, recognized in all current functionals, to correctly describe the two systems H^+ and H_2 [129]. A more accurate picture of periodic systems is addressed by the quantum Monte Carlo (QMC) method, but this is highly demanding [128]. By contrast, the present approach, relying on calculation on a DA pair, is simple enough to overcome those difficulties opening the way towards a reliable description of strongly correlated systems.

Chapter 3

Charge transfer in organic radical dipolar dyes

Probare et reprobare

Dante Alighieri, III Canto Paradiso

3.1   Introduction

In this Chapter we present the work done in collaboration with the group of Prof. J. Veciana (ICMAB, Barcelona) on the radical polar dyes D-π-R$^\cdot$ shown in Figure 3.1. In these dyes the persistent polychlorotriphenylmethyl radical (PTM) plays the role of an electron acceptor, so that two main resonating structures can be considered: D-π-R$^\cdot$ and D$^{\cdot+}$-π-R$^-$. PTM radical is an interesting unit in view of its high stability and persistence. It is composed of three totally chlorinated phenyl rings connected to a central carbon atom with a sp^2 hybridization.

PTM radical is also interesting because it is an electroactive species that can be easily reduced to the anion PTM$^-$. Moreover, its stable derivative PTMH make PTM radical an excellent candidate as building block for functional molecular materials.

Figure 3.1 shows PTM connected to ferrocene through a vinylene bridge (Fc-PTM) as well as to a tetrathiafulvalene-based electron-donor (TTF-PTM) and to monopyrrolo-TTF (MPTTF-PTM). Fc-PTM is an interesting valence tautomeric compound showing thermally induced CT and bistability in solid state [121]. TTF-PTM shows an intriguing aggregation in polar solvents leading to a subtle interplay between intramolecular
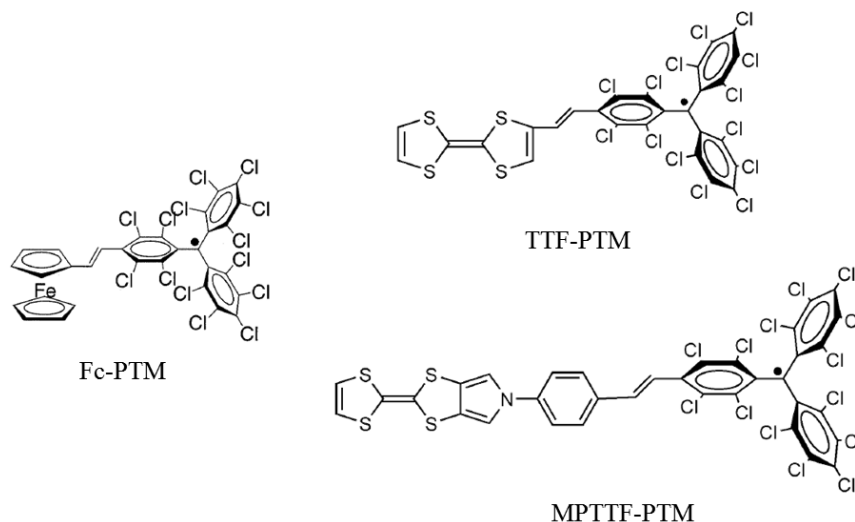
FIGURE 3.1: *Chemical organic radical dyes Fc-PTM, TTF-PTM and MPTTF-PTM theoretically investigated in this Chapter.*

electron transfer and intermolecular charge transfer [25, 130]. TTF-PTM represents the first aim towards a more ambitious effort to investigate a new family of materials based on D-π-R˙ organized in molecular crystals with sizeable intermolecular CT interactions [23]. In this perspective, M. Souto in the group of J. Veciana has recently synthesized the first example of this new family of crystals, MPTTF-PTM [131].

In Chapter I, we have shown the power of essential-state models to describe the low-energy physics of CT dyes. A similar approach could apply to D-π-R˙ systems, governed by the CT between D and R˙. However, these systems are characterized by a very weak conjugation between D and R˙, leading to extremely weak CT absorption bands, making the estimate of model parameters from optical spectra very difficult and uncertain. The success of DFT for *intermolecular* CT (Chapter II) invites to explore similar strategies to attack the problem of *intramolecular charge transfer* in D-π-R˙.

D-π-R˙ dyads based on Fc have been recently used to create self-assembled monolayers (SAM) on metallic (gold) surfaces, with the aim to modify the work function of metals in order to facilitate the charge injection [132, 133]. In this perspective, D. Morales, in the group of J. Veciana, has experimentally investigated SAM based on a radical Fc-PTM complex in comparison with SAM based on the hydrogenated Fc-PTM (Fc-PTMH) complex and with SAM based just on Fc moiety. With the aim to support experimental results, we have performed theoretical calculations at PM7 level on the relevant molecules.

3.2 The case of TTF-PTM and MPTTF-PTM

In this section, experimental and theoretical investigation of the MPTTF-PTM and TTF-PTM is discussed. An extensive characterization was carried out in the Veciana group for these two dyes, including UV-Vis spectroscopy, cyclic voltammetry (CV), X-Ray analysis. The main goal of our theoretical calculations is to support experimental data, setting a firm basis for the parameterization of essential-state models.

3.2.1 Experimental data

Figure 3.2 reports the UV/Vis/near-infrared (NIR) spectra of dyad TTF-PTM and MPTTF-PTM recorded in THF at 300 K. They show an intense absorption band at λ=385 nm, characteristic of PTM radical, with a shoulder at λ=376 nm, attributed to the MPTTF fragment. The two broad bands appearing at lower energies (λ=439 nm and 550 nm) can be assigned to the electronic conjugation of the unpaired electron to the π framework. Interestingly, MPTTF-PTM also shows a weak and broad absorption band at $\lambda \sim 800$ nm, which can be ascribed to CT taking place between the TTF and PTM units, whereas a similar CT band is observed in the region between $\lambda \sim$900-1000 nm for the shorter radical dyad. The hypsochromic shift observed in MPTTF-PTM, compared with TTF-PTM, can be ascribed to the lower donating character of the MPTTF subunit. When MPTTF-PTM is oxidized with one equivalent of $Fe(ClO_4)O_3$, the CT absorption band disappears and a new band appears at $\lambda \sim 600$ nm, assigned to the formation of the radical cation of the MPTTF subunit. Data in Figure 3.3, showing MPTTF-
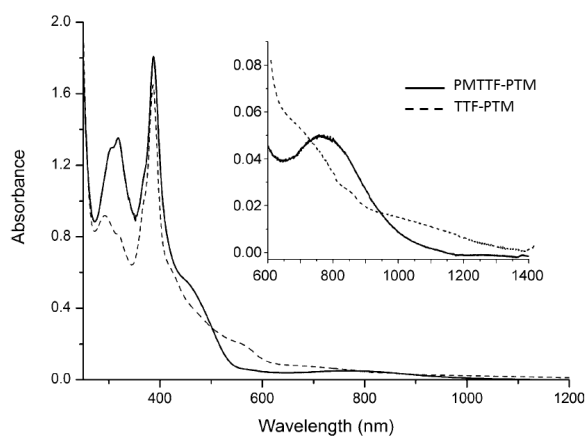
FIGURE 3.2: *UV/Vis spectra recorded at 300 K in THF of 0.05 mM solution of dyads TTF-PTM and MPTTF-PTM.*
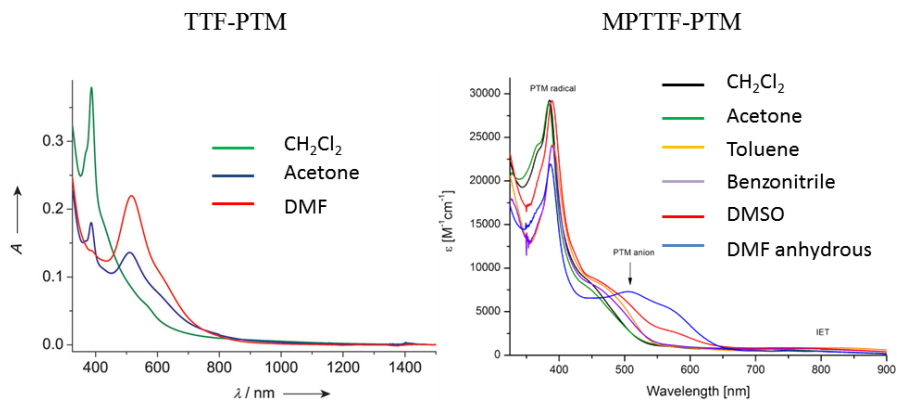
FIGURE 3.3: *UV/Vis-NIR spectra of TTF-PTM (on the left) and MPTTF-PTM (on the right) recorded at 300 K in different solvents.*

PTM spectra collected in different solvents, suggest that MPTTF-PTM stays essentially neutral in all solvents, with the only exception of DMF where a peak at 512 nm is assigned to the PTM anion, supporting the presence in solution of zwitterionic species. For TTF-PTM a more intriguing results are observed: the dye is in fact fully neutral in CH_2Cl_2, where only the band assigned to PTM is seen, it becomes zwitterionic in DMF (the band due to neutral PTM disappears while the band of PTM anion appears), but both species are observed in acetone, a solvent of intermediate polarity [25, 130]. The different behavior of the two dyads can be ascribed to the poorer donating character of the MPTTF unit in comparison with the TTF unit. We observe, however, that the formation of zwitterionic species of TTF-PTM dissolved in medium and high-polarity solvents is actually triggered by the formation of $(TTF^+)_2$ dimers [43, 130]. It is possible that attaching the pyrrole ring to the TTF moiety reduces the well-known tendency of TTF to form dimers, thus hindering the formation of zwitterionic species.

It was not possible to crystallize TTF-PTM. The longer bridge in MPTTF-PTM instead allows to grow crystals suitable for X-rays analysis. Crystallographic data at 150 K and 300 K of MPTTF-PTM crystals, obtained by slow evaporation from a solution in *n*-hexane/CH_2Cl_2, support a monoclinic system with space group P$\bar{1}$. The asymmetric unit reveals two inequivalent molecules (A and B) aligned parally along the *a* axis, as shown in Figure 3.4.

3.2.2   Quantum-chemical calculations: (TD)-DFT

A series of quantum-chemical calculations have been performed on dyads TTF-PTM and MPTTF-PTM in solution, using Gaussian 09 package [114]. Geometries are optimized at (U)CAM-B3LYP/6-31G* level for different oxidation states of both dyads, the
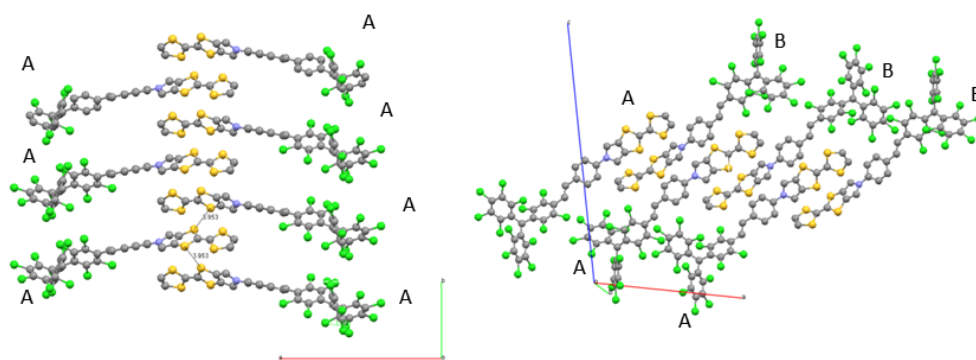
FIGURE 3.4: *Molecular packing of MPTTF-PTM molecules at 300 K: on the left, A units in the ab plane and on the right, A,B units along ac plane.*

neutral open-shell doublet states (neutral species), the closed-shell anions (anionic species), the cation-biradical (cationic species), where the bi-radicaloid character was enforced by considering the triplet state and the dication radical (dicationic species). In all cases, solvent is introduced based on the polarizable continuum model (PCM). The adopted hybrid functional is expected to describe well long range interactions in the charge transfer excited states [134]. In the PCM model the system under scrutiny is described at a quantum-mechanical level, while the surrounding environment is described as a polarizable continuum model characterized by its macroscopic dielectric constant [135].

Dividing the molecule in D and A fragments as sketched in Figure 3.5, the charge on each fragment is calculated of the order of 0.09 and 0.10 for TTF-PTM and MPTTF-PTM in CH_2Cl_2, respectively, and only marginal variations with solvent polarity are obtained (see Table 3.1). At variance with experimental data, the systems do not show a tendency to become zwitterionic. Indeed, according to recent theoretical result for TTF-PTM, zwitterionic species are due to the formation of TTF dimers in polar solvents [26].
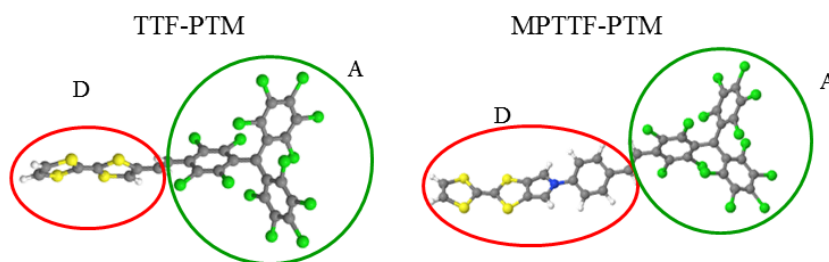
FIGURE 3.5: *Donor and acceptor fragments of TTF-PTM and MPTTF-PTM.*

TABLE 3.1: *The degree of ionicity in D fragment defined in Figure 3.5 referred to neutral, cationic, dicationic and anionic species for both compounds at UCAMB3LYP/6-31G* with PCM level with (Pop=MBS) keyword [136].*

Mulliken charge distribution					
System	*Solvent*	ρ_{Neut}	ρ_{Cat}	ρ_{Dicat}	ρ_{An}
TTF-PTM	CH_2Cl_2	0.09	1.00	1.93	0.04
	AcCN	0.09	1.00	1.93	0.04
MPTTF-PTM	CH_2Cl_2	0.10	1.08	2.06	0.05

Charge distributions in the cationic, dicationic and anionic species confirm the CV data [131], with an excess of electron residing on PTM fragment in the anionic species, and positive charges residing in the TTF/MPTTF fragments in the mono and dicationic species.

The spin distribution in Figure 3.6 shows that in both neutral species, the spin is localized on the PTM moiety and on the vinylene group, in line with the results obtained using EPR spectroscopy. In the cationic and diradicaloid species, the two spin densities on the TTF/MPTTF and PTM units are fully disconnected.
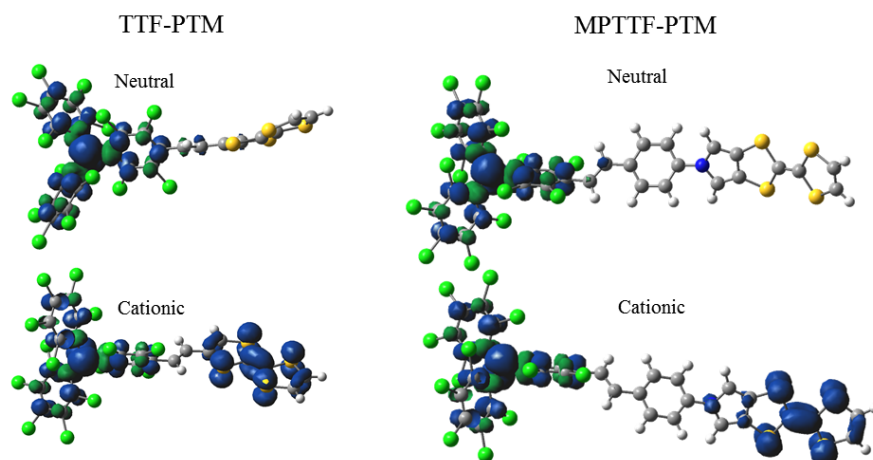
FIGURE 3.6: *Spin density of both radicals in CH_2Cl_2, calculated at UCAMB3LYP/6-31G* level with PCM. Top and bottom panel show results for the neutral and cationic species, respectively. Isovalue of the plot equal to 0.002.*

Calculations on the isolated dyad MPTTF-PTM at the crystallographic geometry support a largely neutral ground state both at room and at low temperature, in agreement with experimental data, as summarized in Table 3.2.

Having characterized the ground state, we turn attention on optical properties. In Table 3.3, we show calculated energies and oscillator strengths (f) for transitions with sizeable oscillator strength (>0.01, corresponding to the f of the lowest energy transition) obtained for TTF-PTM and MPTTF-PTM at TD-UCAMB3LYP/6-31G* at optimized

TABLE 3.2: *Mulliken atomic charges and spin density distributions (for D fragment, see Figure 3.5) calculated at the UCAMB3LYP/6-31G* level for isolated MPTTF-PTM molecule at the crystallographic geometry for A and B, at 300 K and 150 K.*

Charge and spin density		
System	ρ	*spin density*
A 300K	0.093	0.0531
A 150K	0.079	0.0622
B 300K	0.085	0.0549
B 150K	0.110	0.0899

ground state geometries. Results refer to CH_2Cl_2 solutions, but solvent effects are marginal. Relevant MOs are shown in Figure 3.7.

TABLE 3.3: *Lowest and most intense optical transitions calculated for both radicals in CH_2Cl_2 at TD-UCAM-B3LYP/6-31G* level;*

TD-UCAM-B3LYP/6-31G*			
System	λ(nm)	f	*transition nature*
TTF-PTM	365	0.10	(HOMO-4)$\beta \longrightarrow$ SUMO (0.40)
	368	0.50	HOMO-$\alpha \longrightarrow$ LUMO-α (0.21)
			(HOMO-4)$\beta \longrightarrow$ SUMO (0.18)
			HOMO-$\beta \longrightarrow$ LUMO-β (0.15)
	375	0.02	(HOMO-3)$\beta \longrightarrow$ SUMO(0.61)
	474	0.16	HOMO-$\beta \longrightarrow$ SUMO (0.69)
	636	0.01	HOMO-$\beta \longrightarrow$ SUMO (0.13)
			HOMO-$\beta \longrightarrow$ LUMO-β (0.13)
			(HOMO-1)$\beta \longrightarrow$ SUMO (0.12)
			(HOMO-1)$\beta \longrightarrow$ LUMO-β (0.12)
MPTTF-PTM	364	0.47	(HOMO-5)$\beta \longrightarrow$ SUMO (0.11)
			(HOMO-1)$\alpha \longrightarrow$ LUMO-α (0.10)
			(HOMO-3)$\beta \longrightarrow$ SUMO (0.11)
			(HOMO-1)$\beta \longrightarrow$ SUMO (0.21)
	366	0.01	(HOMO-6)$\beta \longrightarrow$ SUMO (0.81)
	372	0.03	(HOMO-5)$\beta \longrightarrow$ SUMO (0.71)
	416	0.08	HOMO-$\beta \longrightarrow$ SUMO (0.76)
	438	0.06	(HOMO-9)$\beta \longrightarrow$ SUMO (0.23)
	516	0.013	(HOMO-1)$\beta \longrightarrow$ LUMO-β (0.14)
			(HOMO-1)$\beta \longrightarrow$ SUMO (0.10)
			(HOMO-3)$\beta \longrightarrow$ SUMO (0.07)
			(HOMO-3)$\beta \longrightarrow$ LUMO-β (0.07)
			(HOMO-1)$\alpha \longrightarrow$ LUMO-α (0.15)

Both radical dyads show in the 364-375 nm region three transitions mainly localized on the PTM unit with minor contributions from bridge states. These transitions are readily assigned to the strong and structured peak observed at $\sim$385 nm. Several transitions are observed at lower energy for both compounds all showing some CT character, even if a large mixing is observed with excitations involving bridge-states as expected on physical basis [137]. These transitions are assigned to the many broad features pointed out in
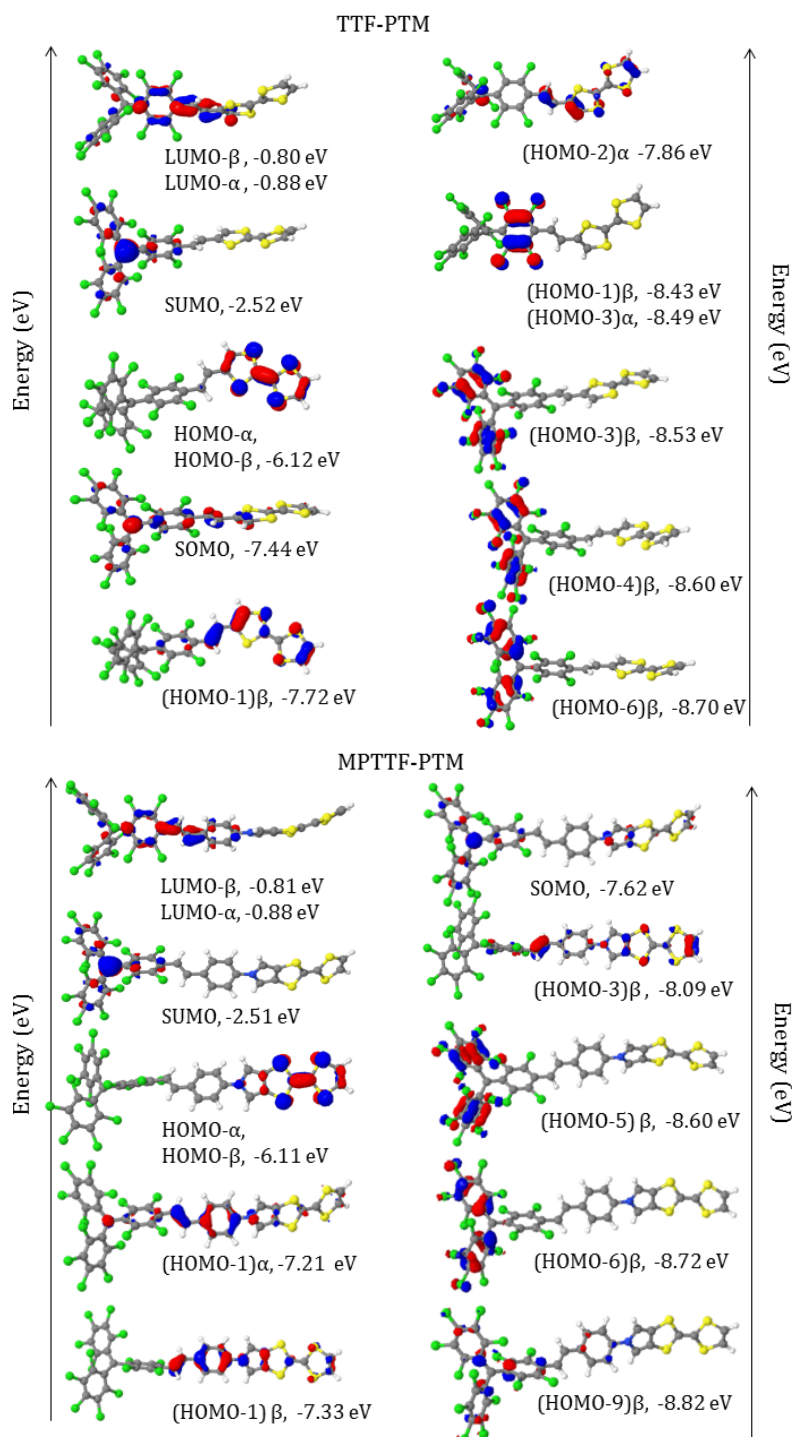
FIGURE 3.7: *Molecular orbitals involved in transitions reported in Table 3.3 in TTF-PTM amd MPTTF-PTM at TD-UCAMB3LYP/6-31G* with PCM model.*

experimental spectra in the low-frequency region. The oscillator strength associated with this lowest energy transition is a small fraction (1/50-1/100) of the oscillator strength associated with the intense peak localized on PTM, in line with experimental data. In addition, TD-DFT calculations predict a shift of the CT-transition energy ($\sim$0.45 eV) in

good agreement with experimental results ($\sim$0.3-0.4 eV). Though TD-UCAMB3LYP/6-31+G* calculations are able to catch the CT nature of the lowest-energy transition and to reproduce the relative CT energy in the two systems, the energy is overestimated by $\sim$0.6 eV. This fact can be attributed to several reasons. In the first place an overestimate of energy for a mixed ICT-valence states is an intrinsic feature for this hybrid functional, as also further supported by ωB97XD/6-31G* results giving an overestimation equal to 0.8 eV [138–140]. Then, Eriksen *et al.* point out some difficulties of CAM-B3LYP functionals to reproduce charge transfer excitation energies in push-pull chromophores [141]; finally, molecules with open shell ground states have absorption spectra which are more difficult to describe with any methods [142].

3.2.3 Semiempirical calculations: ZINDO

Here we briefly summarize results for TTF-PTM and MPTTF-PTM obtained by semiempirical method. In particular, ZINDO calculation implemented in ORCA package has performed [143]. Table 3.4 shows the lowest energy transitions calculated for both radicals at optimized geometry at UCAM-B3LYP/6-31G* level.

ZINDO calculations confirm previous TD-DFT calculations. Results suggest that, in both radicals, calculated excited states around 339-393 nm are mainly localized on PTM moieties and therefore can be assigned to the strong absorption band at 383 nm; in TTF-PTM and MPTTF-PTM, at 584 nm and 614-630 nm respectively, two excited states with weaker oscillator strength and a localized nature on PTM are predicted: they could be assigned to the feature observed around 450 nm for TTF-PTM and 550 nm for MPTTF-PTM. Regarding the lowest excited state in both radicals, ZINDO suggests a CT nature involving also bridge-states in agreement with previous results.

ZINDO offers a reasonable estimate of CT energy as well as of the ionicity in ground state (ρ=0.09 and 0.10 for TTF-PTM and MPTTF-PTM, respectively). Therefore, based on eq. 1.6 (see Chapter I), we can extract the hopping integral, τ, z and μ_0 for both dyads. In the present case, the relevant parameters are summarized in Table 3.5 and the relevant model drawn in Figure 3.9.

For both radicals, the values of μ_0 point out D-π-R$^\cdot$ distances comparable with the length of the molecules. In addition, parameters suggest that MPTTF-PTM is characterized by a lower donating character of the MPTTF subunit and by a higher charge transfer integral respect to TTF-PTM, in agreement with the hypsochromic shift in UV-Vis spectrum.
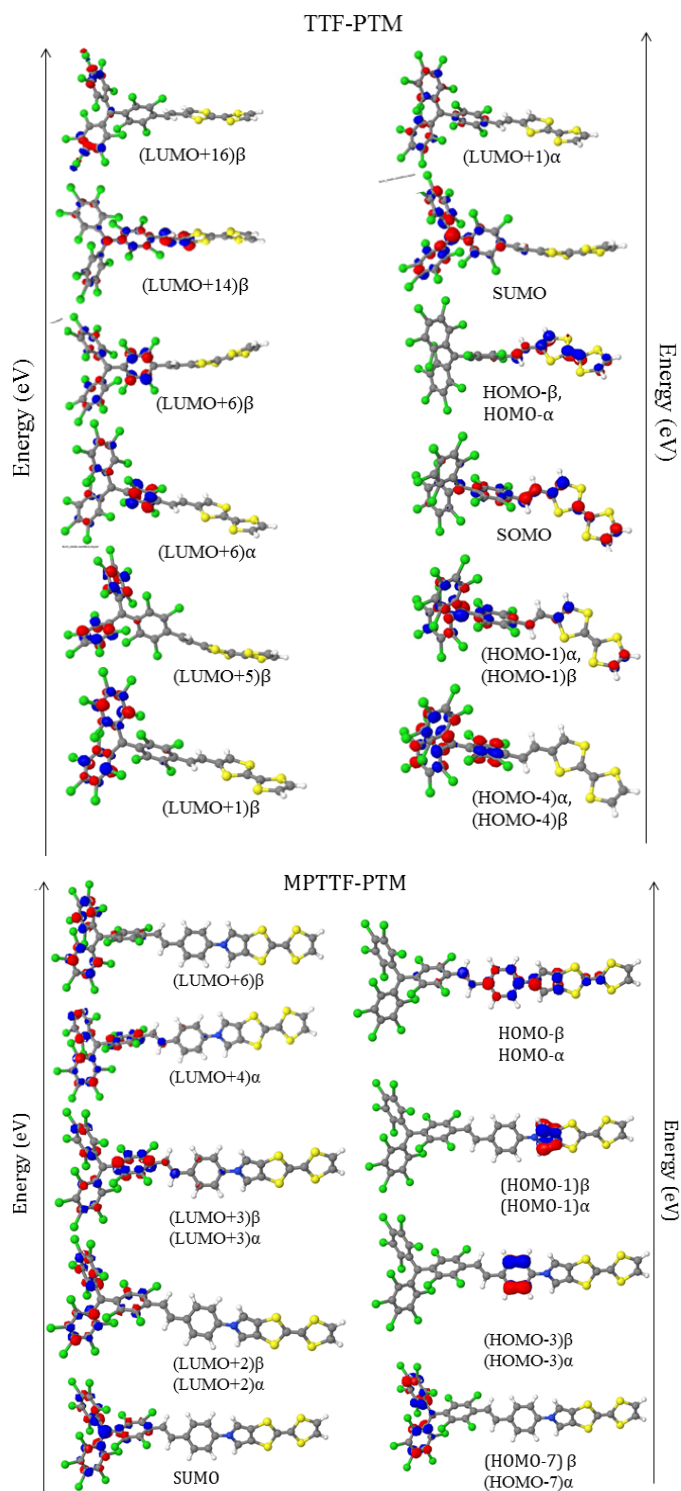
FIGURE 3.8: *Molecular orbitals involved in transitions reported in Table 3.4 in TTF-PTM and MPTTF-PTM with ZINDO at UCAMB3LYP/6-31G* geometry.*

TABLE 3.4: *Lowest and most intense optical transitions calculated for both radicals at ZINDO in gas phase starting at opt. UCAM-B3LYP/6-31G* geometry;*

			ZINDO
System	λ(nm)	f	*transition nature*
TTF-PTM	339	0.2312	(HOMO-4)$\beta \longrightarrow$ LUMO-β (0.60)
	383	0.0011	SOMO $\longrightarrow$ (LUMO+1) (0.50)
	390	0.0023	SOMO $\longrightarrow$ LUMO (0.58)
	617	0.0183	(HOMO-2)$\alpha \longrightarrow$ (LUMO+6)α (0.24)
			(HOMO-4)$\beta \longrightarrow$ (LUMO+4)β (0.23)
			(HOMO-4)$\beta \longrightarrow$ (LUMO+5)β (0.23)
	630	0.0021	(HOMO-4)$\beta \longrightarrow$ (LUMO+6)β (0.23)
			(HOMO-4)$\alpha \longrightarrow$ (LUMO+6)α (0.47)
	873	0.0001	(HOMO-1)$\beta \longrightarrow$ (LUMO+14)β (0.29)
			HOMO-$\beta \longrightarrow$ (LUMO+14)β (0.27)
			(HOMO)$\alpha \longrightarrow$ (LUMO+16)α (0.25)
			(HOMO-1)$\alpha \longrightarrow$ (LUMO+16)β (0.23)
MPTTF-PTM	352	0.56	(HOMO)$\alpha \longrightarrow$ (LUMO+4)α (0.24)
			HOMO-$\alpha \longrightarrow$ (LUMO+6)α (0.25)
			HOMO-$\beta \longrightarrow$ SUMO (0.26)
			HOMO-$\beta \longrightarrow$ (LUMO+3)β (0.26)
	393	0.04	SOMO $\longrightarrow$ LUMO+2 (0.60)
	584	0.071	HOMO-$\beta \longrightarrow$ SUMO (0.76)
			(HOMO-7)$\beta \longrightarrow$ (LUMO+2)β (0.30)
			(HOMO-7)$\alpha \longrightarrow$ (LUMO+3)α (0.26)
	737	0.002	HOMO-$\beta \longrightarrow$ SUMO (0.76)
			(HOMO-1)$\beta \longrightarrow$ SUMO (0.10)
			(HOMO-3)$\beta \longrightarrow$ SUMO (0.07)
			(HOMO-3)$\beta \longrightarrow$ (LUMO+2)β (0.07)
			(HOMO-1)$\alpha \longrightarrow$ (LUMO+2)α (0.15)

TABLE 3.5: *Two-state model parameters for TTF-PTM and MPTTF-PTM from calculated optical spectra by ZINDO;*

System	z (eV)	τ (eV)	μ_0 (D)
TTF-PTM	0.58	0.40	44
MPTTF-PTM	0.65	0.49	69

FIGURE 3.9: *The two-state model derived for TTF-PTM and MPTTF-PTM in according to eq. 1.6 and excitation energy and charge distribution at ZINDO level;*

3.3 Essential-state parameters from ground state properties

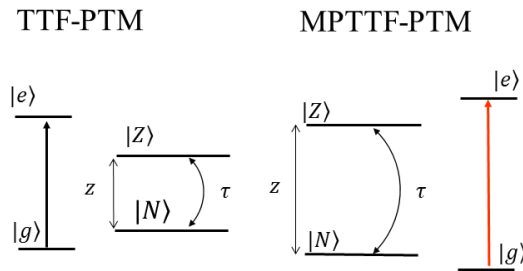While ZINDO results lead to reasonable estimates of essential-state model parameters, TD-DFT fails badly. A strategy to improve this disappointing result implies abandoning the calculation of excited state, limiting attention to ground state properties. Accordingly, we calculate the ground state properties of a D-π-R$\cdot$ dyad under an applied electric field as to drive it from the neutral (N) to the zwitterionic (Z) state. Specifically we plan to extract essential-state model parameters from the fit of curves showing the dependence of the ground state dipole moment versus an applied electric field.

3.3.1 The case of Fc-PTM

To validate the approach we focus on a well-studied system, Fc-PTM [121, 137]. Optical absorption spectra of Fc-PTM collected in solution, reported in Figure 3.10, reveal that solvated Fc-PTM is a largely neutral D-π-A molecule. The CT absorption band, located in the near infrared region around 11000 cm^{-1}, is related to the photoexcitation towards a largely ionic (or zwitterionic) D$^+$ $\longleftarrow$ A$^-$ state. Experimental data are modelled in terms of two-state model [121], as already described in Chapter I, and in terms of three-essential-state model [137].

Shortly, three-essential state model has been introduced to account for the secondary CT band involving the π-bridge observed in a Fc-PTM based dye [137]; the three resonating structures are D-π-A, D-π^+A$^-$ and D$^+$-π-A$^-$, where the first and the last structures largely dominate over the second one, that represents an higher energy state. The CT occurs through the bridge; D-π-A and D$^+$-π-A$^-$ are separated by an energy gap of $2z$ and mixed by τ, while $2x$ and τ' measure, respectively, the energy gap and the hopping integral between D-π^+-A$^-$ and D-π-A (with $x > z$). μ_0, ε_{sp} and ω are defined as in the two-state framework (see Chapter I). Results are summarized in Tables 3.6 and 3.7.

TABLE 3.6: *Two-states model parameters extracted for Fc-PTM to fit optical data [121]; all parameters except $\mu_0(D)$ are in eV;*

		Two-states model			
	z	τ	μ_0	ε_{sp}	ω
Exp. opt. data	0.61	0.35	7.5	0.1	0.18

TABLE 3.7: *Three-states model parameters extracted for Fc-PTM to fit optical data [137];all parameters except $\mu_0(D)$ are in eV;*

			Three-states model				
	$2z$	$2x$	τ	τ'	μ_0	ε_{sp}	ω
Exp. opt. data	0.78	0.87	0.47	0.47	15	0.06	0.18
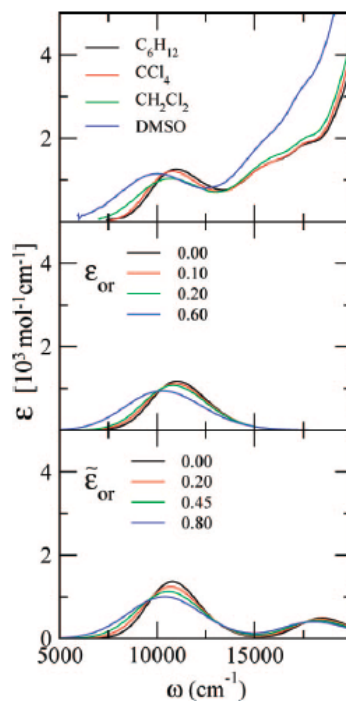
FIGURE 3.10: *Experimental (top panels, [121]) and calculated spectra for Fc-PTM; central panel shows spectra calculated in the two-state model with molecular parameters in Table 3.6 and the ε_{or} values in the legend; bottom panel shows spectra calculated in the three-state model with molecular parameters in Table 3.7 and the ε_{or} values in the legend. The intrinsic bandwidth is set to $\Gamma=0.07$ eV in all calculated spectra [137].*

Semiempirical PM7 (MOPAC package [112, 113]) and DFT (Gaussian 09 package [114]) levels of theory are adopted; specifically, regarding the latter, following Geskin *et al.* hybrid functionals have been selected, as CAM-B3LYP and ωB97XD with the basis set 6-31+G* [144]. All calculations are performed at crystallographic geometry in presence of an external electric field applied along the molecular axis connecting the central Fe-atom of Fc unit to the radical carbon in PTM (x-axis, below), as shown in Figure 3.11.

Due to the open-shell character of the molecule, spin polarized approach is adopted. Actually this approach has been considered just for DFT calculations, whose results do not significantly suffer of spin contamination. By contrast, PM7 results in UHF approximation are rejected ($S^2 \sim 1$ for doublet states) and only RHF results are taken
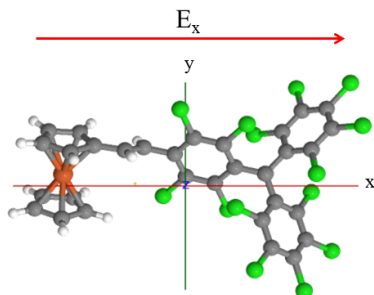
FIGURE 3.11: *The external electric field is applied along x-axis, corresponding to the axis connecting Fc to PTM.*

into account. Calculations are performed in gas phase; PM7 and UCAM-B3LYP are also carried out in a non-polar solvent (toluene).

Figure 3.12 reports the F-dependence of the dipole moment, or better of the x-component of the dipole moment, μ_x.

FIGURE 3.12: *Electric field-dependence of the dipole moment (x-component) calculated for Fc-PTM (crystal geometry) at PM7 in gas phase (blue) and in toluene (red), at UCAMB3LYP/6-31+G* in gas phase (green) and in toluene (magenta) and at ωB97XD/6-31+G* in gas phase (orange line).*

In the following we disregard the role of electron-vibration coupling, focusing just on the electronic part. The coupling is fairly small and in any case it would just lead to a (minor) renormalization of z. Neglecting vibrational coupling is in line with quantum chemical
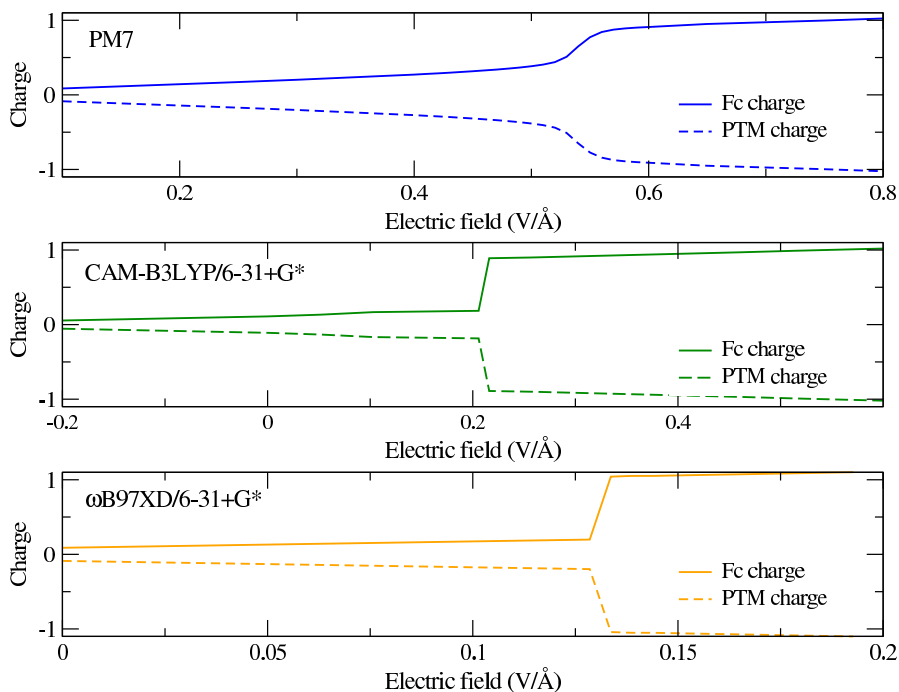
FIGURE 3.13: *Total net charge on Fc and PTM units in Fc-PTM at PM7 (blue line), CAMB3LYP/6-31+G* (green line) and ωB97XD/6-31+G* (orange line) in gas phase.*
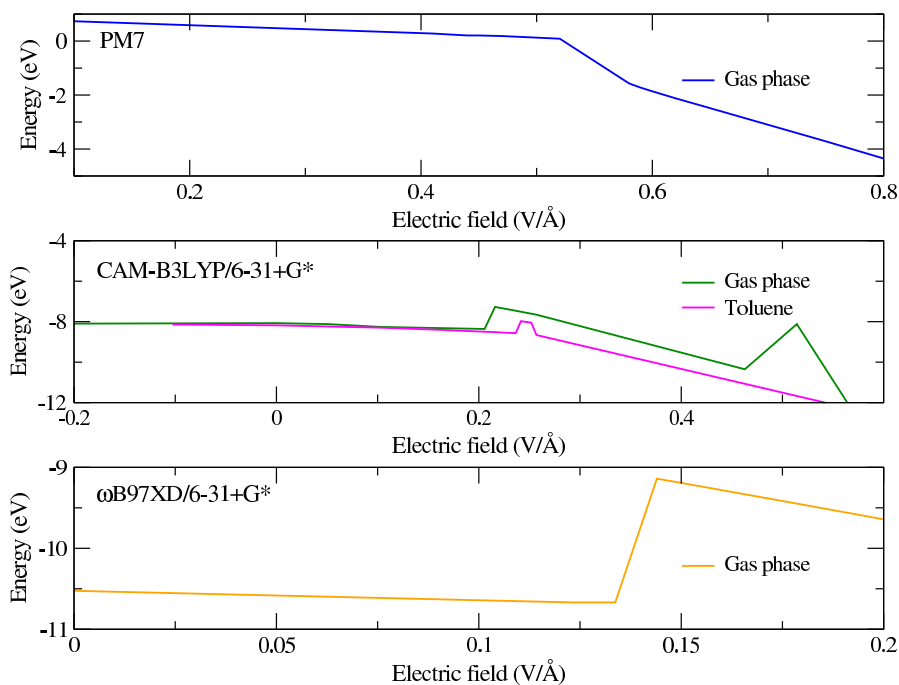
FIGURE 3.14: *Ground state energy in Fc-PTM (crystal geometry) at PM7 (blue line), UωB97XD/6-31+G* (orange line) in gas phase; in CAMB3LYP/6-31+G* ground-state energy is reported in gas phase (green) as well as in toluene (magenta).*

calculations that, as already explained, are run at fixed geometry. Finally, the essential-state model parameters refer to a non-polar solvent. In principle these parameters should

be comparable to those obtained from a calculation run in a non-polar solvent (as to account for the effect of electronic component of the solvent polarization), but, for the sake of comparison, we also show results obtained in the gas phase.

All $\mu(F)$ curves in Figure 3.12 clearly point out two different regimes: a low and a high field regime separated by a region where charge rearranges dramatically. The two regimes correspond to two different charge distributions: at low field the molecule is in a neutral (D-π-A) ground state, while at high fields the molecule turns zwitterionic (D$^+$-π-A$^-$).

To further support this interpretation, Figure 3.13 reports the total charges on the Fc (continuous line) and PTM (dotted line) units for all examined levels of theory. The sum of the charges on the two units is approximately zero, confirming the picture of a charge transfer from D to A. Moreover, in the small F regime the charge transferred from D to A is approximately zero, while the region of the second plateau corresponds to a system where approximately one electron is transferred. The curve at PM7 level of theory in Figure 3.12 clearly shows a characteristic S-shape and is *qualitatively* in line with results published by D'Avino *et al.* and computed at PM6, though in this case, we assist to a *quantitative* shift of the flex point towards higher values of F in comparison with published results [121].

DFT curves in gas phase point out a characteristic step-like shape, suggesting a multi-stable behavior. In support of this, calculations have been performed to distinguish the N and the I regime. In the N regime we use as input for the density optimization, at each F value, the calculated density at the previous lower F point. In the Z regime we start from high F values and do the same. A bistability region clearly emerges when two calculations lead to different $\mu(F)$ values, as reported in the top panel of Figure 3.15.

A bistable feature is expected when a *mean-field approximation* is considered, as described in Chapter II. In general, autoconsistency is introduced when *e-ph* coupling is taken into account and therefore, for example, during an optimization of geometry, as recently encountered by Jankowska *et al.* [145]. By contrast, in the present case, the multistable behavior seems to be ascribed to an *artefact* of UωB97-XD/6-31+G* and UCAM-B3LYP/6-31+G* since geometry is kept fixed. In order to exclude any potential *mf* approximations, introduced in those hybrid functionals to better catch long range interactions, other functionals are tested; in particular, a functional based on the local density approximation, LSDA and the well-known hybrid, B3LYP are selected. Results are reported in the central and bottom panel of Figure 3.15.

The $\mu(F)$ curve at ULSDA level in the central panel of Figure 3.15 is fully linear with the field, in line with the possibility of fractional charges in the framework of DFT
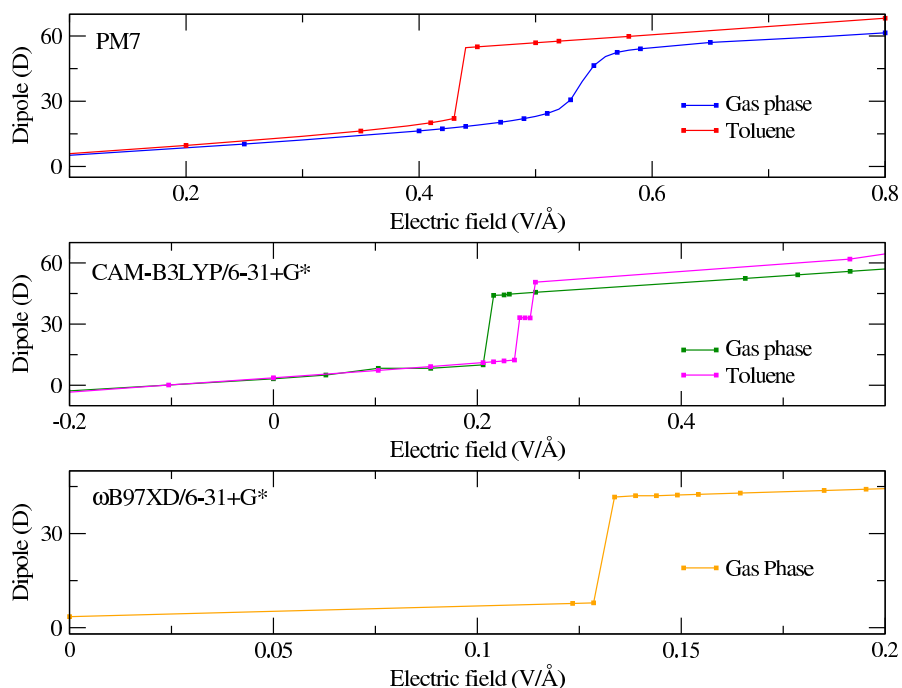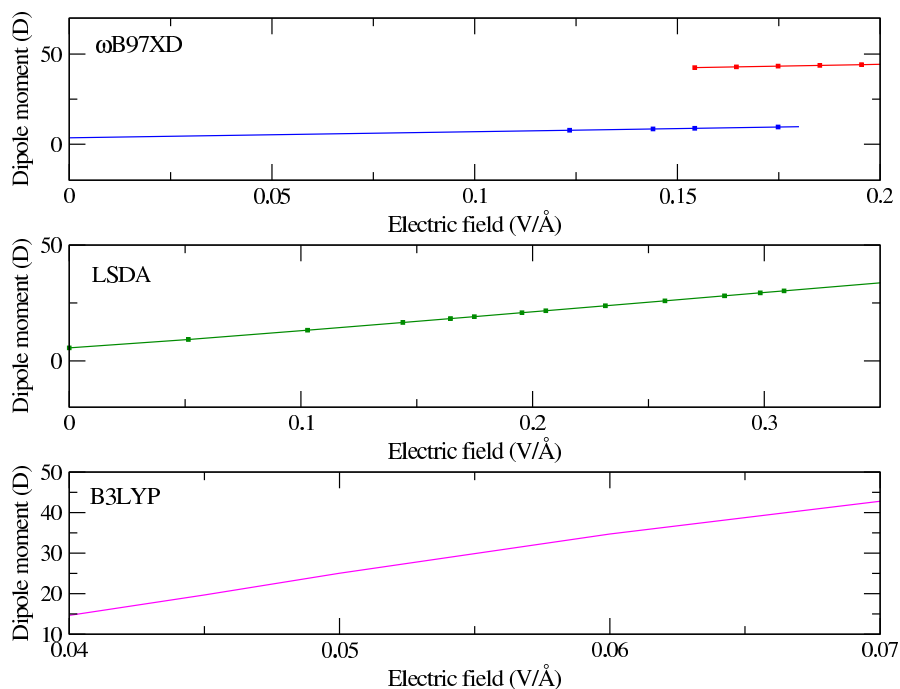
FIGURE 3.15: *Electric field-dependence of the dipole moment (x-component) calculated for Fc-PTM (crystal geometry) at UωB97XD/6-31+G* distinguishing N and I regimes (see text, top panel), at ULSDA/6-31G* (central panel) and at UB3LYP/6-31G* (bottom panel); all calculations are performed in gas phase.*

[144]. As expected according to Geskin *et al.*, the resulting picture (see bottom panel of Figure 3.15) does not change if UB3LYP functional is considered [144]. Such results seem to confirm our assumption pointing out a weakness of functionals including long-range corrections in CT processes. The limitations of DFT in a *closed shell* description of a step like one-electron jump in a D-π-A in presence of an electric field are well-known but to the best of our knowledge there is no systematic investigation by a spin polarized approach of open-shell systems; in this context, the relevant results seem to highlight that previous limitations of DFT are extended also to the description of CT in radical systems by means of spin polarized hybrid functionals. In addition, further doubts regarding DFT reliability are suggested by results with PCM. In fact, based on physical considerations, the zwitterionic state is expected to be stabilized in solution, even in a non-polar solvent, so that the transition from N to Z state is expected to occur at lower fields in solution with respect to the gas phase. This is not true for UCAM-B3LYP and therefore DFT results with PCM are rejected.

Finally, in Figure 3.14, the evolution of ground state energy in presence of an external field is collected. Firstly, in all levels of theory, we observe a steeper $E(F)$ dependence in the Z regime in comparison with the N region, in line with an increasing of the permanent dipole moment in Z state ($E \sim -\mu_Z$). Then, in both functionals at DFT level, we assist to an unexpected destabilization of ground state energy moving from the

N to the Z region equal to ~ 1 eV; at variance, the curve at PM7 clearly points out that the driving force of CT is a stabilization of the energy by an amount of ~ 1.6 eV. These results put doubts on the reliability of DFT method to describe ground-state properties of CT systems.

3.3.1.1 Comparison with essential-state models

We now discuss how essential-state model parameters can be extracted from the μ_F curves. The first point is that essential-state models only account for CT degrees of freedom, so they do not account for the polarizability associated with electrons not involved in CT. This means that the polarizability of the system at $\rho=0$ or 1 vanishes, or, in other terms the two plateaux in the $\mu(F)$ curve are expected to have zero slope. Therefore, in order to compare with essential-state model, the first step is to get rid of the intrinsic (non-CT) polarizability. To do that we subtract to each curves in Figure 3.18 a straight line $y=bx$, with adjusted b for each curve as to obtain flat plateaux (or the best approximation to flat plateaux).

Another correction to the calculated curves concerns the value of the dipole moment in the N state. In the essential-state model it is zero, so we subtract a constant value to each previous curve as to have $\mu=0$ in the N plateau. Moreover, remembering that μ_0 is the dipole moment of the zwitterionic state, we have now its estimate as the μ value in the second plateau. Since in the essential-state model $\mu = \rho\mu_0$, we are now in the position of extracting $\rho(F)$ curves from the $\mu(F)$ data. Results are shown in Figure 3.16, where, for the sake of clarity, also the optimized a and b values, and the μ_0 estimates are shown.

As discussed in Chapter I, the *two-state model* gives closed expressions for the ρ dependence of z, where $2z$ is the energy that separates the Z from N state. In the presence of an applied field, $2z$ becomes an effective value that linearly depends on the field. The basic equations are:

$$\rho = \frac{1}{2}\left(1 - \frac{z_{eff}}{\sqrt{z_{eff}^2 + \tau^2}}\right) \tag{3.1}$$

and

$$z_{eff} = z_0 - \frac{F\mu_0}{2} \tag{3.2}$$

All parameters have to be expressed in SI. Since F is expressed in V/Å(10^{10} V/m), μ_0 in D ($3.336\cdot10^{-30}$ C·m), we have to multiply $F\mu_0$ times 0.2097 to express it in eV. We finally fit the $\rho(F)$ curves using the above equations to extract z_0 and τ.

Results are collected in Table 3.8.
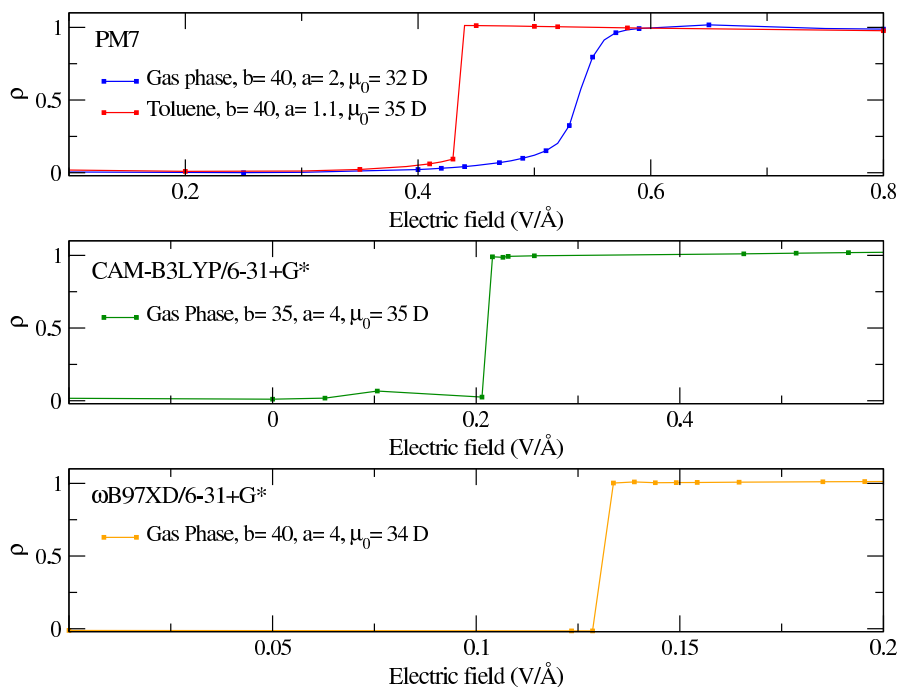
FIGURE 3.16: *The degree of ionicity dependence of external electric field in Fc-PTM at PM7, UCAMB3LYP/6-31+G* and at UωB97XD/6-31+G* in gas phase; at PM7 also results in solution are reported.*

TABLE 3.8: *Two-state model parameters extracted from PM7 calculations for Fc-PTM at fixed geometry; all energies except ω_{CT} (cm^{-1}) are in eV; dipole moments are in D;*

					Calc. properties		
		z	τ	μ_0	ρ	ω_{CT}	μ_{CT}
PM7	vacuo	1.79	0.06	32	0.0003	24202	0.55
	sol.	1.56	0.02	35	0.00004	28472	0.55
UCAMB3LYP	vacuo	0.76	0.02	32	0.0002	11533	0.50
$U\omega$B97XD	vacuo	0.47	0.01	34	0.0001	8065	0.34

(header spanning: "Two-state model")

All levels of theory, and especially DFT, underestimate by one order of magnitude the hopping integral respect to experimental estimates (see Table 3.6). This fact leads, as shown in Table 3.8, to a largely neutral dye and therefore to an almost forbidden CT band, clearly in contrast with experimental data. The z values are grossly overestimated in PM7 and more reasonable in DFT, but with a large dependence on the functional. These results are somewhat disappointing, so we tried to see if a more detailed essential-state model could better reconcile with DFT or PM7. Indeed Grisanti *el al.* showed that a better description of optical spectra of Fc-PTM and related systems can be obtained using a *three-state model*, also accounting for the role of the bridge in the CT process [137]. Therefore we fitted $\mu(F)$ based on the three-state model, as briefly described above. Relevant parameters are collected in Table 3.9.

TABLE 3.9: *Three-state model parameters extracted from PM7 calculations for Fc-PTM at fixed geometry; all parameters except $\mu(D)$ are in eV;*

		Three-state model				
		z_0	x_0	τ	τ'	μ_0
PM7	vacuo	1.79	1.85	0.35	0.35	32
	sol.	1.58	1.68	0.2	0.2	35
UCAMB3LYP	vacuo	0.77	0.87	0.16	0.16	35
$U\omega$B97XD	vacuo	0.45	0.7	0.12	0.12	33

The τ value are somewhat better than in the two-state model, and for PM7 are almost good; but, much as with the two-state model, z (and x) values are largely overestimated by PM7 and largely functional-dependent in DFT. So we conclude that a reliable estimate of essential-state model parameters cannot be obtained along these lines.

3.3.2   The case of TTF-PTM and MPTTF-PTM

For the sake of completeness we also addressed TTF-PTM and MPTTF-PTM. Semiempirical calculations with PM7 (MOPAC [112, 113]) have been performed in gas phase on TTF-PTM and MPTTF-PTM at fixed geometry as well as optimizing geometry at each F value. Since for TTF-PTM the crystallographic structure is not available, for both compounds the optimized geometry in gas phase at UCAMB3LYP/6-31G* is considered. All calculations are performed in presence of an external electric field applied along x-axis as shown in Figure 3.17.
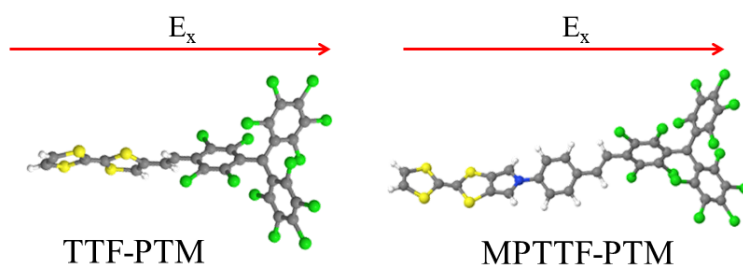
FIGURE 3.17: *The external electric field is applied along x-axis, corresponding to the axis connecting TTF(MPTTF) to PTM.*

Figure 3.18 shows the F-dependence of the x-component of the dipole moment at fixed and at optimized geometry, respectively, for both compounds at PM7.

All curves $\mu(F)$ show the characteristic S-shape and as expected in presence of *e-ph* coupling, the curve obtained optimizing geometry is less smoother than the other. According to the procedure described in the previous Section, from the $\mu(F)$ we can derive $\rho(F)$ and
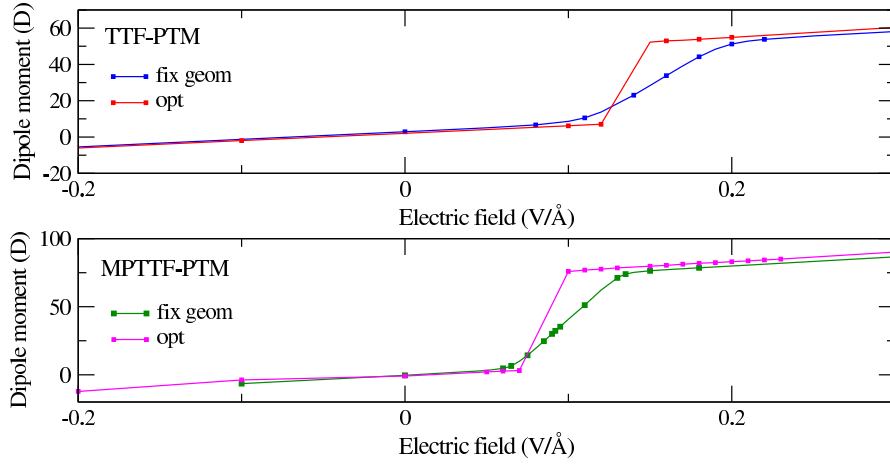
FIGURE 3.18: *Electric field-dependence of the dipole moment (x-component) calculated for TTF-PTM and for MPTTF-PTM at PM7 at fixed geometry and at optimized geometry, both in vacuo.*

its fit through essential-state models. Fit parameters through two- and three-essential states are collected in Tables 3.10 and 3.11, respectively.

TABLE 3.10: *Two-state model parameters extracted from PM7 calculations for TTF-PTM and MPTTF-PTM at fixed as well as at optimized geometry; all energies except ω_{CT} (cm^{-1}) are in eV; dipole moments are in D;*

Two-state model							
					Calc. properties		
System	*geom.*	z	τ	μ_0	ρ	ω_{CT}	μ_{CT}
TTF-PTM	fixed	0.68	0.17	43	0.014	11691	5
	opt.	0.63	0.06	44.5			
MPTTF-PTM	fixed	0.68	0.21	67	0.022	11547	9.8
	opt.	0.58	0.11	69	0.009		

TABLE 3.11: *Three-state model parameters extracted from PM7 calculations for TTF-PTM and MPTTF-PTM at fixed geometry as well as at optimized geometry; all energies are in eV; dipole moments are in D;*

Three-state model						
System	*geom*	z	x	τ	τ'	μ_0
TTF-PTM	fixed	0.68	0.99	0.42	0.42	43
	opt.	0.63	0.65	0.21	0.21	44.5
MPTTF-PTM	fixed	0.68	0.92	0.48	0.48	67
	opt.	0.58	0.62	0.28	0.28	69

The $\rho(F)$ dependence computed at fixed geometry as well as at optimized geometry offer the opportunity to estimate the small polaron binding energy, ε_{sp}; specifically, in the

two-state model we can write z_{eff} as:

$$z_{eff} = z_0 + \mu_0 \frac{F}{2} - \varepsilon_{sp} \qquad (3.3)$$

and we fit the curve $\mu(F)$ obtained optimizing the geometry through the parameters estimated at fixed geometry (see Table 3.10) changing ε_{sp}, in according with eqs. 3.1 and 3.3. Following this procedure, as expected on physical basis, we get a slightly larger relaxation energy for MPTTF-PMT respect with the shorter dye; specifically, we estimate ε_{sp} equal to 0.32 eV and 0.28 for MPTTF-PTM and TTF-PTM, respectively.

3.4   The work function change

Self-assembled monolayers (SAMs) of organothiolate molecules on gold substrate are studied for a wide range of applications, such as supramolecular assembly, biosensors, molecular electronics and microelectronic devices. Two decades ago, Evans and Ulman suggested SAMs to improve charge-injection processes by modulating the work function of the electrodes [146, 147]. A large number of experimental studies have confirmed this early theoretical prediction and have demonstrated that dipolar organic monolayers covalently linked on metal surfaces effectively modulate the work function, opening a way to lower the energy barrier for charge injection and increasing the device performance [148–150].

D. Morales in Veciana's group has investigated the influence of D-π-R$^{\cdot}$-based SAM on the modification of work function of a gold substrate through Kelvin Probe Force Microscopy (KPFM). 5-(1,2-dithiolan-3-yl)pentanoate of Fc-PTM has been extensively characterized in comparison with its hydrogenated counterpart, Fc-PTMH and with SAM with only ferrocene moiety (5-(1,2-dithiolan-3-yl)
pentanoate of Fc). The three different SAMs are shown in Figure 3.19.

Here we report results of semiempirical calculations to address the modification of the work function of the three relevant SAMs in order to rationalize the complex experimental results.

3.4.1   Kelvin Probe Force Microscopy

Kelvin probe force microscopy (KPFM) measures the local contact potential difference (CPD) between a conducting atomic force microscopy (AFM) tip and a sample, related to the charge distribution on a surface, mapping the surface potential of the sample with high spatial resolution. Since its first introduction by Nonnenmacher *et al.* in 1991 [151],
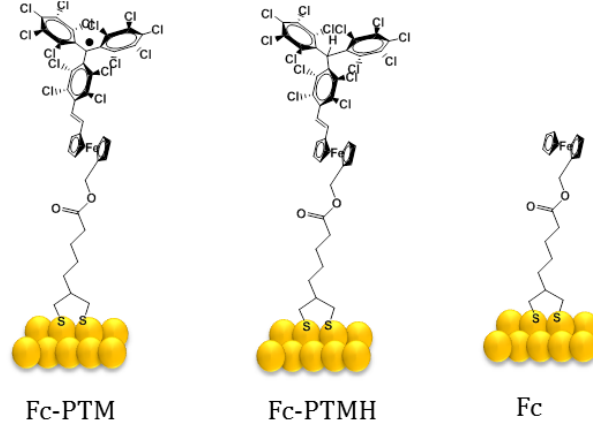
FIGURE 3.19: *Schematic representation of the three monolayers studied.*

KPFM has been used extensively to characterize the nano-scale electronic/electrical properties of metal/semiconductor surfaces and semiconductor devices.

All measurements were done in Barcelona under a continuous flow of anhydrous nitrogen at room temperature, taking as reference the unmodified silicon oxide surface. The variation of CPD of the sample respect to gold (CPD_{SAM-Au}) is measured as:

$$CPD_{SAM-Au} = CPD_{SAM-SiO_2} - CPD_{Au-SiO_2} \qquad (3.4)$$

where $CPD_{SAM-SiO_2}$ and CPD_{Au-SiO_2} are the difference contact potential between SAM-SiO$_2$ and between Au-SiO$_2$. By knowing the CPD_{SAM-Au}, the variation of work function can be easily obtained as [152]:

$$\Delta\Phi = -CPD_{SAM-Au} \qquad (3.5)$$

Table 3.12 shows experimental results obtained for the SAMs under investigation.

TABLE 3.12: *Variation of work function of D-R˙ monolayers;*

System	$\Delta\Phi$ (mV)
Fc-PTM	20
Fc-PTMH	55
Fc	-400

Two different dipoles contribute to the total dipole moment. The first one is related to the formation of the thiolate-Au bond (Au$^{+\delta}$ - S$^{-\delta}$) leading to a net dipole moment at the Au/monolayer interface with its permanent component perpendicular to the surface. The second (and usual dominant) contribution corresponds to the intrinsic dipole moment of the molecule.

A negative $\Delta\Phi$ implies that the CPD measured for the SAM is larger than for the bare gold and implies that the presence of the SAM favors the electron transfer from the KPFM tip towards the surface. This is expected when negative charges are lying close to the surface (see Figure 3.20). By contrast, SAMs of molecules oriented with the negative pole at surface/air interface, increase the work function of the metal [152] (see Figure 3.20). This intuitive picture is confirmed by recent results on fluorinated monolayers [152].
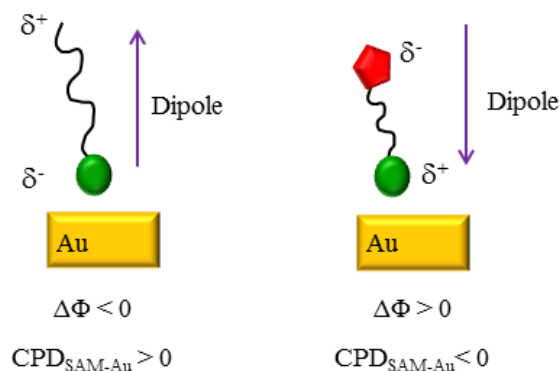
FIGURE 3.20: *Schematic representation of the two different cases of the direction of the intrinsic molecular dipole moment and its relation with the sign of work function change.*

It is important to stress that several factors can affect the direct correlation between the molecular dipole moment and the SAM-induced $\Delta\Phi$:

- the chemical substrate-molecule bonding induces a substantial charge rearrangement;

- structural reorganizations such as dimerization of the molecules, that reduces the monolayer dipole moment, or depolarization of the dipoles due to the neighboring polar molecules;

- significant charge transfer between substrate and SAM, as observed in Ref. [153].

The large negative $\Delta\Phi$ measured for Fc is in line with the presence of a partial positive charge on the Fc unit, a good electron-donor. When decorating the Fc with a strong acceptor like PTM we do expect the presence of a partial negative charge on it, explaining the reversed sign of $\Delta\Phi$. What is more difficult to understand is the behavior of Fc-PTMH, since the PTMH is not an electron acceptor.

3.4.2 The Helmholtz equation for the work function

The relationship between the work-function modification of the electrode and, the chemical nature of the molecular SAM adsorbed on its surface is generally described on the basis of electrostatic considerations by using the Helmholtz equation [154]:

$$\Delta\Phi = -\frac{\mu_\perp}{4\pi\varepsilon_0\varepsilon^{eff}A} \tag{3.6}$$

where $\mu_\perp$ is the dipole moment perpendicular to the surface; ε_0 (Faraday/m) is the vacuum permittivity, ε^{eff} is the effective dielectric constant and A (m^2) is the area density of dipoles on the surface. The ratio $\mu_\perp/\varepsilon^{eff}$ represents the effective perpendicular component of dipole moment in the isolated molecules; actually, as already explained, the total dipole moment could be considered as formed by the contribution of two internal dipoles: the effective dipole moment of the monolayer and the effective intrinsic Au-S dipole. Since the effective Au-S dipole is assumed to be almost independent of the alkane chain length and composition, but strongly dependent on the nature of the metal, it is reasonably considered as a constant. Therefore, following De Boer *et al.*, $\mu_\perp$ corresponds to the perpendicular dipole moment for unbound, isolated molecules with a thiol end group [155].

The dimensionless ε^{eff} value is introduced to take into account the effect of the densely packed layers on the $\mu_\perp$ and its values have typically been estimated to lie between 2 and 3 [149, 154]. According to Romaner *et al.*, the electrostatic expression of ε^{eff} reads [154]:

$$\varepsilon^{eff} = 1 + \frac{\alpha}{4\pi\varepsilon_0}FA^{-\frac{3}{2}} \tag{3.7}$$

where, α is the molecular polarizability (SI units, Cm^2V^{-1}) and F is a factor characteristic of the geometry of the dipole lattice. F has been calculated by Topping for two different packing geometries; hexagonal packing has F equal to 8.892, while cubic packing is 9.0336 [156]. For the sake of simplicity we will set $F=9$ in the following.

To use eq. 3.6, we calculate, for the three molecular structures shown in Figure 3.19, $\mu_\perp$ and α. All calculations refer to gas phase, with geometries optimized at the UCAMB3LYP/6-31G* level. Optimized geometries along the cartesian coordinates are reported in Figure 3.21 and an almost 0° dihedral angle between the 1,2-dithiolane and the alkyl chain is exhibited in all systems under investigation.

The perpendicular component of the dipole moment is evaluated assuming that in the self assembly the optimized molecules are oriented as to have the gold surface parallel to the y-axis, as shown in Figure 4.10; for this assumed orientation, the perpendicular component (μ_x) was computed at PM7 in gas phase. The polarizability was estimated
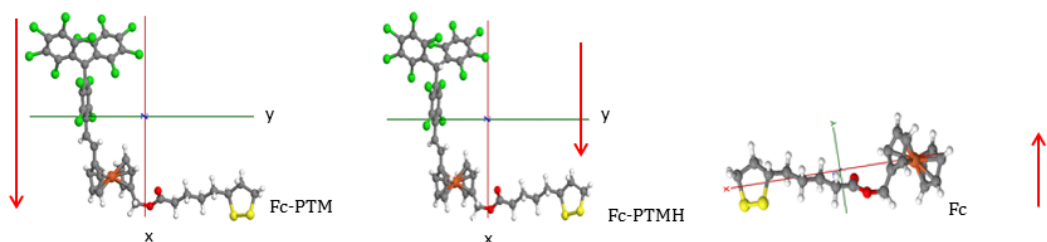
FIGURE 3.21: *Chemical structure of Fc-PTM, Fc-PTM-H and Fc- linked to disulfide-alkyl chain optimized at (U)CAM-B3LYP/6-31+G* level of theory in gas phase along the three cartesian coordinates; we assume that in the formation of SAM, optimized molecules maintain this orientation and gold surface is parallel to y axis; the red arrow indicates the direction of μ_x dipole moment.*

through numerical differentiation of the perpendicular dipole moment and hence PM7 calculations in gas phase at fixed optimized geometry are carried out in presence of an external electric field. The perpendicular component of the dipole moment and the polarizability are reported in Table 3.13

TABLE 3.13: *Perpendicular component and module of the dipole moment and polarizability;*

System	μ_x (D)	$|\mu|$ (D)	α (10^{-24}cm^3)
Fc-PTM	-1.165	1.987	113
Fc-PTMH	-1.201	1.832	99
Fc	1.590	1.920	6

Having obtained μ_x and α values from semiempirical calculations on the isolated species in Figure 4.10, we need an estimate for the average area. A first estimate can be obtained from geometry calculations, estimating the area of the terminal group at the SAM-surface. We have estimated for Fc a rectangular basis of dimension 10.46 x 6.24 $\mathring{A}^2$, and for PTM-based system 4.36 x 3.26 $\mathring{A}^2$. A second estimate of the area can be obtained from the experimental value of the surface charge density, Γ, according to the expression:

$$A(nm^2/molec) = 10^{16}/(N_A\Gamma) \tag{3.8}$$

where N_A is the Number of Avogadro and Γ is evaluated experimentally through cyclic voltammetry, as summarized in Table 3.14. Both estimates are affected by large errors, so that only the order of magnitude is relevant. By the way, the calculated $\Delta\Phi$ is only marginally affected by the adopted A value (see Table 3.15).

Table 3.15 collects the main results of this Section, with the estimated ε_{eff} (eq. 3.7) and $\Delta\Phi$ (eq 3.6) for the three investigated systems. Results obtained with the two different A values, as discussed above, are shown.

TABLE 3.14: *The average area estimated from calculations (A_{calc}) and from experiments (A_{exp}) for the three systems;*

System	A_{exp} (nm^2/molec)	A_{calc} (nm^2/molec)
Fc-PTM	1.30	0.652
Fc-PTMH	0.51	0.662
Fc	-	0.143

TABLE 3.15: *ε_{eff} and $\Delta\Phi_{calc}$ calculated for Fc-PTM,Fc-PTMH and Fc in comparison with $\Delta\Phi_{exp}$ for both the two estimations of area; A is (nm^2/molec) and $\Delta\Phi$ is in mV;*

System		A	ε_{eff}	$\Delta\Phi_{calc}$	$\Delta\Phi_{exp}$
Fc-PTM	Exp.	1.30	1.68	16	20
	Cal.	0.652	2.93	18	
Fc-PTMH	Exp.	0.510	3.45	20	55
	Cal.	0.662	2.67	20	
Fc	Cal.	0.143	2	-167	-400

In PTM-based systems, irrespective of the A value adopted, ε_{eff} is always smaller than 3, in agreement with previous results [149, 154]. The proposed treatment is extremely simple, however, semiempirical calculations on gas-phase molecules allow to understand the different sign of $\Delta\Phi$ for the Fc-SAM if compared with the PTM-decorated SAM. Fc-PTMH-based SAM has a similar response (and possibly a slightly larger response) than Fc-PTM-SAM, in agreement with a very similar dipole moment for the two structures.

3.5 Conclusion

In this Chapter we have theoretically investigated different D-π-R$^{.}$ systems with different donors. The low-energy photophysics of such materials is governed by a CT between D and R$^{.}$ and therefore the essential-state models could be applied. However for such systems, the small ionicities and/or small delocalization leads to weak CT bands, making difficult the parametrization of the essential-state model from optical spectra. In this context, in the first part of the Chapter, we have proposed two strategies to attack the problem of *intramolecular charge transfer* in such materials by means of quantum-chemical calculations as well as semiempirical methods with the aim to identify a reliable alternative for the parameterization of essential-state models respect to the usual parameterization against optical spectra. The first strategy relies on calculated CT transitions through TD-DFT and ZINDO. However, we have demonstrated that TD-DFT fails due to its intrinsic weakness in the treatment of charge-transfer transitions [138–140], in particular in push-pull chromophores [141], and to its intrinsic difficulties to treat excited states of open-shell ground states [142]. At variance, we have shown that ZINDO results

lead to more reasonable estimates of essential-state model parameters, giving an overall picture consistent with experimental evidences. In the second strategy, essential-state model parameters are extracted from ground state properties. More precisely, we have triggered the CT process applying an electric field as to drive D-π-R˙ from the neutral (N) to the zwitterionic (Z) state. We have demonstrated that spin polarized hybrid functionals in the DFT machinery perform poorly on the description of ground-state properties of open-shell CT dyes.

In the second part of the Chapter, we have presented a theoretical investigation of the work function modification of a gold substrate induced by the presence of SAM based on D-π-R˙ or on its hydrogenated counterpart or based just on the D group. Experimental results can be satisfactorily reproduced based on simple model only relying on gas phase calculations for isolated molecules.

Chapter 4

Spectral properties of organic radical-based nanocrystals

Observations always involve theory

-Edwin Hubble

4.1 Introduction

In Chapter III we have introduced organic radicals as acceptor building block for obtaining multifunctional molecular materials. In this Chapter, we focus on optical properties of PTM (already introduced in Chapter III) and TTM, trichlorotriphenylmethyl radical, both shown in Figure 4.1.
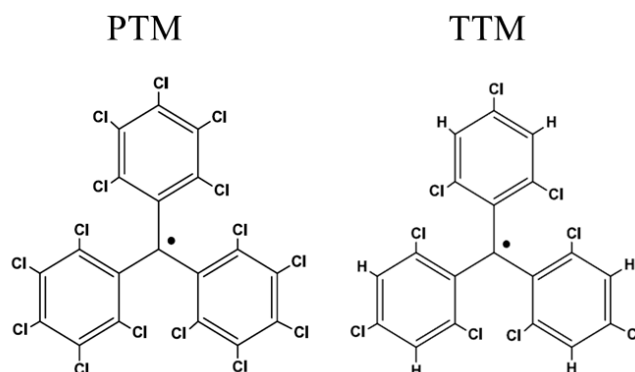

FIGURE 4.1: *Chemical structures of PTM and TTM.*

These neutral organic radicals show magnetic properties by interactions of unpaired electrons and large first-order hyperpolarizabilities due to the presence of accessible low-lying electronic states [157]. The possibility to combine the intrinsic magnetic characteristics with conducting or electrochemical properties make such materials nice examples of multifunctional molecular material and therefore good candidates for memory or spintronics devices or for optical rectification. TTM and PTM are very promising also in the field of bio-imaging. Indeed, the linear absorption spectrum of PTM and TTM exhibits two main bands (see Figure 4.2): a very intense transition at 380 nm and a weaker transition at 540 nm, while their emission spectrum is dominated by a weak broad band in the region 560-700 nm; in addition, both compounds show a TPA band at around 840 nm (see Figure 4.3). The large Stokes shift and the emission band in the region close to the *transparency biological window* (700-1500 nm) are non-trivial features in common closed-shell organic dyes and make these dyes interesting for two-photon microscopy. Two-photon excitation microscopy offers several advantages with respect to standard microscopy, based on one-photon absorption, including highly spatially confined excitation and three-dimensional resolution. Moreover, the energy of the photons used in TPA are half the energy of the photon used in OPA, reducing photodamage and more easily approaching the transparency window as to reduce scattering as well as background fluorescence. While PTM and TTM are promising in this respect, their fluorescence quantum yield must be improved for bioimaging applications.
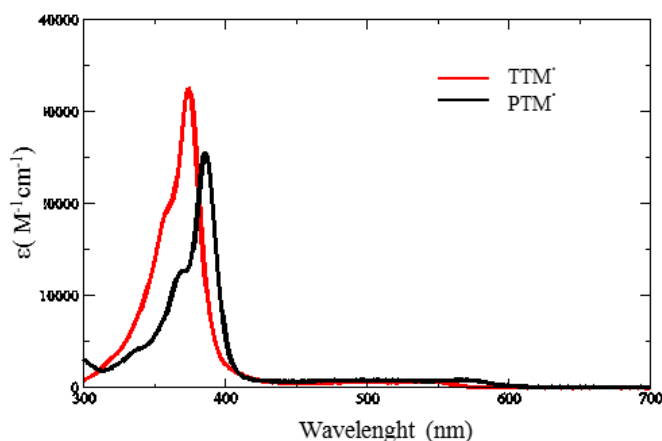
FIGURE 4.2: *Absorption spectrum of TTM and PTM in THF; UV-Vis absorption spectra were recorded on a Perkin Elmer Lambda 650 Spectrometer.*

D. M. Nikolaidau and Prof. F. Terenziani, in collaboration with Dr. Imma Ratera and D. Blasi from ICMAB, Barcelona, tried different strategies to improve the luminescence of PTM and TTM radicals. Firstly, they have investigated the effects induced by different solvents and by temperature. As shown in Figure 4.4, the rigidity of the medium leads to enormous enhancement of fluorescence, increasing, for instance, in TTM from
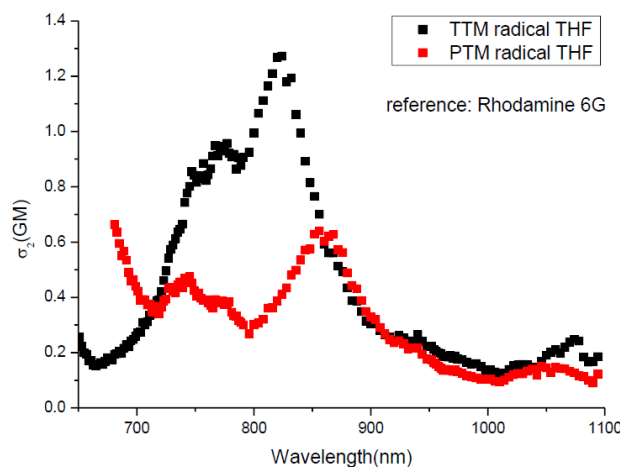
FIGURE 4.3: *Two-photon excited absorption action cross section of TTM and PTM in THF; measurements are collected in the laboratory directed by Prof. E. Vauthey (Geneva University).*

2% to 77% in THF at 77K.
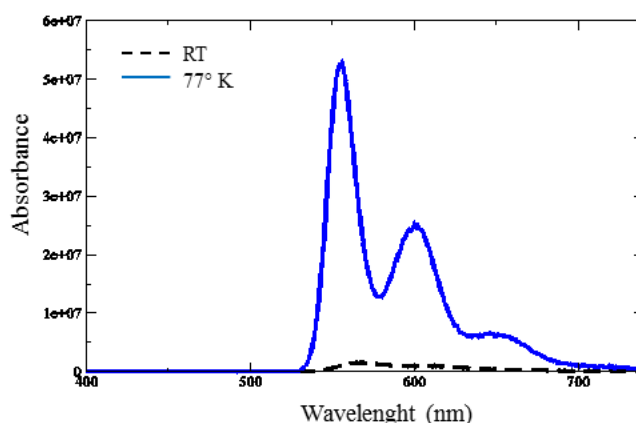
FIGURE 4.4: *Fluorescence spectrum of TTM in THF at room temperature and at 77 K in THF.*

Then, they have investigated nanoparticles behavior. Particularly interesting results are observed for nanoparticles obtained by coprecipitating PTM and TTM species with a second *diluting* optically-neutral organic species (TTM-αH). The spectral properties of nanoparticles are reported in Figure 4.5. The composite organic nanoparticles are highly luminescent and, as shown in Figure 4.5, when increasing the radical amount, a second, red-shifted emission band is obtained, characterized by long lifetime, while the overall luminescence intensity decreases. The absence of changes in the absorption spectrum suggests that this interesting phenomenon only involves excited molecules. These experimental evidences, combined with the dependence on TTM concentration, suggest the formation of multiplet *excimers* in the nanoparticles. The relevant phenomenon is less

ONPs TTM-αH: TTM

ONPs TTM-αH: PTM
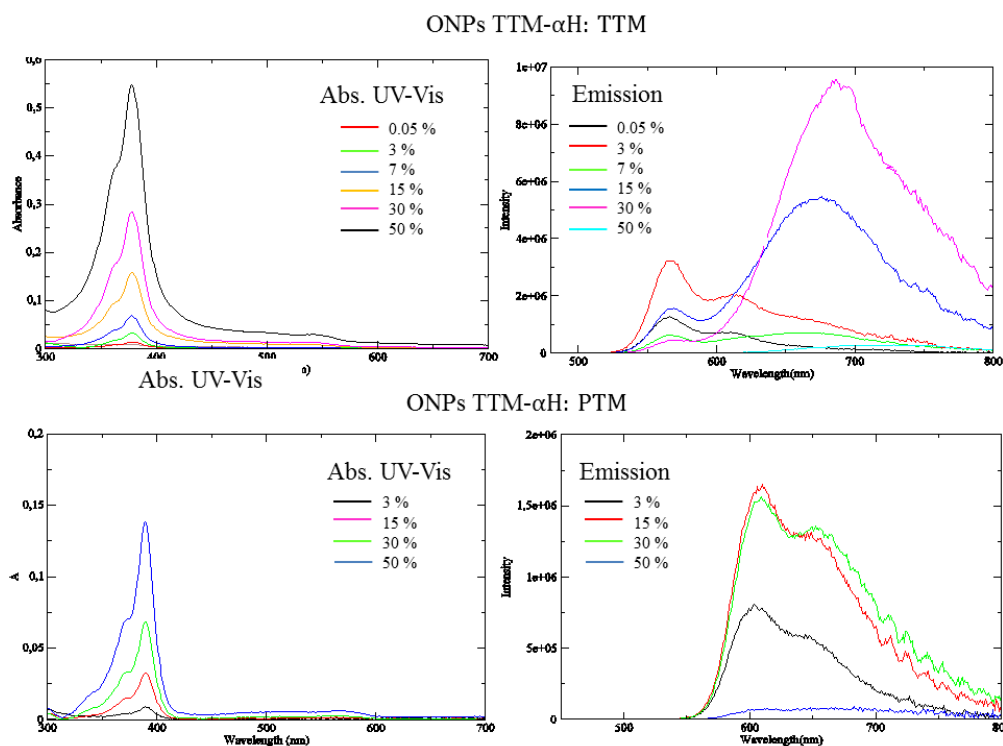
FIGURE 4.5: *Top panels: absorption and emission spectra (λ_{exc}=378 nm) of composite purely organic nanoparticles composed by TTM-αH and TTM with different percentage. Bottom panels: absorption and emission spectra (λ_{exc}=389 nm) of composite purely organic nanoparticles composed by TTM-αH and PTM with different percentage.*

evident in composite organic nanoparticles based on radical PTM and TTM-αH and appears for higher radical amount in comparison with TTM counterpart.

An *excimer* is defined as a complex between two molecules that is stable *only* in the excited state [158]. Pyrene was the first aromatic molecule shown to form excimers in solution, the key observations being the appearance of a red-shifted structurless emission band as a function of pyrene concentration, but with no corresponding changes in the absorption spectrum [159].

In order to understand these intriguing experimental data, theoretical calculations are required. Usually, a potential energy surface involving the ground and the lowest excited state of the relevant molecule as a function of intermonomer separation is invoked to explain this phenomenon [158, 160] as reported in Figure 4.6. The main arguments are as follows. The first step is the excitation of the monomer to its lowest excited singlet state. This is followed by an attractive collision with a ground state monomer and the formation of a bound excited state complex or excimer. Since the interaction is attractive, the energy of the excimer is lower than that of the excited monomer. When the excimer emits a photon to return to the ground state, it is generally believed that the two monomers, at this short distance apart, are in a repulsive portion of the

potential energy curve. As a result, the two ground state monomers rapidly dissociate before the complex can undergo a single vibrational period, resulting in a broad emission bandshape.
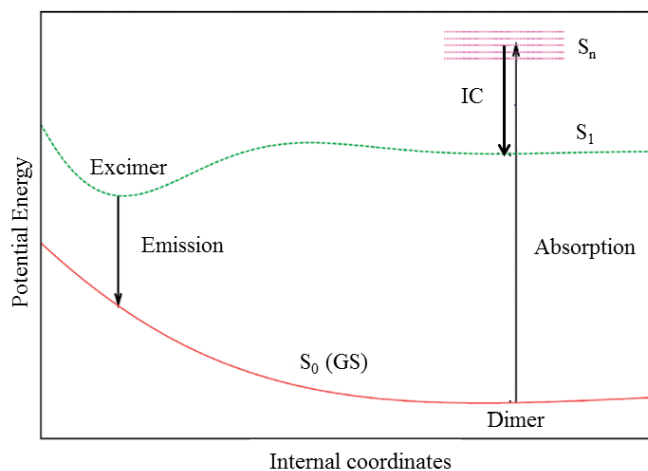
FIGURE 4.6: *Schematic diagram of the relationship between a dimer in the ground state (S_0) and an excimer in the excited state. IC denotes internal conversion from higher singlet excited states (S_n) to the lowest one (S_1).*

However, only few theoretical studies on excimers have been published and they are limited to relatively simple organic molecular systems such as benzene or naphthalene dimers because of the computational cost of excited state calculations involving dimers. Then, most of the investigations rely on semiempirical and TD-DFT methods. In addition, to the best of our knowledge, no theoretical studies on excimers formation involving open-shell systems have been reported.

In this Chapter, TDDFT is adopted to investigate the excited states of open-shell system TTM. Since crystallographic structure is available, we focus on the description of the monomer at crystal geometry and at its optimized ground and lowest-excited state. From the crystal structure we extract a dimeric unit (on the basis of the shortest interplanar and interatomic distances) and, keeping the dimer structure frozen, we evaluate the possibility to the formation of an excimer building the PES for the ground and the lowest excited state. Finally, following Kim D. and J.L. Brédas, we attempted to do a complete optimization of the lowest excited state in the selected dimer unit to compare it with the emission of the monomer [161].

4.2   Quantum-chemical calculations on the monomer

Calculations are performed using the same basis set 6-31+G* but different functionals: CAM-B3LYP, ωB97XD and B3LYP (Gaussian 09 package [114]). CAM-B3LYP was recently shown to be preferable to other functionals, for TD-DFT calculations of excitation energies [138]. By contrast, B3LYP functional has been selected since is more reliable in term of energetics and is suggested to treat excimer interactions [158]. On the other hand, ωB97XD is able to include long range interactions. Finally, to better understand the photophysical (excitation/emission) properties of the system under investigation, we also study the spin density.

4.2.1   Crystallographic geometry

The crystallographic unit for TTM unit is shown in Figure 4.7.
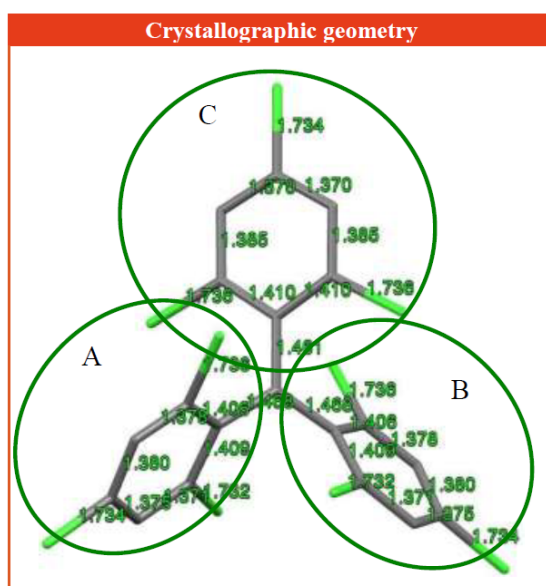
FIGURE 4.7: *Crystallographic structure of TTM; green circles corresponding to A, B and C show the three different fragments;*

In Figure 4.8 frontier MOs for the isolated TTM in the crystallographic geometry are shown; molecular orbitals in the relevant states are qualitatively similar at all different levels of theory in exam. The SOMO (Singly Occupied Molecular Orbital) is delocalized onto aromatic rings and radical carbon and it is similar to SUMO but with a smaller contribute on the radical carbon. HOMO is substantially delocalized on two phenyl groups and LUMO is the corresponding antibonding orbital. Interesting, HOMO-1 is *quasi* degenerate with HOMO.
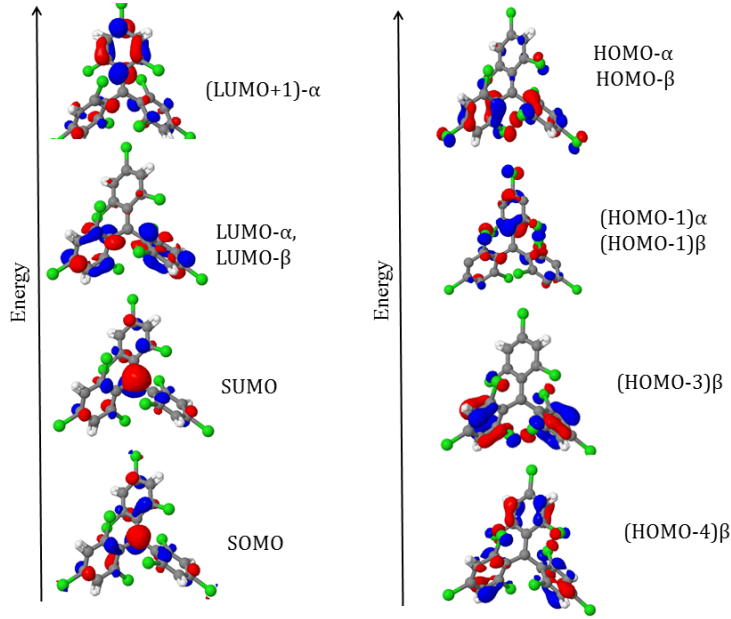
FIGURE 4.8: *Molecular orbitals of TTM radical in ground state at UωB97XD/6-31+G*, UCAMB3LYP/6-31+G* and UB3LYP/6-31+G* at crystallographic structure.*

In Table 4.1, the calculated results for the lowest energy transitions with oscillator strength and wavefunctions are summarized.

TABLE 4.1: *Calculated excited states at TD-UωB97XD, TD-UCAMB3LYP and TD-UB3LYP with 6-31+G* basis set in gas phase assigned to experimental transitions;*

Level of theory	Transition	λ (nm)	f	Transition nature
TD-UωB97XD	S0⟶S1	422 nm	0.009	HOMO-β ⟶SUMO (0.77)
	S0⟶S2	421 nm	0.015	(HOMO-1)β ⟶SUMO (0.76)
	S0⟶S7	332 nm	0.152	(HOMO-4)β ⟶SUMO (0.59)
				SOMO⟶LUMO-α (0.49)
	S0⟶S8	329 nm	0.169	(HOMO-3)β ⟶SUMO (0.55)
				SOMO⟶(LUMO+1)α (0.47)
TD-UCAMB3LYP	S0⟶S1	433 nm	0.007	HOMO-β ⟶SUMO (0.72)
	S0⟶S2	432 nm	0.012	(HOMO-1)β ⟶SUMO (0.73)
	S0⟶S7	335 nm	0.125	(HOMO-4)β ⟶SUMO (0.68)
				SOMO⟶LUMO-α (0.36)
	S0⟶S8	333 nm	0.14	(HOMO-3)β ⟶SUMO (0.66)
				SOMO⟶(LUMO+1)α (0.34)
TD-UB3LYP	S0⟶S1	477 nm	0.020	HOMO-β ⟶SUMO (0.92)
	S0⟶S2	475 nm	0.028	(HOMO-1)β ⟶SUMO (0.92)
	S0⟶S7	377 nm	0.161	SOMO⟶LUMO-α (0.83)
	S0⟶S8	368 nm	0.184	SOMO⟶(LUMO+1)α (0.82)

TD-DFT calculations suggest that the band at lower energy (∼540 nm) can be assigned to the two first excited states characterized by a small oscillator strength and dominated by the transition HOMO-β ⟶SUMO and (HOMO-1)β ⟶SUMO, respectively. The band at higher energy (∼380 nm) can be assigned to the two transitions very close in

energy with a larger oscillator strength. Their wavefunctions are dominated by two configurations involving α and β molecular orbitals except for TD-UB3LYP/6-31+G*. The present assignment is supported by the agreement of the relative energy between the two transitions (0.81 eV, 0.84 eV, 0.73 eV for the three DFT functionals, respectively) with the experimental absorption spectra (0.99 eV). The relative oscillator strength is overestimated (0.075, 0.32, 0.14 for the three functionals, respectively) respect to experimental results (0.024). Our results are in line with those from Hattori *et al.* [162].

In the Figure 4.9, the spin density at ground state and at the lowest excited states is reported. The spin distribution in ground state is localized on the central carbon and on the phenyl groups in agreement with results in Chapter III and experimental data [162]. In the lowest excited state, the spin density moves mainly from A and B phenyl branches (see Figure 4.7 for the fragments) towards the TTM core, involving both radical carbon and α carbons of the relevant phenyl arms. By contrast, C fragment still presents a small amount of spin distribution. The charge distribution in ground and lowest excited state reflects spin distribution results, as shown in Table 4.2, where we can observe an increase of negative charge on the central carbon.
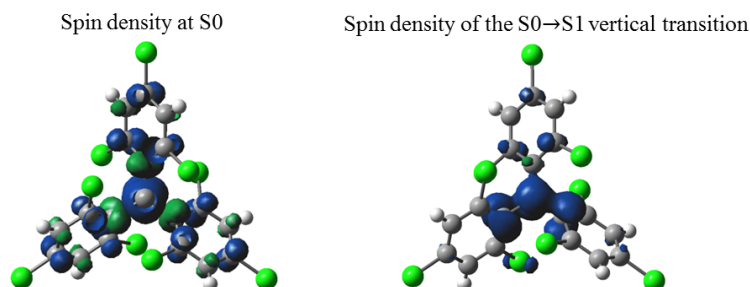
FIGURE 4.9: *Spin density of the radical in ground state and in the lowest excited state at crystallographic geometry; all levels of theory give same results.*

TABLE 4.2: *ESP (Electrostatic Potential) charges distribution in ground state and in S1 at crystallographic structure; A, B and C fragments are shown in Figure 4.7; 1 is referred to radical carbon;*

Fragment	Ground state	S0⟶S1
1	-1.25	-1.49
A	0.44	0.55
B	0.38	0.18
C	0.43	0.83

The picture presented above does not take into account the electron-phonon coupling, responsible for an equilibrium geometry in the lowest excited state different from that in the ground state. In order to evaluate emission properties, an optimization of the lowest excited state is needed.

4.2.2 Optimization of ground and excited states

In Figure 4.10, optimized ground and fluorescent geometry at
TD-ωB97XD/6-31+G*, TD-UCAMB3LYP/6-31+G* and TD-UB3LYP/6-31+G* are
shown. Between the two lowest *quasi* degenerate excited-states, optimization geometry has been successfully computed just for S1. In fact, after first steps, the S2 PES crosses the S1 PES. In all levels of theory, at optimized ground state, we assist just to a slight elongation of all bonds in comparison with crystallographic geometry. Moreover, molecular orbitals at optimized ground and excited state do not change in comparison with those at crystal structure.

FIGURE 4.10: *Optimized ground and fluorescence state geometry at all levels of theory investigated.*

Vertical transitions at optimized ground-state geometry are collected in Tables 4.3. As expected from previous considerations, the calculated absorption spectrum at this geometry do not differ significantly from that at crystal geometry: the oscillator strength is still concentrated in the transition to the degenerate S7 and S8 excited states and S1 and S2 still remain weak allowed (total oscillator strength for S7 and S8 $\sim$0.3 in all levels of theory in comparison with f shown in Table 4.3). In the relaxed excited state geometry the lowest excited state acquires some intensity, possibly explaining the experimental observation of enhanced emission in rigid environments where other decay mechanisms are hindered.

TABLE 4.3: *Vertical transition S0→S1, wavelength, wavefunction and oscillator strength at optimized ground state and excited state at TD-UωB97XD/6-31+G*, UCAM-B3LYP/6-31+G* and UB3LYP/6-31+G* in gas phase;*

	S0→S1 transition	
Level of theory	*Geometry: Opt S0*	*Geometry: Opt S1*
TD-UωB97XD	HOMO-β →SUMO	HOMO-β →SUMO
	λ= 418 nm	λ= 492 nm
	f= 0.0093	f= 0.019
TD-UCAMB3LYP	HOMO-β →SUMO	HOMO-β →SUMO
	λ= 428 nm	λ= 490 nm
	f= 0.0063	f= 0.014
TD-UB3LYP	HOMO-β →SUMO	HOMO-β →SUMO
	λ= 473 nm	λ= 551 nm
	f= 0.022	f= 0.028

By knowing the equilibrium structure of the ground and excited state we can estimate the Stokes shift (SS). Specifically, we determine the reorganization energies associated with relaxation in the ground and excited electronic states, within the adiabatic potential (AP) approach. The so obtained SS are listed in Table 4.4.

TABLE 4.4: *SS and vertical transition energies at optimized ground and excited state in comparison with experimental data (see Figure 4.4);*

Level of theory	*SS* (eV)	λ_{abs} (nm)	λ_{emi} (nm)
TD-Uωb97XD	0.44	418	492
TD-UCAMB3LYP	0.37	427	490
TD-UB3LYP	0.37	473	551
Exp	0.17	540	575

Experimental spectrum registered for a solution of TTM in CH_2Cl_2 reports a SS equal to 0.17 eV. Since calculated SS refers to a gas phase, we would expect a slightly underestimated SS. By contrast, TD-DFT calculations largely overestimate the SS: a value of 0.44 eV for ωB97XD and 0.37 eV for CAMB3LYP and B3LYP.

The spin distribution of the calculated relaxed excited state (see Figure 4.11) is substantially equivalent to that at crystallographic geometry (see Figure 4.9).
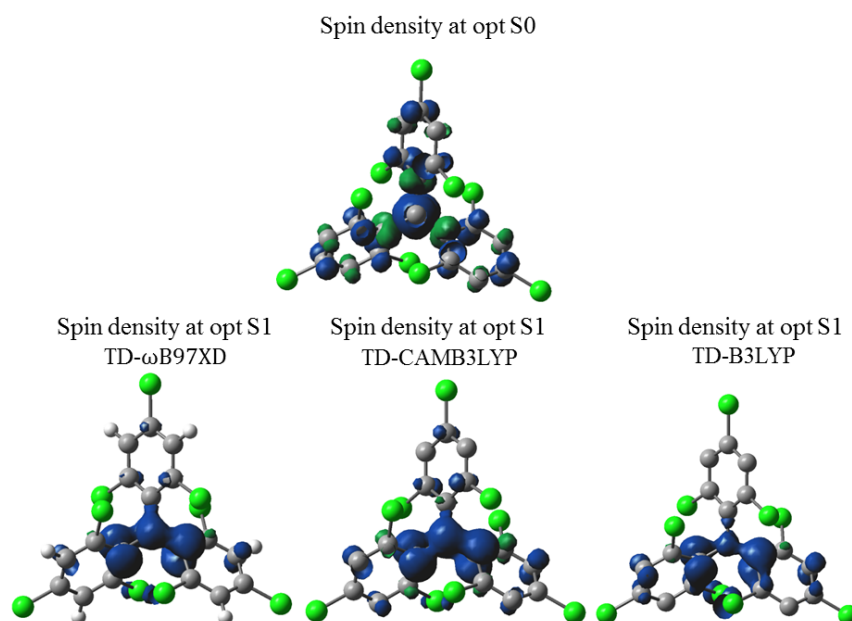
FIGURE 4.11: *Spin density at optimized ground (top) and lowest excited states (isovalue=0.003) at three levels of DFT theory investigated (bottom).*

TD-DFT rationalizes the absorption spectrum of TTM in solution; the agreement with experimental data is both *qualitative* and *quantitative* for TD-B3LYP, while the others functionals slight overestimate the excitation energy. The tendency of CAM-B3LYP and ωB97XD to overestimate the excitation energy (in particular for valence excitations) is well-known [138] and therefore in the two latter cases, all of the computed spectra would be rigidly red-shifted by 2600 cm^{-1}. By contrast, all functionals overestimate the Stokes shift, a fact that can be ascribed to the difficulty of TD-DFT with open-shell systems. Indeed, in general, estimation of Stokes shift in closed-shell aromatic molecules at TD-DFT level compares well with the experimental measurements in a non-polar solvent [163].

4.3   Quantum-chemical calculations on the dimer

From the analysis of the crystal structure, we select one significant dimer (see Figure 4.12) characterized by the shortest interatomic and interplanar distances (between the two units). Ground state and excited states calculation at different levels of theory are performed assuming that the two unpaired electrons combine in an anti-parallel way (singlet dimer).
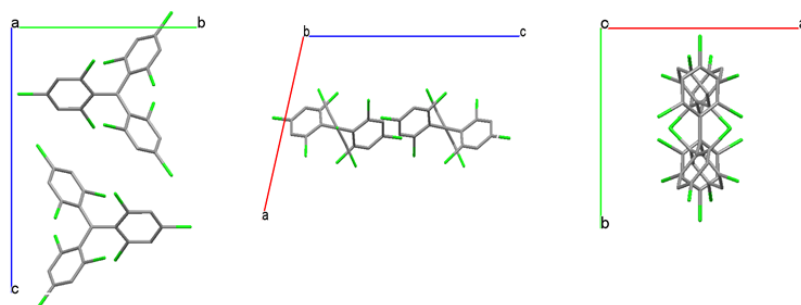
FIGURE 4.12: *Selected dimer along the three crystallographic axis.*

(TD)ωB97XD/6-31+G* and (TD)B3LYP/6-31+G* calculations in gas phase are carried out; UKS singlet calculations are performed with and without adding the keyword *guess=mix*. The *guess=mix* keyword is suggested in producing UKS wavefunctions for singlet state and it requests that HOMO and LUMO be mixed so as to destroy $\alpha - \beta$ spatial symmetry [114]. In order to evaluate the quality of the proposed calculations, also a triplet UKS calculation is carried out. Indeed, by knowing that the coupling between two TTM molecules is negligible in ground state (since no change in the absorption spectrum is observed), we expect that the singlet dimer energy converges to the correspondent triplet state, in virtue of the negligible exchange term in the latter. On the same grounds, we expect that the dimer ground state energy converges to twice the energy of the isolated units as well as the energy splitting between the frontier molecular orbitals, obtained from the combination of the SOMOs of the two isolated molecules, has to be of the same order whatever multiplicity is considered. As reported in Table 4.5 and in Figure 4.13, singlet UKS calculation is not reliable; it does not satisfy any of the previous considerations.

TABLE 4.5: *Ground state energy of the dimer at UωB97XD/6-31+G* with different multiplicity of spin in gas phase;*

Multiplicity of spin	Energy (Ha)
Triplet	-973.77288229
Singlet	-973.76506090
Singlet with *guess=mix*	-973.77288270

The UKS calculation using *guess=mix* keyword gives more reliable results: the gap between the two new frontier OMs is 0.02 eV, comparable with the triplet one, as well as, the relevant energy is *quasi* degenerate with the triplet. The interaction between the originally degenerate SOMO and SUMO molecular orbitals of the two isolated units leads to the formation of four non degenerate levels that constitute the frontier orbitals of the complex.
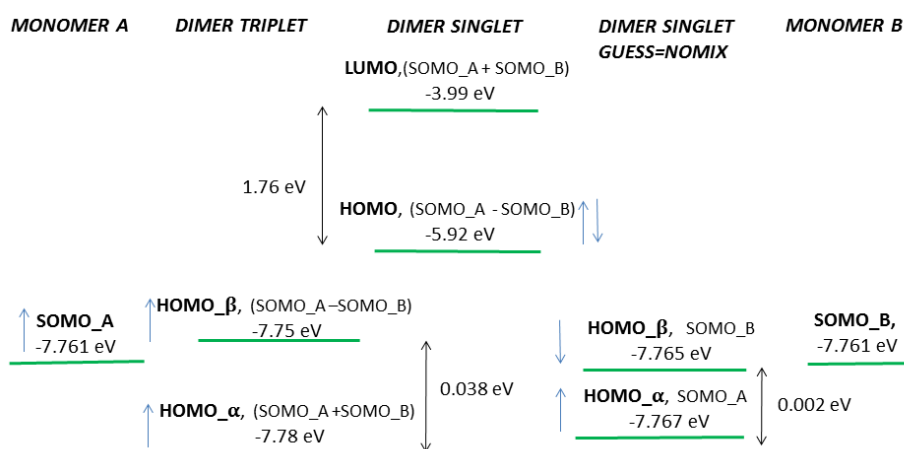
FIGURE 4.13: *Eigenvalues of the frontier molecular orbitals in the monomer in comparison with those of the dimer at singlet, triplet and singlet with* guess=mix *keyword at UωB97XD/6-31+G*.*

From Figure 4.14 we can observe that molecular orbitals are not delocalized over the two units, and, since we are relaxing the spatial orbitals, both spin orbital α and β are present.

FIGURE 4.14: *Frontier molecular orbitals in the dimer at singlet UKS with* guess=mix *keyword at UωB97XD/6-31+G*; molecular orbitals are qualitatively similar at UB3LYP/6-31+G*.*

By starting from this ground state, we perform vertical excitations. The calculated excited states with their energy, wavefunctions and oscillator strength at (TD)UωB97XD/6-31+G* and (TD)UB3LYP/6-31+G* in gas phase at crystallographic structure are reported in Table 4.6 and 4.7, respectively. From TD-UωB97XD/6-31+G* calculations

TABLE 4.6: *Transition energis, wavefunctions and oscillator strengths of the dimer at (TD)UωB97XD/6-31+G* in gas phase at crystallographic geometry. Each wavefunction is reported in terms of the OMs of the dimer (first row) and of the monomer (second row);*

	TD-UωB97XD		
Transition	λ	*Transition nature*	f
S0$\longrightarrow$S1	423 nm	(HOMO-1)$\alpha \longrightarrow$LUMO-α	0.0088
		HOMO-B$\longrightarrow$SUMO-B	
S0$\longrightarrow$S2	423 nm	(HOMO-1)$\beta \longrightarrow$LUMO-β	0.0144
		HOMO-A$\longrightarrow$SUMO-A	
S0$\longrightarrow$S3	422 nm	(HOMO-2)$\beta \longrightarrow$LUMO-β	0.0010
		(HOMO-1)-A$\longrightarrow$SUMO-A	
S0$\longrightarrow$S4	422nm	(HOMO-2)$\alpha \longrightarrow$LUMO-α	0.0220
		(HOMO-1)-B$\longrightarrow$SUMO-B	

TABLE 4.7: *Transition energies, wavefunctions and oscillator strengths of the dimer at (TD)UB3LYP/6-31+G* in gas phase and crystallographic geometry. Each wavefunction is reported in terms of the OMs of the dimer (first row) and of the monomer (second row);*

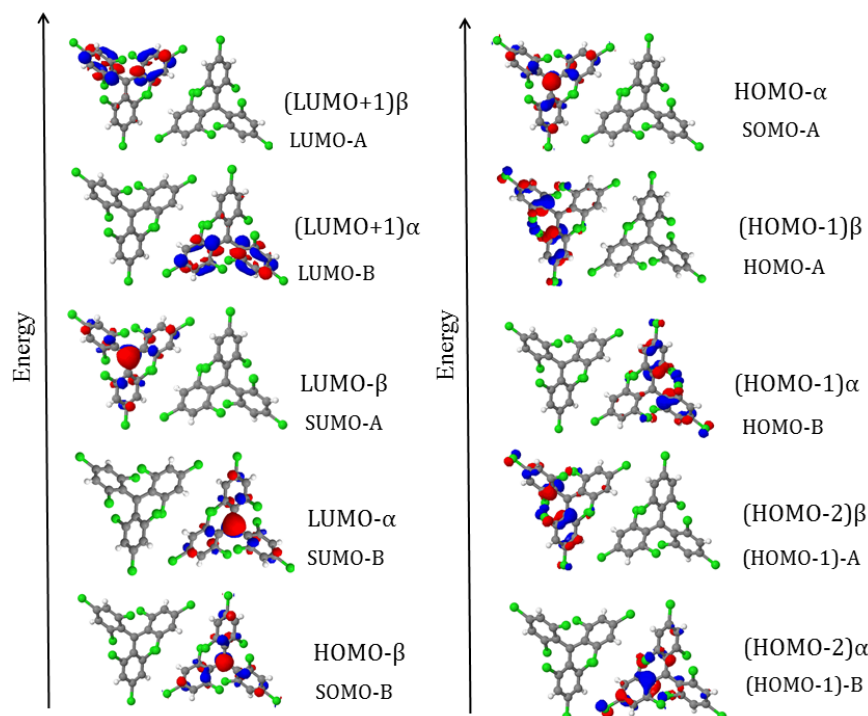|	TD-UB3LYP		
Transition	λ	*Transition nature*	f
S0$\longrightarrow$S1	650 nm	HOMO-$\alpha \longrightarrow$LUMO-α	0.0001
		SOMO-A$\longrightarrow$SUMO-B	
S0$\longrightarrow$S2	650 nm	HOMO-$\beta \longrightarrow$LUMO-β	0.0014
		SOMO-B$\longrightarrow$SUMO-A	
S0$\longrightarrow$S3	478 nm	(HOMO-1)$\alpha \longrightarrow$LUMO-α	0.0444
		HOMO-B$\longrightarrow$SUMO-B	
S0$\longrightarrow$S4	478 nm	(HOMO-1)$\beta \longrightarrow$LUMO-β	0.0052
		HOMO-A$\longrightarrow$SUMO-A	
S0$\longrightarrow$S5	477 nm	(HOMO-2)$\alpha \longrightarrow$LUMO-β	0.0004
		(HOMO-1)A$\longrightarrow$SUMO-A	
S0$\longrightarrow$S6	475 nm	(HOMO-2)$\alpha \longrightarrow$LUMO-α	0.0428
		(HOMO-1)B$\longrightarrow$SUMO-B	

(see Table 4.6), excited states are almost degenerate, not significant changes in excitation energy are observed and the excited states are localized on a single molecule. Such results were expected considering the small splitting in the frontier molecular orbitals of the dimer. At TD-UB3LYP/6-31+G* (see Table 4.7) the two lowest excited states are two dark CT states: an electron is moved from SOMO-A(B) towards SUMO-B(A), in

line with its tendency to underestimate CT states, while the relevant excited states are
S3 and S4 (corresponding to the monomeric S1 and S2 excited states respectively).

Data on Table 4.8, listing ground state and the excited state energy of the monomer and
of the dimer, allow to evaluate the stabilization energy in the dimer in comparison with
a non interacting pair of molecules in the two relevant states. Specifically, we evaluate
the stabilization energy in dimer ground state as the difference between its energy and
that of the two ground state isolated units, while the stabilization energy in excited state
of dimer is estimated as the difference between the dimer in excited state and the two
not interacting molecules with one in its excited state. Results are listed on Table 4.9.

TABLE 4.8: *Energy at (TD)UωB97XD/6-31+G* and (TD)UB3LYP/6-31+G* of
ground and excited states both for monomer and dimer in gas phase at crystallographic
geometry;*

	(TD)UωB97XD	(TD)UB3LYP
Monomer at ground state	-4868.8573771 Ha	-4869.2289449 Ha
Monomer at excited state	-4868.7495299 Ha	-4869.1333994 Ha
Dimer at ground state	-9737.7288270 Ha	-9738.4548618 Ha
Dimer at excited state	-9737.6211919 Ha	-9738.3848754 Ha

TABLE 4.9: *Interaction energy in the dimer at ground and excited states at
(TD)UωB97XD/6-31+G* and (TD)UB3LYP/6-31+G* at crystallographic geometry;*

	Interaction	
	(TD)UωB97XD	(TD)UB3LYP
ground state	0.38 eV	0.082 eV
excited state	0.40 eV	0.075 eV

The scenario emerging from Table 4.9 confirms previous results: the interactions in
the excited state are of the same order of magnitude as those in ground state, not
supporting the excimer picture. In order to exclude that weak interactions inside the
crystal affect experimental results, we run calculations with PCM model; such expedient
has been adopted by Cammi *et al.* to simulate weak interactions inside the crystal;
in the present case we do not observe any significant difference. In conclusion, TD-
DFT characterization on the dimer at frozen crystallographic geometry predicts the
same spectroscopic behavior of the singlet unit suggesting very negligible interactions in
excited state.

4.3.1 Characterization of PES at fixed monomer geometry

We are now discussing the PES obtained by the selected dimer in which the geometry is kept fixed. The effect of the displacement of one monomer with respect to the other is explored in order to better characterize the role of π-π interactions. The excited-state potential energy surfaces are characterized by calculations along the intermolecular translational coordinates x- and y-axis, as reported in Figure 4.15. The PES for such displacements are displayed in Figure 4.16. These calculations predict a repulsive ground state while the lowest excited state does not exhibit any shallow well, indicating no excimer formation.
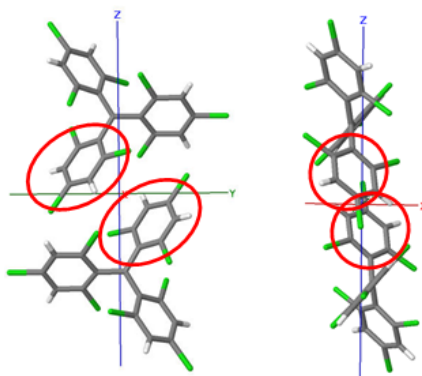
FIGURE 4.15: *Dimer view along x and y axis.*
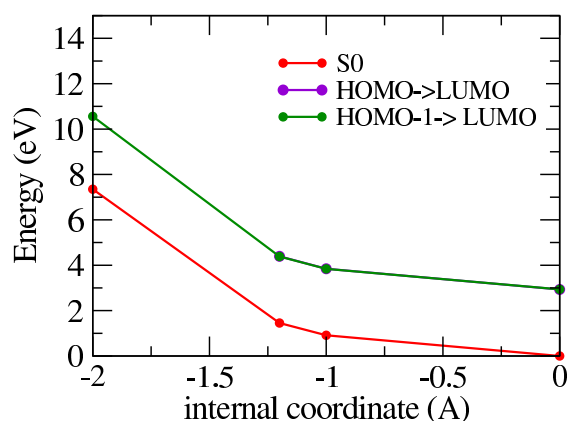
FIGURE 4.16: *Plot of the potential energy surfaces for the dimer in exam in S0 and S1-S2 (HOMO$\longrightarrow$LUMO) and S3-S4 ((HOMO-1)$\longrightarrow$LUMO); the zero of energy corresponds to the ground state dimer at crystallographic structure; S1-S2 and S3-S4 are substantially degenerate.*

This picture does not account for the possible influence of lattice relaxation in the emission properties of the two interacting units. Therefore to investigate the emission properties of the dimer, we have tried to optimize the lowest excited state at TD-ωB97XD but we did not succeed; the optimization of an excited state is not-trivial and difficulties

increase when we treat with a dimer based on two open-shell moieties. For this reason, we have tried to repeat calculations at semi-empirical level of theory.

4.4   Semiempirical calculations on the monomer and dimer

Different semi-empirical theoretical tools have been selected: PM7 and RM1 in the MOPAC package [112, 113] and ZINDO implemented in ORCA [143]. PM7 and RM1 have spotted some difficulties to calculate the weight of each configurations in the relevant excited states and for this reason we just focus on ZINDO tools adopting *cis* package [143]. Basically, we follow the same procedure adopted for TD-DFT. The absorption and emission energy as well as the Stokes shift at the equilibrium geometry of relevant states are listed in Table 4.10. During the optimization of the ground state geometry, we assist to an elongation of all bonds in the phenyl groups except those connecting central carbon to the three phenyl groups.

TABLE 4.10: *Calculated vertical transition energies at optimized ground and excited state and SS at ZINDO level in comparison with experimental data in solution of TTM (see Figure 4.4);*

	λ_{abs} (nm)	λ_{emi} (nm)	SS (eV)
ZINDO	467	517	0.25
Exp. data	540	575	0.15

The computed SS, sum of the two reorganization energy values, amounts to 0.25 eV and compares well with the experimental measurement in dichloromethane. The relevant wavefunction is dominated by SOMO$\longrightarrow$(LUMO+1)α
and HOMO-α $\longrightarrow$(LUMO+1)α configurations and it contains also the main contribute at TD-DFT level ((HOMO-1)β $\longrightarrow$SUMO).

After having characterized the monomer, we turn attention on the relevant physical dimer (see Figure 4.15). ZINDO calculations are performed on frozen crystallographic dimer with the two unpaired electrons arranged in anti-parallel way. The obtained UHF singlet calculation is meaningless: the ground state energy of the dimer is destabilized respect with the two not interacting units (by 3.5 eV) as well as respect with the dimer in the triplet configuration (by 3.35 eV). Unfortunately, differently from Gaussian, in ORCA, there is not implemented the equivalent *guess=mix* keyword and therefore we abandon ZINDO tools to investigate the optimized dimeric lowest excited state.

4.5   Conclusion

In this Chapter we have tried to rationalize the intriguing optical properties of TTM radicals. Experimental evidences of aggregation of TTM into composite nanoparticles suggest the formation of multiplet *excimers*. By means of TD-DFT, we have firstly investigated the monomer unit at crystallographic geometry and at optimized ground and lowest-excited state. We have demonstrated that TD-DFT is able to reproduce the absorption spectrum of TTM in solution predicting the main features in the absorption though an overestimated Stokes shift. Then, from the crystal structure we have extracted a dimeric unit and, keeping the dimer structure frozen, we have investigated the possibility of the formation of an excimer, building the ground and excited state PESs; the obtained repulsive lowest excited state clearly pointed out the lack of excimer formation. Because of the large dimension as well as of the complex nature of the relevant dimer, we were not able to optimize the lowest excited state neither if a smaller basis set is adopted. In any case, our analysis does not support excimer formation.

Concluding remarks

In this work a comprehensive computational effort was devoted to build reliable models for charge transfer processes that govern the physics of different classes of molecular functional materials.

Intramolecular CT in organic dyes is well understood in terms of essential-state models, a family of parametric Hamiltonians, introduced since date in the host laboratory to describe linear and non-linear spectral properties of the dyes in different environments. The contribution of this work to this mature field was the definition of an original model for Brilliant Green, a dye for which a large number of available experimental data put strong constraint on the model itself. Then we were able, for the first time, to apply essential-state models to the ultrafast dynamics of coherently excited dyes in solution. In this context, intriguing results are obtained as for the effects of polar solvation and inhomogeneous broadening on the spectroscopic behavior of polar dyes. Moreover, the non-adiabatic treatment of electron-phonon coupling allowed us to follow the temporal evolution of dynamic Jahn-Teller systems, a fascinating result that sheds light on the power of simple models to understand complex phenomena.

Intermolecular CT is the key process in mixed-stack CT crystals, a family of materials where delocalized electrons in 1D coupled to phonon modes lead to a variety of phenomena ranging from (photoinduced) phase transitions to ferroelectricity. The modified Hubbard Hamiltonian is the model of choice to describe the strongly correlated electronic systems. However the experimental parametrization of the Hamiltonian is a tricky problem and requires a welt of experimental data not readily available for many systems. Here we successfully validate and approach for parameterizing the modified Hubbard model from DFT calculations on dimeric (DA) structures. The analysis of 12 systems demonstrates that a reliable description of each system can be readily obtained based just on the crystal structure.

More delicate is the work on D-π-R$^{\cdot}$ systems. These systems are again CT dyes (more precisely polar D-π-A dyes), but with a radical character due to the choice of the acceptor group as a stable radical (in the specific case the PTM radical). These molecules

associate the interesting physics of CT dyes and systems with magnetic properties, and represent fundamental building blocks for a new family of materials where the concomitant presence of intra and intermolecular CT may lead to new physics and new opportunity for advanced applications. In this perspective a reliable modeling of the intramolecular CT in D-π-R$^{.}$ molecules represents the first fundamental step towards the design of new materials with sought functionality. Unfortunately, TD-DFT proved unable to reliably reproduce the excitation spectrum of these molecules, quite irrespective of the adopted functional. An effort to overcome the problem, parametrizing the essential-state model based on ground state properties (specifically the dependence of the ground state dipole moment on an applied static electric field), demonstrated a failure of DFT itself for this class of molecules. At present best results are obtained from a semiempirical (ZINDO) calculation of optical spectra. Further studies in this direction are in demand. Similarly inconclusive are studies on the presence of excimer states in organic nanoparticles built from radical dyes. In this case TD-DFT works well to reproduce absorption spectra but fails to reproduce emission spectra, while calculations on a dimeric structure are too heavy for a complete study of the excimer problem.

<div align="right">

Appendix A

</div>

Fluorescence anisotropy: main aspects and experimental setup

A.1   Fluorescence anisotropy

Fluorescence anisotropy is a spectroscopic technique based on the principle that upon excitation with polarized light, many samples also emit polarized light. The origin of this phenomenon is related to the presence of transition dipole moments for absorption and emission, which lie along specific molecular axes. In solution, fluorophores are randomly oriented. When exposed to polarized light, molecules with the absorption transition dipole moment oriented along the electric vector of the incident light are preferentially excited. Hence, the excited state population is not randomly oriented. Anisotropy measures the change in orientation of the transition dipole moment relevant to emission with respect to absorption. Depolarization of emission originates from a number of different phenomena. One of the most common reasons of depolarization is rotational diffusion. Since anisotropy measures the average angular displacement between the absorption and emission transition dipole moments, if the rate of diffusion is faster than the rate of the emission, fluorescence is completely depolarized. The rate of diffusive motion depends both on the viscosity of the solvent, on the shape and on the dimension of the fluorophore. Small molecules are characterized by a fast diffusion rate. On the contrary, diffusion is hindered in viscous solvents, or in glassy matrices.

A.1.1   Anisotropy measurements

The experimental setup for fluorescence anisotropy measurements is schematically illustrated in Figure A.1.
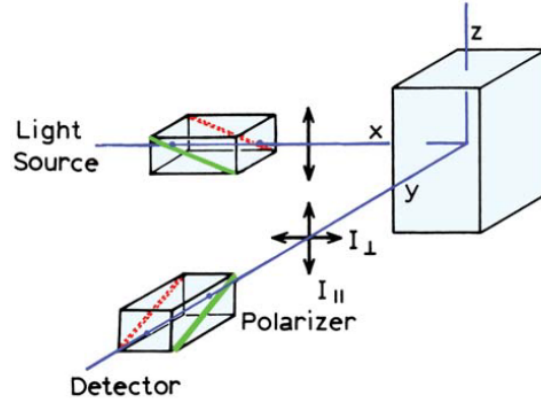
FIGURE A.1: *Schematic diagram for fluorescence anisotropy.*

The sample is excited with polarized light, and emission is detected through another polarizer. Anisotropy is defined as:

$$r = \frac{I_\parallel - I_\perp}{I_\parallel + 2I_\perp} \tag{A.1}$$

where $I_\parallel$ and $I_\perp$ are the emission intensities with emission polarizer oriented parallel and perpendicular to the excitation polarizer, respectively. Anisotropy is a dimensionless quantity, because the difference between the intensity of light emitted parallel and perpendicularly to the excitation ($I_\parallel - I_\perp$), is normalized by the total intensity of emitted light ($I_\parallel + 2I_\perp$). The fundamental anisotropy of a sample of molecules in frozen random orientation in absence of broadening effect is:

$$r_0 = \frac{2}{5} \left(\frac{3\cos^2\beta - 1}{2} \right) \tag{A.2}$$

where β is the angle between transition dipole moments relevant to emission and absorption processes. The term r_0 is used to refer to anisotropy observed in the absence of other depolarizing process such as rotational diffusion.

The maximum value for anisotropy is 0.4, when the absorption and emission transition dipole moments are aligned. Anisotropy is 0 at the magic angle (54.7°), and the lowest value, $r_0 = -0.2$, is obtained when the two dipole moments are perpendicular. Anisotropy is 0 also when some depolarization effect occurs.

Measurements of the fundamental anisotropy r_0 require special conditions. In order to avoid rotational diffusion, the samples are examined in solvents forming transparent glasses. Indeed, the latter are preferred to solvents forming the more common crystallization transition in order to avoid light scattering in crystalline environment. Since the matrix is rigid, photoselection plays a main role, as it will be discussed in the Appendix

B. Moreover, solutions must be optically diluted (absorbance < 0.1) to avoid depolarization processes due to internal absorption and subsequent emission of photons, or due to energy transfer. To measure anisotropy we have adopted a single emission channel (L-format). In particular after excitation with polarized light, emission is collected after a monochromator (see Figure A.1). The monochromator has a different transmission coefficient for vertically and horizontally polarized light, and, as a consequence, the rotation of the polarizer causes a change in the detected intensity even if emission is unpolarized. The G-factor takes into account the sensitivity of the detection system for vertically and horizontally polarized light:

$$G = \frac{I_{HV}}{I_{HH}} \tag{A.3}$$

where I_{XX} is the fluorescence intensity and XX represents the polarization (V=vertical, H=horizontal) of the excitation and emission polarizers. Consequently, anisotropy is defined as follows:

$$r = \frac{I_{HV}}{I_{HH}} = \frac{I_{VV} - GI_{VH}}{I_{VV} + 2GI_{VH}} \tag{A.4}$$

The excitation anisotropy spectrum is a plot of anisotropy detected at a fixed wavelength, as a function of the excitation wavelength. According to the Kasha rule, the lowest singlet state is responsible for emission, independently of excitation. Since the detected wavelength is fixed, the emission dipole moment remains the same. On the other hand, the transition dipole moment relevant to absorption changes for different excited states, so that the anisotropy is different for different absorption bands. The emission anisotropy spectrum is measured exciting the sample at a fixed wavelength and detecting the emission anisotropy at frequencies covering the whole emission band. The main difference with respect to the excitation anisotropy spectrum, is that in this case only two excited states are involved: the lowest singlet excited state, responsible for emission, and the state that absorbs the excitation wavelength (obviously, they can be the same state). Consequently, in the lack of spectral features, the emission anisotropy spectrum is a flat line across the whole emission band.

Fluorescence and fluorescence anisotropy (emission and excitation) spectra are collected on a Fluoromax-3 Horiba Jobin-Yvon spectrofluorometer equipped with a xenon lamp, as the excitation source, and excitation and emission Glan-Thompson automatic polarizers for anisotropy measurements (single-channel L format). All measurements are performed on diluted solutions, with absorbance < 0.1 to avoid inner filter effects. Glassy solution had been rapidly cooled to the relevant temperature with an Oxford Instruments OptistatDN cryostat. Quartz cuvettes specially designed for cryogenics are used. The experimental measurements performed on glassy solution of propylene glycol presented in Chapter I (see section 1.3) have been collected at 200K.

Appendix B

Computational details about optical spectra

In this Appendix we describe the procedure for the calculation of linear and nonlinear spectra. Once defined the coupled electron-vibration problem, according to essential-state models presented in Chapter I, the calculation follows the same steps for dipolar, quadrupolar or octupolar chromophores.

B.0.2 Absorption and fluorescence spectra

The orientational i-th components of the reaction field, $F_{or}^{(i)}$, (where i runs on the relevant component of the reaction field: $i = 1$ for linear molecules or $i = 1, 2$ for planar chromophores) describes a very slow motion that can be treated classically. Therefore, the coupled electron-vibration problem is solved for fixed $F_{or}^{(i)}$ values via a numerically exact diagonalization. Specifically, for each $F_{or}^{(i)}$, the total Hamiltonian is written on the basis obtained as the direct product of the electronic basis state times the eigenstates of the harmonic oscillator. The vibrational basis is truncated to a number of states large enough as not to affect relevant results (the number of vibrational states depends on the molecular parameters and on properties of interest; typical values are 6-10 states). The resulting Hamiltonian matrix is diagonalized numerically to get vibronic eigenstates. A Gaussian bandshape with half-width at half-maximum $\Gamma = \sqrt{2ln2}\sigma$ (cm^{-1}) is assigned to each vibronic transition, so that the molar extinction coefficient (ε) and fluorescence spectrum (I) are calculated as function of the wavenumber, $\tilde{\nu}$ (expressed in cm^{-1}), as follows:

$$\varepsilon(\tilde{\nu}) = \frac{10\pi N_A \tilde{\nu}}{3ln10\hbar c\epsilon_0} \frac{1}{\sqrt{2\pi}\sigma} \sum_n \mu_{gn}^2 exp\left[-\frac{1}{2}\left(\frac{\tilde{\nu}_{gn} - \tilde{\nu}}{\sigma}\right)\right] \tag{B.1}$$

$$I(\tilde{\nu}) \propto \tilde{\nu}^3 \frac{1}{\sqrt{2\pi}\sigma} \sum_n \mu_{fn}^2 exp\left[-\frac{1}{2}\left(\frac{\tilde{\nu}_{fn} - \tilde{\nu}}{\sigma}\right)\right] \tag{B.2}$$

In eq. B.1, N_A is the Avogadro number, c is the speed of light, ε_0 is the vacuum permittivity, $\tilde{\nu}_{gn}$ and μ_{gn} are the transition wavenumber and dipole moment respectively, for the $g \to n$ transition from the ground (g) to the generic excited state (n), and summation runs over all (vibronic) excited states. In eq. B.2, referring to fluorescence, $\tilde{\nu}_{fn}$ and μ_{fn} are the transition wavenumber and dipole moment, respectively, for the $f \to n$ transition from the fluorescent state (f) to the generic lower-energy state (n), and summation runs over all states having lower energy with respect to the fluorescent state, f. The emitting state is recognized as the lowest-energy non-adiabatic excited state having an appreciable transition dipole moment. The calculation of linear spectra is repeated for different F_{or} values and the total spectra are obtained summing up the contributions at different F_{or} weighted by the relevant Boltzmann population.

B.0.3   Two-photon absorption spectra

The two-photon absorption cross section (GM, $1GM=10^{-50}cm^4 sphoton^{-1}$) is calculated according to the following expression [10]:

$$\sigma_2(\omega) = 10^{58} \frac{\hbar\omega^2}{4\epsilon_0^2 c^2} Im\langle\gamma_{ijkl}(-\omega; \omega, \omega, -\omega)\rangle_{IJKL} \tag{B.3}$$

where c is the speed of light, and $\langle\gamma\rangle$ the orientationally averaged second hyperpolarizability ($IJKL$ indices run on the laboratory axis; $ijkl$ run on the axis of the molecular reference system). Tensor elements $\gamma_{ijkl}(-\omega; \omega, \omega, -\omega)$ are given by the following sum-over-states expressions [164]:

$$
\begin{aligned}
\gamma_{ijkl}(-\omega; \omega, \omega, -\omega) & = \frac{1}{\hbar^3}\sum_{mnp}\Bigg\{\frac{\langle g|\mu_i|m\rangle\langle m|\bar{\mu}_j|n\rangle\langle n|\bar{\mu}_k|p\rangle\langle p|\mu_l|g\rangle}{(\Omega_{mg} - \omega)(\Omega_{ng} - 2\omega)(\Omega_{pg} - \omega)} + \\
& \frac{\langle g|\mu_j|m\rangle\langle m|\bar{\mu}_i|n\rangle\langle n|\bar{\mu}_k|p\rangle\langle p|\mu_l|g\rangle}{(\Omega_{mg}^* - \omega)(\Omega_{ng} - 2\omega)(\Omega_{pg} - \omega)} + \\
& \frac{\langle g|\mu_i|m\rangle\langle m|\bar{\mu}_j|n\rangle\langle n|\bar{\mu}_l|p\rangle\langle p|\mu_k|g\rangle}{(\Omega_{mg} - \omega)(\Omega_{ng} - 2\omega)(\Omega_{pg} - \omega)} + \\
& \frac{\langle g|\mu_j|m\rangle\langle m|\bar{\mu}_i|n\rangle\langle n|\bar{\mu}_l|p\rangle\langle p|\mu_k|g\rangle}{(\Omega_{mg}^* - \omega)(\Omega_{ng} - 2\omega)(\Omega_{pg} - \omega)}\Bigg\}
\end{aligned}
\tag{B.4}
$$

where only two-photon resonant terms have been retained and the permutation operator $P(j; k; l; \omega, \omega, -\omega)$ is already considered; g is the ground state and summations run over all vibronic excited states as obtained from the diagonalization; $\Omega_{mg} = \omega_{mg} - i\Gamma_{mg}$ (we set $\Gamma_{mg} = \Gamma$, the width of the Gaussian bandshape defined above, for all transitions) and $\bar{\mu} = \mu - \langle g|\hat{\mu}|g\rangle$.

For linear molecules (dipolar chromophores and linear quadrupolar chromophores), the only tensor element different from zero is the γ_{xxxx} term, where x is the molecular axis. The orientationally-averaged second hyperpolarizability is thus given by $\langle\gamma\rangle_{XXXX} = 1/5\gamma_{xxxx}$. For planar octupolar chromophores (C_3 symmetry), $\langle\gamma\rangle_{XXXX} = 8/15\gamma_{xxxx}$ [16]. For Brilliant Green (see Chapter I), the orientational average of the second hyperpolarizability is

$$\langle\gamma\rangle_{XXXX} = \frac{1}{5}\sum_i \gamma_{iiii} + \frac{1}{15}\sum_{i\neq j}(\gamma_{iijj} + \gamma_{jiji} + \gamma_{jiij}) \tag{B.5}$$

As for OPA, the calculation of TPA spectra is repeated for different $F_{or}^{(i)}$ values and the overall spectrum is obtained summing up the TPA spectra weighted by the Boltzmann population.

B.0.4 Hyper-Rayleigh Scattering

The orientationally averaged HRS response in the laboratory coordinate system is described by:

$$\beta_{HRS}^2 = \langle\beta_{ZZZ}^2\rangle + \langle\beta_{XZZ}^2\rangle \tag{B.6}$$

where X,Y,Z define the laboratory coordinates and $\langle\beta_{IJJ}^2\rangle$ stands for the orientational average of the square of the appropriate β tensor component. To express the HRS response, β_{HRS}, in molecular coordinate system, an average over all possible orientations has to be introduced, in according to the following equation:

$$\begin{aligned}
\beta_{HRS} &= \left[\|\frac{6}{35}(\beta_{xxx}^2 + \beta_{yyy}^2) + \frac{4}{35}(\beta_{xyy}^2 + \beta_{yxx}^2)+\right.\\
&\quad \frac{4}{21}(\beta_{xxy}^2 + \beta_{yyx}^2) + \frac{2}{21}(\beta_{xxx}\beta_{xyy} + \beta_{yyy}\beta_{yxx}) +\\
&\quad \left.\frac{2}{35}(\beta_{xxx}\beta_{yyx} + \beta_{xyy}\beta_{yxx})\|\right]^{1/2}
\end{aligned} \tag{B.7}$$

The molecular tensor components, β_{ijk}, are obtained through the standard sum-over states expression:

$$
\begin{aligned}
\beta_{ijk}(-2\omega;\omega,\omega) \;=\; \frac{1}{6\hbar^3}\sum_{mn}\Bigg\{ &\frac{\langle g|\mu_i|m\rangle\langle m|\bar\mu_j|n\rangle\langle n|\bar\mu_k|g\rangle}{(\Omega_{mg}-2\omega)(\Omega_{ng}-\omega)} + \\
&\frac{\langle g|\mu_j|m\rangle\langle m|\bar\mu_i|n\rangle\langle n|\bar\mu_k|g\rangle}{(\Omega_{mg}^*+\omega)(\Omega_{ng}-\omega)} + \\
&\frac{\langle g|\mu_k|m\rangle\langle m|\bar\mu_j|n\rangle\langle n|\bar\mu_k|g\rangle}{(\Omega_{mg}+\omega)(\Omega_{ng}^*+2\omega)} + \\
&\frac{\langle g|\mu_i|m\rangle\langle m|\bar\mu_j|n\rangle\langle n|\bar\mu_k|g\rangle}{(\Omega_{mg}-2\omega)(\Omega_{ng}-\omega)} \\
&\frac{\langle g|\mu_k|m\rangle\langle m|\bar\mu_i|n\rangle\langle n|\bar\mu_j|g\rangle}{(\Omega_{mg}^*+\omega)(\Omega_{ng}-\omega)} + \\
&\frac{\langle g|\mu_j|m\rangle\langle m|\bar\mu_k|n\rangle\langle n|\bar\mu_i|g\rangle}{(\Omega_{mg}^*+\omega)(\Omega_{ng}^*+2\omega)} \Bigg\}
\end{aligned}
\tag{B.8}
$$

where a factor $1/6$ is introduced to directly compare with experimental results, expressed in the B^* convention as defined by Willetts $et\ al.$ [165].

B.0.5   Emission and excitation anisotropy spectra

The calculation of anisotropy spectra is not trivial, and in particular two tricky problems have to be considered. Firstly, experimental spectra are collected in a glassy matrix at low temperature. This experimental condition has major consequences on inhomogeneous broadening and on the Stokes shift. The excitation wavelength preferentially excites a subset of molecules out of the inhomogeneous distribution (those absorbing at the specific wavelength). The same molecules are responsible for emission. Since the matrix is rigid, the relaxation along the solvation coordinate is hindered, and only vibrational relaxation takes place before fluorescence. Therefore the emitting state is that relevant to the specific subset of photoselected molecules, with a relaxed geometry along the internal coordinates but in the frozen solvent configuration. This phenomenon is called $energy\ photoselection$. The second important aspect concerns $polarization\ photoselection$: when excited with a polarized light beam, molecules with the absorption transition dipole moment oriented along the direction of polarization are preferentially excited. Moreover, because anisotropy is measured in solutions of randomly oriented molecules, an appropriate averaging over all possible orientations has to be performed. In our calculations, inhomogeneous broadening is associated with a distribution of reaction fields weighted according to the Boltzmann distribution for the ground-state energy (frozen solutions).

For the calculation of fluorescence emission and emission anisotropy spectra, we account for *energy photoselection* by considering the probability, for each point of the F_{or} grid, that the incident photons at the excitation wavelength are absorbed by the corresponding subset of solute molecules. For fluorescence excitation and excitation anisotropy spectra, we consider the probability, for each point of the F_{or} grid, that photons at the detection wavelength are emitted by the corresponding subset of solute molecules. The first problem related to energy photoselection is solved considering the probability of each molecule to absorb the incident monochromatic photons, according to the ground-state energy distribution. In particular, the same ground state Boltzmann distribution is assumed for both the ground state and for the excited state responsible for emission, because the solvent molecule are frozen in the configuration they have around the solute molecule in the ground state.

Concerning the problem of *orientational photoselection*, the following expressions allow to estimate the fluorescence intensity, when the polarizers are parallel ($I_{\parallel}$) or perpendicular ($I_{\perp}$), for a sample of randomly oriented molecules in frozen solutions [166]:

$$I_{\parallel} = \frac{|\vec{\mu}_{em}|^2 \cdot |\vec{\mu}_{abs}|^2 + 2(\vec{\mu}_{em} \cdot \vec{\mu}_{abs}^2)}{15} \tag{B.9}$$

$$I_{\perp} = \frac{2|\vec{\mu}_{em}|^2 \cdot |\vec{\mu}_{abs}|^2 - (\vec{\mu}_{em} \cdot \vec{\mu}_{abs})^2}{15} \tag{B.10}$$

These two terms have to be weighted separately for the relevant Boltzmann distribution, to take into account the effects related to inhomogeneous broadening. This is a key point: as $I_{\parallel}$ and $I_{\perp}$ are the experimental results of two independent measurements, they must also be averaged over the inhomogeneous distribution as two independent quantities. Hence, the Boltzmann distribution has to be associated to these two terms, and not to the final anisotropy. Therefore, $I_{\parallel}$ and $I_{\perp}$ are calculated for each point of the F_{or} grid and results are summed according to the (normalized) probability associated with each F_{or} value, giving the total polarized emission intensities entering eq. A.1 to calculate the (emission or excitation) anisotropy.

Appendix C

Theoretical methods

Theoretical methods have been mainly adopted in this thesis with the aim to obtain an accurate and realistic description of ground- and excited-states properties. The following overview briefly describes semiempirical methods and Density Functional Theory.

C.1   Semiempirical methods

In computational chemistry, semiempirical methods occupy an intermediate position between molecular mechanics and ab initio theory. Indeed semiempirical methods are considerably faster than ab initio tools and considerably more versatile than molecular mechanics. Semi-empirical methods reduce the computational cost by considering explicitly only valence electrons and adopting only minimal basis sets (see Section C.2.1). The main assumption of semi-empirical methods is the Zero Differential Overlap (ZDO) approximation, which neglects all basis functions depending on the same electron coordinates when located on different atoms:

$$S = \langle \varphi_\mu^A | \varphi_\nu^B \rangle = \delta_{AB} \delta_{\mu\nu} \tag{C.1}$$

where S is the overlap integral between the basis functions and located on atoms (the so-called *centers* within semi-empirical methods) A and B, respectively; $\delta_{\mu\nu}$ is the Kronecker delta. Under this approximation, the overlap matrix is reduced to a unit matrix, all one-electron integrals involving three centers (two from the basis function and one from the operator) are set to zero and all three- and four-center two-electron integrals are neglected. The remaining integrals are parameterized based upon assignment on the basis of calculation or experiment Several semi-empirical methods have been formulated according to a differently strict application of the ZDO approximation. One of the

more robust families of such methods are the neglect of diatomic differential overlap (NDDO) methods first developed by Pople. In the Neglect of Diatomic Differential Overlap (NDDO) method, ZDO is applied exclusively between atomic orbitals centered on distinct atoms, such as:

$$S = \langle \varphi_\mu^A | \varphi_\nu^B \rangle = \delta_{AB} \tag{C.2}$$

Following the pioneering work of Dewar and Thiel, several modifications were made to the NDDO formalism in attempts to increase accuracy and generality, among which the most popular are AM1 [167], PM3 [168] PM6 [169], PM7 [112] and RM1 [170]. Then other different methods have been developed based on the different treatment of the two-electron integrals. Specifically, in the Intermediate Neglect of Differential Overlap (INDO) [171] model, all two-center two-electron integrals that are not of the Coulomb type are neglected; in addition, in order to preserve rotational invariance, some of the integrals are made independent of the orbital type. Then, in the Complete Neglect of Differential Overlap (CNDO) [172] approximation, only the Coulomb one-center and two-center two-electron integrals remain.

C.2 (TD)-DFT methods

The basis for DFT is the proof by Hohenberg and Kohn that the ground state electronic energy of a molecular system is determined completely by the electron density, which, unlike a wavefunction, is observable. The electron density is defined as a multiple integral over the spin coordinates of all electrons and over all but one of the spatial variables:

$$\rho(\bar{r}_i) = N \int ... \int |\Psi(\bar{x}_1, \bar{x}_2, ..\bar{x}_N)|^2 ds_1 d\bar{x}_2 d\bar{x}_N \tag{C.3}$$

where $\rho(\bar{r}_i)$ determines the probability of finding any of the N electrons within a volume element $d\bar{r}_i$, but with arbitrary spin while the other N-1 electrons have arbitrary positions and spin.

The *first Hohenberg-Kohn* [173] theorem implies that, since $\rho(\bar{r}_i)$ uniquely determines the Hamiltonian operator, the average value of any observable can be written as its functional:

$$\langle A \rangle = A[\rho(\bar{r}_i)] \tag{C.4}$$

Therefore, the total energy of the electronic system can be expressed as a functional of the electron density:

$$E = E[\rho] = T[\rho] + E_{eN}[\rho] + E_{ee}[\rho] \tag{C.5}$$

where $T[\rho]$ represents the kinetic energy of the system, and $E_{eN}[\rho]$ and $E_{ee}[\rho]$ are the nuclear-electron and electron-electron interactions, respectively. The sum of $T[\rho]$ and $E_{ee}[\rho]$ is called the universal functional of Hohenberg and Kohn, $F_{HK}[\rho]$; if $F_{HK}[\rho]$ were known exactly, the Schrödinger equation could be solved exactly. By extracting from $E_{ee}[\rho]$ the Coulomb integral $J[\rho]$, it is given:

$$F_{HK}[\rho] = T[\rho] + J[\rho] + E_{ncl}[\rho] \tag{C.6}$$

where $E_{ncl}[\rho]$ incorporates the non-classically defined electron-electron interactions of self-interaction, exchange, and electron correlation effects.

The *second Hohenberg-Kohn theorem* states that $F_{HK}[\rho]$ provides the lowest energy only if the input density is the true ground state density; therefore, this theorem guarantees the existence of a variational principle for electron densities. Kohn and Sham hypothesized that the Hamiltonian would be simpler if it were one for a system of non-interacting electrons that has the same density of some system where electrons interact [174]. This corresponds to an exact dressed single-particle theory. In analogy to HF theory, the electrons are treated as independent particles moving in the average field of all others but now with included correlation. For such a system of non-interacting electrons, the kinetic energy (T_S) is the sum of the individual electronic kinetic energies and Kohn-Sham (KS) wavefunctions is a Slater determinant obtained from KS orbitals ($\Phi_i(\bar{x}_i)$), in complete analogy to HF orbitals:

$$\Theta_{KS}(\bar{x}_i, \bar{x}_2, ..., \bar{x}_N) = \frac{1}{\sqrt{N!}} = \begin{bmatrix} \Phi_1(\bar{x}_1) & \Phi_2(\bar{x}_1) & ... & \Phi_N(\bar{x}_1) \\ \Phi_1(\bar{x}_2) & \Phi_2(\bar{x}_2) & ... & \Phi_N(\bar{x}_N) \\ \vdots & \vdots & \vdots & \ddots \\ \Phi_1(\bar{x}_N) & \Phi_2(\bar{x}_N) & ... & \Phi_N(\bar{x}_N) \end{bmatrix} \equiv |\Phi_1 \Phi_2 ... \Phi_N|$$

We have to precise that the KS orbitals and their eigenvalues have no physical significance: they are an abstract construct used to solve the many-body problem. Though, the interpretative power of these orbitals is commonly used in rationalizing chemical phenomena; such fact is justified by considering that KS orbitals give back the exact ground state density and fully take into account all non-classical effects. Since T_S does not equal $T[\rho]$, an exchange-correlation energy term $E_{XC}[\rho]$, incorporating both the residual part of the true kinetic energy and the non-classical interactions, is introduced:

$$E_{XC}[\rho] \equiv (T[\rho] - T_S[\rho]) + (E_{ee}[\rho] - J[\rho]) = T_S[\rho] + E_{ncl}[\rho] \tag{C.7}$$

Thus, it is possible to express the total energy for the system as:

$$E[\rho] = T_S[\rho] + J[\rho] + E_{eN}[\rho] + E_{XC}[\rho] \tag{C.8}$$

With the introduction of orbitals, the minimized energy can be found through solving the pseudo-eigenvalue equation:

$$h_i^{KS}\phi_i = \varepsilon_i\phi_i \tag{C.9}$$

where the one-electron KS operator is defined as:

$$h_i^{KS} = -\frac{1}{2}\nabla_i^2 - \sum_{A=1}^{M}\frac{Z_A}{r_{iA}} + \int\frac{\rho(\bar{r}_j)}{r_{ij}}d\bar{r}_j + V_{XC}(\bar{r}_i) \tag{C.10}$$

with

$$V_{XC} = \frac{\delta E_{XC}}{\delta\rho} \tag{C.11}$$

V_{XC} is the exchange-correlation potential which is best described as the one-electron operator for which the expectation value of the KS Slater determinant is E_{XC}; since it is not known how to express $E_{XC}[\rho]$, there is no explicit form for V_{XC} and reasonable approximations need to be made.

The three most commonly adopted approximations are the localized density approximation (LDA), the generalized gradient approximations (GGA) and the formation of hybrid functionals through the incorporation of part of the exact HF exchange in the DFT functionals.

By assuming that electrons move on a positive background charge distribution like a uniform electron gas, the Local Density Approximation (LDA) defines the $E_{XC}[\rho]$ as:

$$E_{XC}^{LDA}[\rho] = \int\rho(\bar{r})\varepsilon_{XC}[\rho(\bar{r})]d\bar{r} \tag{C.12}$$

where $\varepsilon_{XC}[\rho(\bar{r})]$ is the exchange-correlation energy per particle of a uniform electron gas of density $\rho(\bar{r})$. By introducing the spin into eq. C.12, the Local Spin-Density Approximation (LSDA) is obtained, allowing to handle the unrestricted case (UKS). The term $\varepsilon_{XC}[\rho(\bar{r})]$ can be divided into exchange and correlation contributions:

$$\varepsilon_{XC}[\rho(\bar{r})] = \varepsilon_X[\rho(\bar{r})] + \varepsilon_C[\rho(\bar{r})] \tag{C.13}$$

where the exchange contribute is generally expressed as:

$$\varepsilon_X[\rho(\bar{r})] = -3/4\sqrt[3]{\frac{\rho(\bar{r})}{\pi}} \tag{C.14}$$

As for the correlation term, no such explicit expression is known and therefore it is fitted empirically to a set of experimental data or it is modeled on the basis of model systems such as the uniform electron gas and other known properties.

Generally, in a molecular system, the electron density is not spatially uniform. In order to overcome this limitation in the LDA/LSDA approach, the Gradient Corrected (GCA) or Generalized Gradient Approximation (GGA) is introduced. In such approximation, information regarding the gradient of the charge density $\bigtriangledown\rho(\bar{r})$ is added to the density $\rho(\bar{r})$ at a particular point $\bar{r}$. In general, GGA functionals are constructed with a correction added to the original LDA/LSDA term:

$$\varepsilon_{X/C}^{GGA}[\rho(\bar{r})] = \varepsilon_{X/C}^{LDA/LSDA}[\rho(\bar{r})] + \Delta\varepsilon\frac{[\bigtriangledown\rho(\bar{r})]}{[\rho^{\frac{4}{3}}(\bar{r})]} \tag{C.15}$$

where X/C indicates that the same functional form holds for either exchange or correlation. The most popular GGA exchange functional was developed by Becke (B) [175] Popular correlation functionals include those developed by Perdew (P86) [176] Perdew and Wang (PW91), and Lee, Yang, and Parr (LYP)[177]. In general, exchange contributions are significantly larger than correlation effects; thus, an accurate expression for the exchange energy is required for a meaningful exchange-correlation functional. For this purpose, an exact Hartree-Fock exchange contribution can be incorporate into the DFT functional, obtaining a so-called *hybrid functional*. At present, in standard ground state DFT applications [177–179], the functionals B3LYP is one of the most widely used *xc* functionals :

$$,E_{XC}^{B3LYP} = (1-a)E_X^S + aE_X^{HF} + b\Delta E_X^B + (1-c)E_C^{VWN} + cE_C^{LYP} \tag{C.16}$$

which incorporates the exact HF exchange, exchange (Slater, S) and correlation (Vosko-Wilk-Nusair, VWN) terms derived from LSDA, and the Becke exchange and LYP correlation terms. The values optimized for a, b, and c are 0.20, 0.72, and 0.81, respectively, as derived from atomization and ionization energies and proton and electron affinities within 1 kcal/mol of experimental results for 125 reference molecules containing main group elements [175]. This fact clearly highlights the semi-empirical nature in hybrid functionals.

However B3LYP suffer as, all other functionals, for self-interaction energy error (SIE). Indeed, the classical electrostatic repulsion term does not completely vanish for a one-electron system because the density interacts with itself. As $E_{XC}[\rho]$ is never exact and independent of classical electrostatic repulsion, there is generally a residual energy due to self-interaction effects causing an over-delocalized electron density. Because of these short comings, the use of non-corrected DFT methods may be questionable in dealing

with charge-transfer states and systems featuring electrons weakly tied to the molecule. In order to overcome SIE, the long-range interaction corrected CAM [180] and M06 [181] functionals have been proposed. From literature it emerges that CAM seems to be suitable for charge-transfer states, while M06 seems to perform adequately in dealing with non-covalent interactions [180] [181].

Excited states within the DFT methodology are investigated through Time-Dependent DFT (TDDFT) [182], the time-dependent analogue of the first Hohenberg-Kohn theorem [182, 183]. TDDFT is a formally exact theory that relies on the analysis of the time-dependent linear response of the formally exact ground state density to a time-dependent external perturbation, which after Fourier transformation yields exact excited-state energies and oscillator strengths. The derivation of the famous Runge-Gross theorem and the subsequent formulation of a time-dependent Kohn-Sham equations were the cornerstones in the development of the TDDFT formalism. However, since the exact xc functional is not known, approximate xc functionals need to be employed in a practical calculation. Concomitantly, errors in the excitation energies and oscillator strengths are introduced. Still, for most valence-excited states, which lie well below the first ionization potential, TDDFT yields results with high accuracy at relatively low computational cost in comparison with highly accurate methods such as MRCI, CASPT2, or EOM-CCSD, which are applicable only to small molecules up to 20 atoms. Nevertheless, one has to be very careful using TDDFT with approximate xc functionals owing to its failures for Rydberg states, systems with large π-systems, doubly excited states, and CT states. The latter failure limits the applicability of TDDFT to large systems or small molecules in solution or protein environments, because erroneous intramolecular CT excited states occur in the low-energy region of the electronic spectra [183] .

C.2.1   Basis set

Molecular orbitals are described as a linear combination of different basis functions. Therefore, the quality of a calculation depends upon the number of basis functions. Two types of orbitals are typically used in electronic-structure calculations. The first, Slater-Type Orbitals (STOs), have the form:

$$\chi_{\zeta,n,l,m}(r,\theta,\varphi) = NY_{l,m}(\theta,\varphi)r^{n-1}e^{-\zeta r} \tag{C.17}$$

where N is a normalization constant, $Y_{(}l,m)(\theta.\varphi)$ is a spherical harmonic function, and ζ the Slater orbital exponent. Gaussian-Type Orbitals (GTOs) can be written in terms

of polar coordinates:

$$\chi_{\xi,n,l,m}(r,\theta,\varphi) \quad = \quad NY_{l,m}(\theta,\varphi)r^{(2n-2-l)}e^{-\alpha r^2} \tag{C.18}$$

$$\tag{C.19}$$

as well as Cartesian coordinates:

$$\chi_{\xi,l_x,l_y,l_z}(x,y,z) \quad = \quad Nx^{l_x}y^{l_y}z^{l_z}e^{-\alpha r^2} \tag{C.20}$$

where the sum of l_x, l_y, and l_x determine the type of orbital, and α is the Gaussian orbital exponent. GTOs have two complicating factors respect with their STO counterparts, due to their r^2-dependence:

- at the nucleus, GTOs have zero slope versus the *cusp* of the STO; therefore GTOs exhibits difficulty representing the behavior of the wavefunction near the nucleus and consequentially the energetics of the system.

- GTOs fall off too rapidly at distances far from the nucleus, which obviously affects the proper description of chemical bonds as well as non-covalent interactions.

In order to overcome these issues, several GTOs are combined to form contracted GTOs. The simplest form for a contracted GTO is:

$$\Phi^\mu = \sum_{i=1}^{L} d_{i\mu}\varphi_i^\mu(\alpha_{i\mu}) \tag{C.21}$$

where $\varphi_i^\mu(\alpha_{i\mu})$ is the *i-th* GTO constituting the basis function $\varphi^\mu\mu$, L is the contraction length, and $d_{i\mu}$ is a contraction coefficient. A minimal basis set is one that uses one basis function per atomic orbital of the electronic shells occupied in the free atom. In order to get a better description of anisotropic electron distribution in molecules, a double-zeta basis set is introduced. A double-zeta basis set employs two basis functions per atomic orbital. Further extension of the basis sets is done through triple-zeta, quadruple-zeta, etc. basis sets. Each split basis set has a set of two (or more) functions of different sizes or radial distributions for each valence orbital orbital allowing more flexibility.

Basis sets can also extended through the addition of polarization and diffuse functions. Atomic orbitals often become distorted (polarized) under the influence of other atoms within a molecular system. To account for these effects, polarization functions (denoted *) with one additional node (higher angular momentum terms) are added to the basis sets. Diffuse functions, basis functions with small exponents α (denoted +), are added to account for properties that extend far away from the atomic nucleus; for example,

they are added for a proper description of loosely bound electrons in radical anions and molecular polarizability. The most common functional basis are 3-21G, 6-31G and, 6-31+G*.

Acknowledgments

I wish to express my gratitude to my supervisors Prof. Anna Painelli and Prof. Francesca Terenziani for the knowledge they liked to share with me and for the opportunities they gave me during these years. I also thank Prof. Alberto Girlando, Dr. Cristina Sissa and Dr. Matteo Masino for their help and fruitful collaborations. I am grateful to all present and past PhD students of the research team for having get less lonely the solitary computational work making those years nice: Francesco Di Maiolo, Nicola Castagnetti, Cesare Benedetti, Domna Maria Nikolaidou, Somananda Sanyal and Siarhei Kurhuzenkau.

I wish to thank all people I have collaborated with: Prof. Jaume Veciana, Dr. Imma Ratera, Manel Souto, Dyana Morales, Davide Blasi of ICMAB in Barcelona (Spain), Prof. Wim Wenseleers, Jochen Campo of Antwerp University (Belgium), Prof. Swapan Pati, Arkamita Banerjee of JNCASR of Bangalore (India), Dr. Gabriele D'Avino of Mons University (Belgium), Prof. Eric Vauthey and Dr. Arnulf Rosspeintner (Geneva University).

Finally, up so far, I thought that the credit for people's success mainly belongs to them; instead, my PhD experience showed me that this is not always true: I need to thank my parents, my brother, my sister, my enthusiastic granddaughter and all my friends for their precious support. My deepest thank to Raffa for always encouraging me and for bearing with me.

Bibliography

[1] Vogel, E. (2007) Technology and metrology of new electronic materials and devices. *Nature nanotechnology 2*, 25–32.

[2] Brabec, C. J., Winder, C., Scharber, M. C., Sariciftci, N. S., Hummelen, J. C., Svensson, M., and Andersson, M. R. (2001) Influence of disorder on the photoinduced excitations in phenyl substituted polythiophenes. *The Journal of Chemical Physics 115*, 7235–7244.

[3] Lafratta, C. N., Fourkas, J. T., Baldacchini, T., and Farrer, R. a. (2007) Multiphoton Fabrication. *Angewandte Chemie International Edition 46*, 6238–6258.

[4] Sahoo, S. K., Parveen S, P. J. (2007) The present and future of nanotechnology in human health care. *Nanomedicine 3*, 20–31.

[5] Diaspro, A., Chirico, G., and Collini, M. (2005) Two-photon fluorescence excitation and related techniques in biological microscopy. *Quarterly Reviews of Biophysicsly Reviews of Biophysics 38*, 97–164.

[6] Konan, Y. N., Gurny, R., and Allémann, E. (2002) State of the art in the delivery of photosensitizers for photodynamic therapy. *Journal of Photochemistry and Photobiology B: Biology 66*, 89–106.

[7] Kochevar, I. E., and Redmond, R. W. (2000) Photosensitized production of singlet oxygen. *Methods in enzymology 319*, 20–28.

[8] Breitenbach, T., Kuimova, M. K., Gbur, P., Hatz, S., Schack, N. B., Pedersen, B. W., Lambert, J. D. C., Poulsen, L., and Ogilby, P. R. (2009) Photosensitized production of singlet oxygen: spatially-resolved optical studies in single cells. *Photochem. Photobiol. Sci. 8*, 442–452.

[9] Fleming, G. R., and Sholes, G. D. (2004) Quantum mechanics for plants. *Nature 431*, 256–257.

[10] Terenziani, F., Katan, C., Badaeva, E., Tretiak, S., and Blanchard-Desce, M. (2008) Enhanced two-photon absorption of organic chromophores: Theoretical and experimental assessments. *Advanced Materials 20*, 4641–4678.

[11] Beljonne, D., Wenseleers, W., Zojer, E., Shuai, Z., Vogel, H., Pond, S. J. K., Perry, J. W., Marder, S. R., and Brédas, J. L. (2002) Role of dimensionality on the two-photon absorption response of conjugated molecules: The case of octupolar compounds. *Advanced Functional Materials 12*, 631–641.

[12] Painelli, A., and Terenziani, F. (1999) A non-perturbative approach to solvatochromic shifts of pushpull chromophores. *Chemical Physics Letters 312*, 211–220.

[13] Boldrini, B., Cavalli, E., Painelli, A., and Terenziani, F. (2002) Polar dyes in solution: A joint experimental and theoretical study of absorption and emission band shapes. *Journal of Physical Chemistry A 106*, 6286–6294.

[14] Terenziani, F., Przhonska, O. V., Webster, S., Padilha, L. A., Slominsky, Y. L., Davydenko, I. G., Gerasov, A. O., Kovtun, Y. P., Shandura, M. P., Kachkovski, A. D., Hagan, D. J., Van Stryland, E. W., and Painelli, A. (2010) Essential-state model for polymethine dyes: Symmetry breaking and optical spectra. *Journal of Physical Chemistry Letters 1*, 1800–1804.

[15] Sissa, C., Jahani, P. M., Soos, Z. G., and Painelli, A. (2012) Essential State Model for Two-Photon Absorption Spectra of Polymethine Dyes. *ChemPhysChem 13*, 2795–2800.

[16] Campo, J., Painelli, A., Terenziani, F., Van Regemorter, T., Beljonne, D., Goovaerts, E., and Wenseleers, W. (2010) First hyperpolarizability dispersion of the octupolar molecule crystal violet: Multiple resonances and vibrational and solvation effects. *Journal of the American Chemical Society 132*, 16467–16478.

[17] Delchiaro, F., Sissa, C., Terenziani, F., Painelli, A., Campo, J., and Wenseleers, W. A comprehensive spectroscopic and theoretical study of brilliant green. *in preparation*

[18] Sissa, C., Delchiaro, F., Di Maiolo, F., Terenziani, F., and Painelli, A. (2014) Vibrational coherences in charge-transfer dyes: A non-adiabatic picture. *The Journal of Chemical Physics 141*, 164317–164327.

[19] Koshihara, S., Tokura, Y., Mitani, T., Saito, G., and Koda, T. (1990) Photoinduced valence instability in the organic molecular compound tetrathiafulvalene-p-chloranil (TTF-CA). *Physical Review B 42*, 6853–6856.

[20] Horiuchi, S., Okimoto, Y., Kumai, R., and Tokura, Y. (2003) Quantum phase transition in organic charge-transfer complexes. *Science (New York, N.Y.) 299*, 229–232.

[21] Kagawa, F., Horiuchi, S., Tokunaga, M., Fujioka, J., and Tokura, Y. (2010) Ferroelectricity in a one-dimensional organic quantum magnet. *Nature Physics 6*, 169–172.

[22] Horiuchi, S., and Tokura, Y. (2008) Organic ferroelectrics. *Nature Materials 7*, 357–366.

[23] Di Maiolo, F., Sissa, C., and Painelli Anna, (2016) Combining intra- and intermolecular charge-transfer: a new strategy towards molecular ferromagnets and multiferroics. *Scientific reports 6*, 19682–19688.

[24] D'Avino, G., and Verstraete, M. J. (2014) Are Hydrogen-Bonded Charge Transfer Crystals Room Temperature Ferroelectrics? *Physical Review Letters 113*, 237602.

[25] Guasch, J., Grisanti, L., Souto, M., Lloveras, V., Vidal-Gancedo, J., Ratera, I., Painelli, A., Rovira, C., and Veciana, J. (2013) Intra- and intermolecular charge transfer in aggregates of tetrathiafulvalene-triphenylmethyl radical derivatives in solution. *Journal of the American Chemical Society 135*, 6958–6967.

[26] Souto, M., Guasch, J., Lloveras, V., Mayorga, P., and Lo, J. T. (2013) Thermomagnetic Molecular System Based on TTF-PTM Radical: Switching the Spin and Charge Delocalization. *The Journal of Physical Chemistry Letters 4*, 2721–2726.

[27] Mulliken, S. (1952) Molecular Compounds and their Spectra, 111. *Journal of American Chemical Society 3058*, 811–824.

[28] Marcus, R. A. (1992) Electron Transfer Reactions in Chemistry : Theory and Experiment. *Review of Modern Physics 32*, 599–610.

[29] Oudar, J. L., and Chemla, D. S. (1977) Hyperpolarizabilities of the nitroanilines and their relations to the excited state dipole moment. *The Journal of Chemical Physics 66*, 2664–2668.

[30] Painelli, A. (1998) Vibronic contribution to static NLO properties: exact results for the DA dimer. *Chemical Physics Letters 285*, 352–358.

[31] Sissa, C., Terenziani, F., Painelli, A., Abbotto, A., Bellotto, L., Marinzi, C., Garbin, E., Ferrante, C., and Bozio, R. (2010) Dimers of quadrupolar chromophores in solution: electrostatic interactions and optical spectra. *The journal of Physical Chemistry. B 114*, 882–893.

[32] Painelli, A., and Terenziani, F. (2003) Multielectron transfer in clusters of polar-polarizable chromophores. *Journal of the American Chemical Society 125*, 5624–5625.

[33] Terenziani, F., and Painelli, A. (2003) Supramolecular interactions in clusters of polar and polarizable molecules. *Physical Review B 68*, 165405–165413.

[34] Sukegawa, J., Schubert, C., Zhu, X., Tsuji, H., Guldi, D. M., and Nakamura, E. (2014) Electron transfer through rigid organic molecular wires enhanced by electronic and electronvibration coupling. *Nature Chemistry 6*, 899–905.

[35] Painelli, A., Del Freo, L., and Terenziani, F. (2001) Vibronic contributions to resonant NLO responses: two-photon absorption in push-pull chromophores. *Chemical Physics Letters 346*, 470–478.

[36] Terenziani, F., Painelli, A., Katan, C., Charlot, M., and Blanchard-Desce, M. (2006) Charge instability in quadrupolar chromophores: Symmetry breaking and solvatochromism. *Journal of the American Chemical Society 128*, 15742–15755.

[37] Sissa, C., Terenziani, F., Painelli, A., Siram, R. B. K., and Patil, S. (2012) Spectroscopic characterization and modeling of quadrupolar charge-transfer dyes with bulky substituents. *The Journal of Physical Chemistry B 116*, 4959–4966.

[38] Terenziani, F., and Painelli, A. (2003) Time-resolved spectra of polar-polarizable chromophores in solution. *Chemical Physics 295*, 35–46.

[39] Terenziani, F., and Painelli, A. (2015) Two-dimensional electronic-vibrational spectra: modeling correlated electronic and nuclear motion. *Phys. Chem. Chem. Phys. 17*, 13074–13081.

[40] Terenziani, F., D'Avino, G., and Painelli, A. (2007) Multichromophores for nonlinear optics: designing the material properties by electrostatic interactions. *Chemphyschem : a European Journal of Chemical Physics and Physical Chemistry 8*, 2433–2444.

[41] Terenziani, F., Painelli, A., Girlando, A., and Metzger, R. M. (2004) From Solution to Langmuir-Blodgett Films: Spectroscopic Study of a Zwitterionic Dye. *The Journal of Physical Chemistry B 108*, 10743–10750.

[42] D'Avino, G., Grisanti, L., Guasch, J., Ratera, I., Veciana, J., and Painelli, A. (2008) Bistability in Fc-PTM Crystals: The Role of Intermolecular Electrostatic Interactions. *Journal of the American Chemical Society 130*, 12064–12072.

[43] Guasch, J., Grisanti, L., Jung, S., Morales, D., D'Avino, G., Souto, M., Fontrodona, X., Painelli, A., Renz, F., Ratera, I., and Veciana, J. (2013) Bistability of Fc-PTM-Based dyads: The role of the donor strength. *Chemistry of Materials 25*, 808–814.

[44] Sissa, C., Terenziani, F., Painelli, A., Manna, A. K., and Pati, S. K. (2012) Resonance energy transfer between polar charge-transfer dyes : A focus on the limits of the dipolar approximation. *Chemical Physics 404*, 9–15.

[45] Terenziani, F., Morone, M., Gmouh, S., and Blanchard-Desce, M. (2006) Linear and two-photon absorption properties of interacting polar chromophores: standard and unconventional effects. *Chemphyschem : a European journal of chemical physics and physical chemistry 7*, 685–696.

[46] Terenziani, F., Sissa, C., and Painelli, A. (2008) Symmetry breaking in octupolar chromophores: Solvatochromism and electroabsorption. *Journal of Physical Chemistry B 112*, 5079–5087.

[47] Sissa, C., Parthasarathy, V., Drouin-Kucma, D., Werts, M. H. V., Blanchard-Desce, M., and Terenziani, F. (2010) The effectiveness of essential-state models in the description of optical properties of branched push-pull chromophores. *Physical Chemistry Chemical Physics 12*, 11715–11727.

[48] Terenziani, F., Painelli, A., and Comoretto, D. (2000) Solvation effects and inhomogeneous broadening in optical spectra of phenol blue. *Journal of Physical Chemistry A 104*, 11049–11054.

[49] Sissa, C., Painelli, A., Blanchard-Desce, M., and Terenziani, F. (2011) Fluorescence anisotropy spectra disclose the role of disorder in optical spectra of branched intramolecular-charge-transfer molecules. *Journal of Physical Chemistry B 115*, 7009–7020.

[50] Liptay, W. (1969) Electrochromism and Solvatochromism. *Angewandte Chemie International Edition in English 8*, 177–188.

[51] Bella, S. D., Marks, T. J., and Ratner, M. A. (1994) Environmental Effects on Nonlinear Optical Chromophore Performance. Calculation of Molecular Quadratic Hyperpolarizabilities in Solvating Media. *Journal of the American Chemical Society 116*, 4440–4445.

[52] Mongin, O., Porrès, L., Charlot, M., Katan, C., and Blanchard-Desce, M. (2007) Synthesis, fluorescence, and two-photon absorption of a series of elongated rodlike and banana-shaped quadrupolar fluorophores: a comprehensive study of structure-property relationships. *Chemistry - A European Journal 13*, 1481–1498.

[53] Patra, A., Anthony, S. P., and Radhakrishnan, T. P. (2007) Tris(4-cyanophenyl)amine: Simple Synthesis via Self-assembly; Strong Fluorescence in Solution, Nano/microcrystals, and Solid. *Advanced Functional Materials 17*, 2077–2084.

[54] Katan, C., Terenziani, F., Mongin, O., Werts, M. H. V., Porrès, L., Pons, T., Mertz, J., Tretiak, S., and Blanchard-Desce, M. (2005) Effects of (multi)branching of dipolar chromophores on photophysical properties and two-photon absorption. *Journal of Physical Chemistry A 109*, 3024–3037.

[55] Le Droumaguet, C., Mongin, O., Werts, M. H. V., and Blanchard-Desce, M. (2005) Towards "smart" multiphoton fluorophores: strongly solvatochromic probes for two-photon sensing of micropolarity. *Chemical Communications 2*, 2802–2804.

[56] Kolpashchikov, D. M. (2005) Binary Malachite Green Aptamer for Fluorescent Detection of Nucleic Acids. *Journal of the American Chemical Society 127*, 12442–12443.

[57] Vogel, M., and Rettig, W. (1985) Efficient intramolecular fluorescence quenching in triphenylmethane-dyes involving excited states with charge separation and twisted conformations. *Ber.Bunsenges.Phys.Chem. 89*, 962–968.

[58] Brey, L. A., Schuster, G. B., and Drickamer, H. G. (1977) High pressure studies of the effect of viscosity on fluorescence efficiency in crystal violet and auramine O. *The Journal of Chemical Physics 67*, 2648–2650.

[59] Van Der Meer, M. J., Zhang, H., and Glasbeek, M. (2000) Femtosecond fluorescence upconversion studies of barrierless bond twisting of auramine in solution. *Journal of Chemical Physics 112*, 2878–2887.

[60] Yoshizawa, M., Suzuki, K., Kubo, A., and Saikan, S. (1998) Femtosecond study of S2-S0 fluorescence in malachite green in solutions. *Chemical Physics Letters 290*, 43–48.

[61] Janowski, A., and Rzeszotarska, J. (1980) Anomalous (S2-S0) luminescence of some derivatives of triphenylmethane dyes and their complexes with rare earth metals. *Journal of Luminescence 21*, 409–416.

[62] Campo, J., Wenseleers, W., Goovaerts, E., Szablewski, M., and Cross, G. H. (2008) Accurate Determination and Modeling of the Dispersion of the First Hyperpolarizability of an Efficient Zwitterionic Nonlinear Optical Chromophore by Tunable Wavelength Hyper-Rayleigh Scattering. *The Journal of Physical Chemistry C 112*, 287–296.

[63] Thorley, K. J., Hales, J. M., Kim, H., Ohira, S., Brédas, J. L., Perry, J. W., and Anderson, H. L. (2013) Cyanine-like dyes with large bond-length alternation. *Chemistry - A European Journal 19*, 10370–10377.

[64] We are not fully convinced about the solvent used in this paper since BG is non fluorescent in acetonitrile, making it impossible to obtain two-photon excited fluorescence data.

[65] Rafiq, S., Yadav, R., and Sen, P. (2010) Microviscosity inside a nanocavity: A femtosecond fluorescence up-conversion study of malachite green. *Journal of Physical Chemistry B 114*, 13988–13994.

[66] Ferretti, A., Granucci, G., Lami, A., Persico, M., and Villani, G. (1996) Quantum mechanical and semiclassical dynamics at a conical intersection. *Journal of Chemical Physics 104*, 5517–5527.

[67] Schmidt, J. R., Parandekar, P. V., and Tully, J. C. (2008) Mixed quantum-classical equilibrium: Surface hopping. *The Journal of Chemical Physics 129*, 44104–44110.

[68] Matsika, S., and Krause, P. (2011) Nonadiabatic events and conical intersections. *Annual review of physical chemistry 62*, 621–643.

[69] Nelson, T., Fernandez-Alberti, S., Roitberg, A. E., and Tretiak, S. (2014) Nonadiabatic excited-state molecular dynamics: Modeling photophysics in organic conjugated materials. *Accounts of Chemical Research 47*, 1155–1164.

[70] Persico, M., and Granucci, G. (2014) An overview of nonadiabatic dynamics simulations methods, with focus on the direct approach versus the fitting of potential energy surfaces. *Theor. Chem. Acc. 133*, 1526–1554.

[71] Painelli, A., and Terenziani, F. (2000) Optical Spectra of Push-Pull Chromophores in Solution: A Simple Model. *The Journal of Physical Chemistry A 104*, 11041–11048.

[72] Weigel, A., Pfaffe, M., Sajadi, M., Mahrwald, R., Improta, R., Barone, V., Polli, D., Cerullo, G., Ernsting, N. P., and Santoro, F. (2012) Barrierless photoisomerisation of the simplest cyanine: Joining computational and femtosecond optical spectroscopies to trace the full reaction path. *Physical Chemistry Chemical Physics 14*, 13350–13364.

[73] Dhar, L., Rogers, J. A., and Nelson, K. A. (1994) Time-resolved vibrational spectroscopy in the impulsive limit. *Chemical Reviews 94*, 157–193.

[74] Chesnoy, J., and Mokhtari, A. (1988) Resonant impulsive-stimulated Raman scattering on malachite green. *Physical Review A 38*, 3566–3576.

[75] Fragnito, H. L., Bigot, J.-Y., Becker, P. C., and Shank, C. V. (1989) Evolution of the vibronic absorption spectrum in a molecule following impulsive excitation with a 6 fs optical pulse. *Chemical Physics Letters 160*, 101–104.

[76] Pollard, W. T., Fragnito, H. L., Bigot, J.-Y., Shank, C. V., and Mathies, R. A. (1990) Quantum-mechanical theory for 6 fs dynamic absorption spectroscopy and its application to nile blue. *Chemical Physics Letters 168*, 239–245.

[77] Heller, E. J. (1981) The Semiclassical Way to Molecular Spectroscopy. *Acc. Chem. Res. 14*, 368–375.

[78] Zhang, W.-M., Feng, D., and Gilmore, R. (1990) Coherent states: Theory and some applications. *Reviews of Modern Physics 62*, 867–927.

[79] Painelli, A., Terenziani, F., Angiolini, L., Benelli, T., and Giorgini, L. (2005) Chiral interactions in azobenzene dimers: a combined experimental and theoretical study. *Chemistry - A European Journal 11*, 6053–6063.

[80] Girlando, A., Painelli, A., Bewick, S. A., and Soos, Z. G. (2004) Charge fluctuations and electron-phonon coupling in organic charge-transfer salts with neutral-ionic and Peierls transitions. *Synthetic Metals 141*, 129–138.

[81] McConnell, H. M., Hoffman, B. M., and Metzger, R. M. (1965) Charge Transfer in Molecular Crystals. *Proceedings of the National Academy of Sciences of the United States of America 53*, 46–50.

[82] Soos, Z. G., and Painelli, A. (2007) Metastable domains and potential energy surfaces in organic charge-transfer salts with neutral-ionic phase transitions. *Physical Review B 75*, 155119–155130.

[83] Painelli, A., and Girlando, A. (1987) Zero-temperature phase diagram of mixed-stack charge-transfer crystals. *Physical Review B 37*, 5748–5760.

[84] Torrance, J. B., Vazquez, J. E., Mayerle, J. J., and Lee, V. Y. (1981) Discovery of a neutral-to-ionic phase transition in organic materials. *Physical Review Letters 46*, 253–257.

[85] Torrance, J. B., Girlando, A., Mayerle, J. J., Crowley, J. I., Lee, V. Y., Batail, P., and LaPlaca, S. J. (1981) Anomalous nature of neutral-to-ionic phase transition in tetrathiafulvalene-chloranil. *Physical Review Letters 47*, 1747–1750.

[86] Girlando, A., and Painelli, A. (1986) Regular-dimerized stack and neutral-ionic interfaces in mixed-stack organic charge-transfer crystals. *Physical Review B 34*, 2131–2139.

[87] Soos, Z. G., Bewick, S. a., Peri, A., and Painelli, A. (2004) Dielectric response of modified Hubbard models with neutral-ionic and Peierls transitions. *The Journal of chemical physics 120*, 6712–6720.

[88] Okamoto, H., Mitani, T., Tokura, Y., Koshihara, S., Komatsu, T., Iwasa, Y., Koda, T., and Saito, G. (1991) Anomalous dielectric response in tetrathiafulvalene-p-chloranil as observed in temperature- and pressure-induced neutral-to-ionic phase transition. *Physical Review B 43*, 8224–8232.

[89] Horiuchi, S., Okimoto, Y., Kumai, R., and Tokura, Y. (2003) Quantum phase transition in organic charge-transfer complexes. *Science (New York, N.Y.) 299*, 229–232.

[90] Collet, E., Buron-Le Cointe, M., and Cailleau, H. (2006) X-ray diffraction investigation of the nature and the mechanism of photoinduced phase transition in molecular materials. *Journal of the Physical Society of Japan 75*, 1–9.

[91] Cavatorta, L., Painelli, A., and Soos, Z. G. (2015) Coherent excitations at the neutral-ionic transition: Femtosecond dynamics on diabatic potential energy surfaces. *Physical Review B 91*, 1–10.

[92] Masino, M., Girlando, A., and Soos, Z. G. (2003) Evidence for a soft mode in the temperature induced neutral-ionic transition of TTF-CA. *Chemical Physics Letters 369*, 428–433.

[93] Girlando, A., Masino, M., Painelli, A., Drichko, N., Dressel, M., Brillante, A., Della Valle, R. G., and Venuti, E. (2008) Direct evidence of overdamped Peierls-coupled modes in the temperature-induced phase transition in tetrathiafulvalene-chloranil. *Physical Review B - Condensed Matter and Materials Physics 78*, 1–12.

[94] Ranzieri, P., Masino, M., Girlando, A., and Lemée-Cailleau, M.-H. (2007) Temperature-induced valence and structural instability in DMTTF-CA: Single-crystal Raman and infrared measurements. *Physical Review B 76*, 134115–134123.

[95] Painelli, A., and Girlando, A. (1986) Electronmolecular vibration (e-mv) coupling in charge-transfer compounds and its consequences on the optical spectra: A theoretical framework. *The Journal of Chemical Physics 84*, 5655–5673.

[96] Girlando, A., Painelli, A., and Pecile, C. (1985) Electron-Intramolecular Phonon Coupling in regular and Dimerized Mixed Stack Organic Semiconductors. *Molecular Crystals and Liquid Crystals 120*, 17–26.

[97] Girlando, A., Marzola, F., Pecile, C., and Torrance, J. B. (1983) Vibrational spectroscopy of mixed stack organic semiconductors: Neutral and ionic phases

of tetrathiafulvalenechloranil (TTFCA) charge transfer complex. *The Journal of Chemical Physics 79*, 1075–1085.

[98] Horiuchi, S., Okimoto, Y., Kumai, R., and Tokura, Y. (2000) Anomalous valence fluctuation near a ferroelectric transition in an organic charge-transfer complex. *Journal of the Physical Society of Japan 69*, 1302–1305.

[99] D'Avino, G., Masino, M., Girlando, A., and Painelli, A. (2011) Correlated electrons in soft lattices: Raman scattering evidence of the nonequilibrium dielectric divergence at the neutral-ionic phase transition. *Physical Review B 83*, 161105–161109.

[100] Buron-Le Cointe, M., Lemée-Cailleau, M. H., Cailleau, H., Ravy, S., Bérar, J. F., Rouzière, S., Elkaïm, E., and Collet, E. (2006) One-dimensional fluctuating nanodomains in the charge-transfer molecular system TTF-CA and their first-order crystallization. *Physical Review Letters 96*, 205503–205507.

[101] Collet, E., Lemée-Cailleau, M. H., Buron-Le Cointe, M., Cailleau, H., Ravy, S., Luty, T., Bérar, J. F., Czarnecki, P., and Karl, N. (2002) Direct evidence of lattice-relaxed charge transfer exciton strings. *Europhysics Letters 57*, 67–73.

[102] D'Avino, G., Girlando, A., Painelli, A., Lemée-Cailleau, M.-H., and Soos, Z. G. (2007) Anomalous dispersion of optical phonons at the neutral-ionic transition: evidence from diffuse x-ray scattering. *Physical Review Letters 99*, 156407–156411.

[103] Del Freo, L., Painelli, A., and Soos, Z. G. (2002) Giant Infrared Intensity of the Peierls Mode at the Neutral-Ionic Phase Transition. *Physical Review Letters 89*, 027402–027408.

[104] Soos, Z. G., Bewick, S. A., Peri, A., and Painelli, A. (2004) Dielectric response of modified Hubbard models with neutral-ionic and Peierls transitions. *The Journal of chemical physics 120*, 6712–6720.

[105] Rice, M. J. (1979) Towards the experimental determination of the fundamental microscopic parameters of organic ion-radical compounds. *Solid State Communications 31*, 93–98.

[106] Soos, Z. G., and Ramasesha, S. (1989) Valence Bond Theory and Chemical Structure. *Valence Bond Theory and Chemical Structure* 81.

[107] Girlando, A., Painelli, A., Pecile, C., Calestani, G., Rizzoli, C., and Metzger, R. M. (1993) Ground state optical properties of charge transfer crystals close to the neutral-ionic interface: Tetrathiafulvalene-2,5-dichloro-p-benzoquinone. *The Journal of Chemical Physics 98*, 7692–7698.

[108] Painelli, a., and Girlando, A. (1987) Mixed regular stack chargetransfer crystals: Fundamental microscopic parameters from optical spectra. *The Journal of Chemical Physics 87*, 1705–1711.

[109] Ida, T., Yakushi, K., and Kuroda, H. (1989) Pressure dependence of the polarized reflectance spectrum of a solid chargetransfer complex, perylene-hexacyanobutadiene (HCBD). *Journal of Chemical Physics 91*, 3450–3455.

[110] Girlando, A., Pecile, C., and Torrance, J. B. (1985) A key to understanding ionic mixed stacked organic solids: Tetrathiafulvalene-bromanil (TTF-BA). *Solid State Communications 54*, 753–759.

[111] Masino, M., Girlando, A., Farina, L., and Brillante, A. (2001) A new type of neutral-ionic interface in mixed-stack organic charge-tranfer crystals: Temperature induced ionicity change in ClMePD-DMeDCNQI. *Phys. Chem. Chem. Phys. 3*, 1904–1910.

[112] Stewart, J. J. P. (2013) Optimization of parameters for semiempirical methods VI: more modifications to the NDDO approximations and re-optimization of parameters. *Journal of Molecular Modeling 19*, 1–32.

[113] Stewart, J. J. P. (2012) Computational Chemistry. *Mopac2012 Volume 94*.

[114] Frisch, M. J. et al. Gaussian09 Revision E.01.

[115] Chai, J.-D., and Head-Gordon, M. (2008) Long-range corrected hybrid density functionals with damped atomatom dispersion corrections. *Physical Chemistry Chemical Physics 10*, 6615–6620.

[116] Reed, A. E., Weinstock, R. B., and Weinhold, F. (1985) Natural population analysis. *Journal of Chemical Physics 83*, 735–746.

[117] Besler, B. H., Merz, K. M., and Kollman, P. A. (1990) Atomic charges derived from semiempirical methods. *Journal of Computational Chemistry 11*, 431–439.

[118] Méndez, H., Heimel, G., Opitz, A., Sauer, K., Barkowski, P., Oehzelt, M., Soeda, J., Okamoto, T., Takeya, J., Arlin, J.-B., Balandier, J.-Y., Geerts, Y., Koch, N., and Salzmann, I. (2013) Doping of Organic Semiconductors: Impact of Dopant Strength and Electronic Coupling. *Angewandte Chemie International Edition 52*, 7751–7755.

[119] Bewick, S. A., Pascal, R. A., Ho, D. M., Soos, Z. G., Masino, M., and Girlando, A. (2005) Disorder in organic charge-transfer single crystals: dipolar disorder in ClMePD-DMeDCNQI. *The Journal of Chemical Physics 122*, 24710–24718.

[120] Zhu, L., Yi, Y., Li, Y., Kim, E. G., Coropceanu, V., and Brédas, J. L. (2012) Prediction of remarkable ambipolar charge-transport characteristics in organic mixed-stack charge-transfer crystals. *Journal of the American Chemical Society 134*, 2340–2347.

[121] D' Avino, G., Grisanti, L., Guasch, J., Ratera, I., Veciana, J., and Painelli, A. (2008) Bistability in Fc-PTM crystals: the role of intermolecular electrostatic interactions. *Journal of the American Chemical Society 130*, 12064–72.

[122] Collet, E., Buron-Le Cointe, M., Lemée-Cailleau, M., Cailleau, H., Toupet, L., Meven, M., Mattauch, S., Heger, G., and Karl, N. (2001) Structural evidence of ferrielectric neutral-ionic layered ordering in 2,6-dimethyltetrathiafulvalene-p-chloranil. *Physical Review B 63*, 1–12.

[123] Iwasa, Y., Koda, T., Tokura, Y., Kobayashi, A., Iwasawa, N., and Saito, G. (1990) Temperature-induced neutral-ionic transition in tetramethylbenzidine-tetracyanoquinodimethane (TMB-TCNQ). *Physical Review B 42*, 2374–2377.

[124] Castagnetti, N., and Girlando, A. private communication.

[125] Mayerle, J. J., Torrance, J. B., and Crowley, J. I. (1979) Mixed-stack complexes of tetrathiafulvalene. The structures of the charge-transfer complexes of TTF with chloranil and fluoranil. *Acta Crystallographica Section B 35*, 2988–2995.

[126] Torrance, J. B., Scott, B. a., Welber, B., Kaufman, F. B., and Seiden, P. E. (1979) Optical properties of the radical cation tetrathiafulvalenium (TTF+) in its mixed-valence and monovalence halide salts. *Physical Review B 19*, 730–741.

[127] García, P., Dahaoui, S., Fertey, P., Wenger, E., and Lecomte, C. (2005) Crystallographic investigation of temperature-induced phase transition of the tetrathiafulvalene-p-bromanil, TTF-BA charge transfer complex. *Physical Review B - Condensed Matter and Materials Physics 72*, 1–10.

[128] Huang, P., and Carter, E. A. (2008) Advances in correlated electronic structure methods for solids, surfaces, and nanostructures. *Annual Review of Physical Chemistry 59*, 261–290.

[129] Cohen, A. J., Mori-Sanchéz, P., and Yang, W. (2012) Challenges for Density Functional Theory. *Chemical Reviews 112*, 289–320.

[130] Guasch, J., Grisanti, L., Lloveras, V., Vidal-Gancedo, J., Souto, M., Morales, D. C., Vilaseca, M., Sissa, C., Painelli, A., Ratera, I., Rovira, C., and Veciana, J. (2012) Induced self-assembly of a tetrathiafulvalene-based open-shell

dyad through intramolecular electron transfer. *Angewandte Chemie - International Edition 51*, 11024–11028.

[131] Souto, M., Solano, M. V., Jensen, M., Bendixen, D., Delchiaro, F., Girlando, A., Painelli, A., Jeppesen, J. O., Rovira, C., Ratera, I., and Veciana, J. (2015) Self-Assembled Architectures with Segregated Donor and Acceptor Units of a Dyad Based on a Monopyrrolo-Annulated TTFPTM Radical. *Chemistry A European Journal 21*, 8816–8825.

[132] Heimel, G., Romaner, L., Brédas, J.-L., and Zojer, E. (2006) Organic/metal interfaces in self-assembled monolayers of conjugated thiols: A first-principles benchmark study. *Surface Science 600*, 4548–4562.

[133] Saito, N., Hayashi, K., Sugimura, H., Takai, O., and Nakagiri, N. (2001) Surface potentials of patterned organosilane self-assembled monolayers acquired by Kelvin probe force microscopy and ab initio molecular calculation. *Chemical Physics Letters 349*, 172–177.

[134] Dreuw, A., Weisman, J. L., and Head-Gordon, M. (2003) Long-range charge-transfer excited states in time-dependent density functional theory require nonlocal exchange. *The Journal of Chemical Physics 119*, 2943–2946.

[135] Tomasi, J., Mennucci, B., and Cammi, R. (2005) Quantum mechanical continuum solvation models. *Chemical Reviews 105*, 2999–3093.

[136] Montgomery, J. a., Frisch, M. J., Ochterski, J. W., Petersson, G. a., and Introduction, I. (2001) A complete basis set model chemistry. VI. Use of density functional geometries and frequencies. *Journal of Chemical Physics 110*, 2822–2827.

[137] Grisanti, L., D'Avino, G., Painelli, A., Guasch, J., Ratera, I., and Veciana, J. (2009) Essential state models for solvatochromism in donor-acceptor molecules: the role of the bridge. *The Journal of Physical Chemistry. B 113*, 4718–4725.

[138] Jiang, W., Xiao, C., Hao, L., Wang, Z., Ceymann, H., Lambert, C., Di Motta, S., and Negri, F. (2012) Localization/delocalization of charges in bay-linked perylene bisimides. *Chemistry - A European Journal 18*, 6764–6775.

[139] Jacquemin, D., Wathelet, V., Perpète, E. a., and Adamo, C. (2009) Extensive TD-DFT benchmark: Singlet-excited states of organic molecules. *Journal of Chemical Theory and Computation 5*, 2420–2435.

[140] Peach, M. J. G., Benfield, P., Helgaker, T., and Tozer, D. J. (2008) Excitation energies in density functional theory: An evaluation and a diagnostic test. *The Journal of Chemical Physics 128*, 044118–044126.

[141] Eriksen, J. J., Sauer, S. P., Mikkelsen, K. V., Christiansen, O., Jensen, H. J. A., and Kongsted, J. (2013) Failures of TDDFT in describing the lowest intramolecular charge-transfer excitation in para-nitroaniline. *Molecular Physics 111*, 1235–1248.

[142] Casida, M. E. (2009) Time-dependent density-functional theory for molecules and molecular solids. *Journal of Molecular Structure: THEOCHEM 914*, 3–18.

[143] Neese, F. (2012) The ORCA program system. *Wiley Interdisciplinary Reviews: Computational Molecular Science 2*, 73.

[144] Geskin, V., Stadler, R., and Cornil, J. (2009) Multideterminant assessment of mean-field methods for the description of electron transfer in the weak-coupling regime. *Physical Review B - Condensed Matter and Materials Physics 80*, 1–13.

[145] Jankowska, J., Sadlej, J., and Sobolewski, A. L. (2015) Electric field control of proton-transfer molecular switching: molecular dynamics study on salicylidene aniline. *Phys. Chem. Chem. Phys. 17*, 14484–14488.

[146] Evans, S. D., and Ulman, A. (1990) Surface potential studies of alkyl-thiol monolayers adsorbed on gold. *Chemical Physics Letters 170*, 462–466.

[147] Evans, S. D., Urankar, E., Ulman, A., and Ferris, N. (1991) Self-Assembled Monolayers of Alkanethiols Containing a Polar Aromatic Group: Effects of the Dipole Position on Molecular Packing, Orientation, and Surface Wetting Properties. *Journal of American Chemical Society 113*, 4121–4131.

[148] Knapp, A. G. (1973) Surface potentials and their measurement by the diode method. *Surface Science 34*, 289–316.

[149] Campbell, I., Rubin, S., Zawodzinski, T., Kress, J., Martin, R., Smith, D., Barashkov, N., and Ferraris, J. (1996) Controlling Schottky energy barriers in organic electronic devices using self-assembled monolayers. *Physical Review B 54*, R14321–R14324.

[150] Love, J. C., Estroff, L. a., Kriebel, J. K., Nuzzo, R. G., and Whitesides, G. M. *Chemical Reviews*; 2005; Vol. 105; pp 1103–1169.

[151] Nonnenmacher, M., OBoyle, M. P., and Wickramasinghe, H. K. (1991) Kelvin probe force microscopy. *Applied Physics Letters 58*, 2921.

[152] Lübben, J. F., Baše, T., Rupper, P., Künniger, T., Macháček, J., and Guimond, S. (2011) Tuning the surface potential of Ag surfaces by chemisorption of oppositely-oriented thiolated carborane dipoles. *Journal of colloid and interface science 354*, 168–174.

[153] Egger, D. a., and Zojer, E. (2013) Anticorrelation between the Evolution of Molecular Dipole Moments and Induced Work Function Modi fi cations. *Phys. Chem. Lett. 4*, 3521–3526.

[154] Romaner, L., Heimel, G., Ambrosch-Draxl, C., and Zojer, E. (2008) The Dielectric Constant of Self-Assembled Monolayers. *Advanced Functional Materials 18*, 3999–4006.

[155] de Boer, B., Hadipour, A., Mandoc, M. M., van Woudenbergh, T., and Blom, P. W. M. (2005) Tuning of Metal Work Functions with Self-Assembled Monolayers. *Advanced Materials 17*, 621–625.

[156] Topping, J. (1927) On the Mutual Potential Energy of a Plane Network of Doublets. *Proceedings of the Royal Society A: Mathematical, Physical and Engineering Sciences 114*, 67–72.

[157] Ratera, I., and Veciana, J. (2012) Playing with organic radicals as building blocks for functional molecular materials. *Chemical Society Reviews 41*, 303–349.

[158] Amicangelo, J. C. (2005) Theoretical study of the benzene excimer using time-dependent density functional theory. *The Journal of Physical Chemistry. A 109*, 9174–9182.

[159] Stevens, B., and Hutton, E. (1960) Radiative Life-time of the Pyrene Dimer and the Possible Role of Excited Dimers in Energy Transfer Processes. *Nature 186*, 1045–1046.

[160] Stevens, B., and Ban, M. I. (1964) Spectrophotometric determination of enthalpies and entropies of photoassociation for dissolved aromatic hydrocarbons. *Trans. Faraday Soc. 60*, 1515–1523.

[161] Kim, D., and Brédas, J. L. (2009) Triplet excimer formation in platinum-based phosphors: A theoretical study of the roles of Pt-Pt bimetallic interactions and interligand π-π interactions. *Journal of the American Chemical Society 131*, 11371–11380.

[162] Hattori, Y., Kusamoto, T., and Nishihara, H. (2014) Luminescence, Stability, and Proton Response of an Open-Shell (3,5-Dichloro-4-pyridyl)bis(2,4,6-trichlorophenyl)methyl Radical. *Angewandte Chemie International Edition 53*, 11845–11848.

[163] D'Agostino, S., Grepioni, F., Braga, D., Moreschi, D., Fattori, V., Delchiaro, F., Di Motta, S., and Negri, F. (2013) Exciton coupling in molecular salts of 2-(1,8-naphthalimido)ethanoic acid and cyclic amines: modulation of the solid-state luminescence. *CrystEngComm 15*, 10470–10480.

[164] Orr, B. J., and Ward, J. F. (1971) Perturbation theory of the non-linear optical polarization of an isolated system. *Molecular Physics 20*, 513–526.

[165] Willetts, A., Rice, J. E., Burland, D. M., and Shelton, D. P. (1992) Problems in the comparison of theoretical and experimental hyperpolarizabilities revisited. *Journal of Chemical Physics 97*, 7590–7599.

[166] Andrews, S. S. (2004) Using rotational averaging to calculate the bulk response of isotropic and anisotropic samples from molecular parameters. *Journal of Chemical Education 81*, 877.

[167] Dewar, M. J. S., Zoebisch, E. G., Healy, E. F., and Stewart, J. J. P. (1985) Development and use of quantum mechanical molecular models. 76. AM1: a new general purpose quantum mechanical molecular model. *Journal of the American Chemical Society 107*, 3902–3909.

[168] Stewart, J. J. P. (1989) Optimization of parameters for semiempirical methods I. Method. *Journal of Computational Chemistry 10*, 209–220.

[169] Stewart, J. J. P. (2013) Optimization of parameters for semiempirical methods VI: more modifications to the NDDO approximations and re-optimization of parameters. *Journal of Molecular Modeling 19*, 1–32.

[170] Rocha, G. B., Freire, R. O., Simas, A. M., and Stewart, J. J. P. (2006) RM1: A reparameterization of AM1 for H, C, N, O, P, S, F, Cl, Br, and I. *Journal of Computational Chemistry 27*, 1101–1111.

[171] Pople, J. a. (1967) Approximate Self-Consistent Molecular-Orbital Theory. V. Intermediate Neglect of Differential Overlap. *The Journal of Chemical Physics 47*, 2026–2033.

[172] Pople, J. a., and Segal, G. a. (1966) Approximate Self-Consistent Molecular Orbital Theory. III. CNDO Results for AB2 and AB3 Systems. *The Journal of Chemical Physics 44*, 3289–3296.

[173] Hohenberg, P., and Kohn, W. (1964) Inhomogeneous electron gas. *Physical Review B 136B*, B864–B871.

[174] Kohn, W., and Sham, L. J. (1965) Self-Consistent Equations Including Exchange and Correlation Effects. *Physical Review 140*, A1133–A1138.

[175] Becke, A. D. (1988) Density-functional exchange-energy approximation with correct asymptotic behavior. *Phys. Rev. A 38*, 3098–3100.

[176] Perdew, J. P. (1986) Density-functional approximation for the correlation energy of the inhomogeneous electron gas. *Physical Review B 33*, 8822–8824.

[177] Lee, C., Yang, W., and Parr, R. G. (1988) Development of the Colle-Salvetti correlation-energy formula into a functional of the electron density. *Physical Review B 37*, 785–789.

[178] Becke, A. D. (1993) Density-functional thermochemistry.III. The role of exact exchange. *The Journal of Chemical Physics 98*, 5648–5652.

[179] Devlin, F. J., Finley, J. W., Stephens, P. J., and Frisch, M. J. (1995) Ab Initio Calculation of Vibrational Absorption and Circular Dichroism Spectra Using Density Functional Force Fields: A Comparison of Local, Nonlocal, and Hybrid Density Functionals. *The Journal of Physical Chemistry 99*, 16883–16902.

[180] Yanai, T., Tew, D. P., and Handy, N. C. (2004) A new hybrid exchangecorrelation functional using the Coulomb-attenuating method (CAM-B3LYP). *Chemical Physics Letters 393*, 51–57.

[181] Zhao, Y., and Truhlar, D. G. (2008) The M06 suite of density functionals for main group thermochemistry, thermochemical kinetics, noncovalent interactions, excited states, and transition elements: two new functionals and systematic testing of four M06-class functionals and 12 other function. *Theoretical Chemistry Accounts 120*, 215–241.

[182] Runge, E., and Gross, E. K. U. (1984) Density-functional theory for time-dependent systems. *Physical Review Letters 52*, 997–1000.

[183] Dreuw, A., Dreuw, A., Head-gordon, M., and Head-gordon, M. (2005) Single-Reference ab Initio Methods for the Calculation of Excited States of Large Molecules. *Chemical Reviews 105*, 4009–4037.

List of Publications

5) Delchiaro F., Sissa C., Terenziani F., Painelli A., Campo J., Wenseleers W., *A comprehensive spectroscopic and theoretical study of brilliant green*, in preparation;

4) Delchiaro F., Girlando A., Painelli A, Banerjee A., D'Avino G. *Intermolecular charge transfer: Hubbard model parameters from quantum-chemical calculations*, in preparation;

3) Souto M., Solano M.V., Jensen M., Bendixen D., Delchiaro F., Girlando A., Painelli A., Jeppesen J.O., Rovira C., Ratera I., Veciana J., *Self-Assembled Architectures with Segregated Donor and Acceptor Units of a Dyad Based on a Monopyrrolo-Annulated TTFPTM Radical*, Chemistry A European Journal, 21 (2015) 8816-8825;

2) Sissa C, Delchiaro F., Di Maiolo F., Terenziani F., Painelli A., *Vibrational coherences in charge-transfer dyes: A non-adiabatic picture*, The Journal of Chemical Physics, 141 (2014) 164317-164327;

1) D'Agostino S., Grepioni F., Braga D., Moreschi D., Fattori V., Delchiaro F., Di Motta S., Negri F., *Exciton coupling in molecular salts of 2-(1,8-naphthalimido)ethanoic acid and cyclic amines: modulation of the solid-state luminescence*, CrystEngComm, 14 (2013) 10470-10480;